Cardiff University

Development of a Wireless Structural Health Monitoring System for Aerospace Application

Stephen Grigg

A thesis submitted in partial fulfilment for
the degree of Doctor of Philosophy

Mechanics, Materials and Advanced Manufacturing
School of Engineering

June 2018

Abstract

Structural health monitoring has a number of benefits to the aircraft industry, including improvements to safety, reduction in maintenance costs and potential weight savings. One reason why the aircraft industry is reluctant to apply such systems is the additional weight and integration issues caused by wiring them into the structures. The solution to this is the application of wireless technology, unfortunately this has its own problems and restrictions primarily due to the lack of available power, which would need to be sourced through energy harvesting.

One structural health monitoring technique which has been investigated for aircraft use is Acoustic Emission, which enables the detection and localisation of damage within a structure. A major problem with the application of this technology using a wireless system is that adequate time synchronisation of each node would require significantly more power than is available through energy harvesting methods.

This work presents the development of a technique to locate damage in complex aircraft structures, which was previously only applicable within simple plates. This method is used to successfully locate damage within fatigue testing on an aircraft wing panel. Furthermore, it can be applied within a wireless system without the need for highly accurate time synchronisation.

The work includes the development of a prototype wireless system which applies a simplified version of the developed localisation technique. This hardware is tested on a range of composite and metal structures, including two aircraft wings. The accuracy of the results and the low power requirements of the system support further development in order to apply the system to an aircraft structure.

DECLARATION

This work has not been submitted in substance for any other degree or award at this or any other university or place of learning, nor is being submitted concurrently in candidature for any degree or other award.

Signed …… (candidate) Date ……

STATEMENT 1

This thesis is being submitted in partial fulfilment of the requirements for the degree of PhD.

Signed …… (candidate) Date ……

STATEMENT 2

This thesis is the result of my own independent work/investigation, except where otherwise stated, and the thesis has not been edited by a third party beyond what is permitted by Cardiff University's Policy on the Use of Third Party Editors by Research Degree Students. Other sources are acknowledged by explicit references. The views expressed are my own.

Signed …… (candidate) Date ……

STATEMENT 3

I hereby give consent for my thesis, if accepted, to be available online in the University's Open Access repository and for inter-library loan, and for the title and summary to be made available to outside organisations.

Signed …….. (candidate) Date ……

Acknowledgements

There are a number of people who I would like to thank for their support throughout the process of completing this thesis. I will mention some of these below, however this section could easily be much longer and I very much appreciate everyone who has assisted me in any way over the last few years.

Firstly I would like to thank my supervisors Prof Carol Feartherston and Dr Rhys Pullin for their academic guidance and support throughout this process. Their input throughout my PhD has been invaluable and feedback on the content of this thesis has been very important. I would also like to thank Dr Matthew Pearson for his support from day one of my PhD, as well as Dr Ryan Marks and Dr Davide Crivelli whose technical assistance has been invaluable. I also owe a lot to everyone within the Structural Performance research group at Cardiff University, who are always on hand to give feedback and assistance whenever possible. Being part of such a fantastic research group was one of the reasons that I started the PhD process and without such a positive environment, I may not be where I am today.

As part of the SENTIENT (Innovate UK funded) project which funded my PhD I was lucky to work with a number of individuals from a range of companies. I would like to thank all these involved, it was a pleasure working with you. In particular I would like to thank David Jenman from BAE systems, who I spent many hours working over the phone and in person with to make the SENTIENT project as successful as it could be. Your drive and commitment to the project was inspiring and the light-hearted humour made the long days much more enjoyable. Another mention must also go to Dr Christophe Paget from Airbus. His input was not only vital at guiding the SENTIENT project, but he was the one who first inspired me to work within the field of Structural Health Monitoring during my time working with him as an intern six years ago.

I would also really like to thank my mum, Michelle, who's proof reading of this work has been very helpful as well as the rest of my family, Pete and Martin, who are always at hand to listen to me talk about things I'm sure they have little interest in over a beer or two. Also thankyou to our family friend Roger, who's additional proof reading was very beneficial.

My time at Cardiff University has been the best of my life, I would like to thank everyone who has made my time here so enjoyable throughout both my undergraduate and postgraduate study. A huge amount of this enjoyment is a result of the mountaineering club, which has allowed me to follow my passion for climbing and has taken me to some truly amazing places with some fantastic people. To everyone who has held my ropes in the last few years, thank you, when work is too much climbing clears my mind and I wouldn't have been able to do so without you.

Finally I would like to thank my girlfriend (and climbing partner) Lottie, who has supported me immensely this last year. You looked after me when I needed you after surgery and whenever I was a bit down in the dumps because of work, I look forward to the next stage of our life together.

List of Abbreviations

ADC - Analogue digital converter

AE - Acoustic emission

AIC - Akaike Information Criterion

AU - Acousto-Ultrosonics

BPF - Bandpass filter

BVID - Barely visible impact damage

CFRP - Carbon fibre reinforced polymer

CWT - Continuous wavelet transform

DIC - Digital Image Correlation

FFT - Fast Fourier transform

GLW - Guided Lamb Waves

GUI - Graphical user interface

HPF – High pass filter

H-N - Hsu-Nielsen

LISA - Local Interaction Simulation Approach

MAR - Measured Amplitude Ratio

MFC - Macro Fibre Composite

MRO - Maintenance, Repair and Overhaul

NDT - Non-Destructive Testing

PM - Phase Modulation

PZT – Lead Zicronate Titanate

RF - Radio Frequency

RMS - Root Mean Squared

RoD – Rate of Dispersion

SPS - Samples per Second

SHM - Structural Health Monitoring

SSMA - Single sensor modal analysis

TEG - Thermoelectric generators

TOA - Time of arrival

WSN - Wireless Sensor Networks

Contents

1 Introduction

Safety is of upmost concern to aircraft manufacturers and operators, with strict guidelines in place to ensure that any operational aircraft is as safe as possible, and as a result of this very few serious accidents occur. In addition to safety, operators require their aircraft to be cost effective, meaning that they require little maintenance and are as light as possible, so consuming less fuel. These goals have the potential to compromise safety if not applied correctly. Structural health monitoring can increase safety, reduce maintenance costs and allow for weight savings in the long term.

1.1 Damage, Maintenance and Repair of Aircraft

In the history of aircrafts a number of catastrophic failures have occurred due to fatigue of the structure, a select few will be mentioned here. From each of these accidents the industry has developed and learnt in order to prevent the same happening again. In 1948 a Martin-202 carrying 40 passengers crashed due to a fatigue crack in an aluminium joint on the wing spar causing failure of the wing. This accident was put down to poor design and choice of material, and prompted more thorough fatigue testing of similar parts (Schijve, 2009). Six years later in 1954 one of the most famous air accidents occurred where two Comet aircraft failed very early on in their lives, after 1286 and 903 flights. This was due to the depressurisation of the cabin causing additional stress on a square window in the fuselage, resulting in the growth of cracks due to the stress concentration at the corners (Swift, 1987). A lesser known fact is that fatigue testing had been conducted on the Comet fuselage before it entered service, with only minor cracks found after 16,000 flight cycles. This was because to save money the same specimen had already undergone high design load testing which resulted in small scale plastic yielding in the window area, which induced favourable residual stresses reducing crack growth (Schijve, 2009). The Comet disasters were caused by a lack of understanding of the effect of fatigue in aircraft and design has since changed significantly to address these problems. Not all failures however

can be attributed to fatigue damage, or even damage sustained during flight. In 1969 an F-111 aircraft crashed due to wing failure after only 120 flying hours. This was due to a large flaw on a heat treated steel part introduced during manufacture and undetected in the pre-commissioning tests. This led to the introduction of the damage tolerance concept, but more specifically the assumption that flaws were already present in the structure, meaning design considerations could be made accordingly (Schijve, 2009).

This is by no means a full account of accidents and definitely not all the accidents caused by fatigue, however it gives an indication of the types of failure which can happen in aircraft. Before each of these accidents the aircraft concerned were certified for airworthiness and so to the best of the expert's knowledge at the time, would have been safe. This highlights that when doing something that has never been done before, such as flying with a pressurised cabin or using a new material, even if all the precautions possible are taken problems can still occur, as the unknown can happen.

In recent years airworthiness guidelines and maintenance schedules have become more thorough however this doesn't rule out the possibility of serious incidents occurring due to fatigue. A good example of this is the problems that Airbus had in 2012 with their newest (at the time) and largest aircraft the A380, where significant cracks were discovered on the wings' rib feet, shown in Figure 1. The reason for this was the material chosen was more brittle than the stronger alternative and the interaction between composite and aluminium was not fully understood (Kaminski-Morrow, 2012a). After the discovery of this a retrofit was made with a more appropriate material resulting in an increased weight of around 90kg, on a total of 122 aircraft at great expense to Airbus. It is worth noting that these cracks were only discovered during repairs to structural damage to an airframe caused by engine failure (Kaminski-Morrow, 2012b). It cannot be said either way if the cracks would have been detected without this and if a serious incident would have occurred because of it. It does however highlight that unexpected

damage is still possible in a structure due to fatigue, especially in modern aircraft where new materials are being used and weight reduction is sought after.

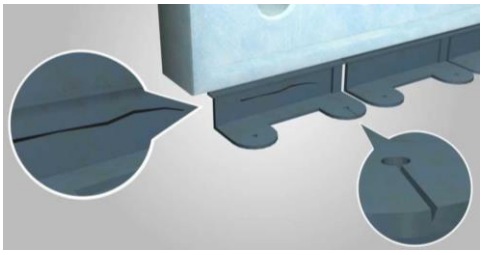

Figure 1 – Animation of A380 rib feet crack locations (News-Direct, 2012)

The constant changes within the aviation industry are well demonstrated by the introduction of composite materials in aircraft structures, predominantly the increase in the use of carbon fibre reinforced polymers (CFRP). Both of the two largest aircraft manufacturers (Airbus and Boeing) are investing heavily in CFRP with the newest generation of aircraft each having substantial usage, including for structural components, with the A350 XWB being 53% composite (Airbus, 2017) and the 787 Dreamliner being 50% (Boeing, 2017). The growth in popularity of composites is because of their high stiffness and greater strength to weight ratio when compared to metal. They do have some disadvantages, in particular regarding their tolerance to damage. Damage growth within metals is a very mature field and engineers are able to properly model a structure and have years of experience working with them, composites however are far less well established. In addition to this, if composite materials are impacted they are prone to what is known as a barely visible impact damage (BVID) which if undetected and allowed to grow could pose significant risk to aircraft safety (Lammering et al., 2018).

As mentioned previously, engineers view fatigue as a vital consideration when designing an aircraft and will do everything reasonably possible to prevent it from happening. That being said, to produce an aircraft that did not suffer from fatigue would probably be impossible so a great deal of effort is made to ensure fatigue damage doesn't become a safety issue. Before any flights

take place with a newly designed aircraft, fatigue tests are conducted on both small elements of the aircraft and on full scale aircraft structures. This is done within a laboratory based environment, loading the structure in a way which replicates the effect of a series of flight cycles. In the case of the full scale structure after a number of cycles the entire aircraft is stripped down and non-destructive testing (NDT) conducted upon each part. Any damage detected may trigger a redesign of certain parts, or lead to the area highlighted being closely monitored and replaced on a regular basis. The aircraft is then put together again and the process is repeated until the number of flight cycles that are needed have been conducted, which is typically much higher than any aircraft will ever fly.

For in-service aircraft it is not feasible to strip down the entire aircraft often, this would take a very long time and not be profitable for the airline. It also cannot be assumed that an aircraft in service will perform the same as the fatigue test craft, due to random events such as impacts and hard landings influencing the life of the aircraft. To ensure their safety a variety of different checks are performed at time or flight hours based intervals. Each aircraft operator has different inspection intervals and the time between them will depend on a number of factors including the aircraft's age and usage. Typically an aircraft's Maintenance, Repair and Overhaul (MRO) accounts for around 12-15% of its operating costs, however this can be much higher for old aircraft (Vieira, 2016). It must also be considered that while an aircraft is undergoing MRO it isn't making money, so minimising downtime is very important for the operator.

The simplest inspection is a transit check which is performed most days and involves quick checks to the vital system (usually by the pilot) as well as an external visual inspection of the structure for obvious damage. 'A' and 'B' checks are more intensive inspections of systems and are performed every 1-6 months. Neither of these tests require the aircraft to be taken out of service for an extended period. 'C' checks take 3-5 days and requires the aircraft to be taken to a specialist facility approximately every 20 months. These inspections are again mainly on the aircraft's systems however they do involve some specialist inspection of the aircraft structure,

in particular for areas where damage is expected. The final, and longest, inspection is a 'D' check, sometimes referred to as the 'structural check' which takes upwards of 20 days and is required approximately every 6 years. The 'D' check involves partial disassembly of the aircraft to allow for non-destructive testing to detect any structural damage over the airframe (Vieira, 2016).

If any of these tests reveal damage to the structure it will be repaired, or if possible the part will be replaced. These repairs have the potential to cause additional damage to the structure, especially in the case of a mechanically attached repair as additional holes need drilling. Such a repair may also cause stress concentrations in other areas of the structure which could result in more damage (Baker, 1999). It must also be considered that the repair may be ineffective at stopping the damage growing, so continuing inspections must be conducted on the repair on the assumption that it hasn't worked. Ideally the repair would be made as early as possible after the damage starts to grow, to reduce the size of the required repair, minimising potential complications and weight.

As thorough inspections are often many years apart, aircraft structures have to be damage tolerant, and for this to be the case it must be overdesigned to be able to allow fatigue damage growth as well as, in the case of composites, any undetected BVID (Baaran, 2009). This overdesign adds weight to the structure which in turn leads to higher fuel consumption and so environmental impact. The aircraft industry is now trying to move away from time based maintenance schedules and move towards condition based maintenance. Doing so could improve safety and make the aircraft more profitable, by reducing maintenance costs and more importantly decreasing the amount of time the aircraft is out of service due to scheduled maintenance (Joshi et al., 2012). To move to condition based maintenance the operator would need to be confident that damage wasn't growing within their aircraft. Structural health monitoring aims to do this.

1.2 Structural Health Monitoring

Structural Health Monitoring (SHM) is the process of continually monitoring a structure for damage, ideally throughout its entire life, meaning that when damage occurs a central system knows about it, and repairs can be made. This could consist of impact monitoring during the manufacture and transportation of parts prior to the aircraft flying, all the way through to fatigue damage and impact monitoring throughout the life of the aircraft. The core goals of an SHM system are to detect damage, locate where it came from, characterise what kind of damage it is and evaluate if it is a problem (Lammering et al., 2018). Ideally this process would be automated, so damage would be identified without the need for skilled operators to analyse and interpret the data.

Applying SHM to an aircraft structure has a number of benefits to the safety of the aircraft, the cost of its operation and its environmental impact. In terms of safety an SHM system on an aircraft adds an additional tool to monitor the structure, in particular with regard to BVID which may go un-detected and so may become a structural problem if allowed to grow (Lammering et al., 2018). Removing humans from the equation also improves the safety of an aircraft, as unfortunately humans can make mistakes.

For aircraft to fly commercially they must be profitable for the operator, this means that it must be on the ground undergoing MRO as little as possible. SHM has the potential to greatly reduce the costs associated with MRO on an aircraft structure. The application of SHM to an aircraft would not only allow damage to be identified as it occurs, but it would also mean that areas could be identified as 'clear' without the need for time consuming NDT techniques, reducing the required downtime for inspection (Lammering et al., 2018). Taken one step further SHM would allow for repairs to be made quickly in-between inspections if damage had been identified within the structure. This would reduce the impact the repair would have on the aircraft as a smaller repair could be applied. In addition to this, once a repair has been performed, SHM

allows the operator to know if it has been successful and whether it has caused damage to grow elsewhere without the need for regular inspections, as is usually the case (Baker, 1999).

Finally, SHM has the potential to improve the environmental impact and operational cost of aircraft by reducing fuel consumption. This is possible because of increased experience and confidence in using composites combined with SHM's ability to ensure the detection of damage allowing a more optimal structure to be designed (Lammering et al., 2018). Doing so would allow some of the redundancy within the structure to be removed without compromising safety. Investigation into the redesign of individual components has identified that weight savings upwards of 15% are possible in some cases with the proper application of SHM, so reducing the fuel consumption and cost of flying the aircraft (Speckmann, 2006).

1.3 Structural Health Monitoring Techniques

A large variety of SHM techniques exist. These can be split broadly into two categories, active and passive. Passive techniques are the most widely used and involve monitoring a physical parameter on a structure, for example Acoustic Emission (AE), vibration or strain. Active techniques require some form of input into the structure and the response is then measured.

The most applicable active technique for the aviation industry is known as Acousto-Ultrosonics (AU) or Guided Lamb Waves (GLW). This process involves exciting ultrasonic waves in the structure, typically using piezo-electric transducers and recording the received signals at other sensors. These can then be compared to a baseline signal where any change is an indication of damage within the structure (Zhao et al., 2007).

A number of passive techniques are viable for aircraft application, others less so. The monitoring of strain using fibre optic sensors is able to give an indication of the presence of damage (Güemes et al., 2018) by analysing irregularities in strain. This process does however require a large number of fibre optics to be bonded to, or embedded in, the structure. The monitoring of

vibration and analysis of frequency change has been shown to be an effective method of damage detection for a number of applications, for example bridge structures (Kim et al., 2007), however its sensitivity is typically too low to detect cracks within complex aircraft structures (Abbas et al., 2018).

One promising area of SHM which has previously been applied to aircrafts is the monitoring of AE. AE is the spontaneous release of energy caused by the growth of damage. When an AE event occurs in an aircraft, the stress waves produced form into Lamb waves, which are ultrasonic wave which form in plate like structure. These waves propagate through the aircraft and can be detected using piezo-electric transducers. Monitoring a structure for AE gives an indication of damage growing. AE monitoring is very common within bridges (Nair and Cai, 2010) and has some history of application in aircraft (Chuang, 1987). When initially applied on a large scale, AE monitoring wasn't very successful in aircraft and large scale testing has since died down due to a reluctance from the industry to test what was seen as unreliable technology. This led engineers to take a step back until they could better understand the technology they were working with.

One of the issues experienced was the reliability of the technique to always detect damage and properly locate it within complex structures. In recent years significant developments have been made regarding location techniques (Paget et al., 2003, Al-Jumaili et al., 2016) which have significantly improved the ability to locate AE within complex and composite structures, these are discussed in greater detail later in this thesis. Another problem was non-damage related noise causing false positives. This noise can be due to a number of factors, for example friction between two surfaces, however it tends to produce a significantly different wave then one produced by damage. However, advances in classification algorithms allow damage to be distinguished from noise in a wide range of cases, meaning certain events can be ignored, reducing the number of false positives. Other advances include research into the optimisation of sensor placement (Marks et al., 2017) and a greater understanding of wave propagation and interaction with complexity (Cho and Rose, 1996, Chang and Mal, 1999). The aforementioned

research and the positive results obtained show that the field of AE monitoring is more mature than it was when the less successful early aircraft testing took place, giving a positive indication that future testing and application of AE may be more successful.

One major issue that hasn't be properly addressed, and must be before AE monitoring can be applied on a large scale however, is that aircraft manufacturers are moving away from using wired systems. The main motivation for this is the weight reduction potential. Given that an A380 has over 300 miles of cables (Yedavalli and Belapurkar, 2011) the potential weight savings are huge if reliable wireless communications can be implemented. Given this move away from wired systems, it's very unlikely that anyone would want to add significant weight to the structure if the benefits achieved by doing so were not significant and beneficial in the short term. This means that any new SHM technology applied to an aircraft will most probably need to be wireless, both in terms of data communication and power.

Wireless AE monitoring systems are commercially available (MISTRAS, 2013a, Soundwel, 2017) and have been use for monitoring AE in bridges, however what is currently available is relatively large, heavy and not particularly low power. For wireless AE monitoring to be implemented in aircraft structures the hardware would ideally be completely self-powered through energy harvesting, which currently can only offer limited power levels. This means that any wireless system must be very low power.

1.4 Aims and Objectives

Wireless SHM monitoring has been successfully applied in a variety of applications such as bridge structures (Kim et al., 2007), however the aircraft industry has yet to implement this technology. With a focus on AE monitoring, this thesis aims to identify problems which limit the use of wireless SHM in aircraft structures, to propose and develop solutions to some of these problems and to use this information to specify the requirements of the wireless hardware developed as part of the SENTIENT project.

The key objectives are:

- Investigate all areas of wireless SHM systems and identify the problems which require further research for AE monitoring to be successfully applied within aircraft.
- Develop a low power wireless system that has the potential to be self-powered if combined with suitable energy harvesting methods
- Further develop an AE source location technique so that it can be applied to complex structures, such as aircraft.
- Test the techniques developed using a commercial wired system and the developed wireless system to locate artificial sources on a variety of structures.
- Locate fatigue damage in a real aluminium aerospace structure using the developed techniques.

1.5 Novelty statement

Within this thesis the application of the three sensor AE localisation technique has been investigated. The key areas of novelty are:

- The development of what is referred to as the 'second differential method' for the detection of the A_0 mode arrival.
- Development and testing of significant improvements to the three closely spaced sensor technique. These modifications have included the application of the second differential method. A mapping approach was also developed based on these modifications.
- Applying the three closely spaced sensor localisation technique to locate artificial and actual damage in complex structures.
- Significant input into the development of a low power wireless AE monitoring system. Design choices and specifications of the system are directly based on results presented within this thesis.

1.6 Thesis organisation

This thesis is presented in eight chapters, with Chapter one being an introduction to aircraft maintenance and SHM in aircraft structures.

Chapter two presents background information and a review of literature around important areas including AE theory, AE source location, wireless SHM, wireless communication and energy harvesting.

Within Chapter three information regarding the equipment and specimens used for the testing throughout this thesis is provided, as well as some preliminary characterisation testing on each specimen.

Chapter four presents details of the basic approach used throughout the later chapters of this thesis. Modifications to this approach are also presented as well as substantial testing on a variety of structures.

In Chapter five the application of the techniques presented in the previously chapter within a wireless system is presented. The development of the wireless system which consists of three versions of the hardware, which were improved with each iteration is described. Testing is presented using each version of the hardware.

Chapter six presents additional improvements to the technique presented in Chapter four by using a mapping approach. Results from artificial testing on a number of real aircraft structures are also presented as well as the results from an impact test.

Chapter seven presents a fatigue test performed on an aluminium A320 panel, where the techniques presented in the previous chapter are applied to find a crack.

Chapter eight summarises the findings of the thesis and discusses potential future work.

2 Literature Review

This chapter aims to give a background to a number of subjects which are applicable for wireless AE monitoring in aircraft structures as well as a review of current research in the field. Initially subjects relevant to AE will be introduced, including source location methods. A review has also been conducted on current wireless SHM systems which will also include subjects which are very important to consider when working with such a system: communication and energy harvesting.

2.1 Acoustic Emission

In this section the basics of the Acoustic Emission (AE) phenomenon will be discussed, including the basic theory of wave propagation in a solid medium, AE source mechanisms and a variety of source location methods as well as a selection of other relevant topics.

AE occurs in a structure due to the sudden release of energy, for example crack growth. From this a high frequency elastic wave is produced. This ultrasonic wave propagates, first as a bulk wave and then, if boundaries such as the surfaces of a plate, are present, a Rayleigh or Lamb wave. These waves can be detected by piezoelectric sensors bonded to the surface of a structure. Monitoring this data over time gives an indication of the health of the structure, additionally locating the source of the emission allows potential areas of damage to be identified. Classification of sources allows the distinction between noise and damage to be made.

AE was first discovered by Joseph Kaiser in post war Germany in the late 40s and early 50s whilst researching sounds in stressed metals (Tensi, 2004). His work notably included the discovery of the Kaiser effect, which is the discovery that AE will typically not be produced if a greater load has already been applied during a tensile test. The first documented case of AE monitoring of a structure was in 1964 when Green et al. monitored rocket motor casings (Scruby, 1987) and in the following years the technology branched out to many other fields. Industries where AE is

well established on a large scale include the oil and gas industry e.g. pressure vessels, civil bridge structures and wind turbines (MISTRAS, 2017).

2.1.1 Wave Theory

When an AE event occurs a high frequency (typically in the region of 50 kHz - 400 kHz) elastic wave is produced. How this wave propagates and at what frequency is dependent on a number of factors, including the material type. For simplicity, at this stage only isotropic materials where wave velocities are not dependent on direction will be considered. Another very important factor is the present of any boundary conditions. In the case where no boundaries are present the wave propagates as a bulk wave, which is in some ways similar to the way in which sound travels through air. In a gas sound travels in longitudinal pressure waves, shown in Figure 2 (a). In a solid medium without boundaries similar waves from, known as longitudinal bulk waves and travel according to Equation 1, where μ and λ are Lamé constants and P is the density of the material (Worden, 2001).

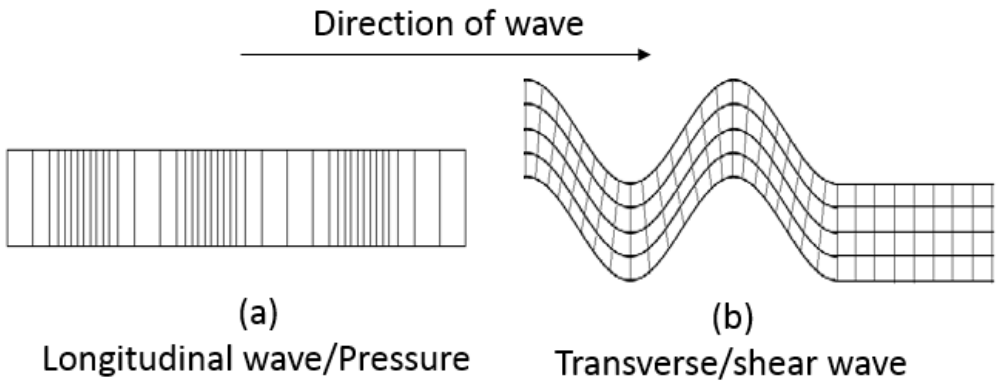

Figure 2 – Types of bulk waves longitudinal/pressure waves (a) and transverse/shear waves (b)

$$c_L = \sqrt{\frac{\lambda+2\mu}{P}} \qquad (1)$$

The major difference between the way in which waves travel in gas and solid mediums is due to the fact that that solids can also support shear forces, so transverse waves can form, shown in

Figure 2 (b). The velocity of these is dependent on the Lamé constant μ which is known as the shear coefficient of rigidity and relates to velocity as shown in Equation 2.

$$c_T = \sqrt{\frac{\mu}{P}} \qquad (2)$$

It can be seen from Equations 1 and 2 that the velocity of the longitudinal wave is greater than that of the transverse wave however neither of these velocities are dependent on the frequency of the wave, so they are described as nondispersive.

Waves' interaction with boundaries changes the way in which they propagate significantly. The introduction of one surface will allow Rayleigh waves to form from the transverse and longitudinal waves combining. These waves are often referred to as surface waves as they only exist on the surface of the structure, as opposed to through the 'bulk' of it. Rayleigh waves were first demonstrated theoretically by Lord Rayleigh (Lewis, 1995) in 1885 and exist when all dimensions are much greater than zero, so effectively infinite. A diagram of one of these waves formed on a surface can be seen in Figure 3. Rayleigh waves decay in amplitude with depth below the surface with the amplitude at one wavelength below the surface being approximately 10% of what it is at the surface. As for bulk waves, Rayleigh waves are nondispersive as their velocity is not dependent on their frequency (Worden, 2001).

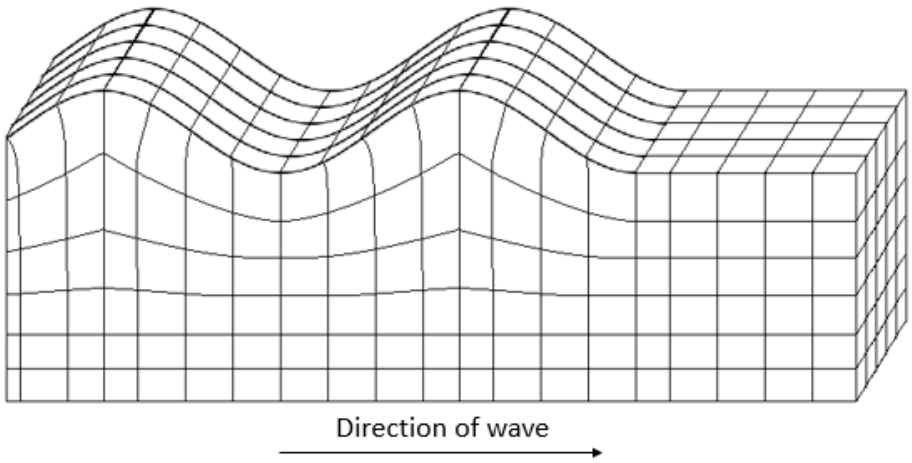

Figure 3 – Diagram of a Rayleigh wave

The final scenario to be discussed in this section is when two boundaries are in parallel at a distance *d* apart; this is typically referred to as a plate structure. The waves which form in this scenario are known as Lamb waves, first demonstrated theoretically by Horace Lamb in 1917 (Lamb, 1917). There are two ways in which a Lamb wave forms; leading to what are typically referred to as symmetric and antisymmetric (or asymmetric) waves. The surface displacements for each of these modes can be seen in Figure 4. These displacements can be calculated using equations derived by Lamb (Lamb, 1917). A simplified version in two dimensions has been presented by Worton (Worden, 2001).

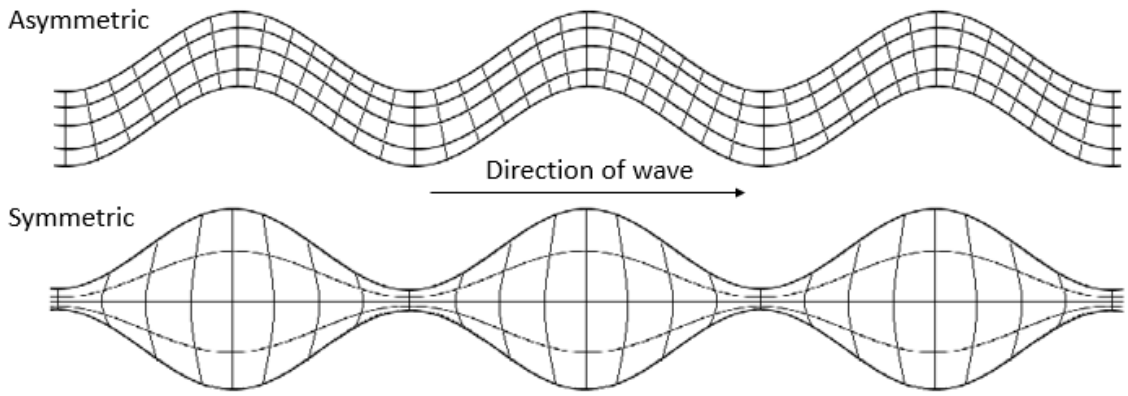

Figure 4 – Asymmetric and symmetric Lamb wave modes

The work by Lamb showed a number of important things, the first of which is that the velocities of Lamb waves are not only dependent on the material and its thickness, but also on the frequency of the wave, meaning they are what is known as dispersive. It was also shown that the equations describing these waves have an infinite number of possible solutions, meaning that an infinite number of symmetric and asymmetric modes are possible in a material. The number of modes present increases with frequency and also as the thickness of the plate decreases. In the majority of SHM applications only the first two modes exist. These two modes are typically referred to as the fundamental modes and are known as S_0 and A_0 with any additional modes called S_n and A_n, where 'n' is the mode number. A material's modal velocities can be presented in dispersion curves against frequency, where both phase velocity and group

velocity can be shown. Sample dispersion curves for group and phase velocities in a 3mm thick aluminium plate are shown in Figure 5.

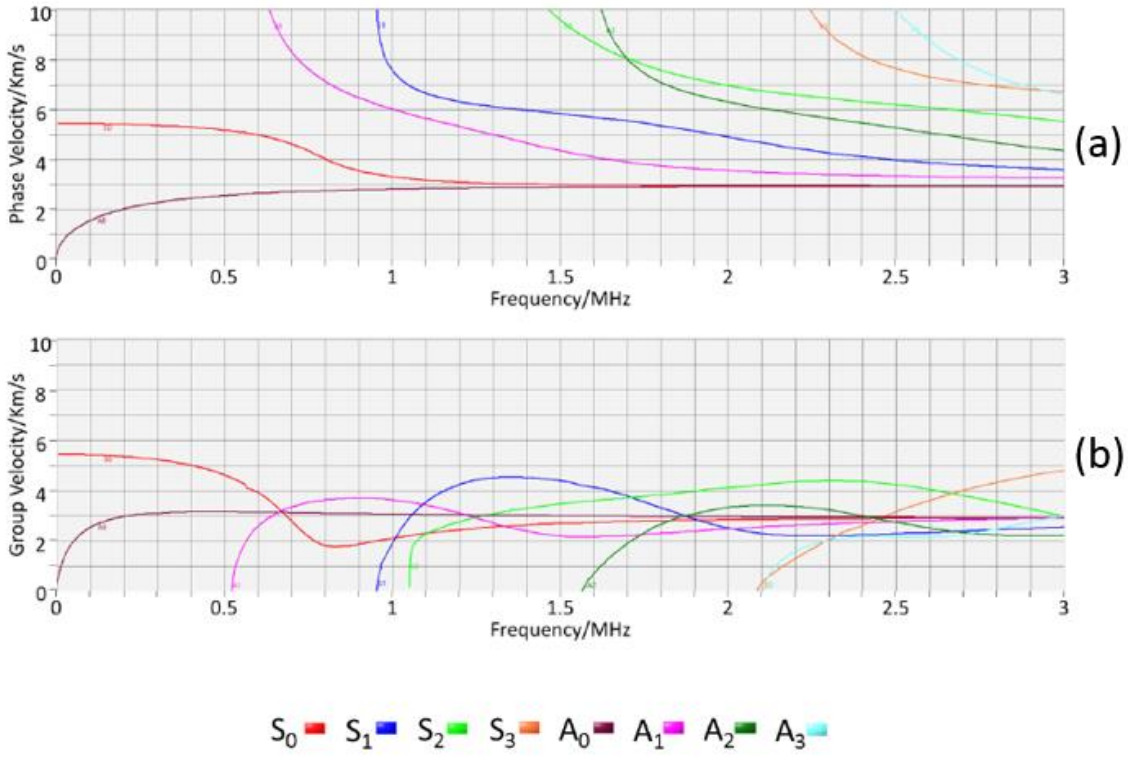

Figure 5 – Theoretical phase (a) and group (b) velocity dispersion curves for a 3mm thick aluminium plate (Marks, 2016)

Shown in Figure 5 are dispersion curves for both phase and group velocities. The phase velocity is the rate at which a single frequency component of a wave travels through a material, and is given by Equation 3, where ω is the angular frequency and k is the wavenumber (Crawford, 1968).

$$c_p = \frac{\omega}{k} \tag{3}$$

Waves however do not typically travel independently; and will more readily travel in a packet or group at the rate of the group velocity c_g, given by Equation 4.

$$c_g = \frac{d\omega}{dk} \tag{4}$$

The phase velocity can be equal to, greater than or even less than the group velocity. In the case when it is greater than group velocity, the waves form at the back of the group, propagate through it, then dwindle away (Crawford, 1968). An example demonstrating how this happens can be seen in Figure 6, where the phase velocity is marked by a red dot which moves through the group. In this example the phase velocity is twice that of the group velocity. As would be expected the opposite would happen if phase is less than group velocity, i.e. waves form at the front and dwindle away at the back. Throughout this thesis when the velocity of a wave is mentioned, unless otherwise stated, what is being referred to is the group velocity.

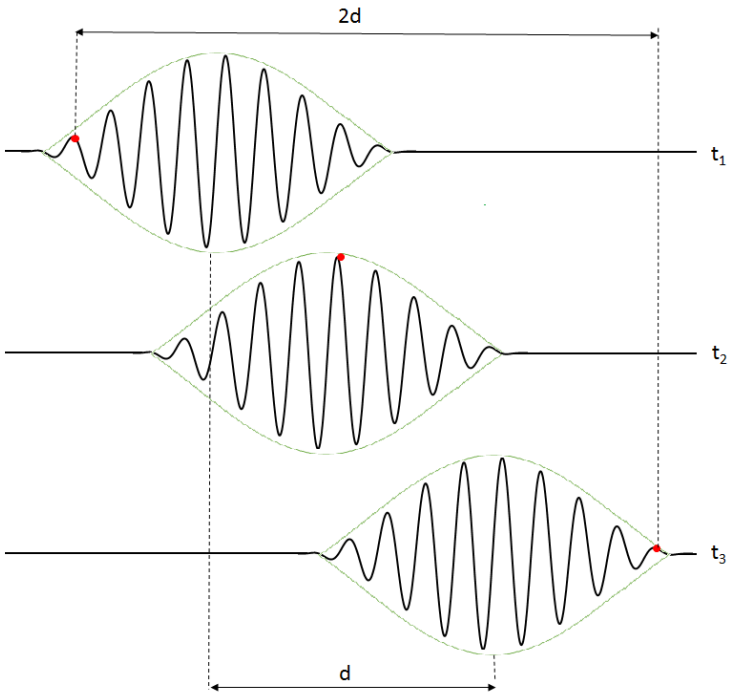

Figure 6 – An example where phase velocity (marked in red) is twice that of group velocity

As mentioned previously the work described so far in this section is only fully applicable for isotropic materials, where the velocities are equal in all directions. However composite materials, for example CFRP which are increasingly being used in the aerospace industry are anisotropic, so it is not possible to use many of the same calculations when dealing with them (Su et al., 2006). Equations relating to these materials will not be discussed in this thesis however

additional reading can be found within (Rose, 2014) as well as additional research by Lowe et al. (Lowe, 1995) who has modelled ultrasonic waves in anisotropic materials.

A very important and relevant point regarding Lamb wave propagation in an anisotropic medium however is that the velocity of a mode is dependent on direction (Rose, 2014). It has been shown (Paget et al., 2003) that the velocity of a wave is greater in the direction of fibres than it is when crossing them, creating an elliptical wave front in certain materials. Grigg et al. (Grigg et al., 2015) elaborated on this by showing that it is also the case that the velocity of the S_0 mode is significantly more dependent on fibre orientation than the A_0 in 0/90 composite plates. This was visualised experimentally using 3D scanning laser vibrometry.

Another important phenomenon in relation to Lamb wave propagation within composites is the mode conversion that exists as the wave interacts with different layers of the material (Lammering et al., 2018). This has been documented in both unidirectional and woven CFRP materials.

2.1.2 Attenuation

As a wave propagates through a medium the amplitude of the signal will drop as it loses energy. The rate at which this happened is known as attenuation. A major cause of this is that as the wave propagates its energy will drop with distance as it spreads over an increasingly large wave front. In the case of Lamb waves this rate is $r^{-1/2}$ (Miller, 1987), where *r* is the distance from the source. In addition to this loss there are a number of other reasons for the dissipation of energy as the wave propagates. These can be broken down into two areas, absorption/ conversion of the energy and deflection of energy from the wave's path. Though many mechanisms are present, a typical example of absorption in a material is the wave's movement within the structure releasing thermal energy due to friction. Deflection of energy refers to anything that obscures an ultrasonic wave's path typically by reflection, refraction, diffraction and scattering. Internal scattering by inhomogeneities in the material is a major cause of

attenuation, for metals this includes material voids and grain boundaries and for composites fibre orientation. Scattering will cause lots of small reflections and significant amounts of energy will be lost (Cracknell, 1980). In addition to internal features of the material, attenuation will be caused by any complexity in the structure. Holes, edges and material changes will cause reflection, diffraction and refraction of ultrasonic waves within a material all of which will result in energy loss (Miller, 1987). The following section reviews how a number of different structural complexities affect the propagation of lamb waves.

2.1.3 Structural Complexity

Lamb wave propagation in an isotropic material is relatively simple with waves propagating in the same velocity in each direction, with equal attenuation. Composites add additional complexity in particular in terms of modelling, however if the velocities in each direction are known, it is possible to predict propagation. Other complexities however, make wave propagation significantly harder to predict. One particular example of this is the case of an aircraft structure which will typically contains holes, stiffeners (often bonded and/or riveted), thickness changes and edges all together in one structure (Figure 7). This is further complicated by the fact that any damage within the structure will also affect wave propagation (Feng et al., 2017). As mentioned previously complexity in the structure will cause significant attenuation and any thickness changes will affect the velocity of the wave (Lammering et al., 2018). In addition to this mode conversions are known to take place, i.e. part of the S_0 wave turning into an A_0 or S_1 wave and vice versa (Cho, 2000).

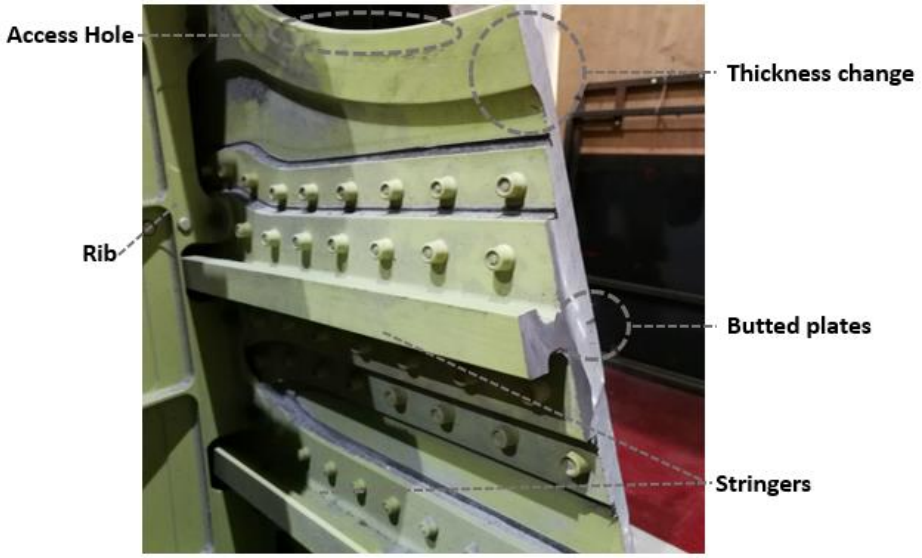

Figure 7 – Internal structure of an aluminium A320 wing showing a stringer and rib bonded and riveted. Also shown are a thickness change, an edge due to access hole and where two plates are butted together and reinforced by the stiffeners

As can be seen in Figure 7, small riveted holes are very prevalent in aluminium aircraft structures. Lamb waves propagating over long distances are therefore likely to interact with a number of these, significantly affecting their propagation. Numerous authors have modelled the effects caused by holes on Lamb waves including McKeon et al. (McKeon and Hinders, 1999) who showed significant scattering when a Lamb wave passed a hole. A study by Cho et al. (Cho and Rose, 1996) modelled mode conversions in reflections at the edges of structures, which is effectively what interaction with a hole is. It was shown that mode conversion occurs between A_0 and A_1 and S_0 and S_1, but not between symmetric and asymmetric modes.

Another significant structural complexity typical in aircraft structures is the presence of stiffeners. Reusser et al. (Reusser et al., 2014) created a simple model of Lamb waves crossing a stiffener and compared it to experimental data. This model and testing are an oversimplification of the problem as they assume the material is all one part, where in reality, as can be seen in Figure 7, a stiffener is a separate part bonded and/or riveted to the structure. The results do however give some relevant information. It was seen that S_0 waves travelled well across the

stiffener with minimal losses, however the A_0 mode was not so unaffected. It was also shown that the ratio of reflection to transmitted wave was heavily dependent on the frequency of wave. Marks et al. (Marks et al., 2016) used 3D scanning laser vibrometry to investigate Lamb wave interaction with an adhesively bonded stiffener mounted on a thick aluminium plate. The stiffener was seen to significantly attenuate the signal due to waves being reflected and energy absorbed. As in other research the level of effect was heavily dependent on the frequency of the wave.

Changes in thickness within a specimen will not only affect the velocity of a Lamb wave propagating through it, due to the frequency-thickness relationship, but have been shown to cause mode conversions and reflections where a sharp thickness change in present. Numerous authors (Cho, 2000, Lammering et al., 2018) have modelled and tested experimentally a number of step thickness changes in aluminium specimens. Mode conversions were demonstrated not only between A_0 and A_1 but between A_0 and S_0 and vice versa for non-symmetric waveguides. The waves reflected by the thickness change were also monitored.

Studies have shown that in addition to structural complexity, damage within a structures will cause disruption to Lamb wave propagation. Feng et al. (Feng et al., 2017) modelled Lamb waves interacting with damage in composite structures, investigating both S_0 and A_0 interaction with a delamination. It was shown that mode conversions occur at the edges of the delamination for both modes, however most significantly for S_0 when crosses back into non-delaminated material. This mode conversion occurs due to a change in boundary conditions when the wave splits between the top and the bottom sub laminates either side of the delamination, reforming into a single wave at the end. This process is effectively a thickness change, so backing up the work by Cho (Cho, 2000). This interaction have been visulaised (Grigg et al., 2015) using a 3D scanning laser vibrometer to investigate S_o and A_o interaction with delamination in composite structures and Pieczonka et al. (Pieczonka et al., 2017) processed similar results to automatically

find damage based on the presence of mode conversions. A study by Staszewski et al. (Staszewski et al., 2007) showed an energy drop across cracks in metallic structures.

A final factor to consider is external forces and their effects on wave propagation. Drinkwater et al. (Drinkwater et al., 2003) investigated experimentally the velocity and amplitude change in attenuation between a compressively loaded and unloaded glass plate with an elastomer interface. It was found that mode velocity was unaffected, however the attenuation of both S_0 and A_0 increased as load was applied, the influence being greater for the A_0 mode.

2.1.4 Source Mechanisms

AE is emitted within a material for a number of reasons, not just the growth of damage. Damage growth can broadly be classified as material degradation which is ideally what AE monitoring of an aircraft structure is aiming to detect. These events are typically transient (short bursts) and broadband in terms of the waves produced, the different damage source mechanisms in metallic and composite structures are discussed later in the following paragraphs. Other sources are normally referred to as noise when looking for damage growth and are often continuous rather than just short bursts, however in some cases the monitoring of these sources gives an indication of the presence of damage. Reversible processes are a very common source of AE, these include crystallographic phase changes, thermoelastic effects, and friction between surfaces (Scruby, 1987). Because of this AE monitoring is often applied to monitoring the health of gears (Prieto et al., 2016). AE will also be released during fabrication, for example during drilling and machining, and hence although not directly relevant, the monitoring of AE can give an indication of the health of a tool in use (Ostasevicius et al., 2017). The flow of fluids also often causes AE to be emitted, in particular when leaks occur in pressure vessels and pipes, the monitoring of which is a well-established use of AE monitoring (MISTRAS, 2017).

Within metal aircraft structures a major cause of structural degradation as a result of fatigue loading is from crack growth (Schijve, 2009). The sudden change in stress and displacement

required for a new crack face to form releases AE. This typically occurs very quickly (<1μs) and releases a broadband stress wave into the structure. The amount of energy released from a crack varies depending on whether the material is brittle or ductile. A brittle fracture releases energy in the way described above, a ductile one however is slightly different. In this case much of the energy is needed to cause the dislocation in the plastic zone of the crack, this slows the process and so less energy is released meaning detection is more difficult (Scruby, 1987). A pre-existing crack in a structure is able to generate AE events, even if it isn't growing. When undergoing fatigue loading the faces of a crack will rub against each other, which emits AE and is known as fretting. Though the detection of fretting doesn't indicate the growth of damage, it assists with the detection of damage and can be distinguished from crack growth, as discussed later in this thesis.

Damage in composite materials is more complicated than in metals due to the complex nature of their construction. A typical composite consists of layers of long fibres running in parallel, laid on-top of each other at various orientations and bonded together with a resin matrix, normally under pressure and heat. Although these materials tend to have a higher strength to weight ratio than metals, damage is harder to detect within them. A number of mechanisms cause damage each of which generates AE events. The main mechanisms within composites are given below and in Figure 8.

Fibre Breakage – If a tensile stress is applied which is greater than the strength of the weakest fibre an isolated fibre break may occur. From this a stress concentration can occur causing additional damage in the surrounding area (Talrenja, 1981).

Matrix cracking – Under cyclic loading the resin between fibres will crack in a similar way to within metals. These cracks can grow and cause a stress concentration on a fibre leading to further damage (Talrenja, 1981).

Debonding – The process of the fibre becoming detached from the matrix (Deng, 1995).

Delamination – The matrix separating across the plane between fibres (Deng, 1995).

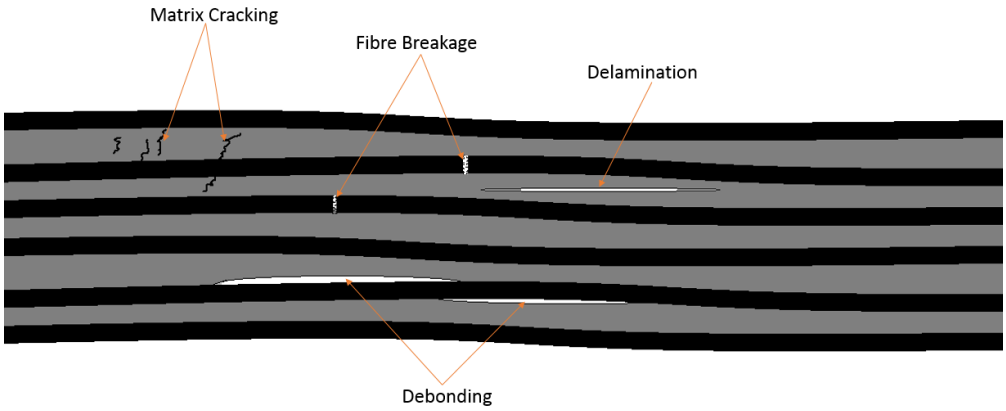

Figure 8 – Damage mechanisms of composite materials

Typically these types of damage will not occur individually, in the majority of cases many will happen simultaneously or be the cause of one another. In addition to the cases above a common cause of failure in complex composite structures is the de-bonding of stiffeners bonded using adhesives to the surface of the structure.

For research, development and testing of AE systems, including localisation algorithms and wave propagation, it is not normally feasible to induce real damage in a structure, at least in the early stages of testing and development, as this is a time consuming and costly process where sources are hard to control. Instead artificially created Lamb waves are typically used to replicate waves similar to those produced by an AE event. The standard used by researchers and industry to generate these waves is known as a Hsu-Nielson (H-N) source, developed by Hsu in 1981. Generation of a H-N source involves breaking a 0.5mm 2H pencil lead on the surface of a structure at an angle of 30^{o}, kept constant by using a shoe as shown in Figure 9. This releases a transient stress wave into the structure, similar to that of an AE event. The technique has been written as a standard for sensor calibration (ASTM, 1999) and is the generally accepted technique within industry (Vallen, 2002). Within research this technique is regularly used for repeatable replication of an AE-like event in structures, both to understand the way a wave

propagates and for mapping a structure (Baxter et al., 2007, Al-Jumaili et al., 2016, Pearson et al., 2017).

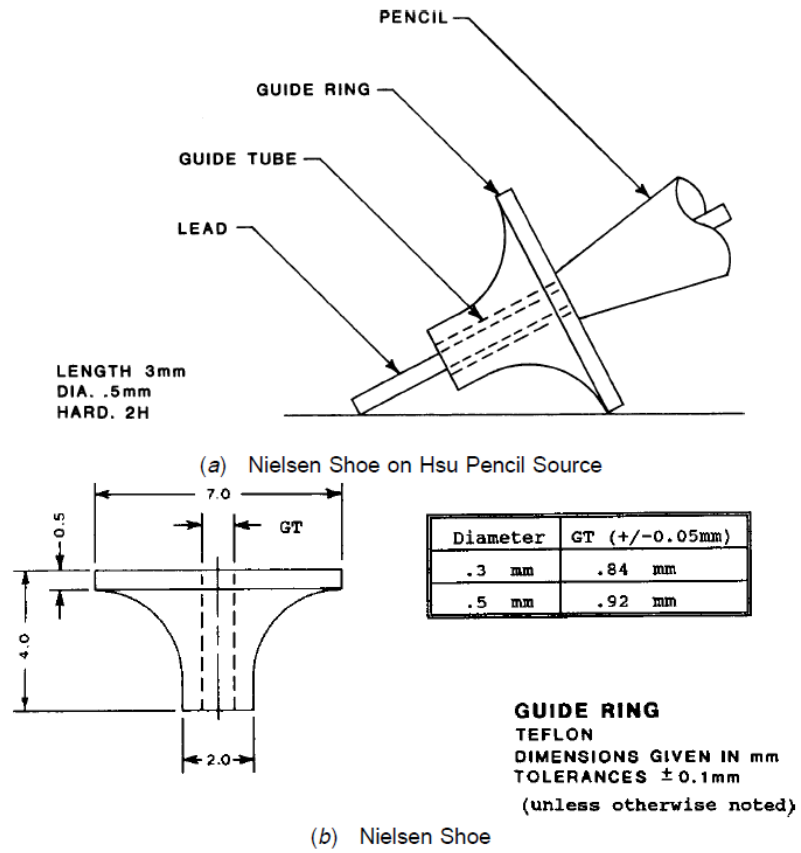

Figure 9 – Diagram of a Hsu-Nielsen pencil source (a) and dimensions of Nielsen shoe (b) (ASTM, 1999)

Other methods of source replication are possible, for example using a laser to thermoelastically generate AE (Hensman et al., 2010). Though this method shows promise, the cost effectiveness, ease and repeatability of a H-N source means it is likely to remain the standard indefinitely.

2.1.5 Event Classification

Once an event has been detected, the next stage is to predict where that event has come from, this is discussed is depth later in this chapter. It is also important to know if the event is caused by damage or background noise. Better still is to know what kind of damage caused the event, for example is it due to matrix cracking or fibre breakage. To do this requires some form of

classification which can be done by extracting parameters from the received waveform. Relatively basic parameter extraction is available in commercial MISTRAS AE systems, which extract certain parameters from the waveform. The following list describes some of these parameters with assistance from Figure 10 (Physical Acoustics Corporation, 2004). Other values are available in the MISTRAS systems, however they tend to be variants on energy approximations and simple frequency extraction techniques.

- **Time of Event** – The time at which the AE signal crosses the threshold
- **Amplitude** – The maximum (positive or negative) amplitude of the AE signal
- **Counts** – The number of times the AE signal crosses the threshold (positive only)
- **Duration** – The time from when the signal first crosses the threshold, until it last crosses it
- **RMS** –The average signal level in volts (root mean squared)
- **Rise time** –The time from when the AE signal first crosses the threshold to its peak value
- **Absolute Energy** –The absolute energy of the signal in attoJoules. This is proportional to the RMS

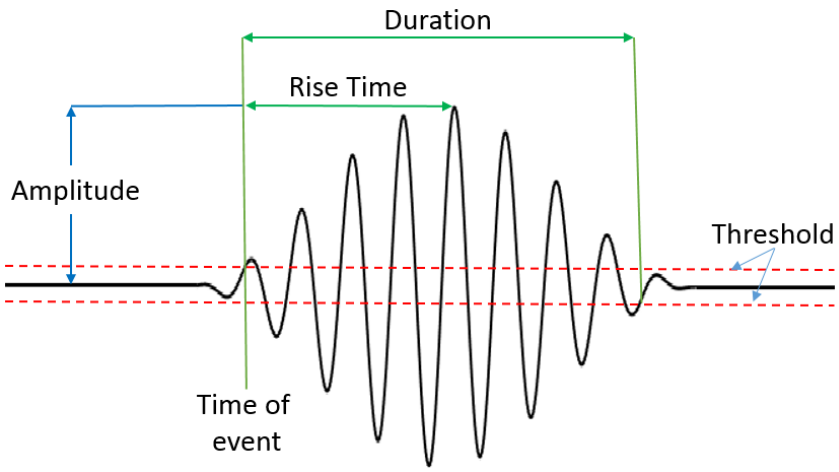

Figure 10 - AE Hit feature extraction (based on (Physical Acoustics Corporation, 2004))

This parameter information is vital for understanding if an event is important or not, for example a low amplitude/energy event is likely to be less important than a high one. It does not however distinguish between crack growth and fretting, or matrix cracking and delamination; for this more complex techniques are required. Examples of some of the simpler of these techniques are described, however the majority require high levels of processing which is unfeasible for a wireless system due to power requirements and are therefore not relevant here.

One popular technique involves taking parameters extracted from the waveform, like those described above, and clustering them using a neural network. Godin et al. (Godin et al., 2005) clustered AE data based on six parameters (amplitude, duration, rise time, counts, counts to peak and energy) and based on these was able to distinguish between delamination and matrix cracking on static coupon tests. This method requires minimal processing on board any device, with in fact only basic parameters needing to be extracted from the waveforms. Additional processing required to construct the neural networks can be performed by a wired device. It has however only been shown to work by Godin on simple tests, with minimal noise, so additional parameters may be needed in more complex tests. Crivelli et al. (Crivelli et al., 2014) used additional parameters based on frequency analysis to classify AE events. This improved the robustness of the technique and its ability to classify bad events, however would not be feasible for a low power wireless system due to the computational requirements of the frequency analysis.

A technique called the corrected Measured Amplitude Ratio (MAR) works on the theory that damage caused in the out-of-plane direction in a structure e.g. delamination causes a higher amplitude A_0 mode to be produced. Conversely, in plane movement i.e. fibre breaking causes more S_0. The MAR method finds the amplitude of the two modes and whichever is dominant indicates the type of damage. The generic MAR technique distinguishes between the modes using band pass filters then compares their amplitudes (Eaton et al., 2011). This has been shown to work effectively in distinguishing between damage types, however S_0 and A_0 modes are

known to attenuate at different rates meaning that the relationship between the two changes with propagation. A modification to this approach is the corrected MAR technique addresses this by using the predicted source location and known attenuation data to 'correct' each mode's amplitudes. McCrory (McCrory et al., 2015) showed that the corrected MAR technique was able to distinguish between two types of AE event data during a compression test in a composite structure. The influence of structural complexity has not yet been taken into account with this testing, however some form of mapping/modelling could compensate for this and enable this to be a feasible technique for use in a real structure. In terms of application to a low power wireless system, this technique is feasible if the correct system architecture is applied.

2.1.6 Sensors

Sensors used to detect AE almost always use a piezoelectric element for transduction (Miller, 1987). Discovered in 1880 by Jacques and Pierre Curie, the piezoelectric effect is the phenomenon that causes certain crystals become electrically polarised when they are subjected to mechanical strain. They also discovered that the inverse was also possible, i.e. that the same crystals would deform when an electric field was applied (Waanders, 1991). In the case of AE sensors the material used is typically a lead zirconate titanate (PZT) acoustically coupled to the surface.

A typical sensor is shown in Figure 11 and consists of a number of parts, protected physically and from electromagnetic interference, by a case. Here the sensor is bonded to the surface with a couplant which allows the transmission of waves to the sensor. Protected by a wear plate the piezo ceramic element will then deform and the electrodes on the top will transmit the voltage generated to the output of the sensor. The electrode on the bottom will ground the element. The damping material at the back of the element acts to absorb and scatter the energy of the wave as well as loading the element to assist with tailoring its resonance (Miller, 1987). For AE testing the output will then go through a pre-amplifier which will apply some form of filter (for example 20kHz-1MHz) to remove noise and a gain stage typically 20, 40 or 60dB. This data is

then transmitted to the AE system which will perform relevant processing on the received waveforms.

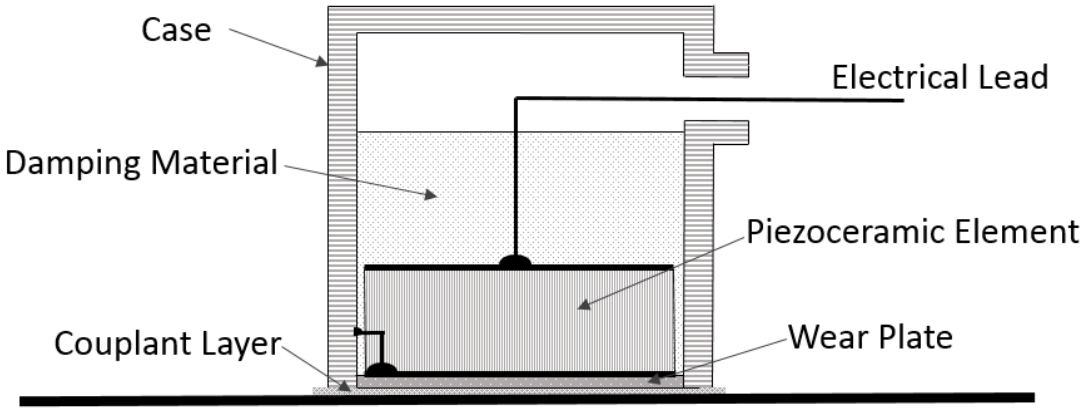

Figure 11 – Schematic of a generic piezoelectric sensor used for AE testing (based on (Miller, 1987))

The resonant frequency of the sensor can be tailored by altering the thickness and width of the PZT element as well as altering the damping material. A sensor can be designed to be either broadband, resonant or wideband with regard to its response to a certain frequency of wave. A perfect broadband sensor would have a completely flat response for any frequency, in reality they are normally only flat between around 10 kHz-1 Mhz (Marks, 2016). Broadband sensors are very useful for analysing the frequency of a signal, however due to high levels of noise are less feasible for use in AE monitoring. Resonant sensors are the opposite, they are designed to respond to a certain frequency. If the frequency of interest in a particular application is known, then resonant sensors will be more sensitive to this than a broadband alternative. Often the best option is something in-between, which is where wideband sensors are ideal. These are designed to have a flat response over a specific region, allowing for different frequency modes to be detected by a single sensor. For this reason they are often chosen for AE monitoring. In reality however they are not perfectly flat and have some resonance over this region, as can be seen from the calibration certificate of a NANO-30 sensor in Figure *12*, where a relatively good response can be seen between 125 kHz and 750 kHz. NANO-30s are small sensors and due to

their good response for the required region are used extensively throughout the testing presented in this thesis (Physical Acoustics Corporation, 2017).

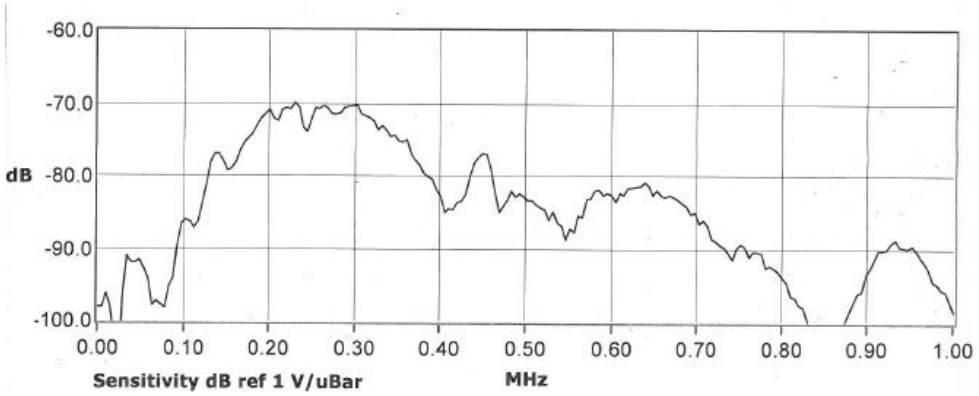

Figure 12 – *Calibration certificate for NANO-30 sensor (Sensor ID GB39)*

Another factor that must also be considered when using a sensor is the type of couplant used to acoustically bond it to the structure. Many options are available, ranging from just using water or grease, to bonding the sensor with silicon or superglue. For most applications a high viscosity couplant is adequate for AE testing. However if the frequency of interest is above 500 kHz, shear waves are important or if a more permanent bond is needed, i.e. for a fatigue test, the ASTM standard advises bonding the sensor to the surface (ASTM Committee E07 on Nondestructive Testing, 2017). The standard also describes how the couplant layer will affect the resonance of the sensor, recommending therefore that as thin a layer as possible should be used to couple the sensor to the surface.

Macro fibre composite (MFC) sensors were invented by NASA between 1996 and 1999, then developed for commercial use by 'Smart Materials' in 2002. An MFC consists of piezo ceramic rods aligned next to each other and sandwiched between adhesive, electrodes and a polyimide film (Figure 13 (a) & (b)). This creates a low profile, durable, flexible and directional device which will apply a voltage when deformed (Smart Material Corp, 2017). These sensors have been used for both Lamb wave actuation and detection (Pullin et al., 2012) where they can be embedded

into a structure. Due to their construction, MFC sensors are directional meaning they have a better response to signals in a certain direction; a study into this effect was conducted by Pearson (Pearson, 2013). MFC's also have application within energy harvesting (Pearson et al., 2012, Zhang et al., 2015) enabling energy to be generated from vibration or strain in a structure.

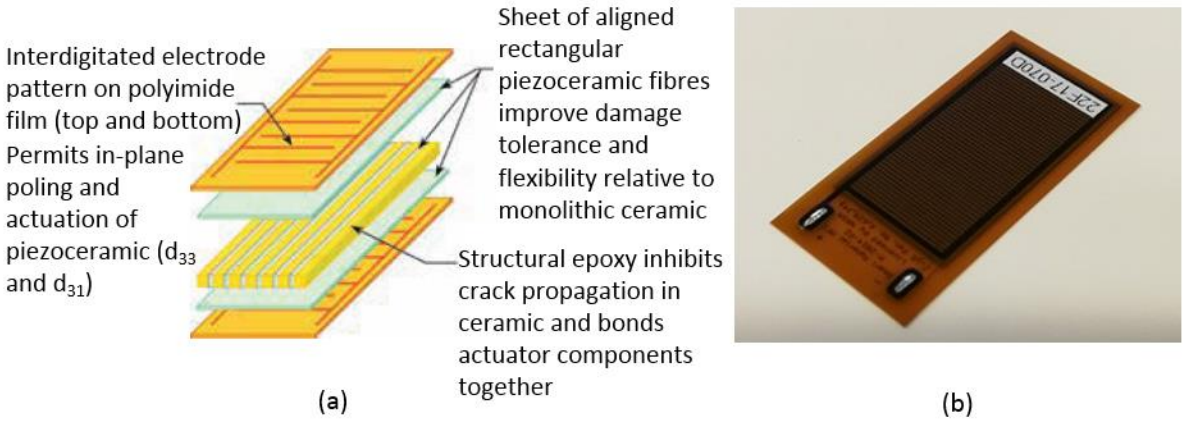

Figure 13 – MFC sensor schematic (Smart Material Corp, 2017) (a) and image of MFC sensor (b)

2.2 Acoustic Emission Source Location

The detection of an AE event in a structure need not necessarily be of concern, as it may not actually be damage. Thousands of events being detected by the same sensor on the other hand may be of more significance. Furthermore if all these events can be shown to be coming from the same location, this gives a strong indication that something of interest is happening there. To achieve this the source of an AE event must be able to be found.

In this section a number of source location techniques will be introduced, ranging from simple 2D location techniques which require minimal processing to complex algorithms designed to give better accuracy in certain situations. These advanced techniques will also be assessed on their suitability for a wireless system.

It must be noted that in most cases, although pin point accuracy would be useful, it is not always needed. Normally grouping a large number of events to a general area will be more than

adequate to identify a location for further inspection. This means that the best source location method for a wireless system is not necessarily the most accurate, but the one that fits a number of criteria, including processing requirements, setup time, sensor requirements and compatibility with a given sensor architecture.

2.2.1 Time of Arrival Source Location

The simplest form of source location is for a problem with only one dimension, i.e. linear source location. Similar principles can be applied to locate in two dimensions and if required three. The Non-Destructive Testing Handbook (Miller, 1987) gives a good step by step guide of the equations required for this. This method is typically known, and will be referred to throughout this thesis, as the time of arrival (TOA) method.

Linear location can be easily explained with reference to the setup of the three sensors shown in Figure 14. In simple terms, each sensor has its zone, if it is the first one to detect an event, the source is within this zone. Greater accuracy can be achieved by looking at which sensor next detected the event. It is then known that it was between these two. The time difference ($\Delta t = T_2 - T_1$) between the first and second hit is then considered and Equation 5 is used to give the distance from the sensor which received the signal first (in this case sensor B).

$$d = \frac{1}{2}(D - \Delta tV) \tag{5}$$

Where D is the distance between the two sensors and V is the velocity of the wave.

If the event took place to the left of sensor A i.e. outside the array, then Δt will be constant with distance from the sensor, meaning exact location would not be possible.

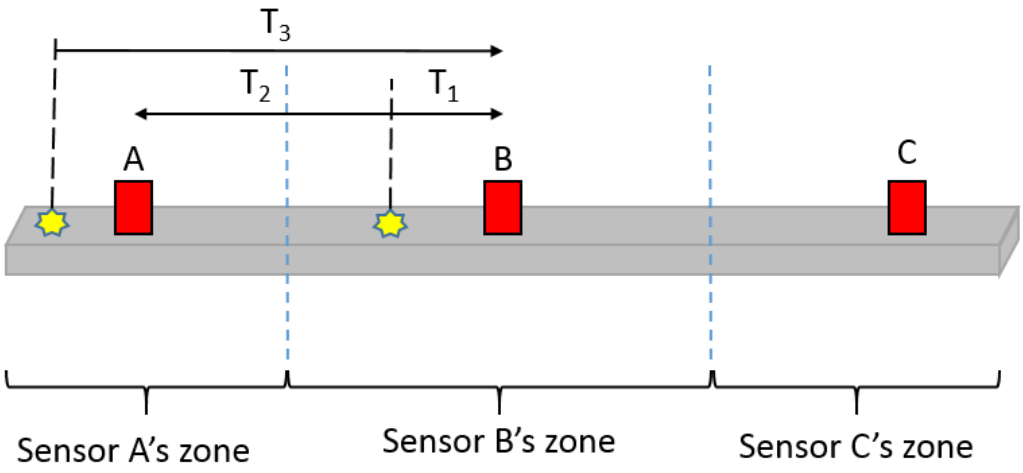

Figure 14 – Linear source location (based on (Miller, 1987))

This linear source location method is only applicable in situations where the distance between sensors is much greater than the width of the plate for example in pipes, beams or wind turbine blades. To locate AE in larger structures a 2D location method is required. Figure 15 shows an example of two sensors being used to locate a source on an infinite plate with isotropic properties.

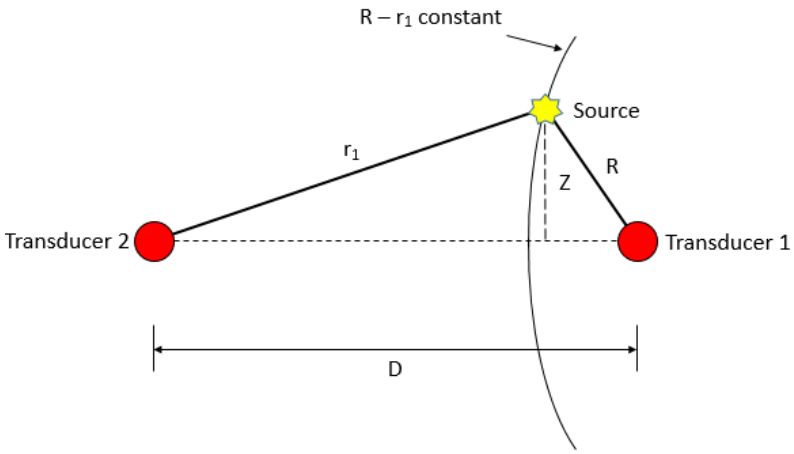

Figure 15 – Source location using two sensors on infinite plate (based on (Miller, 1987))

As for linear location, when the transducers detects an event a time difference will be present. The relationship between Δt, the distance R and angle θ is given in Equation 6, a full derivation can be found in the non-destructive testing handbook (Miller, 1987).

$$R = \frac{1}{2}\frac{D^2 - \Delta t^2 V^2}{\Delta t V + D\cos\theta} \tag{6}$$

Equation 7 is not enough to locate the source, it only give a hyperbola where the source could be located, however with the addition of another sensor this becomes possible. In the case shown in Figure 16, two Δt values can be calculated, t_{12} i.e. the second hit sensor minus the first hit sensor and t_{13}, the third hit minus the first.

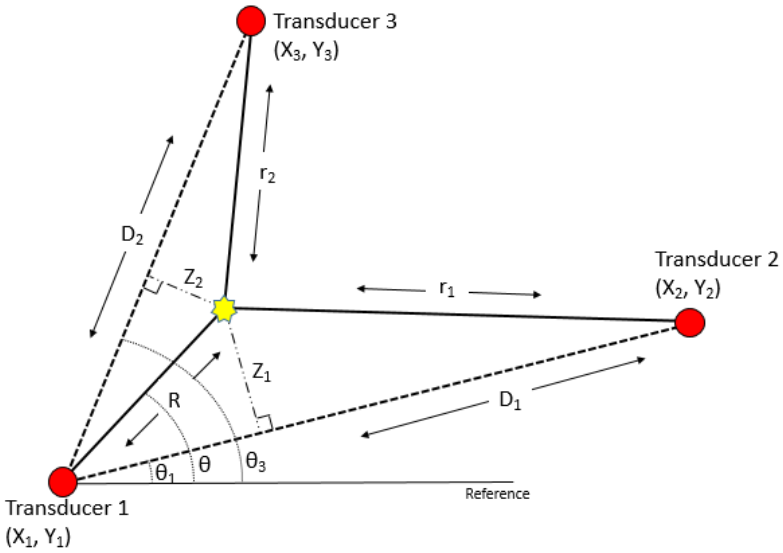

Figure 16 – Source location in two dimensions using three sensors (based on (Miller, 1987))

Much in the same way as the previous example, two equations can be produced, Equations 7 and 8. By simultaneously solving these equations it is possible to find the θ and R, and therefore the source location.

$$R = \frac{1}{2}\frac{D^2 - {\Delta t_{12}}^2 V^2}{\Delta t_{12} V + D\cos(\theta_3 - \theta)} \tag{7}$$

$$R = \frac{1}{2}\frac{D^2 - {\Delta t_{13}}^2 V^2}{\Delta t_{13} V + D\cos(\theta - \theta_1)} \quad (8)$$

The aforementioned method is one of a selection of TOA location approaches to locate a source using three sensors spread apart over a plate-like structure, however to locate a source where more sensors are present a more complex solution is needed. TOA localisation working in a commercial system has been achieved by MISTRAS. The process used to locate a source is shown below, a more complete explanation can be found in the hardware handbook (Physical Acoustics Corporation, 2004).

The way in which the difference in arrival times between sensors 1 and sensor i (ΔT_{1i}) relates to the locations of the source, sensor 1 and the '*i*'th sensor is shown in (9).

$$\Delta T_{1i} = \left(\sqrt{(x_i - x_s)^2 + (y_i - y_s)^2} - \sqrt{(x_1 - x_s)^2 + (y_1 - y_s)^2}\right)\Big/_{v} \quad (9)$$

Where v is the constant wave velocity, x_1, x_i, y_1 and y_i are the locations of the two sensors and finally x_s and y_s is the source location.

When running a test, the system will receive an observed difference in arrival times, i.e. $\Delta T_{1i,obs}$. The system then calculates a values of $\Delta T_{1i,calc}$ by inputting a generic value of x_s and y_s into Equation 9. A method called multiple regression is then used to minimise the difference between these two values through an iterative process of changing the calculated source location, so changing $\Delta T_{1i,calc}$. It is then required to minimise this for all sensor pairs, to do this a values know as chi squared is calculated using Equation 10, and when this value is at its smallest is the predicted location from the system.

$$\chi^2 = \sum\left(\Delta T_{1i,obs} - \Delta T_{1i,calc}\right)^2 \quad (10)$$

The TOA methods covered within this section have been shown to be effective in locating sources in real time within simple metallic plates, however in real world applications they have a number of limitations. These include locating sources in anisotropic materials or those with

structural complexity, for example holes, stiffeners and thickness changes when the accuracy can be significantly affected. The following section includes a number of techniques that have been developed to improve source location in more complex structures.

2.2.2 Improved Source Location Methods

Extensive literature exists on techniques designed to improve AE source location in simple aluminium and composite structures as well as structures with more complexity. As the focus of this thesis is wireless SHM systems for application in aircrafts, this section will concentrate on techniques that could feasibly be applied to a wireless system operating on a large scale on a real aircraft structure. This rules out some techniques proposed by others as they require excessive computational power and waveform analysis to operate. Also, as mentioned at the start of the source location section, pin point accuracy of location is not generally a necessity, so techniques that require an excessive number of sensors, to achieve precise accuracy will also not be considered.

A technique that has been applied on a large scale to improve source location in anisotropic materials, which many carbon fibre aircraft parts could be classified as, was developed by Paget (Paget et al., 2003). As opposed to the standard TOA technique which assumes a circular wavefront, the technique assumes the wavefront is elliptical, as S_0 modes are known to travel more quickly along the fibre direction. To use this algorithm the velocity is required in both longitudinal and transverse directions, which can be calculated experimentally. The approach improved the accuracy of artificial damage localisation in an anisotropic composite structures from a 78.8mm error using the normal TOA approach to 0.8mm error, when locating a H-N source with sensors covering a 0.3m x 0.2m area. This method shows a distinct improvement for certain materials without significant additional computational requirements making it very feasible for use in composite aircraft structural testing. However, it takes no account of structural complexities which will cause wave velocity to become non-linear throughout the structure, meaning significant errors could still be present. An improvement has also been

proposed by Paget (Paget and Rehman, 2017) in which the triggered mode of each sensor is assumed not necessarily to be the faster travelling S_0 but to also potentially be the slower A_0 mode. This is possible as the S_0 mode is typically of lower amplitude than the A_0. In his work Paget demonstrates how each sensor having a different mode of arrival will mean traditional techniques cannot locate a source, whereas if the velocities each sensor uses to locate are dependent on which mode triggers it the accuracy would be much better. Though no practical testing has been conducted this approach looks like a viable technique, as long as the system knows which mode has triggered the sensor. This question has not been answered within the paper, however the rise time of the wave and analysis of the frequency of the arriving mode will give a good indication of the mode the system has triggered on.

2.2.3 Delta-T Mapping

Though the methods of AE source location described so far have been shown to be able to locate accurately in isotropic and in some cases anisotropic structures, none of them address the major problem of structural complexity causing significant error in source location. A method know as delta-t mapping developed by Baxter (Baxter et al., 2007) addresses this issue and has since been improved significantly by a number of researchers (Baxter et al., 2007, Hensman et al., 2010, Eaton et al., 2012b, Al-Jumaili et al., 2016, Pearson et al., 2017). The technique utilises H-N sources to create a map of the difference in arrival times between sensor pairs over the structure. When real data is then received it can be compared with the maps and a location found. The process consists of drawing a regular grid over the area of interest and conducting a number (typically five) of H-N sources at each location. Each pair of sensors will record a difference in arrival times (ΔT) for each location and a map of the structure can then be created for each pair. If four sensors are used, six maps can be created 1-2, 1-3, 1-4, 2-3, 2-4 and 3-4 based on the average ΔT at each location. To increase the accuracy further interpolation can be used between grid locations. Once test/real data has been recorded the ΔT can be compared to the maps creating contours where the values of ΔT are the same which are therefore possible

source locations for that sensor pair. By combining the lines for each map a convergent point should be seen. This isn't always the case however, and normally the most likely location is then found using a weighted mathematical algorithm. This technique was tested by Baxter on a variable thickness metallic structure with a large hole in the centre of a 400mm x 800mm grid with 50mm spacing between test locations. The delta-t mapping technique for this test was able to locate a number of randomly located H-N sources to an average of 14mm accuracy, as opposed to 39mm seen with the TOA method.

In the work by Baxter only artificial sources were located, however Eaton (Eaton et al., 2012b) used the approach to locate damage in a composite panel with a large hole in the centre during a tensile fatigue test. A number of cycles were conducted, and between each test thermoelastic stress analysis was used to identify any redistribution of the stress field due to damage. Both TOA and delta-T mapping were able to locate the source to the location identified by thermoelastic stress analysis, however delta-T mapping showed a slight increase in accuracy and a tighter cluster of data. Eaton also demonstrated that the change in accuracy if sensors were removed and re-bonded in the same location was minimal, increasing the error no more than 1mm in 3 out of 4 cases and 2.7mm in the final case when locating H-N sources. This means that in the case of sensor removal and re-bonding, the same maps can be used. In addition to sensors being removed and re-attached Hensman (Hensman et al., 2010) showed that maps produced on one structure could be used on an identical structure with sensors in the same locations. In this testing similar accuracy was seen making the method more feasible for large scale application without the need for new maps to be acquired on identical structures, which may make the technique infeasible due to time requirements.

Further improvements to the technique have been made by a variety of authors, both to improve its accuracy and to speed up the time to process the data. Pearson (Pearson et al., 2017) utilised the Akaike Information Criterion (AIC), discussed in further detail below, to greatly improve the accuracy of the triggering in terms of detecting the exact arrival time of a waveform.

This technique was shown to increase the location accuracy of the delta-T technique in particular for low energy events. By using the AIC function instead of the threshold crossing technique the accuracy of locating a fatigue crack in a complex aluminium structure went from 18.9mm to 4.2mm.

Al-Jumaili (Al-Jumaili et al., 2016) significantly reduced the time needed to process the data for map creation. His technique used a complete link hierarchical clustering algorithm to remove 'bad' training data automatically, so improving the quality of the maps created and allowing the work to be conducted by less skilled operators. This technique was tested on a variety of complex specimens and in addition to reducing processing time from around 8 hours manual processing time to 18s, it was able to increase accuracy by around 1mm.

Marks (Marks, 2016) used a modelling method known as 'Local Interaction Simulation Approach' (LISA) to model an aluminium structure with a number of holes in it (the same structure as that used by Pearson). The aim of this work was to create training maps based on simulations and remove the need to conduct artificial PLBs all over the structure, significantly reducing the setup time in large scale structures. Using the LISA maps created to locate a fatigue crack in the structure gave an error of 10.3mm, significantly more than the 4.2 achieved by Pearson, however still significantly more accurate than the TOA approximation. It also showed that modelling approaches can be used to create delta-T maps, which if properly applied on an aircraft structure could allow these methods to be used without huge setup times.

2.2.4 Event Arrival Prediction

A major factor affecting the ability of a location algorithm to accurately locate the source of a wave is the ability of the system to detect the exact arrival of an incoming wave at a sensor. The normal way in which a system detects the start of a wave is a threshold crossing based technique. This technique is more than adequate when acquiring data, as no additional processing is needed making the process quick. However if a more accurate location is required

threshold crossing will only detect when the wave crosses the threshold not the actual start of the wave, meaning additional, though possibly insignificant, error will be present as shown in Figure 17. In some cases, however the error due to threshold crossing will be greater. This is when significant attenuation has occurred and a lot of signal passes (possibly the entire S_0 mode) before the threshold crossing triggers an event and may cause the event location to be very inaccurate.

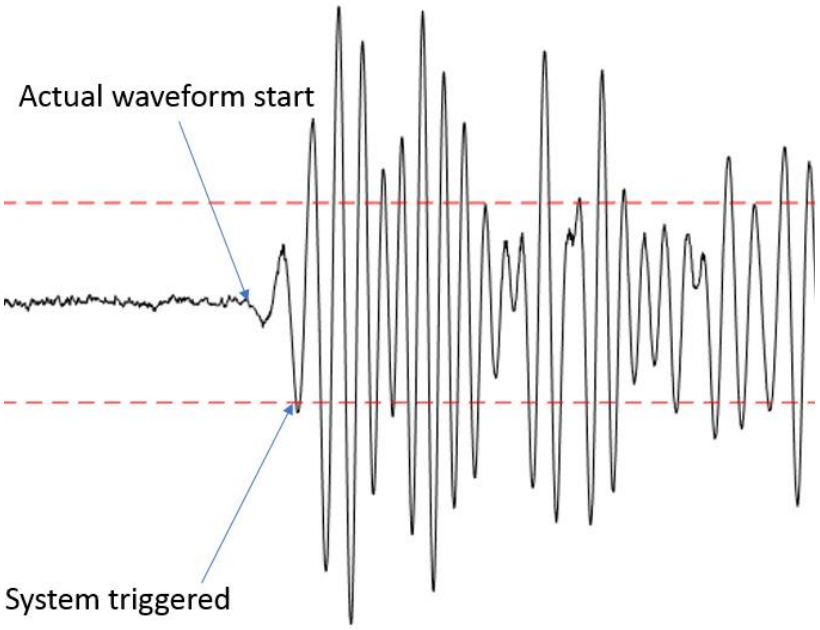

Figure 17 – Threshold crossing missing the start of the waveform

The most accurate way to pick the start of the waveform would be to do it manually. Though accurate, this would take considerable time and is completely unfeasible for an in-situ SHM system on an aircraft structure, meaning some form of additional processing is required. One area where techniques have been developed to detect the onset of waveforms is the field of seismology, where accurate detection is required to locate the source of earthquakes. Work conducted by Kurz et al. (Kurz et al., 2005) compared threshold based triggering with other methods, the best of which was found to be Akaike Information Criterion (AIC). This approach

known as AIC function (Equation 11) was developed by Maeda (Maeda, 1985) to calculate the onset of a waveform.

$$AIC(t) = t\log_{10}\big(var(\{x(1:t)\})\big) + (T - t - 1)\log_{10}\big(var(\{x(t:T)\})\big) \quad (11)$$

Where '*var*' denotes the classic variance of a vector, in this case split between two vectors *x*(1:t) and *x*(t:T), where T is the length of the waveform. The function compares these two vectors for similarity, the point at which the first vector is purely noise and therefore has a high-entropy and the second is only signal with low-entropy, will return the lowest correlation and therefore identify the start of the waveform. An example of this being used to detect the start of an AE signal compared with the traditional threshold crossing technique can be seen in Figure 18.

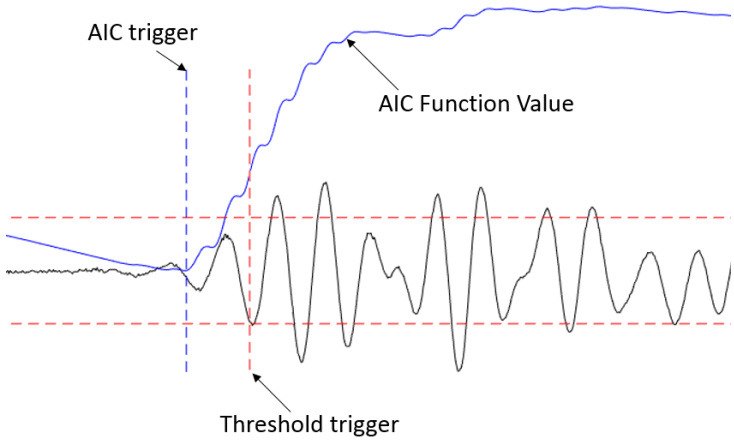

Figure 18 - The Akaike Information Criterion function being used to detect the onset of an Acoustic Emission signal. Threshold crossing shown in red and the AIC function in blue

The AIC technique has been utilised by others since Kurz et al. (Kurz et al., 2005) who showed its increased accuracy for picking the start of an AE source. Pearson et al. (Pearson et al., 2017) applied it to the delta-t mapping technique, discussed earlier in this section and showed a significant increase in accuracy over the normal TOA method.

2.2.5 Single Sensor Modal Analysis

Single sensor modal analysis (SSMA) is the process of determining the arrival times of the different modes within an AE signal and in doing so being able to predict the distance the wave has travelled. This idea was shown to locate AE linearly by Wevers et Al. (Wevers, 1999), however this was done without an automated modal detection. Since then this work has been combined with continuous wavelet transforms (CWT) which is a method for representing a wave's frequency content relative to time; meaning it is possible to see when a certain frequency is present within a waveform. This can be used to identify the S_0 and A_0 modes which typically exist at a given frequency for a material. Finding the point of maximum magnitude for a given frequency gives the location of the mode. This combined with knowledge of the dispersion properties of the material allows for an accurate approximation of the distance the wave has travelled. An example is shown in Figure 19 where the CWT is visualising frequencies associated with the S_0 and A_0 modes present within the waveform.

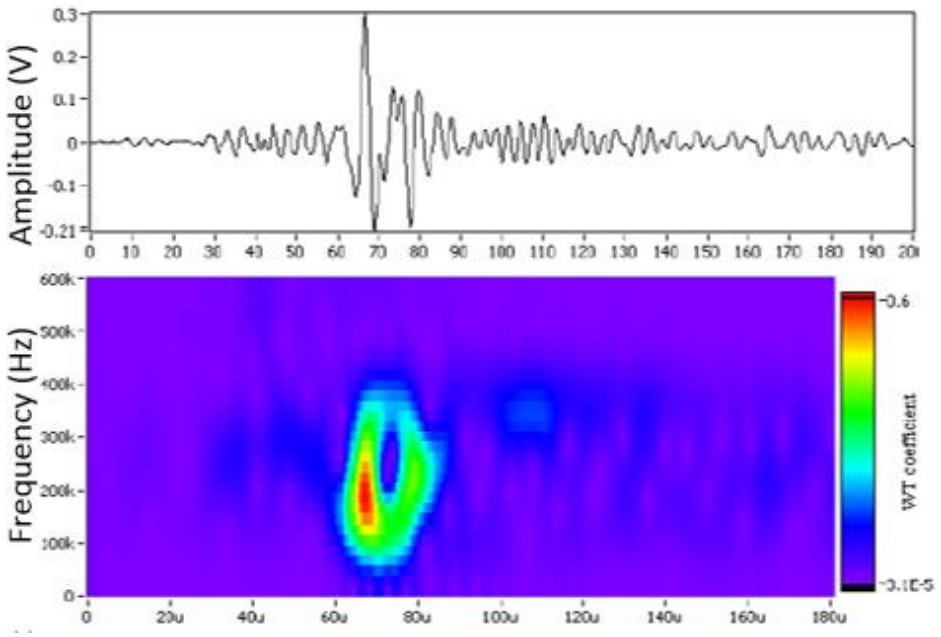

Figure 19 – Wavelet transform of a pencil lead break (Hamstad et al., 2002)

Once two arrival times have been have been predicted, a difference in arrival time 'ΔT' can be calculated. From this the distance the wave has travelled 'd' can be found using Equation 12 where V_{S_0} and V_{A_0} are the group velocities of the two modes (Aljets, 2011).

$$d = \Delta T \times \left(\frac{1}{\frac{1}{V_{A_0}} - \frac{1}{V_{S_0}}} \right) \tag{12}$$

Hamstad et al. (Hamstad et al., 2002) investigated the effect of edges on the accuracy of SSMA by comparing the results for various sized aluminium coupons to an effectively infinite plate. It was found that edges significantly affected the accuracy of the method, which when scaled up could lead to significant location errors if sensor or source were located close to an edge.

All of the work published using SSMA of AE is based only on simple plate-like structures without complexity and it is often stated that this technique will not be accurate for complex structures (Hamstad et al., 2002, Aljets, 2011). In addition CWT's are highly unfeasible for use in a low power wireless system as they have a high computational requirement. However it has been shown (McCrory et al., 2015) that the S_0 and A_0 modes can be differentiated by use of a band pass filter at the required frequency which would make it possible to implement SSMA in a low power system.

2.2.6 Sensors Closely Spaced

A number of authors have taken a different approach to AE source localisation. Rather than using the normal TOA method of an array of sensors spread over the structure, they have instead bonded the sensors closely together and calculated the arrival angle of an AE source. Pairs of arrival angles could then be combined to predict the location of the source or techniques like SSMA could be used to give the distance travelled and so a prediction of the source location. Using closely spaced sensors isn't an approach new for AE, technologies like sonar uses dense arrays of sensors to locate sound within three dimensions to locate submarines, fish, the sea

bed etc. This is done either passively, i.e. listening to something making a noise, or actively by transmitting an acoustic pulse and analysing the reflected waves (Waite, 2005).

An early instance of AE source location using a closely spaced array was patented by Sachse et al. in 1986 (Sachse and Sancar, 1986). This method consisted of 4 small PZT sensors spaced less than 25mm apart, which were able to predict the arrival angle of a wave based on solving a set of simultaneous equations. The distance could then be calculated by picking features from the two different modes present in each waveform and comparing the difference, i.e. manual SSMA. Horn patented a slightly different approach in 1996 (Horn, 1996). Instead of using SSMA a method of modelling known as 'Reverse Ray Tracing' was used. This method involved predicting the angle of arrival using 4 closely spaced sensors and from this modelling the most likely source of the wave, taking into account edge reflections.

Wavelet analysis was integrated into the closely spaced sensor approach by Aljets et al. (Aljets et al., 2011). In his initial work Aljets spaced three sensors in a close triangular array, around 50mm apart. Wavelet analysis was used to find the A_0 arrival time by identifying the frequency at which A_0 was dominant and extracting the wavelet transform coefficients at this frequency. From these plots the maximum value was found and a threshold of 70% of this was used to find the A_0 arrival time. The same process was performed for the S_0 arrival, however in this case a 20% threshold was used. This process can be seen in Figure 20. SSMA was then used to find the average distance of wave travel for the three sensors and the angle found from the A_0 arrival times. The A_0 mode was used as it was identified to be non-dependant on fibre direction in composites, unlike the S_0 mode. The technique was applied to a composite tensile test where it was able to locate the failure of the specimen within an acceptable levels of accuracy.

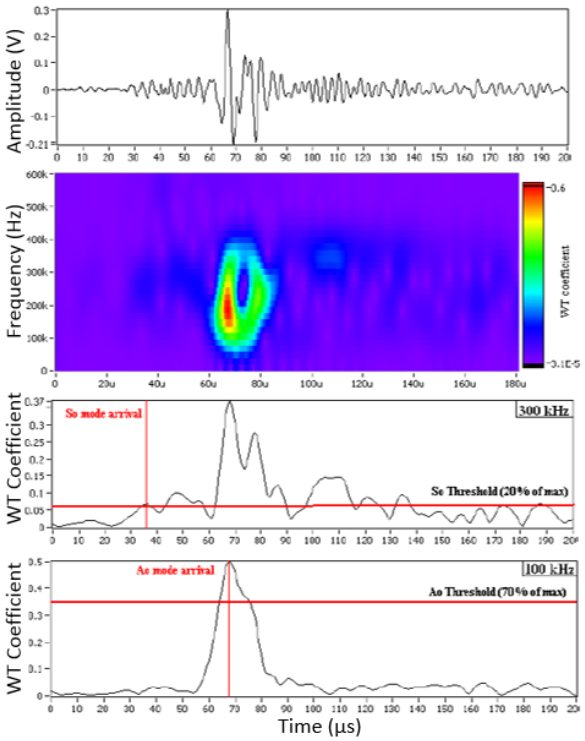

Figure 20 – A_0 and S_0 mode detection using wavelet transforms (Modified from (Aljets et al., 2011))

Following on from his initial work Aljets integrated mapping (Aljets et al., 2012), similar to the work conducted by Baxter (Baxter et al., 2007), to the approach. In total six maps were created on a large composite plate using H-N sources, three of which were for the difference in A_0 arrival times between sensor pairs. The other three maps were created based on the dispersion of the S_0 and A_0 modes. The maps were tested with a large number of H-N sources in a grid over the structure. Up to a 375mm radius over 99% of these were located to within 100mm of the actual point, increasing this area to the whole plate (750mm x 1150mm) only 84% were located accurately.

A method using MFC sensors in a closely spaced rosette to locate AE has been published by Matt and Di Scalea (Matt and Di Scalea, 2007). This work utilises the directionality of MFC sensors in detecting the A_0 mode to give an angle of arrival of the wave by utilising the rosette principles. The combination of pairs of rosettes allows for a location to be found in Cartesian co-ordinates.

This technique was tested by locating H-N sources on aluminium, composite and composite sandwich panels where good accuracy was seen in each.

Using a closely spaced array of sensors to locate AE has a number of advantages over traditional location algorithms, especially if used within a wireless sensor network. Firstly, the sensors being close together means that there is less risk of sensors seeing the waves from two different events and assuming they are the same, so giving an incorrect location (Horn, 1996). Secondly, sensors close together monitoring an area of a radius (r) have the potential to increase the redundancy of a network without significantly increasing the number of sensors needed to monitor a structure. Figure 21 shows the two types of setup possible, a network of sensors using TOA distance 'r' apart (a) and sensors close monitoring the area around them (b). Assume r is equal to the maximum distance a wave can travel before being too attenuated to be useful, and so the maximum spacing for sensors in a standard TOA method of localisation. In example (a) 25 sensors are needed, whereas in (b) this is reduced to nine (although in reality a minimum of three sensors is needed for each of these locations, so the total is 27). The overlap of the sensor monitoring areas adds redundancy to the network. The cost of the second setup is also likely to be less if implemented in a wireless network as although two extra sensors are needed, only nine wireless nodes are required, meaning less hardware. Finally locating sensors close together also combats issues regarding time synchronisation within a wireless network, an issue discussed further in the following section. The major issue with closely spaced arrays is that typically they haven't been shown to be effective at locating AE in complex structures, and in some cases they require some complex computing to find the source, something not feasible for a wireless system.

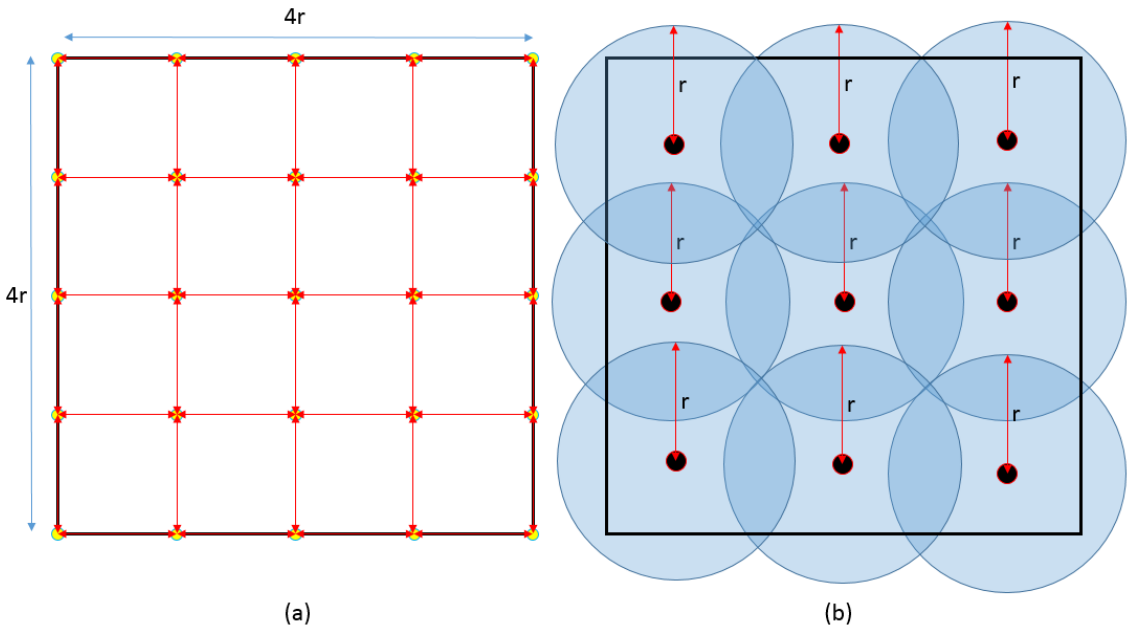

Figure 21 – A sensor network of 25 sensors locating using TOA covering an area of 4r (a) and a sensor network of 9 closely spaced sensors each monitoring radius 'r' covering the same area of 4r (b)

2.3 Wireless SHM system

2.3.1 Introduction

Wireless sensor networks (WSN) enable the monitoring of parameters in remote or hard to reach locations, including environmental parameters such as temperature and pressure, or physical ones such as strain or AE. The earliest application of a WSN was in the 1950's during the cold war where wireless sonar systems were deployed into the sea to track submarines (Panatik et al., 2017). Since then WSN have been applied to many industries for monitoring different environments and even into people's homes to achieve home automation. The first application of WSN on a large scale was within the civil industry where Kim et al. (Kim et al., 2007) used a 64 node network of sensors to monitor ambient vibration on the Golden Gate Bridge in California using accelerometers. Although development has been conducted for other sensors, the majority of WSN being used for SHM use accelerometers (Zhu et al., 2018).

The aircraft industry has been investigating the potential use of WSN in recent years for both safety critical, e.g. flight systems, and non-critical systems like SHM. There are many reasons for this, predominantly the potential weight saving achieved by removing wiring from an aircraft. In the case of an A380 for example, 530km of wire is installed into an aircraft causing significant additional weight, using more fuel and therefore creating a significant expense to the operator (Logan and Sankareswaran, 2015). Another example is a Black Hawk helicopter which has almost 900kg of wires (Jianhua et al., 2008).

As well as the additional weight on the airframe, the actual installation of wiring can be a significant problem. In many cases it can be difficult to get wires to an area and doing so can be time consuming and costly. This is worse when retrofitting an old aircraft, as would often be the case when installing AE monitoring, since wiring is already in place and no design compensation has been made for the additional wired system to be installed. Another issue with wired systems is that when they go wrong, trouble shooting and maintenance of a wired system can be time consuming and costly, for example the U.S. Navy spend two million man hours a year finding and fixing wiring issues (Jianhua et al., 2008). In some cases they have become a serious safety issue, with an average of two in-flight fires every month due to wiring problems and six aircraft lost over a 10 year period within the U.S. Navy (Yedavalli and Belapurkar, 2011).

It is clear from a variety of sources (Logan and Sankareswaran, 2015, Alexandrov et al., 2016) that aerospace manufacturers, both civil and military are intending to reduce the amount of wiring within their structures. This means that additional, non-essential monitoring systems, including SHM, would need to be wireless to encourage implementation on a large scale. One example of this in a large aerospace company is the investment NASA are making in wireless SHM systems, in particular after the loss of Space Shuttle Columbia in 2003 (Prosser, 2003).

In addition to the aerospace industry, many other applications could benefit from the use of wireless SHM systems. As already mentioned civil bridge structures, where SHM systems are

already in commercial use. Widespread use in this industry is limited due to the cost, vulnerability and time required to install a wired system (Carpinteri et al., 2013). Wind turbines could also utilise wireless SHM systems for the monitoring of a number of problems including impact and overload detection (Schubel et al., 2013).

2.3.2 Network Overview

Shown in Figure 22 is a typical wireless sensor network that could exist on an aerospace structure to monitoring strain, acceleration or AE. Within this system there are a number of nodes each connected to a sensor. These nodes could be powered by either a battery or energy harvester with a power management system. Also within the node would be some form of processing subsystem which would then transmit data wirelessly, typically via RF or Bluetooth (Anastasi et al., 2009). A central hub would then receive this information and store it/send it to a cloud based network.

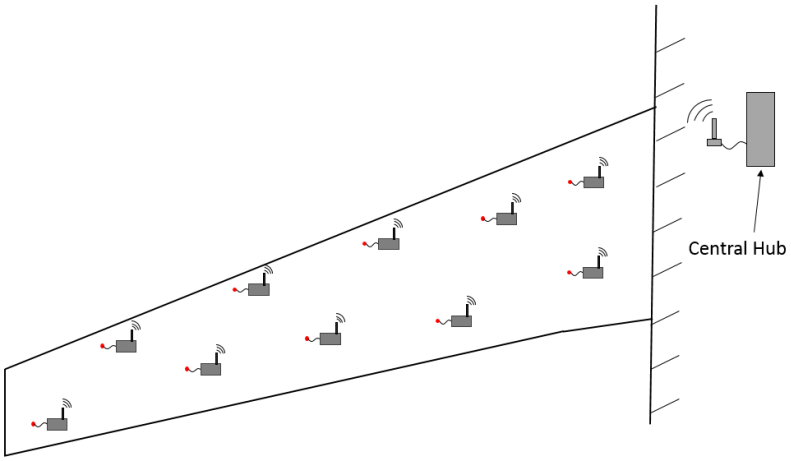

Figure 22 – Typical wireless sensor network for an aerospace structure

Although wireless SHM systems are very promising and some large companies are commercially selling them (MISTRAS, 2013a, Soundwel, 2017), they do pose a number of problems, the primary one being lack of locally available power. In order to solve this, it has been proposed that for some systems, only communications would be wireless, which would mean a power

cable would still be required. Whilst this would significantly reduce the number of wires on board an aircraft, it would not eliminate the problems of fault finding, but would maintain ease of integration etc. Another alternative option therefore would be to use batteries, which combined with a low energy system, could provide maintenance free power to a device for months or even years. This does however pose a number of problems, with batteries being relatively heavy, expensive and having a number of restrictions for use in the aerospace industry (Civil Aviation Authority, 2015). Another issue with batteries is their low performance in cold environments (Wilson and Atkinson, 2014), something very common in flying aircraft, all hardware on board an aircraft must be certified down to -55°C (Radio Technical Commission for Aeronautics, 2004). In addition to these issues batteries have a finite life, meaning they need changing at regular intervals adding to the required maintenance. For a truly wireless system, which ideally any SHM would be, energy harvesting is a requirement. Energy harvesting is discussed in more depth later on however it must be assumed that only limited electricity can be produced, so any wireless system must be very low power.

This drive for a low power system causes a number of limitations on what is currently possible for a wireless system and so compromises must be made for it to be possible. One significant issue is the amount of data being sent from the node, to the central hub. For most low power wireless sensor networks the most power demanding element is the communication subsystem (Anastasi et al., 2009). In fact for approximately 1 bit of data to be sent around a thousand processing operations could be performed in a typical sensor node (Pottie and Kaiser, 2000). For this reason, it is more appropriate to process on-board and only send certain parameters, such as arrival time and energy rather than transmitting entire waveforms for processing elsewhere.

Though far less of an issue for most wireless sensor networks, time synchronisation is a significant problem for the implementation of an AE monitoring system if a one sensor – one node architecture is used. The reason for this is that all the sensors would then need to have clocks accurately synced to achieve accurate time of arrival at each sensor, and so location of AE

sources through the traditional TOA approach. A typical wired AE system has a sample rate of between 1 MHz and 10MHz. To achieve the lower end of this clocks would need to be reliably synced to 1µs accuracy. This can easily be achieved using GPS-based clock-synchronisation, however this is expensive and energy hungry. It is also very easily obstructed, so not very reliable (Akhlaq and Sheltami, 2013). Time synchronisation is discussed in greater detail as well as lower power approaches within the RF communications section of this thesis.

An easy fix for this would be to design a system that operates independently of the others around it, as shown in Figure 23, with each node monitoring an area within its sensors. This approach would remove the need for high accuracy clock-synchronisation, however it is a big compromise as full monitoring of a structure would be difficult and ease of integration into the structure would also be harder. Alternatively, a method of closely located sensors, as described in Section 2.2.6 could be implemented with this system, which would remove the integration issue.

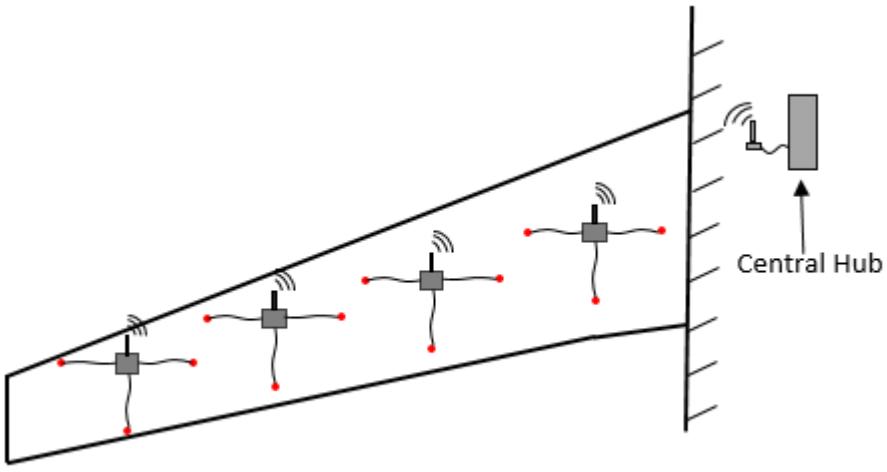

Figure 23 – Architecture of wireless AE network, with sensors independent of each other

RF wave propagation between a hub and a set of nodes is a major problem for wireless systems, as depending on the material the waves will either be reflected or partially absorbed by the

material. A radio waves' ability to pass through a material is dependent on both the frequency of wave propagation (Weir, 1974) and the material's permittivity, which is a measure of the ease with which a magnetic field is able to form in a medium (IEEE, 1998). The permittivity of a metal is effectively infinite, so it will only reflect, meaning that a wave may only reach the hub if a clear path is present. Carbon fibre on the other hand has a lower value of permittivity (though still high), meaning it will reflect some energy, absorb some, and allow some through (Hong et al., 2015). These issues mean that nodes can only be a located a certain distance from their respective hub before they will no longer work. It may even mean that some locations cannot transmit communications wirelessly. Due to this, if wireless communication is applied to aircraft structures, an in-depth analysis of wave propagation within the aircraft's structure must be performed.

2.3.3 Environmental Conditions

Another issue for wireless systems is the harsh environments in which they operate. This means any device on board an aircraft must pass a number of tests, ranging from temperature to vibration based testing. The Radio Technical Commission for Aeronautics with input from the European Organisation for Civil Aviation Equipment developed the standard RTCA DO-160E entitled 'Environmental Conditions and Test Procedures for Airborne Equipment'. This standard details the tests which must be performed for all equipment, wired or wireless (Radio Technical Commission for Aeronautics, 2004). The current version of the document RTCA DO-160G, released in 2010, only has minor changes to the previous version, predominantly clarifications (Federal Aviation Administration, 2011).

One major environmental test specified within DO-160E requires that equipment must be demonstrated to be operational between 70^{o}C and -55^{o}C for 2 hours. These conditions are not at the extreme ends of those for which the performance of wireless sensor networks are being explored, NASA are investigating sensors for conditions over 1,800^{o}C and below -150^{o}C (Wilson and Atkinson, 2014), however problems are still present. A study into temperature effects on RF

propagation (Bannister et al., 2008) investigated the change in received signal stretch for an RF network in temperatures ranging from 25°C - 65°C and found a significant drop in propagation range with an increase in temperature.

Some of the other environmental tests within DO-160E include humidity testing, waterproofness and dust testing, to ensure a device can operate when exposed to these. A sensors' casing can be designed to withstand the aforementioned issues, however to do so may involve the use of a case that will restrict RF propagation. Doing so will further attenuate a RF signal and so restrict its use.

2.3.4 Current Wireless Structural Health Monitoring Systems

Work has been conducted by both universities and industry to develop wireless SHM systems. These range from commercial AE systems not dissimilar to a standard wired system to very low power strain gauges operating at less than 10mW and only tested within a lab environment (Hew et al., 2011).

One example of a commercially available wireless AE system is the MISTRAS 1284. This device consists of 4 channels in one central node with built in RF communications (MISTRAS, 2013a). The system was designed for AE monitoring of bridges and civil infrastructure in remote locations and can be run from 12V batteries. Data can be saved to an SD card at 80 hits/s per channel without waveforms, and 10 if waveforms are needed. The data can also be transmitted live via RF between 40m and 500m, depending on obstructions, at a rate of 10 hits/s per channel without waveforms. In terms of power, the system will run at around 360mW for 4 hits/s per channel sent wirelessly. This can be minimised by using a variety of parameter based filtering techniques to reduce the amount of data being send wirelessly. A study (Godínez-Azcuaga and Obdulia, 2013) using the MISTRAS system looks into monitoring a three point bend test on a CFRP specimen with the 1284 system, saving to an SD card, and comparing its performance to a regular MISTRAS wired system. As expected the wireless system acquired less data than the

standard, due to its data acquisition limitations, however it showed similar trends. This system is capable of implementing the architecture shown in Figure 23, however as it requires hundreds of mW to operate, its energy consumption is currently well above what is possible from energy harvesting on an aircraft structure.

Another commercially available system which applies a one sensor, one node approach has been developed by Soundwel (Soundwel, 2017). This system utilises GPS to achieve a time synchronisation accuracy of 30 µs. Shen (Shen, 2017) used this system to locate a leaking pipe to within 0.5m over a 50m distance, however this level of clock-synchronisation would be unsuitable for AE monitoring in aerospace applications as accuracy would be too low. The system does contain a range of filters and the ability to connect a network of up to 64 sensors together meaning certain elements of the system are very suitable for aerospace application. However, within literature no exact values are given for power consumption, other than an 8 hour battery life, indicating that very little attention has been paid to keeping power consumption low.

As well as commercially available systems, universities and research institutes have developed systems, primarily for the monitoring of AE in civil structures and rotating machinery. The system closest to the requirements of the aerospace industry is a 4 channel system called 'AEPod' (Ledeczi et al., 2009). This system uses four sensors in one node to avoid the issue of clock synchronisation. The system was designed to monitor railway bridges and when tested alongside a wired system achieved similar amounts of data and location accuracy. This is achieved by each channel having its own 12-bit resolution 3MHz Analogy-Digital converter (ADC). When each channel crosses a set threshold parameter extraction is performed on each waveform. The system then checks to see if at least three channels have extracted information, if not it will ignore the event. The times of arrival are then checked to see if their difference is too large, this would indicate that the data source is outside the array and so the event can be discarded. The location of the event can then be found using standard TOA algorithms. Finally,

if the maximum amplitude of the signal is below a certain threshold the data is discarded and if above a certain value it is sent via RF to a central hub. If the amplitude is of medium intensity the data is stored on an SD card for later review. These processes help to minimise the amount of data sent via RF, so minimising power usage. In addition to this the system has a sleep mode, for when no trains are passing, again reducing average power usage. Since energy consumption was not a primary design factor, when operating it consumes around 450mW and in sleep mode around 15mW. Though not low enough to be powered by energy harvesting on an aircraft, a high level of functionality has been achieved with minimal power utilising the techniques described above.

Another example of the clock-synchronisation issue being solved by having multiple sensors into one node has been developed by Grosse (Grosse et al., 2010). This sensor operates in much the same way as the previous example, however it utilises an interrupt to turn on the ADC. This, combined with a comparator significantly lowers the power consumption as the ADC will only be activated if the voltage is within a specified level. Though only minimal testing has been published from this system and no power values have been reported, at least in terms of sensing, this system has the potential to consume less power than the previous example.

Wireless AE monitoring has not only been applied to the monitoring of static structures, some very interesting low power systems have also been made to monitor things like cutting tools and gears. Some of the solutions to the problems these designs have faced could be applied to the aerospace industry. The monitoring of rotating machinery using wireless sensor networks is particularly appealing because as well as the normal benefits, energy harvesting is able to generate a useable amount of power. One study by Prieto et al. (Prieto et al., 2016) created a wireless sensor for the AE monitoring of gears. Unlike the monitoring of structures, gear monitoring doesn't rely on hit based sensing, but is instead based on a sample known as a wavestream. Damaged gears produce different AE signals, so by analysing this wavestream it is possible to differentiate between a healthy and unhealthy gear. The system developed contains

3 channels for AE monitoring which aims to sample at 2MHz for 10 ms. This data is then sent via a ZigBee wireless communication device and analysed at a central PC. By using wavestreaming the system is able to only turn on once enough power has been generated by energy harvesting. If the system only turns on once a minute, it only needs an average of 1.76mW to maintain this level of operation. Through both vibrational energy harvesting and thermal energy harvesting an average of 4.93mW was generated, easily enough to power the system at 1 sample per minute. Although of course this approach to AE monitoring is not suitable for use on an aircraft as analysing wavestreams is not a viable method of SHM, it does demonstrate that it is fully possible to create a system with low enough energy requirements to be powered by energy harvesting, even if it isn't on all the time.

Wireless sensor nodes designed for AE monitoring are not very common, only a few examples are available, most WSN currently in production used accelerometers to monitor the structure (Zhu et al., 2018). Although as a whole less applicable for the development of an AE monitoring system, some very impressive systems have been developed. A wireless sensor node for the acquisition of accelerometer data with multiple sensors on wind turbines has been reported by Herrasti (Herrasti et al., 2016). To operate this system needs to take samples from multiple sensors at ±10 μs or less clock accuracy. To do this the sensors wait in sleep mode with their RF modules turning on at regular intervals, this is known as duty cycling and is discussed later in this chapter. If a message is received from the base station the sensor turns on to record and send data. The message from the base station contains clock synchronisation data which is shown to achieve accuracy of ±1 μs. Exact power requirements for the system are given to be 66mW for RF communication and the same for the sensing part of the system. As in other studies (Prieto et al., 2016) this is beyond what is achievable for EH for constant operation, however for incremental operation could be powered.

Only limited examples are available of wireless systems applying active SHM techniques, presumably due to the high level of energy required for the generation of ultrasonic waves. A

system (Liu et al., 2017) which was developed for use on simple aluminium structures uses ultrasonic waves to detect cracks, whilst also taking a low power strategy. The system utilises the phenomenon of crack induced nonlinearity, detecting distortions in ultrasonic waveforms frequency caused by cracks. Two different frequency waves are generated from two PZT sensors each with a peak to peak amplitude of 28V. A third PZT sensor located close to the other two is then used to analyse the structure's response with a sample rate of 1Mhz. Processing is then conducted on board the sensor, in particular looking at the frequencies in the response, with a frequency shift in the response indicating the presence of damage. The results are then sent wirelessly using a ZigBee RF transceiver. The power required for the excitation and sensing is 1563.2mW and for data acquisition and processing is 634.6mW. This is much higher than could be achieved by EH in an aircraft, however this power would only be needed on occasion and would be turned off the majority of the time. The wireless communication module takes around 100mW whether it is in use or not as it is always waiting for a message to turn the system on, however no duty cycling has been used which would reduce this power consumption further. Choi et al. (Choi et al., 2018) produced an active system which required less power than those produced before it, which was able to detect the presence of holes in an aerospace part. This was achieved by exiting a lower amplitude wave and using a simplified technique. Overall, although these system has been shown to detect damage in simple metallic structures it would not be suitable for aircraft due to their complexity. This does not rule out active SHM techniques such as AU for aerospace application, as they have been shown to work in complex structures (Zhao et al., 2007) and if a similar system could be developed this study shows that it may well be possible to power it with energy harvesting. The development of a number of new systems with lower power in recent years shows a trend of reduced power, which may mean that an active wireless system is soon viable.

2.4 Wireless Communication

2.4.1 Introduction

Wireless communication in its current form has been in use since the late 19th century, the catalyst for this being the first electrical transmission through free space demonstrated by Heinrich Hertz in 1886 (Schiller, 2003). This major development led to the first use of long wave transmission for communications in 1895 by Gugielmo Marconi, this process was known as wireless telegraphy or the telegram and by 1907 commercial transatlantic wireless communication was available. Development has continued ever since, with the development of wireless communication for radio, television and mobile phones to give just a few examples. Alongside this development national and international standards for radio communications have been created which aim to standardise RF and define frequency allocation.

Wireless communication is based on the transmission of electromagnetic waves, which is the transfer of energy in free space. The electromagnetic spectrum classifies waves based on their frequency, or wavelength, which are inversely proportional. This spectrum ranges from audio signals in the 10s of Hz to gamma radiation with frequencies of 10^{17} Hz, however the area of interest for wireless communications is up to the optical range at 860 THz (Hall et al., 1996). Between these there are a number of bands used for wireless communication, the general trend with these being that the higher the frequency, the greater the attenuation in free space and so the lower the range of communication. Higher frequency does generally mean higher data transmission rates, and so the frequency used depends greatly on what it is being used for.

Before information can be sent via RF communication multiple stages are required, the first of which is passing the message to a modulating circuit, which turns a digital message of 1's and 0's into an analogue signal capable of being sent wirelessly via a transmitter. This signal is then received and demodulated, producing the original digital message (Silva, 2001).

2.4.2 Communication for Wireless Sensor Networks

Wireless sensor networks have specific requirements in terms of communication, predominantly being low power. In general, wireless communication is the highest drain of power for a wireless sensor (Anastasi et al., 2009). Typically a large range is not required, although too short would be problematic, and neither is a high data rate. Though local networks had existed before, the IEEE 802.11 standard became the norm for local area networks soon after its release in 1997. Operating at 2.4GHz and within the licence-free 'Industrial, Science, Medical' band this standard has remained ever since. Many alterations and developments have been made, the IEEE.15.4 being the most relevant for wireless sensor networks. Though very similar to 802.11, the IEEE 802.15.4 is designed to be simpler, lower cost and lower power, resulting in a low data rate which for certain applications, for example WSNs, isn't an issue (Callaway et al., 2002).

A commercially available RF module is available from the Zigbee alliance which utilises IEEE 802.15.4 standard, and is the most widely used device doing so. This module has been used for numerous commercial products, predominantly household sensing and automation systems (ZigBee, 2017). The ZigBee module itself has been used in research for the development of wireless SHM systems (Bouzid et al., 2015, Prieto et al., 2016, Liu et al., 2017, Kim and Demo, 2017, Zhu et al., 2018).This is predominantly due to its low power and ease of use.

2.4.3 Network Topology

Something that is vital to consider when developing a wireless network is the network topology that is required for a given application. The topology of a network is the layout of the communication occurring within it (Lewis, 2004). There are a number of potential network designs, some of which are suitable for wireless SHM of an aircraft, others that are less so. For example a fully connected network, where every node can communicate with every other node, would be overkill as in reality it is only necessary to get a message to and from a central point

and so connecting all nodes would only add complexity. Two potential topologies are available for a wireless SHM network, the simplest of these being the star (single hop) network, shown in Figure 24 (a). In this network a central hub is able to communicate with each node connected to it. This has a number of advantages for a network, predominantly the low power requirements of each node which is especially desirable for wireless SHM. Such systems also tend to be much simpler to implement and if a node fails, it will not affect the communication of other nodes. The biggest problem with a star network however is that the nodes must all be within range of the central hub, this will mean more hubs will be required over the structure, which will all need to be wired.

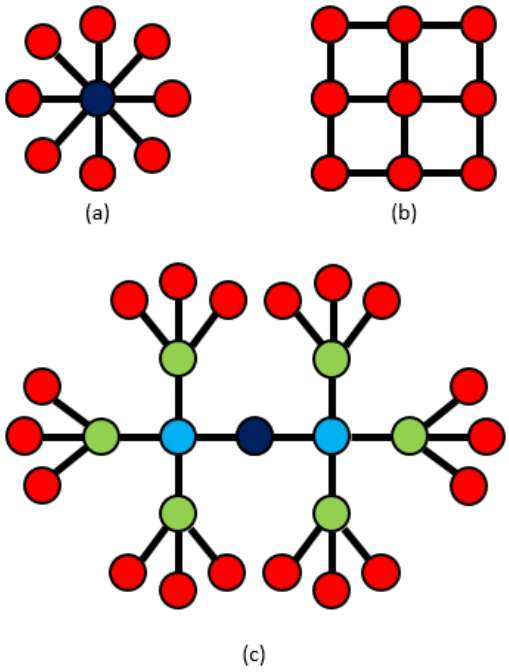

Figure 24 – Network topologies (a) Star, (b) Mesh and (c) mesh with 'group leaders'

The other option for the topology of wireless SHM on an aircraft is the most common topology for WSN. It is known as a mesh network (multi-hop) and in its simplest form is one where any node can communicate with any other node within range, as shown in Figure 24 (b) (Stankovic, 2008). In this form a mesh network wouldn't be very useful, as data wouldn't have a direction of flow and a central point for information to end up at. In reality these networks look a lot more

like Figure 24 (c) where group leaders, which are also full sensor nodes, are assigned to receive and transmit data to and from other nodes until the data reaches a central hub (Lewis, 2004). This topology allows for large areas to be monitored without wires, which are only needed for a single hub. Although having the advantage of increased range, this topology does add a lot of complexity to the system and also has the lack of redundancy, meaning that if one sensor fails many more could also go offline. In addition to this the power requirements of the nodes will go up due to the extra data transmission, for example even in the simple example in Figure 24 (c) if a red node wants to communicate with the hub, messages must be sent and received three times.

In general, the communication levels occurring in a WSN are not particularly high once data reduction and compression has taken place. This means that the RF module of a node only needs to be on when data is being sent to the central hub, which can be on at all times. The main issue with this is that it does not allow for the hub to contact the node, which is needed to change settings, for clock synchronisation messages (discussed later in this section) or to tell the node to enter sleep mode between aircrafts flights. This also makes a multi-hop network impossible, as a signal is not able to hop without the other nodes' RF modules being on at the same time. Both of these issues can be addressed, whilst maintaining lower power than required for continuous operation, by using a duty cycling protocol.

Duty cycling involves the RF module being in sleep mode for the majority of the time and 'waking up' periodically to send or receive messages. The times at which RF modules are active needs to be synchronised to allow for all communication to take place in a short period and prior to the sensors going back into sleep mode (Anastasi et al., 2009). As usual this protocol is easier to implement in a single-hop network than in a multi-hop one, with more potential issues occurring in a busy network, with lots of messages being sent in both directions (Schiller, 2003).

2.4.4 Time synchronisation

Each node has its own internal clock and to properly control a duty cycle in a network these clocks must be synchronised on a regular basis to maintain accuracy. Accurate time synchronisation is also needed to apply the majority of localisation algorithms required for AE monitoring, where an accuracy of around 1 µs is needed. It is clear that this high accuracy is a major hurdle for the application of wireless AE monitoring as demonstrated by considering other WSN and their accuracy requirements. For example modal shape analysis is a common use of WSN for SHM on bridge structures and within this technology time synchronisation is an issue. This is despite the accuracy required for this being 120 µs, which is far lower than that needed for AE monitoring (Noel et al., 2017).

Constant synchronisation is necessary due to inherent inaccuracy in the oscillating crystals used in the clock, with minor deviations in frequency being present from manufacture. External factors will also affect the stability of the crystal, for example temperature and frequency changes due to ageing effects (Mahmood and Jäntti, 2009). Mahmood et al. (Mahmood and Jäntti, 2009) monitored the clock drift of five high accuracy clocks at room temperature, they were found to drift up to 2.4µs/s. This value is likely to be greater if extreme temperatures were experienced as is the case on an aircraft. This large shift would mean that for accurate AE location, time synchronisation would be needed multiple times per second.

Very accurate time synchronisation - well within 0.1µs, is possible using GPS (Guo and Crossley, 2017), however this requires high levels of power (Fotedar and Saini, 2017) and is unreliable as GPS signal can be lost.

An alternative is to send a time stamp thought the RF network. In a single hop network this process of time synchronisation involves the hub transmitting a message containing a time stamp, this message is then received by each node and the clocks within these nodes can be adjusted. This process must be done at regular intervals to ensure the accuracy stays within an

acceptable level. This is slightly more complicated for mesh networks as multiple time synchronisation messages will be sent via multiple transmitters which would collide, and so be lost. This issue can be countered by using proper protocols. The accuracy achieved using such a system however is affected by four factors: send time, access time, propagation time and receive time. These minor delays will all add to the error in the time sync and the more times the message is received and sent on, the greater the error (Akhlaq and Sheltami, 2013). Akhlaq et al. (Akhlaq and Sheltami, 2013) investigated a number of methods of time sync and their accuracy for single and multi-hop networks, the most effective of these had an accuracy of around 0.23µs for single hop, which increased slightly with each hop.

Though not impossible time synchronisation accurate enough for AE monitoring in a single sensor-single node network is very difficult and very power intensive. Because of this issue the application this kind of network may not be feasible for a self-powered wireless network within an aircraft structure, unless a lot of power can be harvested.

2.5 Energy Harvesting

2.5.1 Introduction

A major recurring theme throughout this chapter is that many things are not possible in a wireless SHM system due to a lack of available power. Thus a balancing act is necessary between making a system functional whilst also making it very low power. In many applications which use wireless systems a low power system enables batteries to last longer periods without the need to change them. This situation however is not ideal, and an optimal system would be one that never needed to have its batteries changed and instead utilized power sourced though energy harvesting. Energy harvesting (also known as power harvesting, energy salvaging or the use of ambient energy) is the process of extracting power from the environment by converting one form of energy into electrical energy. The types of energy on which harvesting has so far been focused are mechanical, radiant and thermal energy and fluid flow. Mechanical energy broadly

consists of energy gained from movement, which includes vibration and strain. Radiant energy comes from electromagnetic waves, for example light and RF energy. Thermal energy is typically based on the generation of energy from thermal gradients, and fluid flow can be from either gas or liquid. These sources all provide different levels of energy, the highest of which are for solar and fluid flow (Dutoit et al., 2005), with solar being the most widely used for WSN application. For the majority of applications for WSN within the aerospace industry solar is ruled out as sensors need to be located within structures, so having no access to light. Fluid flow is also extremely limited, although air flow is available in certain locations as small gaps are present around the leading and trailing edge of wings, however for the majority of the structure this isn't a viable option. Due to this the primary sources of energy available, and so covered within this section, are thermal and vibration. In addition to harvesting this energy, it is also important to consider how any power harvested will be converted into a useful form and stored, so this process will also be briefly covered at the end of this section.

2.5.2 Vibration Harvesting

Vibration harvesting is a promising area of energy harvesting because it is often universally available in structures that require SHM, whether they be bridges, gearboxes or aircraft. In the case of an aircraft, vibration is predominantly generated from the engines and airflow, which cause a range of vibrations in the structure. Engine vibrations within the structure are more predictable in terms of the frequencies produced and their magnitudes, however this energy isn't available over the entire structure. Vibration due to airflow is much more random and is very dependent on the type of airflow over the structure. Turbulence will significantly increase vibration as will the pilot applying the airbrake (Carbaugh, 2001). This vibration will significantly vary in terms of frequency and will be different in each location over the structure, however data has shown that vibration in an aircraft structure will vary between approximately 100Hz and 300Hz (Paget).

It is clear that an aircraft structure has a lot of vibration present throughout, the challenge for energy harvesting is to convert this energy into electricity. The use of piezoelectric harvesters is the most popular method used and relies on using piezoelectric materials to generate electricity from strain. This is typically done by bonding it to a cantilever whilst it vibrates, as can be seen in Figure 25 (a). The cantilever used can be tuned to a certain resonance, typically by adding weight. Wu et al. (Wu et al., 2008) created a harvester with variable resonance by having a movable weight on the end of a cantilever. Piezoelectric harvesters can also be miniaturised into Microelectromechanical systems (MEMS), so having the potential to fill the power requirements of micro sensors as has been demonstrated by Dutoit et al. (Dutoit et al., 2005). The main disadvantage of cantilever based harvesters is that they are inherently very resonant, meaning that they are very effective at one narrow frequency range and are ineffective outside of this. This issue makes a normal cantilever based harvester ineffective for aircraft structures which see a wide range of frequencies. Even though harvesters could be tuned to resonate at the most common local frequency, this would vary at each location, which is unfeasible on a large scale. Changes in vibration throughout the flight would mean that the harvester may only be optimal at certain times. The best solution would therefore be a wide band harvester which, although at resonant frequency would have a lower power output, would be effective at a range of frequencies.

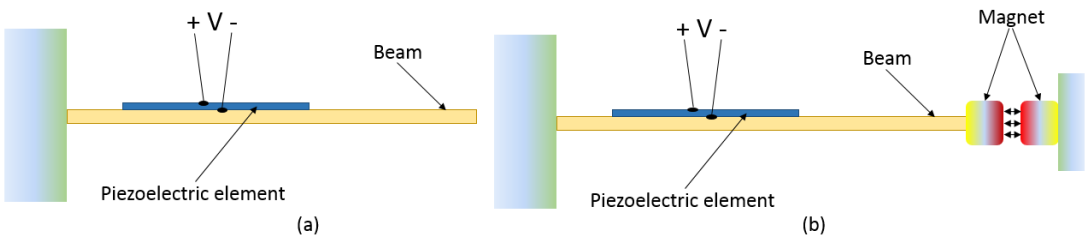

Figure 25 – Piezoelectric energy harvester (a) and non-linear piezoelectric energy harvester (b) (based off (Daqaq et al., 2014))

A common way in which a broader band harvester has been produced is by making a nonlinear energy harvester (Daqaq et al., 2014). The principal of a nonlinear harvester is that the magnitude of deflection can be altered by introducing a nonlinear restoring force to the system, broadening its frequency response, which is often done using a magnet (Figure 25 (b)). Alternatively a complex structure can be used to create a nonlinear oscillation as was done by Liu et al. (Liu and Jing, 2016) who created an X-shaped supporting structure which was also able to broaden the frequency range. Authors have also tried to alter the shape of the cantilever to tailor resonant modes to frequencies. Erturk et al. (Erturk et al., 2009) modelled an L-shaped cantilever beam structure with applied mass with the aim of bringing the first and second resonant modes close together, creating an effectively wide band harvester.

MFC (Section 2.1.6) sensors have been also been used by a number of authors (Pearson et al., 2012, Zhang et al., 2015, Shi et al., 2017) for energy harvesting applications primarily because of their increased durability over traditional PZT elements, which are brittle and prone to breakage. In addition to this, MFCs are easy to work with and bond to curved surfaces as well as being able to operate in harsh environments (Pearson, 2013).

Determining the exact power output of vibrational harvesters is difficult, as research tends to be based on resonant harvesters or harvesters operating at peak efficiency rather than its response over a broad frequency range. In addition to this there is no standard vibration acceleration value, some research is at 0.1g others at around 20g. It is clear however, that the power available through vibration is minimal, a summary of research conducted by Wei et al. (Wei and Jing, 2017) found very few vibrational harvesters with power output above 1mW. This means that current wireless SHM sensors working in continuous operation are unlikely to be able to be powered by vibration alone, unless a large number of harvesters are used which would make the sensor very large.

2.5.3 Thermal Harvesting

Thermoelectric generators (TEG) are able to convert heat gradients between one face of the generator to the other into electrical energy. This is possible because of a solid-state phenomenon called the Seebeck effect. TEG are not popular for commercial power generation because of their lower efficiencies compared to other methods, for example heat pumps. In spite of their lower efficiencies there are a number of reasons why they are perfect for energy harvesting. Unlike heat pumps TEG are practically maintenance free due to their having no moving parts or chemical reactions, they also release no toxic residuals and have a long life span (Elsheikh et al., 2014). Though TEG have low efficiencies compared to other mechanisms of thermal energy conversion, the power they have been seen to harvest is much higher that of vibrational harvesters (Samson et al., 2011).

TEG show good potential for powering WSN on aircraft structures due to the abundance of temperature gradients over the structure (Thangaraj et al., 2014). By bonding one face of a TEG to the inner skin of a structure and using some form of heat sink or phase change material (for example water) on the other an energy gradient can be created between the inner environment of the aircraft and the outside environment. Samson et al. (Samson et al., 2011) states temperature differences on an aircraft fuselage to be between 20.4 ◦C to −21.8 ◦C, this change occurs within the first 14 minutes after take-off and is maintained at the low temperature throughout the length of the flight, until landing where it increases back to the higher temperature. As a difference in temperature is required, once both sides of the generator reach a constant temperature no voltage is generated, therefore TEG only have the ability to generate power during and shortly after take-off and the same for landing. Although the power generated therefore isn't consistent the power levels are much higher levels than vibration offers, with peaks of 200mW seen in Samsons testing.

2.5.4 Power management

Energy harvested from a source isn't generally instantly available to be used to power a sensor. At a minimum the input voltage usually requires rectifying and stabilising at the required voltage for the node it is powering. These processes have losses meaning the energy usable for the sensor is much less than that output from the harvester. It should be clear from the previous pages that a single source is unlikely to be feasible for powering a wireless sensor on board an aircraft. A good solution is therefore to use multiple sources in combination to power a sensor. In the case of a combination of TEGs and vibrational harvesters for example, the TEGs would aim to charge up the storage device and the vibrational harvester would aim to keep the system topped up. This would require more complex power management, with the requirements of each harvester being different, something which is more difficult but entirely possible (Alghisi et al., 2017).

Unless the energy harvested is always greater than the power required by the sensor and not fluctuating, some form of power storage will be needed within the wireless node. For this there are two viable options, rechargeable batteries and supercapacitors (Thangaraj et al., 2014). Rechargeable batteries are able to store high levels of energy and typically have low current leakage. However, they have low power density (their ability to quickly discharge power) meaning that for certain applications such as generating GLW in a structure, they would be unsuitable. They are also known to degrade over time, meaning replacements may be required during the life of the part. The wide range of temperatures an aircraft is subjected to is also a key issue for batteries, which do not perform well at low temperatures (Zhang et al., 2003). Another problem with batteries is the fire/chemical risk that they present, in particular regarding lithium batteries where a number of high profile cases have caused issues with aircraft, and even grounded entire fleets (BBCNews, 2013). Super capacitors are an alternative option as they are not affected by temperature (Thangaraj et al., 2014) and do not pose the same fire risk as some batteries do. Unfortunately supercapacitors do not have the same energy density, in fact the

energy density of a supercapacitor is commonly around 10%-20% of that of a battery of the same size so proper selection of an appropriate super capacitor would be required.

2.6 Summary

Within this literature review the fundamentals of AE have been presented including wave propagation, interaction with complexity and source mechanisms. Additionally the current methods used to detect the presence of AE and locate the source of an event have been described. A review of current wireless SHM systems from academia and industry has also been given, focusing on the capability and power requirements of available systems. Finally an overview of the requirements of a wireless system has been presented, which includes wireless communication and energy harvesting.

A recurring theme which has been present throughout this literature review; is that the power requirements of the system must be as low as possible, as available power through energy harvesting is minimal in many locations on an aircraft. Although no commercial SHM system is currently available that could be powered by energy harvesting available on an aircraft, a number of academics have presented hardware which operates at very low power meaning they could be powered long term by energy harvesting, if used intermittently. These examples show that WSN for SHM on aircrafts is possible, however a number of additional hurdles are present for AE monitoring to be successfully applied.

The fundamental problem with applying a single sensor to single node wireless AE monitoring system using TOA to located sources on an aircraft is time synchronisation. As discussed within this chapter each node would require time synchronisation ideally to at least 1µs to accurately predict the location of an AE event using the traditional TOA method. Although this is possible with both GPS and RF, due to clocks drifting at a rate of approximately 2.4 µs/s, the clocks would need to be re-synchronised very regularly. Given that the wireless communication is typically the most power hungry element of a wireless node, this isn't ideal. The alternative is to use multiple sensors connected to a single node. In this case clock synchronisation is no longer an

issue, however if sensors need spacing away from the node, wires are still needed, which potentially causes problems with system integration and weight. Alternatively, using a technique where sensors are closely located removes the need to time synchronisation, without requiring additional wiring.

AE source location methods using a number of sensors closely located have been presented within this chapter. Currently the approaches which have been investigated are unfeasible for application in a wireless system due to the processing requirements, however modifications could make it a possible option. It is also clear that no closely spaced sensor technique has been shown to effectively located sources in complex structures, primarily due to their inability to perform SSMA. These issues must be solved for a closely spaced array of sensors to be applied on a complex structure.

3 Equipment and Test Specimens

For the work conducted in this thesis to be possible a number of types of equipment and test specimens were required. This chapter gives an overview of the essential equipment used throughout the testing conducted within this thesis. The specimens are also described and the results of preliminary structural testing, performed by the author of this thesis, presented for each.

3.1 Equipment

Within this section the key pieces of equipment which have been used repeatedly throughout this work are presented. This is not a complete list and where other equipment has been used additional information will be given where relevant.

3.1.1 Acoustic Emission testing equipment

AE acquisition is possible using only a sensor and some form of data logger, e.g. an oscilloscope. This is useful when raw data is required however is unfeasible for large scale application, in particular when conducting a structural test. For large-scale testing it is better to use an AE system which is able to handle large quantities of data over a number of channels. In-between the sensors and the system, pre-amplifiers are used which both amplify and filter the signal. A preamplifier and sensors can be seen in Figure 26.

Figure 26 - Pre-amplifier and Nano-30 AE sensor

Currently most AE testing is conducted using commercial wired systems, manufactured by a number of companies including Mistras, Vallen and Soundwel. The manufacturer whose systems are used within the testing presented in this thesis are Mistras. Mistras produce a large selection of systems for a variety of applications, including the PCI Express-8 system which was used for the AE testing in this thesis.

The PCI Express-8 system is a compact AE systems produced by Mistras. It consists of eight channels, each able to record waveforms at 10 MSPS in both hit configuration, where data is recorded once a threshold is crossed, and in wave streaming mode for continuous recording. Full technical specifications are available from Mistras (MISTRAS, 2013b). The system operates using the software AE-win which enables a number of additional functions including filtering to reduce unneeded (unnecessary) data, parameter extraction and TOA location (Physical Acoustics Corporation, 2004).

In between the piezoelectric sensor and the AE system a preamplifier takes the very low amplitude signal and amplifies it to a more useable form. In addition to this, filters reduce background noise improving the signal-to-noise ratio. The preamplifiers used for the work within this thesis are Mistras 2/4/6 preamplifiers with a 10 kHz to 2 MHz band pass filter. These preamplifiers have a variable gain of either 20dB, 40dB or 60dB. The broad filter is well-suited to research, as the exact frequency of interest is often unknown. Full technical specification can be found from Mistras (Physical Acoustics Corporation, 2011a).

Within AE testing, piezoelectric sensors are typically used and are discussed in more detail in Section 2.1.6 of this thesis. The most common sensor used within the work presented is the Mistras Nano-30 sensor, shown in Figure 27. This wideband sensors has a good frequency response from 125 kHz to 750 kHz and a relatively good response outside of this range as can be seen in Figure 28, which shows a calibration certificate supplied by the manufacturer. A major advantage of these sensors is their small size, with a sensor face of less than 8mm, allowing for

increased accuracy in source localisation as the location at which the wave is detected is more precise.

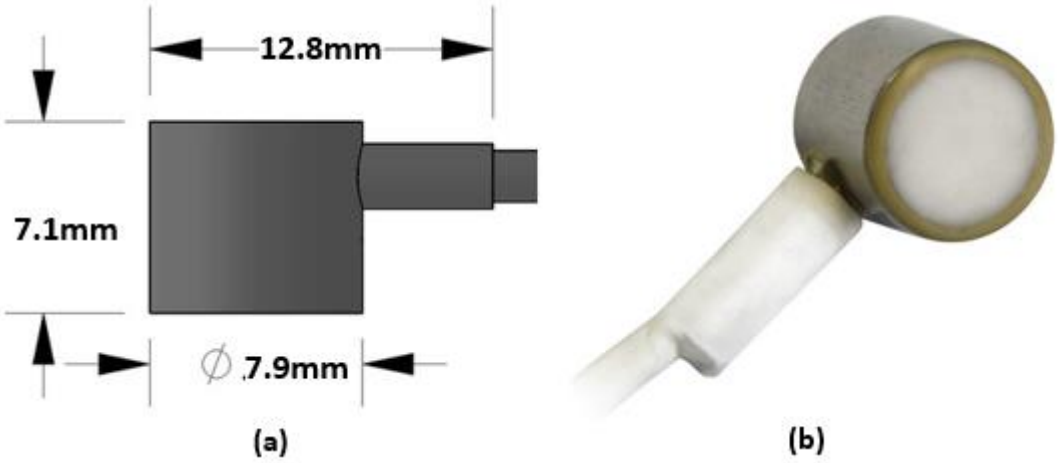

Figure 27 – Dimensions of Nano-30 sensor (a) and image (b) (from (Physical Acoustics Corporation, 2011b))

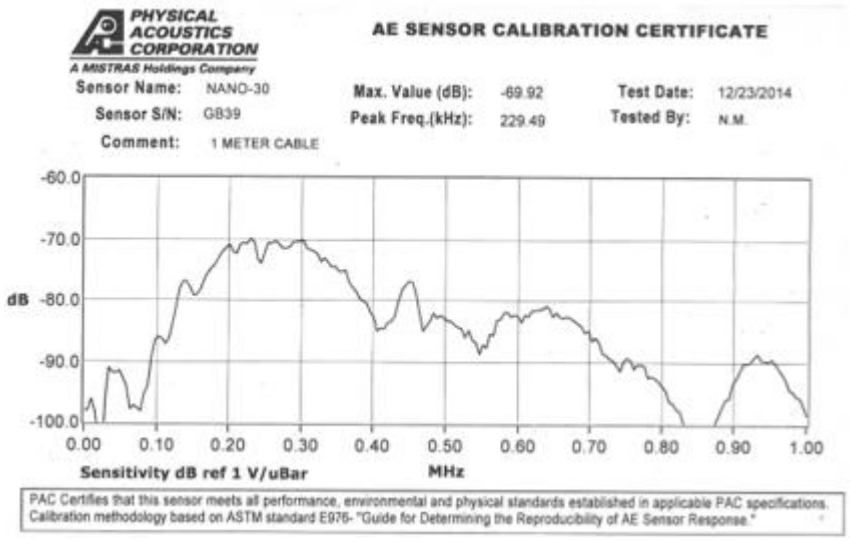

Figure 28 – Calibration certificate for a Nano-30 sensor number GB39

3.1.2 Phased Array Scanner

In order to detect the presence of damage and assess the quality of manufacture an Olympus OmniScan MX2 phased array scanner was used at various stages throughout testing and at the end of the manufacturing process. This commercial piece of NDT equipment combined with a

5L64-NW1 probe is able to quickly assess the presence of defects, such as delamination and the disbond of adhesively bonded stiffness, in composite materials.

A phased array scanner is a piece of ultrasonic inspection equipment. Ultrasonic inspection involves transmitting ultrasonic waves through a structure and analysing the wave reflected off its back surface, with differences between the transmitted and received wave indicating the presence of damage. In techniques such as C-scanning, a probe containing a single pulsing and receiving element is moved robotically above the surface of the structure to give a full field measurement of the health of the structure. This is a time consuming process and requires the specimen to be submerged in a tank of water to allow the ultrasonic waves to propagate, meaning it is less feasible for the inspection of very large parts. In addition to this, non-flat plates are significantly more difficult to scan and only possible with extensive programming. A phased array probe on the other hand contains multiple elements (the 5L64-NW1 has 64) in a linear array which each pulse ultrasonic waves simultaneously (the 5L64-NW1 pulses at 5MHz). This probe must be properly coupled to the structure, typically using water, grease or some other fluid. Moving the probe over the area of interest allows the user to quickly create a C-scan image and identify the presence of any discrepancies. The addition of an encoder, in this case a roller, means scale can be added to the C-scan. The main advantage of a phased array scanner is that areas of interest on large parts can be inspected quickly without having to move the specimen. Getting a full field measurement however is much more difficult and often requires a specialist probe to be conducted effectively, so a C-scanner is still often the best option. In both cases the user must be skilled in order to detect the presence of damage and to understand what they have detected.

3.2 Test Specimens

To test the techniques presented within this thesis a number of specimens were used. Some of the panels were manufactured in the past for other research, others were manufactured for the purpose of these tests. A number of specimens were also real aircraft structures and once a

method had been established on smaller specimens these parts were used to test the techniques on actual structures. Presented here are the dimensions, material properties and the results from some characterisation testing for each specimen used. Throughout this testing, and the testing later in this thesis, the plate structures were mounted on bubble wrap in order to acoustically decouple them from their surroundings as best as possible.

3.2.1 Composite panel A

A composite panel shown in Figure 29 was manufactured for a previous project but used at numerous stages throughout the testing within this thesis. Made from 8 plies of HexPly® M21 unidirectional pre-peg in a layup of $(0/90)_{2S}$ this panel is 1m x 1m and 3mm thick. Due to its large size and lack of any complexity this panel is used for preliminary testing.

Figure 29 – Composite Panel A

As the panel has a simple 0/90 layup its wave velocity is greater in the direction of fibre orientation meaning the wave front of the S_0 mode is dependent on direction (Paget et al., 2003). A study to analyse the velocity of the wave dependent on orientation was performed. This was done using two Nano-30 sensors, one coupled using grease to the centre of the plate and the other 150mm away from this at various angles. For each test five H-N sources were made behind the second sensor as shown in Figure 30, the data was recorded using the Mistras

Express 8 system. The S_0 arrival at each sensor was then found using the AIC technique and the difference in arrival times at the two sensors used to find the S_0 wave velocity, this was repeated at each angle. To find the A_0 mode arrival the waveforms were passed through a 60-80 kHz band pass filter within Matlab and the arrival found using a threshold crossing technique. The five different readings for each test were then averaged to give the results shown in Figure 31.

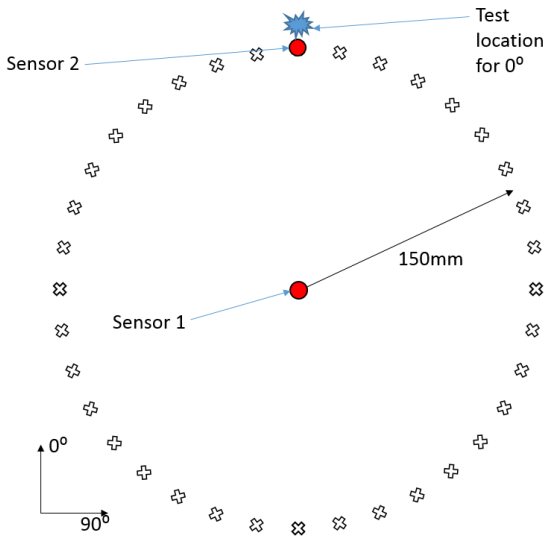

Figure 30 – Diagram of test setup to find the velocities in composite panel A ('X's' show test locations)

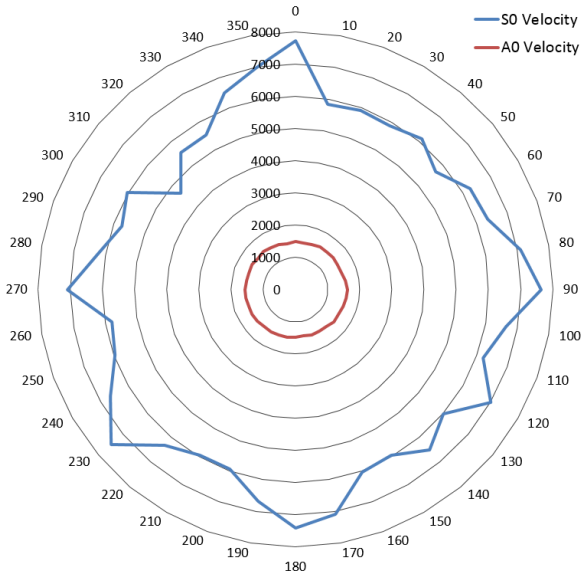

Figure 31 – Wave velocity dependency on direction within composite panel A

The results in Figure 31 confirm that the A_0 mode is not dependent on direction; the average velocity was calculated as 1600 m/s and all data was within 100 m/s of this. As expected the S_0 wave velocity was dependent on direction and in general travelled faster along the fibres. The average velocity was found to be 6350 m/s, significantly quicker than the A_0 mode. This value varied from 4655 m/s to 7723 m/s depending on direction.

The velocity data can also be used to calculate the rate of dispersion (RoD) of the modes, this was done for each direction via two methods. The first was by substituting the calculated values of velocity into the equation for RoD (Section 2.2.5) shown in Equation 13.

$$\text{RoD} = \left(\frac{1}{\frac{1}{V_{A_0}} - \frac{1}{V_{S_0}}} \right) \tag{13}$$

RoD was also calculated based on the difference in each modes arrival times at the central sensor. The two sets of results are compared in Figure 32, where a maximum 10% difference can be seen between the two methods. Errors can be attributed to the error in the threshold crossing method at detecting the onset of the A_0 mode. The average calculated RoD from both methods was around 2200 m/s.

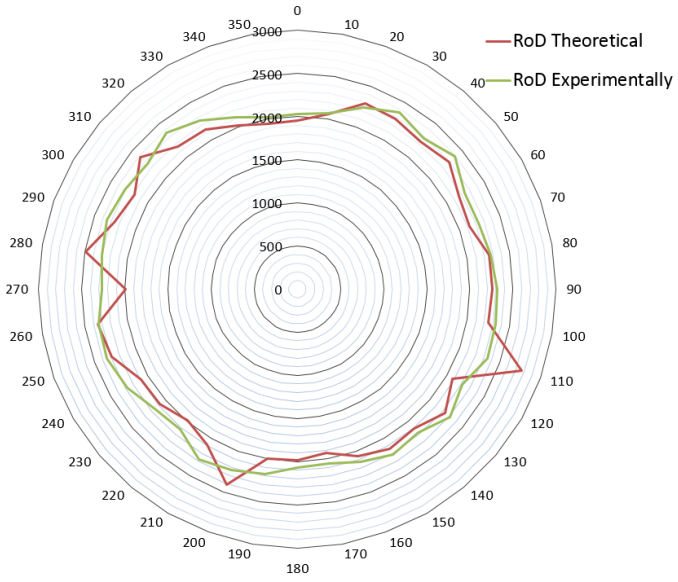

Figure 32 - RoD calculations in composite panel A

To analyse the attenuation in the panel a test was performed where H-N sources were created at 0°, 45° and 90° with varying distance from a Nano 30 sensor. Results from this test can be seen in Figure 33. This shows only slight differences in attenuation dependent on direction, meaning that the A_0 modes attenuation, likes its velocity, is independent on fibre orientation.

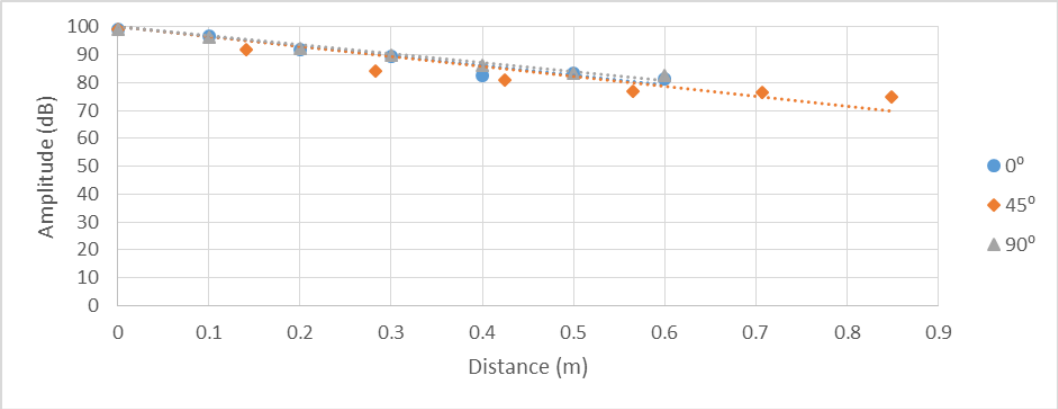

Figure 33 – Attenuation test results in composite panel A

To analyse the attenuation of the S_0 mode waveforms were put through a 200 kHz to 400 kHz band pass filter, removing the A_0 component. The maximum value within the first 30µs after triggering was then recoded to ensure the amplitude of the initial group of S_0 mode wave was found. 30µs was used as testing showed this was adequate to each the peak of the S_0 mode without detecting the A_0 mode after 100mm of dispersion. If the maximum of the entire filtered wave was used the high frequency component of the A_0 mode may have had a higher amplitude especially when combined with any reflected waves. The results from test this can be seen in Figure 34 where, as expected, the S_0 attenuation is significantly greater at 45° than along the fibre orientation. In each attenuation plot a trendline has been added, this is to calculate a gradient and find the attenuation/metre. This trendline is fixed at distance x = 0m at a value calculated from the average of the other points within the plot. In this case the A_0 attenuation is similar for each, ranging from 32dB/m to 35dB/m whereas the S_0 attenuation is less so, with

0^o and 90^o at 8 dB/m and 18 dB/m whereas 45^o is 43dB/m. The point at which it crosses x = 0m gives a good approximation of the S_0 amplitude of the H-N source, in this case 62dB, the A_0 this is typically 100dB.

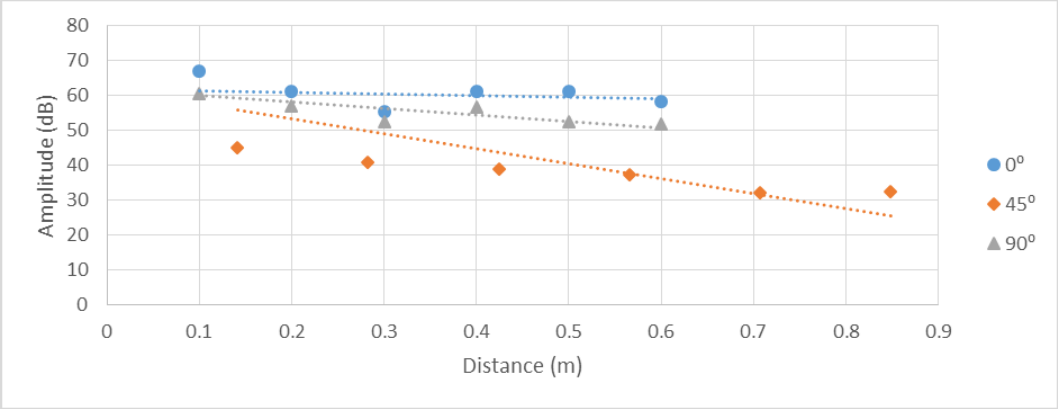

Figure 34 – Attenuation test results in composite panel A after a bandpass filter to remove the A_0 mode

In order to understand the frequency of S_0 and A_0 propagation in composite panel A the wave produced by a H-N source was recorded using a Nano-30 sensor positioned 200mm from the source along the fibre direction. Data was recorded using a Picoscope oscilloscope instead of a commercial AE system in order to give a true representation of a Nano 30's response to the structure without the gain and filter stages of a preamplifier distorting the recorded wave. A fast Fourier transform (FFT) with a Hanning window was performed on this waveform to convert it from the time to the frequency domain as can be seen in Figure 35. In this example, and those later in this chapter, the waveform has been cut in order to show the two modes, the FFT is of the entire waveform. The results show the A_0 peak amplitude as 60 kHz and the S_0 peak at 300 kHz.

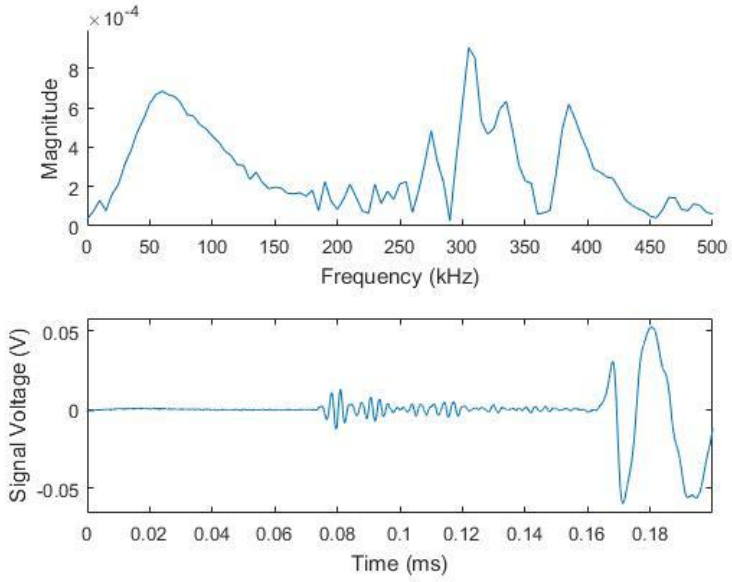

Figure 35 – FFT of H-N source (top) and a waveform (bottom) on composite panel A

3.2.2 Composite Panel B

Manufactured for the testing within this thesis Panel B was a flat composite panel with additional complexity added throughout testing. The panel was manufactured using 16 plies of 'UT210 38% RWB' unidirectional carbon fibre pre-peg with a fibre orientation of $(0/45/90/-45)_{2s}$. This layup creates what is known as a quasi-isotropic material, meaning that its extensional stiffness is the same as for an isotropic material (Paradies, 1996). Quasi-isotropic materials are much more common in composite design (Lammering et al., 2018), so this panel is more representative of a real structure than composite panel 'A'. The CFRP was supplied in a reel of 600mm width, so butting of fibres was required to create the 900mm x 900mm panel. The panel was vacuumed bagged and a porous membrane used to remove excess resin whilst being cured within an autoclave. The finished panel, seen in Figure 36, has the dimensions 900mm x 900mm x 3.5mm.

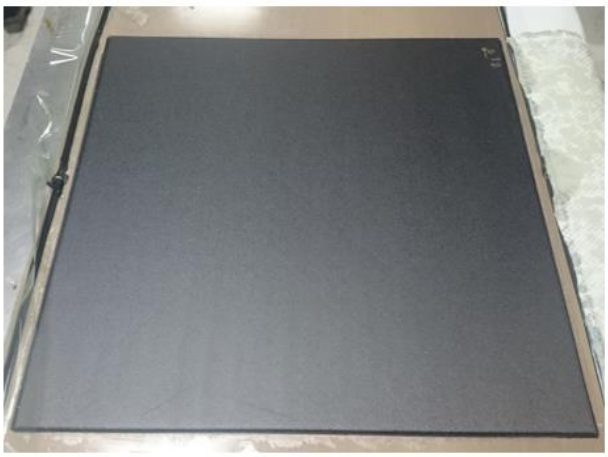

Figure 36 –Composite plate B

An ultrasonic C-scan was conducted by TWI Port Talbot to determine if any significant defects could be found within the final panel. The results from this, seen in Figure 37, show no significant defects present, apart from the expected flaws due to fibre butting.

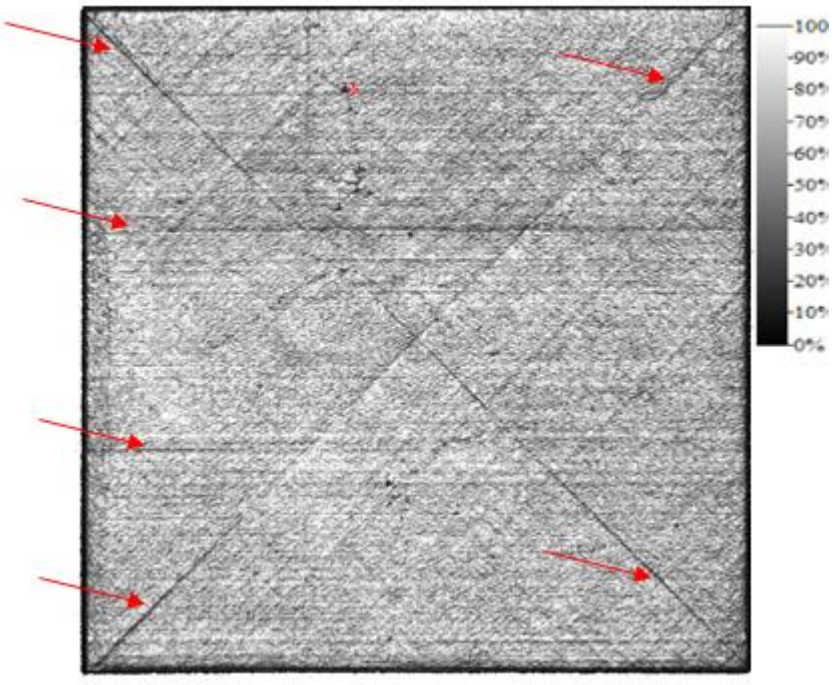

Figure 37 – C Scan of composite panel 'B' (Performed by TWI Port Talbot) with flaws caused by fibre butting marked with red arrows. The scale shows the percentage of maximum returned ultrasonic signal at each location.

To analyse the RoD of the S_0 and A_0 lamb wave propagation in this specimen a Nano-30 sensor was coupled to the centre of the panel using grease and a small weight on top to ensure pressure was applied. PLB's were then made 300mm away from the sensor at 5^o intervals from 0-90^o. The S_0 and A_0 arrival times were then picked manually to increase accuracy and the ΔT of arrival found. The wave's RoD was then calculated for each angle using these differences in arrival times, the results from this can be seen in Figure 38. It can be seen that the RoD varies slightly over the range tested, however it never deviates by more than 5% of its average of 2100m/s. These results show the assumption that this quasi-isotropic panel does not have significantly different wave RoD depending on direction is true.

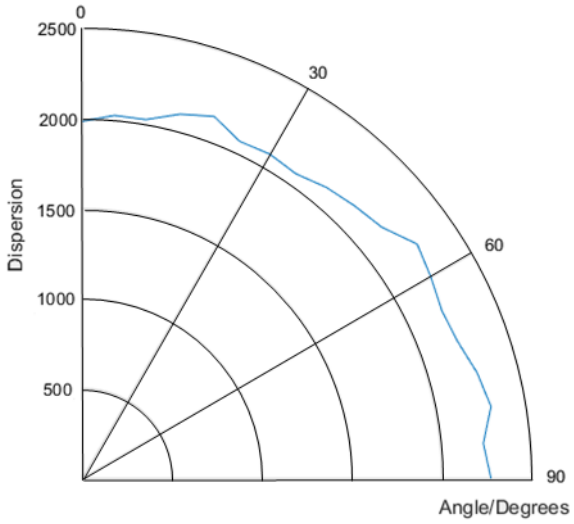

Figure 38 – RoD of S_0 and A_0 on composite panel

As for composite panel A an attenuation study was performed where H-N sources were created at 0°, 45° and 90° from a Nano 30 sensor at varying distances and recorded using an Express 8 AE system. The results from this test can be seen in Figure 39 where only minor differences in attenuation can be seen depending on direction.

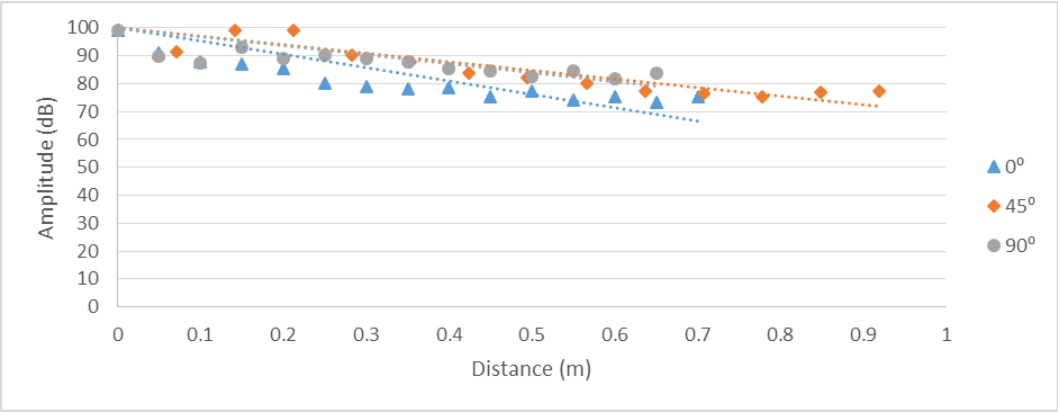

Figure 39 – Attenuation test on composite panel B

As for composite panel A the data was filtered to remove the A_0 mode to plot the attenuation of the S_0 mode with distance. The results from this can be seen in Figure 40 where only minor differences in attenuation can be seen between each direction. From the trendlines in Figure 39 and Figure 40 the A_0 attenuation ranges from 18 dB/m to 28 dB/m and the S_0 attenuation ranges from 33 dB/m to 43 dB/m. The S_0 amplitude at x=0m is 82dB.

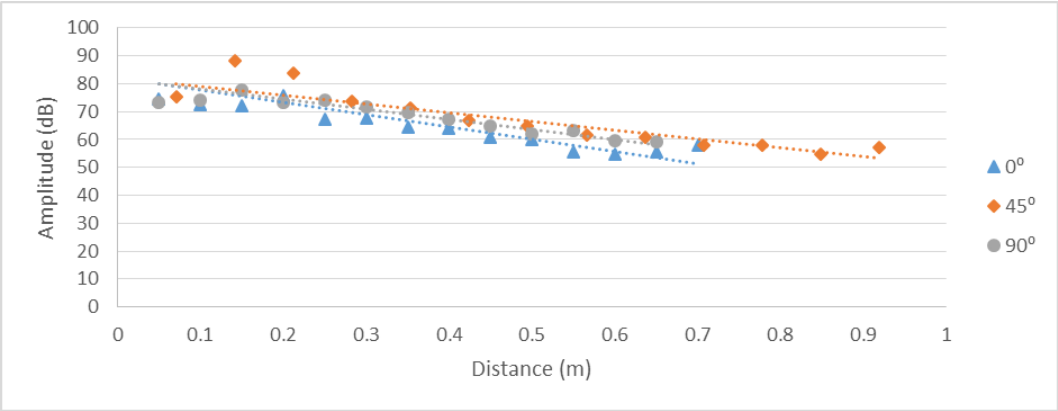

Figure 40 – Attenuation test results in composite panel A after a bandpass filter to remove the A_0 mode

As was performed on 'composite panel A' an FFT was conducted on the waveform of a H-N source produced 300mm away from a Nano-30 sensor recorded using a Picoscope oscilloscope.

The result is shown in Figure 41 where the A_0 frequency peaks at 50 kHz and the S_0 peaks at 300 kHz.

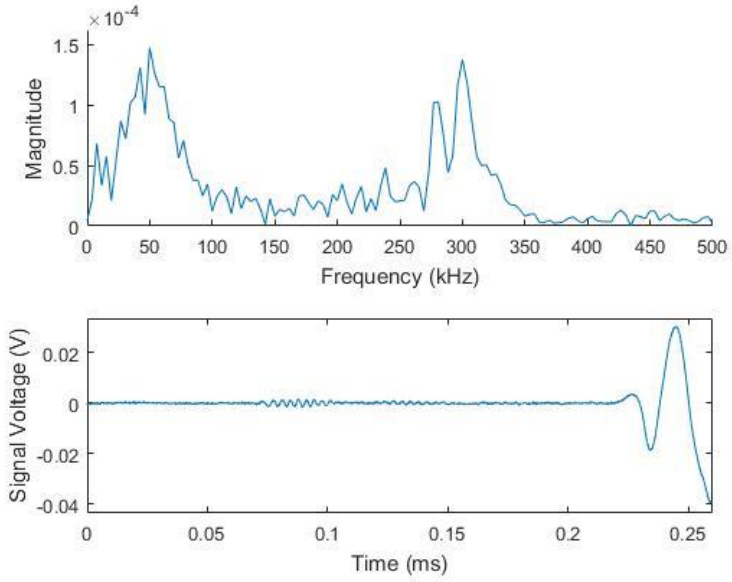

Figure 41 – FFT and waveform of H-N source on composite panel B

A number of tests were performed on composite panel B prior to any complexity being added, these are presented in later chapters. Gradually however four composite 'L' shaped stiffeners, dimensions shown in Figure 42 (a), were bonded to the panel at a regular spacing of approximately 200mm, although some error in the location of the stiffener occurred during the bonding. The exact location of the stiffeners is shown in Figure 42 (b) and the order in which they were bonded is shown in red.

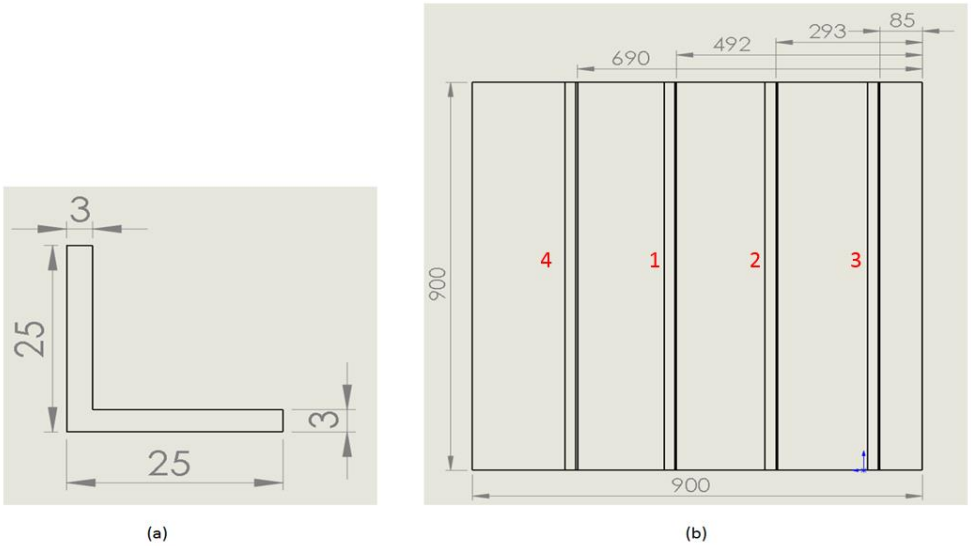

Figure 42 – Composite 'L' shaped stiffener dimensions (a) and locations of stiffeners on the plate (b)

The stiffeners were bonded using Araldite 420 a/b. The process required roughening up the surface of the stiffener and plate with sand paper to ensure a good bond, then cleaning both with acetone. Mixed Araldite was then spread over the surface of the stiffener before being aligned in the correct location. Clamps and weights were used to ensure a good bond, then the excess araldite cleaned. This was then left for 48 hours to allow the Araldite to cure under pressure. The final plate is shown in Figure 43.

Figure 43 – Composite panel B with four stiffeners bonded

To check for voids in the bonding a phased array scanner was used. The results from this are shown in Figure 44. In these scans a blue-white region represents an area where little to no ultrasonic wave has returned at the predetermined time at the probe, indicating that the wave is passing into the stiffener and the bond is good. A red – yellow response indicates a high return of ultrasonic waves on the back surface of the plate, in a non-stiffener region this indicates that no damage is present however in the stiffened region is a sign that bonding is not present in this region. Stiffener 2 is the most successful bond, as only a very small area is not bonded. The others all have regions which are less well bonded, this complexity will affect the propagation of Lamb waves as reflections will be more scattered by the irregular boundary.

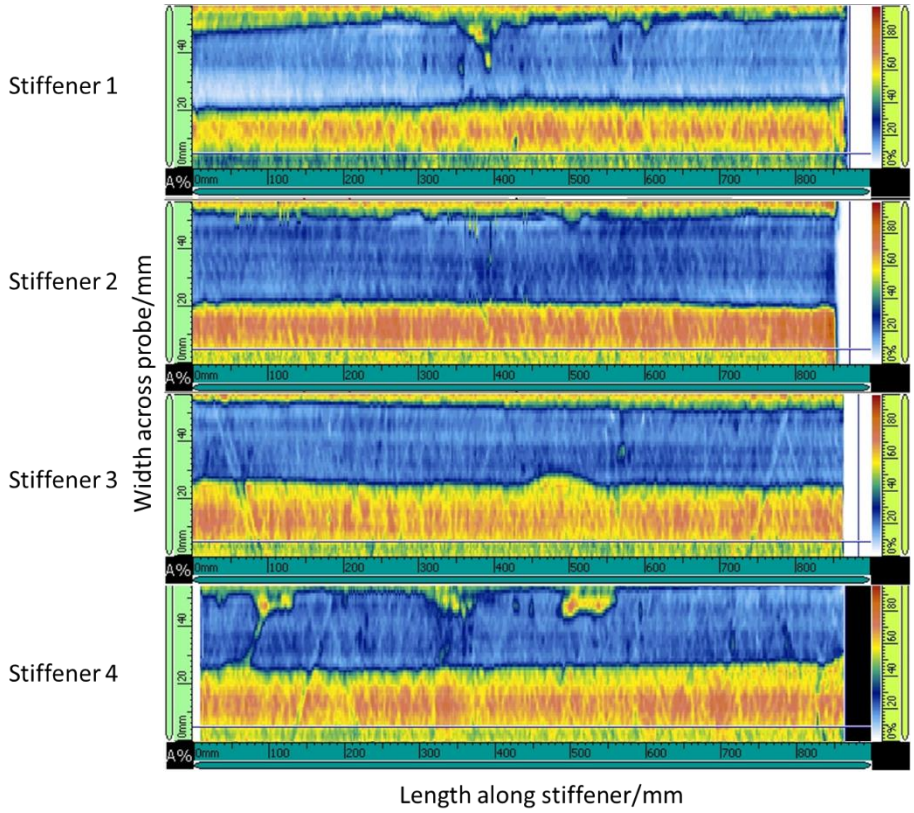

Figure 44 – Phased array C-Scan images of stiffeners

3.2.3 Simple Aluminium Plate

Another specimen used for the testing presented within this thesis was a 1250mm x 1250mm, 3 mm thick 6082-T6 aluminium plate. This plate was used extensively in the early stages of testing due to its simplicity.

As for the composite panels an attenuation test was performed. The Nano-30 sensor used was bonded using grease in the centre of the plate. Only a single direction was tested, as wave velocity and attenuation is not dependent on direction in aluminium (Paget et al., 2003). H-N sources were created at 100mm intervals away from the sensor, five at each location. The overall amplitude of the signal (A_0 amplitude) and the S_0 amplitude, predicted using the same method as with composite panels A and B, are shown in Figure 45. These results show clearly that the S_0 mode attenuates significantly quicker at 44 dB/m than the A_0 mode which attenuates at 15 dB/m. The non-linearity at the greater distances is likely to be due to edge reflections increasing the signal amplitude. The S_0 amplitude at x=0m has been approximated as 80dB.

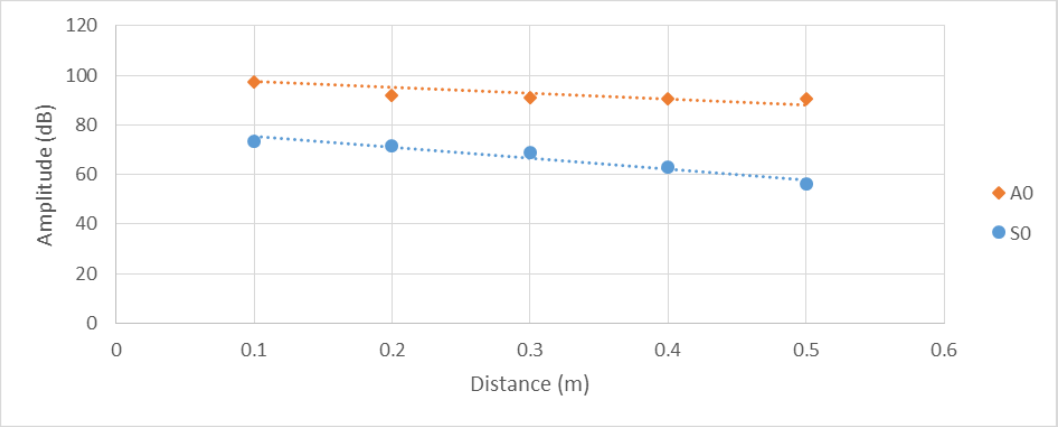

Figure 45 – Attenuation test on aluminium panel

The same test was then performed using a second sensor in order to calculate the mode velocities, and so the RoD in the plate. The average S_0 velocity was calculated as 5250 m/s and the A_0 was calculated as 2980 m/s. Substituting these values into the equation for RoD gives a

value of 8400 m/s. Analysing the arrival times at the single sensor at different distances gives a RoD value of 6900 m/s.

As was performed on the previous specimens an FFT was conducted on the waveform of a H-N source 200mm away from a Nano-30 sensor recorded using a Picoscope oscilloscope. The result from this is shown in Figure 46 where the A_0 frequency peaks at 70 kHz and the S_0 peaks at 240 kHz.

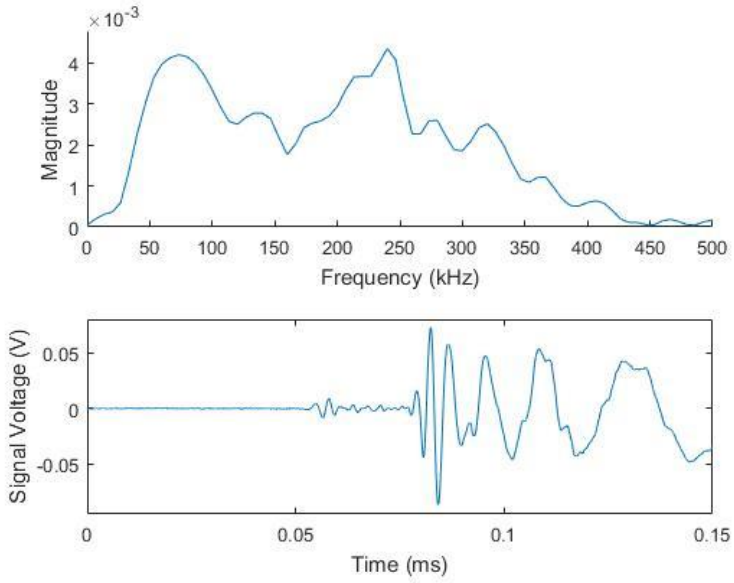

Figure 46 – FFT and waveform of H-N source on simple aluminium plate

3.2.4 Complex Aluminium Plate

Once testing had been conducted upon the simple aluminium plate presented in the previous section complexity was added. Four extruded aluminium 'C' shaped stiffeners (of the same grade as the panel with the dimensions shown in Figure 47 (b)) were attached at regular intervals to the plate and another identical plate attached to the bottom of this, as can be seen in Figure 47 (c) and (d) to explore the transmission of AE through a series of more complex paths. Instead of all stiffeners being bonded with Araldite, half of the stiffeners were riveted to the structure with twenty-five 4mm aluminium rivets attached every 5mm in a zig-zag fashion, as seen in Figure 47 (a) to explore the effect of different attachment methods on the transmission of AE through the

stiffener area. The way in which each stiffener is attached is shown in Figure 47 (d). Simple testing showed velocity and RoD values were equal to those within the simple aluminium panel as expected.

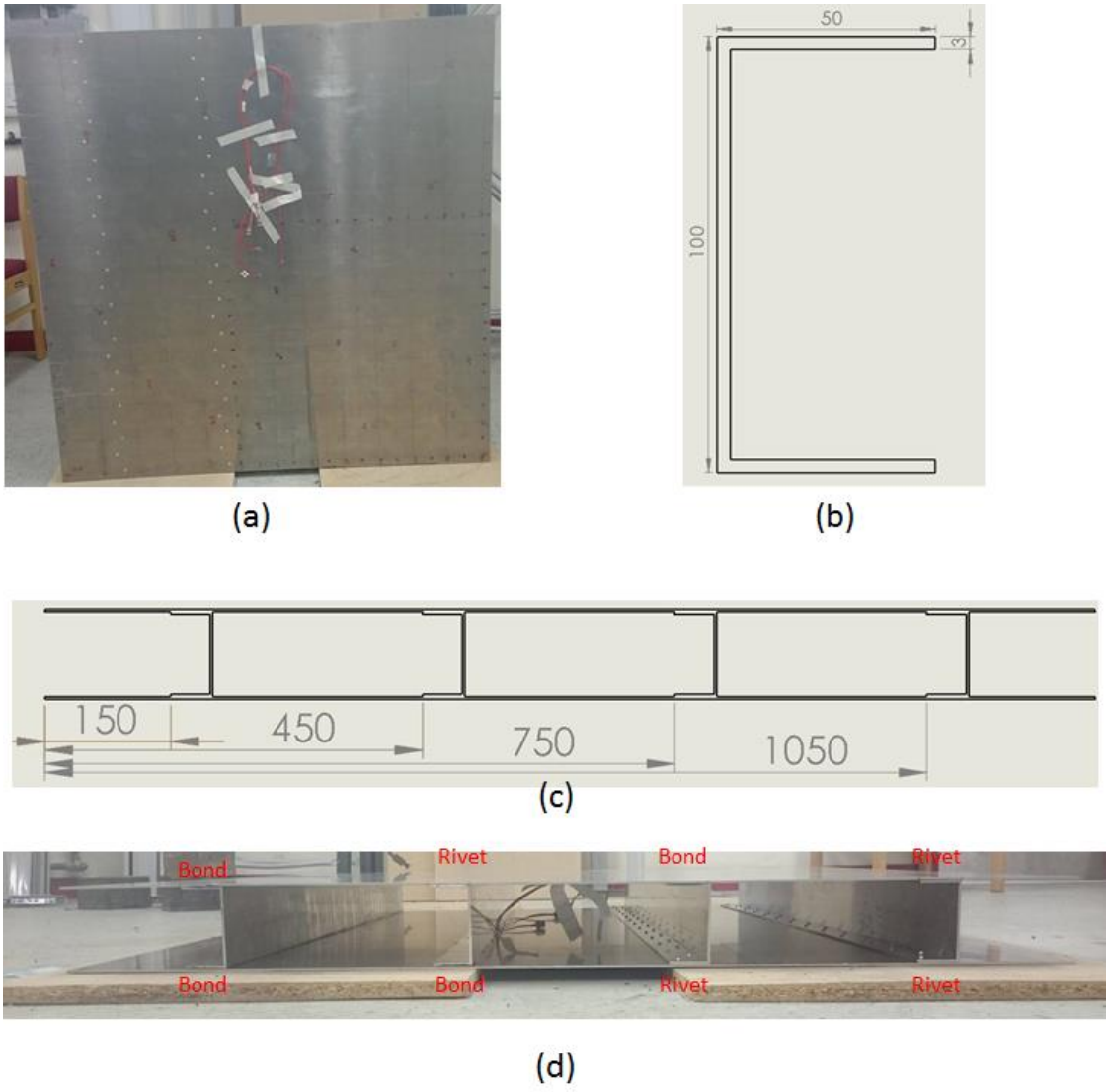

Figure 47 – Complex aluminium panel front view (a), 'C' section stiffener schematic (b), side view schematic (c) and side view with type of attachment shown in red (d). All dimensions in mm.

3.2.5 A320 Wing

A number of tests were conducted on an aluminium A320 wing situated within Cardiff University, seen in Figure 48 (a). An idea of the internal structure of the wing can be seen in Figure 48 (b) where significant complexities include of a number of stringers and ribs riveted to

the top and/or bottom skin of the wing. An additional complexity present is skin butting, shown in Figure 48 (c), where the two sheets of aluminium that make up the top (or bottom) skin are attached together. The section of wing is from rib 10 onwards (just after where engines would be attached) and is 12m in length. The majority of testing was conducted on the top skin around ribs 11, 12 and 13; as this area best avoids the edge effects found at the boundaries of the skin, this area is indicated in Figure 48 (a). In this region the skin was approximately 8mm thick, however this varied.

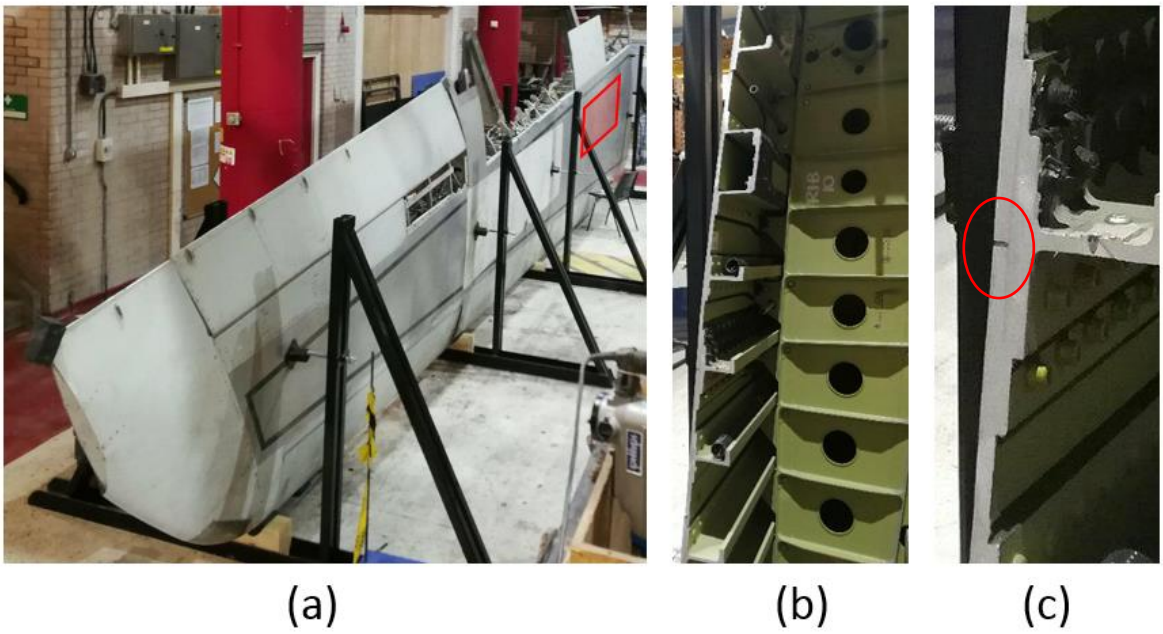

Figure 48 – A320 Wing with test area marked in red (a), internal structure (b) and skin butting (c)

As with the previous specimens an attenuation test was performed on the A320 wing. A nano-30 sensor was coupled with grease centrally between two stiffeners on the outside skin of the structure. H-N sources were then created at 50mm intervals at 0^o, 45^o and 90^o from the sensor, where 90^o ran parallel to the stiffeners, the waveforms from these were recorded with an Express 8 AE system. The data for the A_0 mode amplitude at each location are shown in Figure 49.

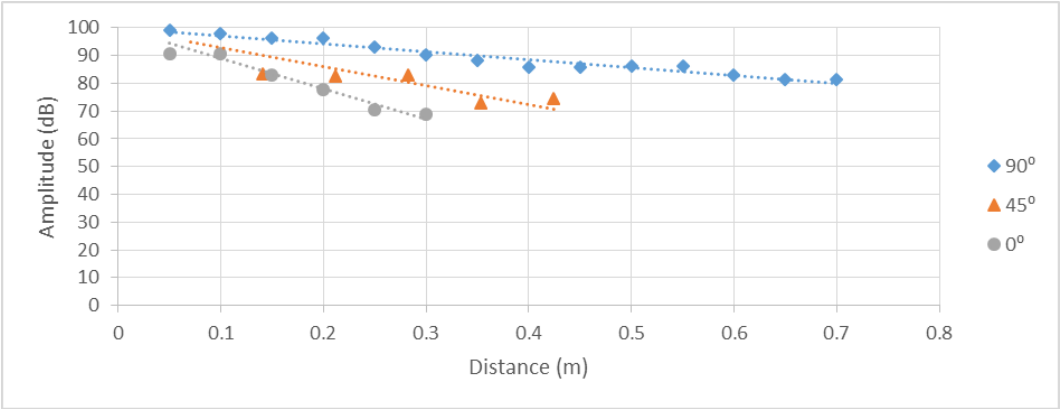

Figure 49 – A320 wing attenuation test results

Figure 50 shows the S_0 attenation produced using the same filtering method as for previous structures. The trendline data from the A_0 plot shows a 0^o attenuation of 110dB/m, 45 attenuation of 69dB/m and a 90^o attenuation of 28dB/m. For S_0 mode the 0^o attenuation is 118 dB/m, 45^o is 100 dB/m and 90^o is 23 dB/m. The S_0 amplitude at x=0m has been approximated as 90dB.

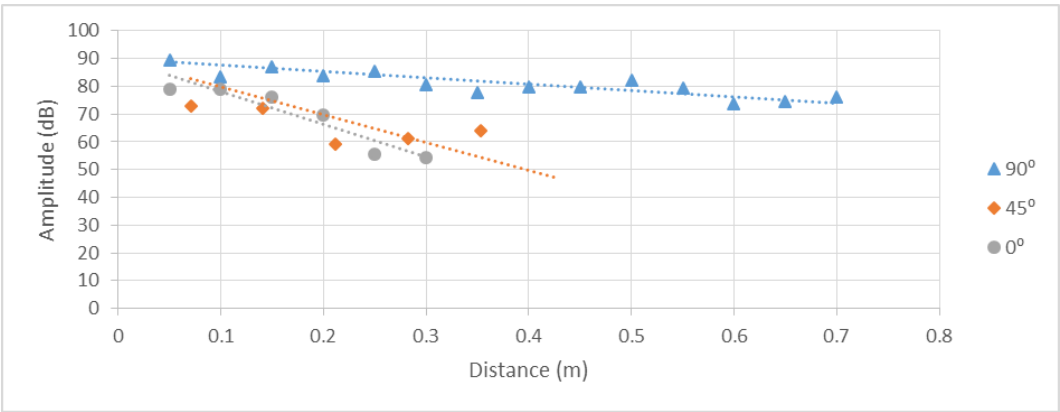

Figure 50 – Attenuation test results on A320 wing after a bandpass filter to remove the A_0 mode

Another attenuation test was performed on the A320 wing to understand the distance the wave produced from a H-N source would travel whilst still crossing a 45 dB threshold. For this test a Nano-30 sensor was bonded using silicon to the skin of the A320 wing in-between two stiffeners. Five H-N sources were then produced at 100mm intervals moving away from the sensors at 90^o, i.e. between the stringers, until the 45dB threshold was not crossed. The process was then

repeated at 0° running across the stringers. As expected the waves propagated much further at 90° as the stringers act as a wave guide for the lamb waves, i.e. they reflect off the stringers keeping more energy in between the stiffeners. At 0° the waves travel only 25% of the distance at 90°, this is due to reflections caused by the stringers attenuating the wave. This is reduced further still due to the skin butting (seen in Figure 48 (c)) at 450mm distance. The full results can be seen in Figure 51, where attenuation occurs at 18 dB/m parallel to the stiffeners and 80 dB/m across them.

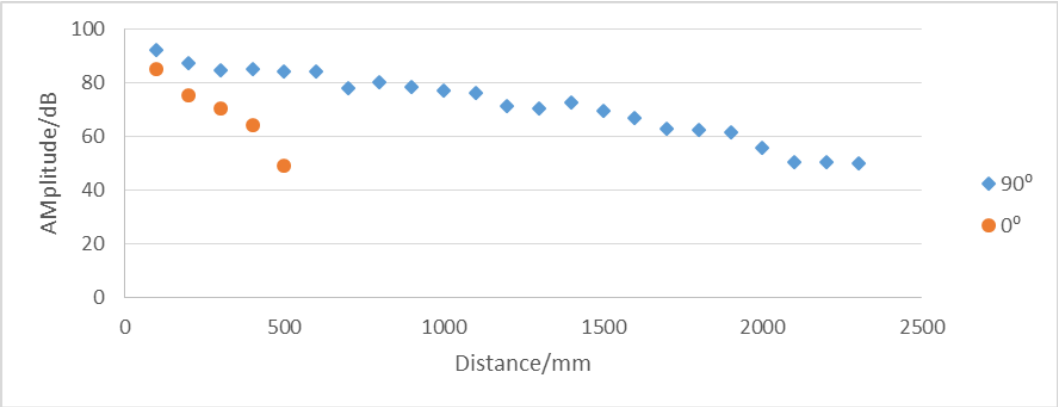

Figure 51 – Attenuation test on A320 wing using a Nano-30 Sensor, 90° parallel to stringers

Additional testing with other sensor types saw waves propagating significantly further - up to 4.8m at 0° in the case of highly resonant 300 kHz McWade sensors. This is to be expected as resonant sensors are much more sensitive to their given frequency, hence their common use in structural testing.

Modal analysis on the A320 wing is far more complex than a simple specimen as filtering with threshold crossing and more advanced techniques such as continuous wavelet transforms are not able to repeatedly detect the arrival of the A_0 mode. More investigation is presented later in this thesis on accurate prediction of the A_0 arrival in this structure.

As for the other specimens an FFT was performed using the same equipment. The H-N source used for these was 200mm from the sensor with both the source and the sensor located in-

between the same two stiffeners. The results are shown in Figure 52 where the A_0 peak frequency is 90 kHz and the S_0 peak frequency is 210 kHz.

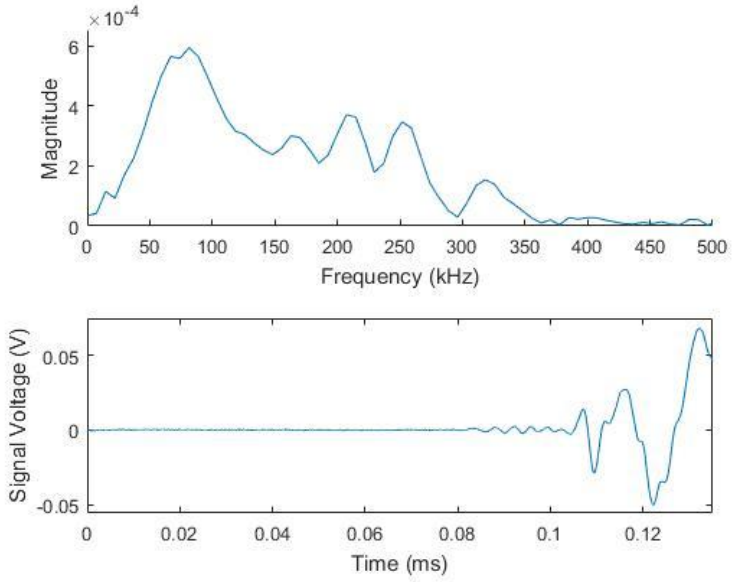

Figure 52 – FFT and waveform of H-N source on A320 wing

3.2.6 A320 Vertical Stabiliser

Another real aircraft structure tested on at Cardiff University was an A320 vertical stabiliser, shown in Figure 53. This complex structure consists of a 1.6mm thick CFRP skin of unknown layup stiffened by a number of CFRP stringers running along its length. Ribs then run across the width of the specimen which connect the two surfaces together with the front and rear spar.

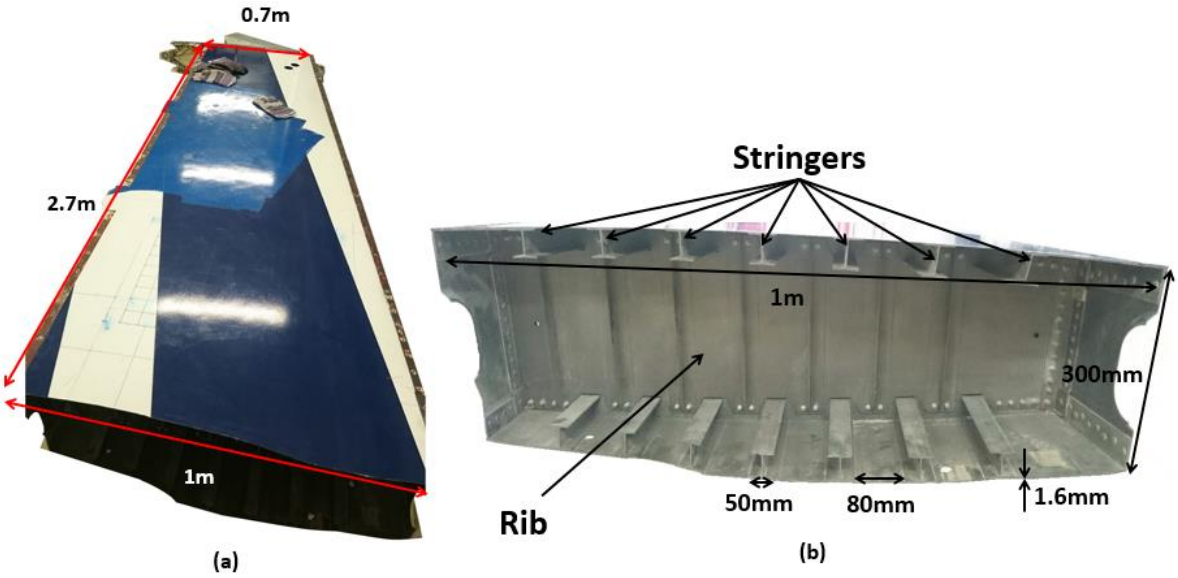

Figure 53 – A320 vertical stabiliser (a) and side view showing internal structure (b) with dimensions

As with the previous specimens an attenuation test was performed on the vertical stabilizer. A nano-30 sensor positioned halfway between two stiffeners was coupled with grease to the outside skin of the structure. H-N sources were then created at 100mm intervals at 0^o, 45^o and 90^o from the sensor where 90^o ran parallel to the stiffeners. The waveforms from these were recorded with an Express 8 AE system. The data for the A_0 mode amplitude at each location are shown in Figure 54.

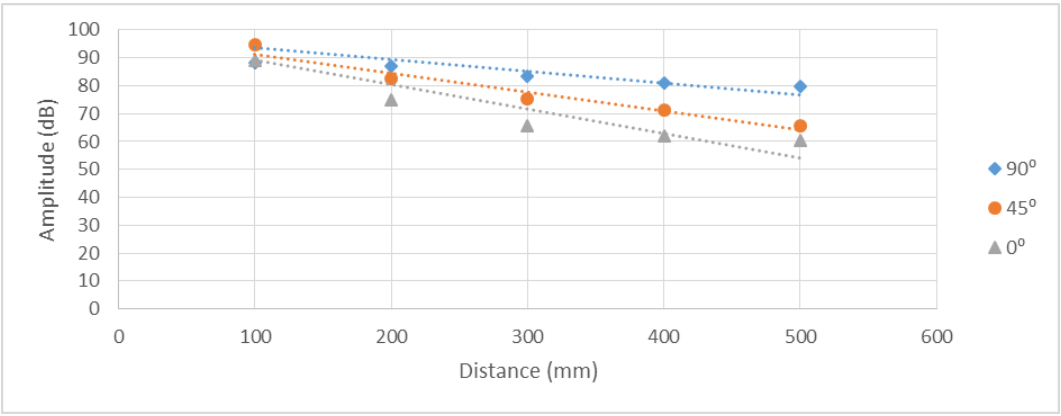

Figure 54 – A320 vertical stabilizer attenuation test results

Figure 55 shows the S_0 attenation produced using the same filtering method as for previous structures. The trendline data from the A_0 plot shows a 0^o attenuation of 88dB/m, a 45^o attenuation of 67dB/m and a 90^o attenuation of 43dB/m. For the S_0 mode the 0^o attenuation is 109 dB/m, 45^o is 75 dB/m and 90^o is 85 dB/m. The higher attenuation in the 90^o direction when compared with the 45^o is potentially due to the layup of the plate, more fibres at 45^o will affect the S_0 mode more than the A_0. The S_0 amplitude at x=0m has been approximated as 89dB.

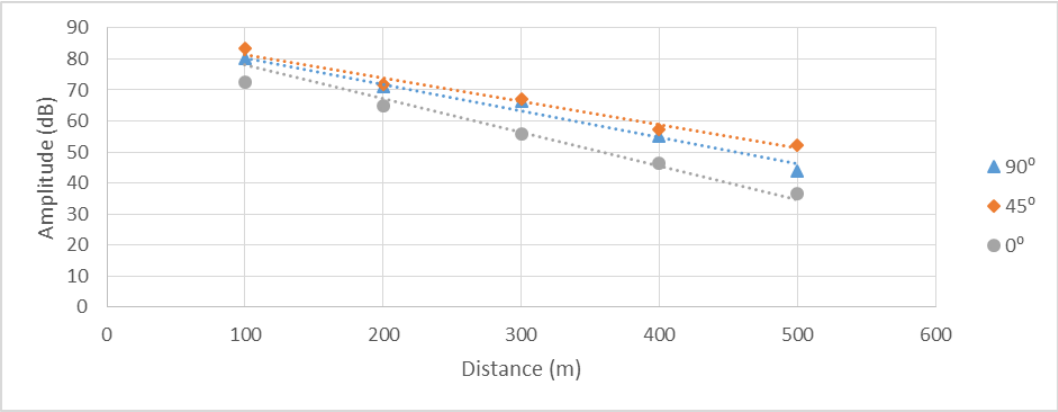

Figure 55 – Attenuation test results on A320 vertical stabilizer after a bandpass filter to remove the A_0 mode

As for the other specimens an FFT was performed using the same equipment. The H-N source was 200mm from the sensor with both located halfway between the same two stiffeners. The results are shown in Figure 56 where the A_0 peak frequency is 50 kHz and the S_0 peak frequency is 240 kHz.

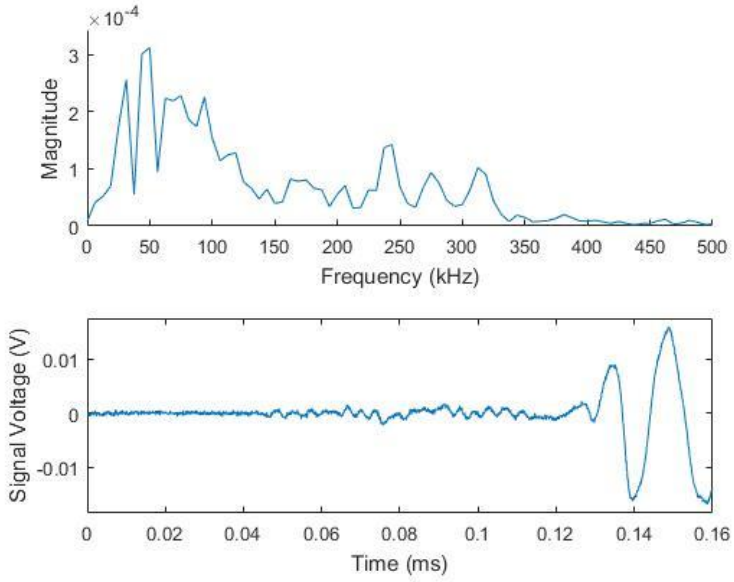

Figure 56 – FFT and waveform of H-N source on A320 vertical stabalizer

3.2.7 A350 Wing

Access was available for a limited time for testing to be performed on a full scale A350 wing at Airbus Broughton. The wing is a static structure used for NDT and composite repair training purposes and contains additional holes that would not be present in a flying aircraft's wing structure. The fully composite structure can be seen in Figure 57 (a). The wing skin varies in thickness over the aircraft, ranging from over 30mm thick to under 10mm. The area of interest was 11mm thick and the layup is unknown. The internal structure is typical of a wing and consists of ribs running from the leading to the trailing edge of the wing and bolted to the top and bottom skin. Stringers run along the length of the wing and unlike the A320 wing, where they are riveted, in the A350 the stringers are bonded to the skin. The internal structure between two ribs can be seen in Figure 57 (b), where it should be noted that more of the skin has a stiffener attached than does not.

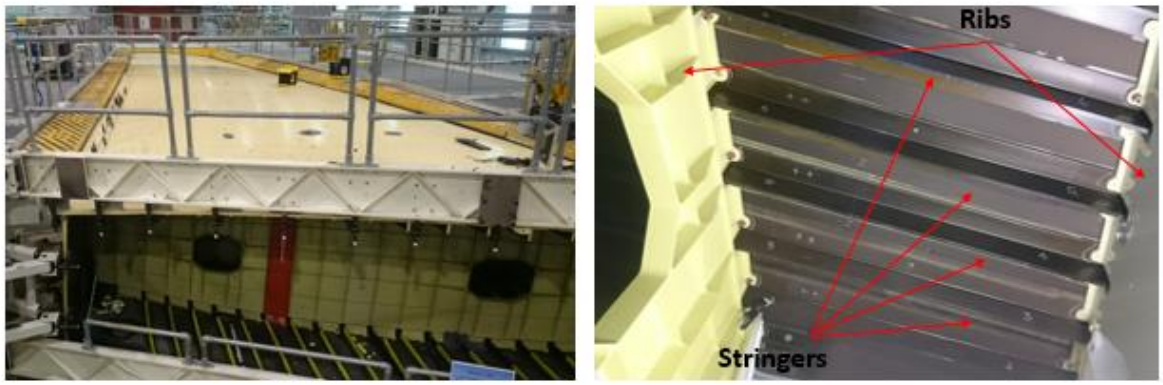

Figure 57 – A350 composite wing within access rig at Airbus Broughton (a) and typical internal structure of wing (b)

As for the previous specimens an attenuation test was performed on the wing using a Nano-30 sensor and an Express 8 AE system. H-N sources were created every 50mm at 0°, 45° and 90° from the sensor, where 90° was parallel to the stiffeners. The results are shown in Figure 58 where as expected 0° is the most attenuated, as it crosses the most stiffeners.

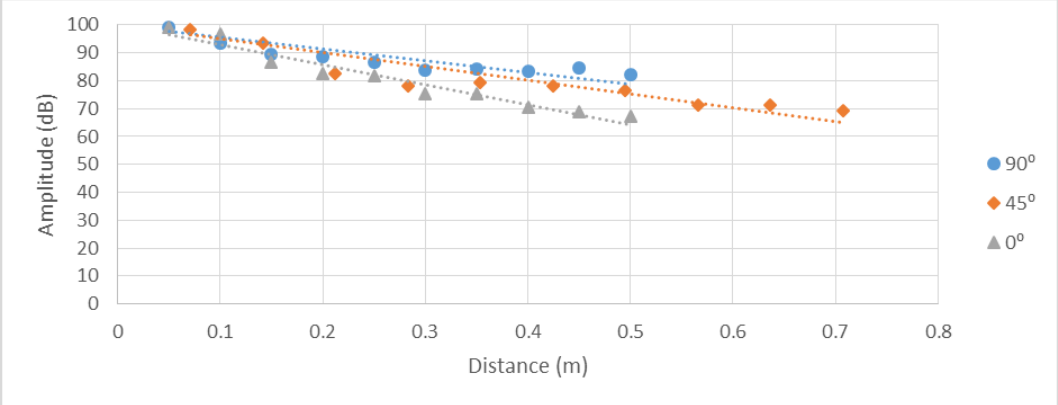

Figure 58 – A350 attenuation test results

Figure 59 shows the S_0 attenuation produced using the same filtering method as for previous structures. As for the unfiltered attenuation, 0° is the most attenuated signal and the overall attenuation for all channels is greater. The trendline data from the A_0 plot shows a 0°

attenuation of 71dB/m, a 45° attenuation of 49dB/m and a 90° attenuation of 42dB/m. For S_0 the 0° attenuation is 91dB/m, 62 dB/m for 45° and 56dB/m for 90°. The S_0 amplitude at x=0m has been approximated as 90dB.

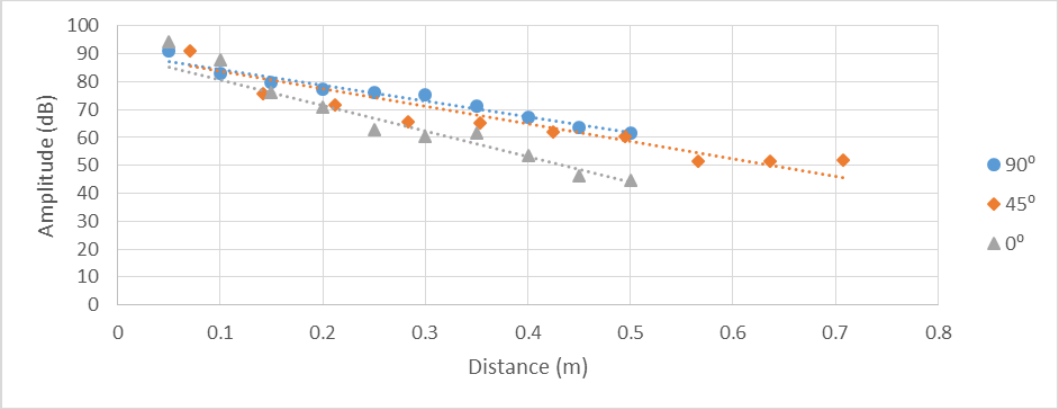

Figure 59 – Attenuation test results on A350 wing after a bandpass filter to remove the A_0 mode

As for other specimens an FFT was performed upon the waveform recorded from a H-N source by a Nano-30 sensor, in this case the event was 300mm from the sensor. The varying distance compared to the previous specimens were to ensure adequate dispersion occurred for the waveforms, allowing for a suitable waveform to be processed. Both sensor and source were in-between the same stiffeners. The result from a typical FFT of an event is shown in Figure 60 where a peak A_0 frequency of 40 kHz and a peak S_0 frequency of 275 kHz can be seen.

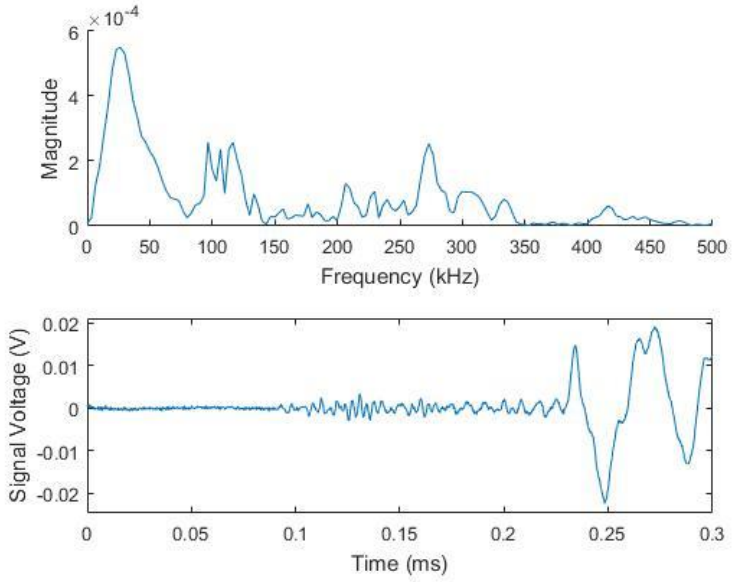

Figure 60 – FFT of and waveform H-N source on A350 wing

3.2.8 A320 Wing Panel

Up to this point all real structures tested have been too large to conduct a fatigue loading investigation. In order for this to be done, a larger section of aluminium A320 wing top skin was cut to 1.38m x 0.5m, this test piece is shown in Figure 61. The skin of the panel is not of uniform thickness and ranges from 9mm thick to 6mm. The panel has four stiffeners running down its length each attached by approximately 90 rivets, there are also a number of holes running across its width which would be used to attach the ribs if they were present.

Figure 61 – Image of cut down A320 wing panel

As for previous specimens an attenuation test was performed using a Nano-30 sensor and an Express 8 AE system. H-N sources were created every 50mm at 0°, 45°, -45° and 90° from the sensor, where 90° was parallel to the stiffeners. As expected, results from this test, shown in Figure 62, show less attenuation parallel to the stiffeners and a greater level when crossing them.

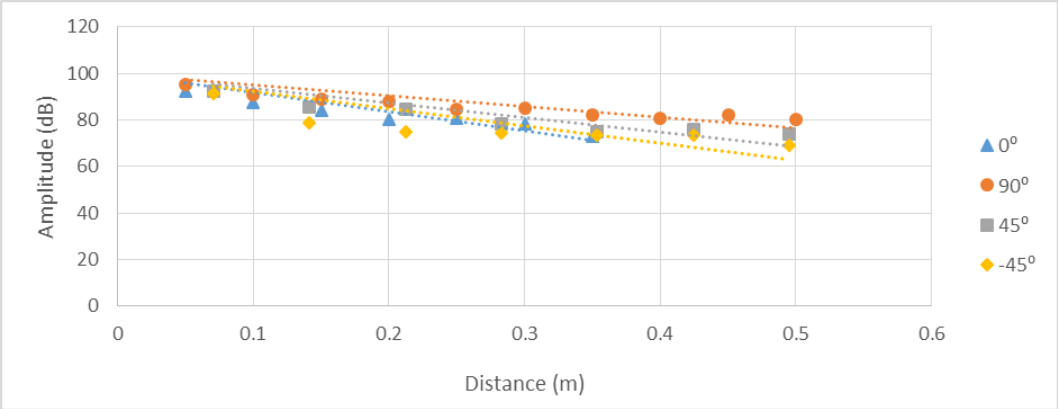

Figure 62 – Attenuation test on A320 Wing Panel

Figure 63 shows the S_0 attenation produced using the same filtering method as for previous structures. The trendline data from the A_0 plot shows a -45° and 45° attenuation of 74dB/m, a 0° attenuation of 82dB/m and a 90° attenuation of 47dB/m. For the S_0 mode -45° and 45° attenuations are 59 dB/m and 49dB/m respectively, 0° is 40 dB/m and 90° is 50 dB/m. These values shown that unlike the A_0 mode, the S_0 mode appears to be relativeley unaffected by the complexity. This correlates with the work by Reusser (Reusser et al., 2014) which showed that S_0 modes were less effected by structural complexity than A_0 modes. The S_0 amplitude at x=0m has been approximated as 90dB.

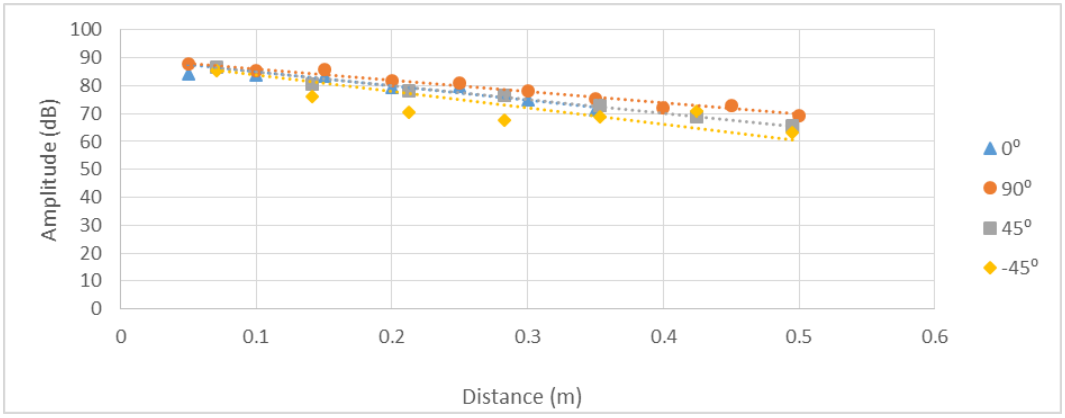

Figure 63 – Attenuation test results on A320 panel after a bandpass filter to remove the A_0 mode

As for the other specimens an FFT was performed using the same equipment. The H-N source was 200mm from the sensor with both located between the same two stiffeners. The results from this test are shown in Figure 64 where the A_0 peak frequency is 70 kHz and the S_0 peak frequency is 160 kHz.

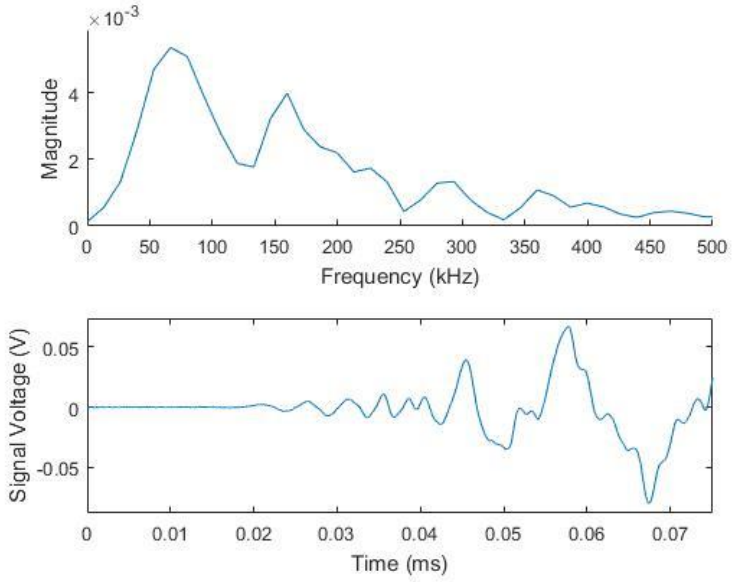

Figure 64 – FFT and waveform of H-N source on A320 panel

3.2.9 Summary

Within this section a number of specimens have been introduced along with the results of preliminary testing for each. Table 1 shows the frequency, RoD and attenuation results for each structure. Throughout the testing performed within this thesis the data in Table 1 was used regularly, the frequency data for example was used to properly create filters for the post processing of data. The RoD data was used to perform SSMA and the attenuation data was used to ensure sensors were correctly spaced.

Table 1 –Summary of frequency, RoD and attenuation data

Specimen	Propagation Frequency (kHz)		Average Dispersion (m/s)	Direction	Attenuation rate (dB/m)		S_0 Amplitude (dB)
	S_0	A_0			A_0	S_0	
Composite panel A	300	60	2200	0	34	8	62
				45	35	43	
				90	32	18	
Composite panel B	300	50	2100	0	30	33	82
				45	28	43	
				90	18	36	
Aluminium Panel	240	70	6300	N/A	23	44	80
Aluminium A320 Wing	210	90	N/A	0	110	118	90
				45	69	100	
				90	28	23	
Composite A320 Vertical Stabiliser	240	50	N/A	0	88	109	89
				45	67	75	
				90	43	85	
Composite A350 Wing	275	40	N/A	0	71	91	90
				45	49	62	
				90	42	56	
Aluminium A320 Panel	160	70	N/A	-45	74	59	90
				0	82	40	
				45	74	49	
				90	47	50	

4 Three Closely Spaced Sensor Source Location

The use of three closely spaced sensors to locate an acoustic emission source was tested extensively by Aljets (Aljets et al., 2011, Aljets, 2011, Aljets et al., 2012). This technique requires the three sensors to be closely located in an equilateral triangle and was shown to locate sources in simple aluminium and composite structures. This is done by using the difference in A_0 and S_0 mode arrival times at each sensor to predict the distance, and the difference in A_0 arrival between sensors to predict the angle of arrival. Further information regarding this work can be found in Section 2.2.6 of this thesis.

This chapter gives an overview of the method Aljets used to predict the location of events, followed by the proposal of modifications to increase the accuracy and reliability of the method. The modifications are both to the way in which the three sensors locate an event and the way in which the S_0 and A_0 mode arrivals are predicted, including a novel method of A_0 mode detection. The modifications proposed aim to allow the method to locate events in complex aircraft structures, something not attempted in the work by Aljets or other authors who have used closely spaced sensors to locate AE. The original and modified techniques have been tested on a range of simple and complex structures in order to assess their accuracy and reliability. Accuracy will be measured based on the average absolute location error when locating artificial events over a given area of a structure, reliability is based on the number of points in this area that have been located within a given level of accuracy.

Within this chapter all testing was conducted using conventional wired AE systems, typically a Mistras Express 8 system, unless stated. Thought was given throughout to the suitability of the techniques being applied to a wireless system. In some cases it was found that whilst the methods used are not suitable for wireless systems they give an improvement in accuracy for application within a wired system. Using a technique where three sensors are close together has two main advantages over a traditional localisation method even when using a wired system. Firstly, on large scale tests it reduces the number of locations wires need to be run to, easing

the integration to the structure. Secondly the technique offers the potential for a reduced number of sensors to be required to monitor an area, this reduces the weight and cost of the implementation of AE monitoring of a structure, as demonstrated in Section 2.2.6, Figure 21.

4.1 Overview of Current Method

4.1.1 Mode Arrival Prediction

A key requirement of the three sensors technique is the ability to accurately detect the arrival of the S_0 and A_0 modes to enable the distance to be predicted. As discussed in Section 2.2.5 a number of authors (Hamstad et al., 2002, Aljets, 2011) have used wavelet transforms in order to do this. Once the wavelet analysis has been performed the arrival time is found by firstly identifying the maximum amplitude of the frequency associated with the A_0 mode; the predicted arrival time is then the first point at this frequency which crosses a predetermined percentage of this maximum. In the work by Aljets different percentages are used, either 70%, 80% or 90% dependant on the specimen. A constantly changing threshold value is something that should be avoided when possible, as tailoring to achieve the best results in each specimen is not feasible for large scale testing. This also requires a specialist to set up the system, rather than a technician, something that would add significant cost to its implementation.

Within this thesis wavelet transforms have not been used in order to predict the arrival times, this is for two main reasons. Firstly, the computational power required for wavelet analysis is far higher than is possible in a wireless system and as the aim of this work is to test techniques that could theoretically be used within a wireless system this approach becomes infeasible. Secondly the technique only works within simple, plate like structures with complexity significantly affecting its accuracy (Aljets et al., 2012). As the aim of this work is to apply the three sensor approach to complex structures another approach was investigated.

Instead, within this chapter the S_0 mode arrival has been predicted using a threshold crossing technique on the unfiltered waveform. In order to predict the arrival of the A_0 mode the waveforms have then been processed using digital filters to remove the S_0 mode. Once filtered,

methods of predicting the A_0 arrival were used, for initial testing a threshold crossing method was used with both a fixed threshold and one which is dependent on the maximum amplitude. In later sections more complex methods of predicting the arrival of the A_0 mode are presented and tested.

Waveforms were filtered within Matlab using a bandpass finite impulse response filter. The 'designfilt' function was used to create the filters with pass frequencies 20 kHz above and below the value identified from the FFT tests presented within Chapter 3. In the case of composite panel B the peak A_0 frequency was 50 kHz. Figure 65 shows the waveform produced by the H-N source in composite panel B (Section 3.2.2) as well as the output of a 30 kHz – 70 kHz 250th order filter. This filter was chosen based on results from preliminary testing, a high order filter was used in order to get a sharp transition. The output of the filter shows that the S_0 mode has been removed from the signal.

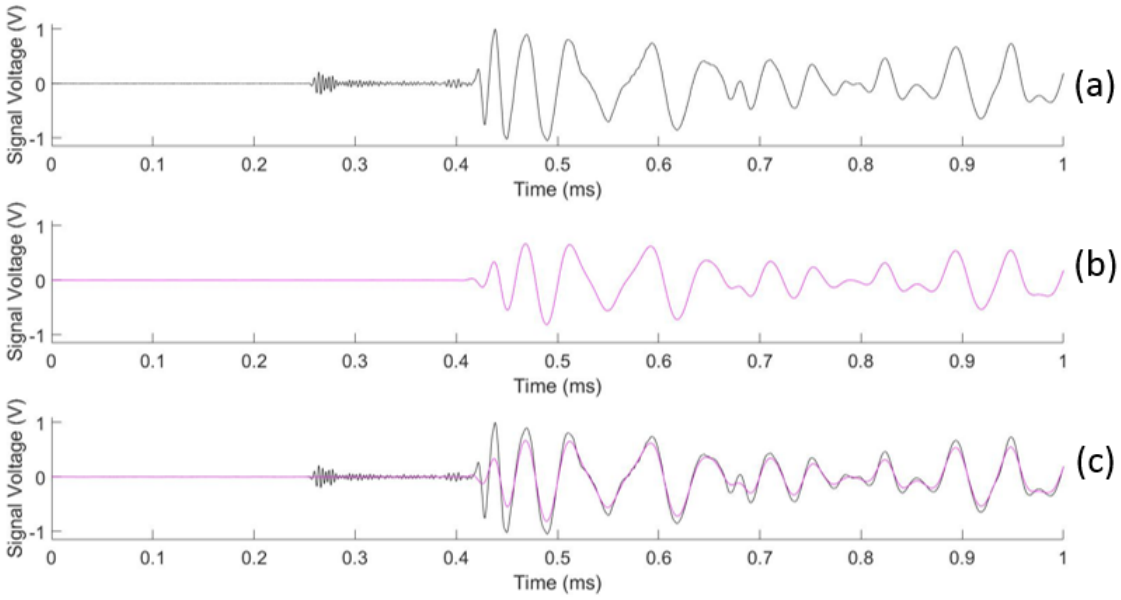

Figure 65 – Waveform from a H-N source on composite panel B plotted in black (a), the same waveform filtered plotted in purple (b) and both plotted alongside each other (c)

4.1.2 Angle of Arrival Prediction

Using multiple sensors in a closely spaced array to locate an arriving wave is an approach not only used to locate AE; sonar technology, for example, uses similar general techniques to those being presented within this chapter (Waite, 2005). In general, the assumption is made that the wave front arriving at the sensors is straight and linear to the angle of arrival at the array, as shown in Figure 66. In reality this isn't the case: the wave front is circular, or even elliptical depending on material and mode. This causes some error in the angle prediction, however unless the event is very close to the sensor array this error is negligible. If the event is close to the array significant angular error may be present due to this issue, however as the distance to the source is low, the overall location error is minimal.

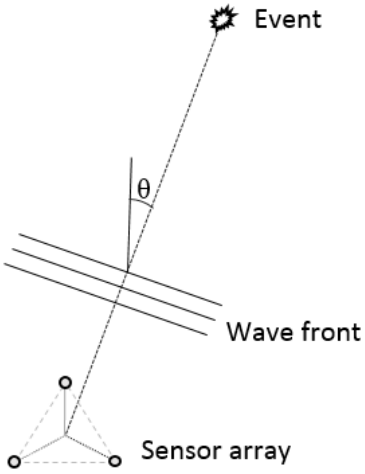

Figure 66 – wave front from an AE event traveling towards a three sensor array

In the work conducted by Aljets (Aljets et al., 2011, Aljets, 2011, Aljets et al., 2012) the angle was predicted using what shall be referred to as the $dT_{min/max}$ method. This was conducted using the A_0 mode arrival times due to the fibre orientation making the velocity of the S_0 mode direction dependent. When an event occurs the wave takes times T_1, T_2 and T_3 to arrive at each sensor, as shown in Figure 67 (a). The angle of arrival can be found using the smallest difference between their arrival times, known as dT_{min} (shown in Figure 67 (b)) and the maximum time a

wave could take to travel between two sensors (dT_{max}). This can then be represented as in Figure 67 (c), allowing the angle to be found using Equation 14.

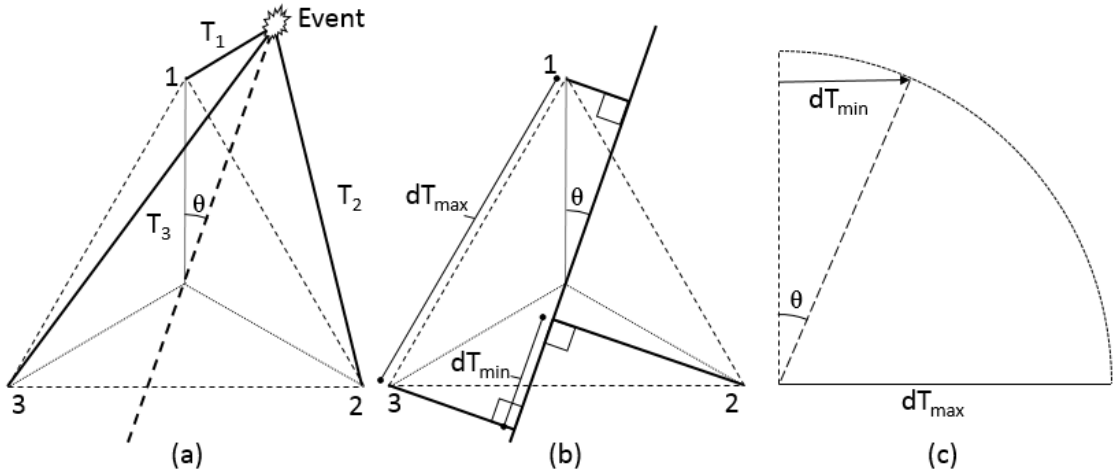

Figure 67 – $dT_{min/max}$ method of angle prediction (based on (Aljets et al., 2011)). Where the time for each wave to reach each sensor (a) and difference in arrival at each sensor (b) are represented as vectors. The wave in which the angle can be predicted using the $dT_{min/max}$ method is also shown (c)

Equation 14 gives the angle of arrival at a point half way between the two sensors with the smallest dT, which could be in either direction from the pair. This, combined with data from the third sensor and knowledge of the first hit sensor, allows the angle of arrival to be predicted.

$$\theta = \sin^{-1}\left(\frac{dT_{min}}{dT_{max}}\right) \qquad (14)$$

This technique was shown by Aljets et al. to be relatively effective at predicting the angle of arrival of AE, however it is reliant on a constant predetermined value of dT_{max}. Wave velocity is dependent on not only thickness and material type, but also frequency (Lamb, 1917). Therefore whilst this value can be changed for each setup to account for the structure, any change in frequency will cause error, and this cannot be accounted for. Different mechanisms of damage are known to generate different frequency Lamb waves (Lu et al., 2011), meaning different damage types will propagate at slightly different velocities. This may cause some effect in the accuracy of the angle calculation, a method of prediction that doesn't rely on a constant wave velocity would be beneficial.

4.1.3 Change to angle

An alternative new method has been applied and is presented within this thesis that does not rely on wave velocity or sensor spacing. Instead it uses the ratio between the difference in arrival times at the first and second hit sensors (dT_{12}) compared to the second and third (dT_{23}). Note that this is the order in which the sensors are hit, not the sensor number. This work is a simplification of a method applied Kadri et al. (Kadri et al., 2017) where three sensors in any shaped triangle, not just an equilateral one as is the case with this work, were able to locate the angle of arrival of underwater waves.

The relationship between the ratio and the angle of arrival can be found by deriving the vectors in Figure 68 using trigonometry and is shown in Equations 15-18.

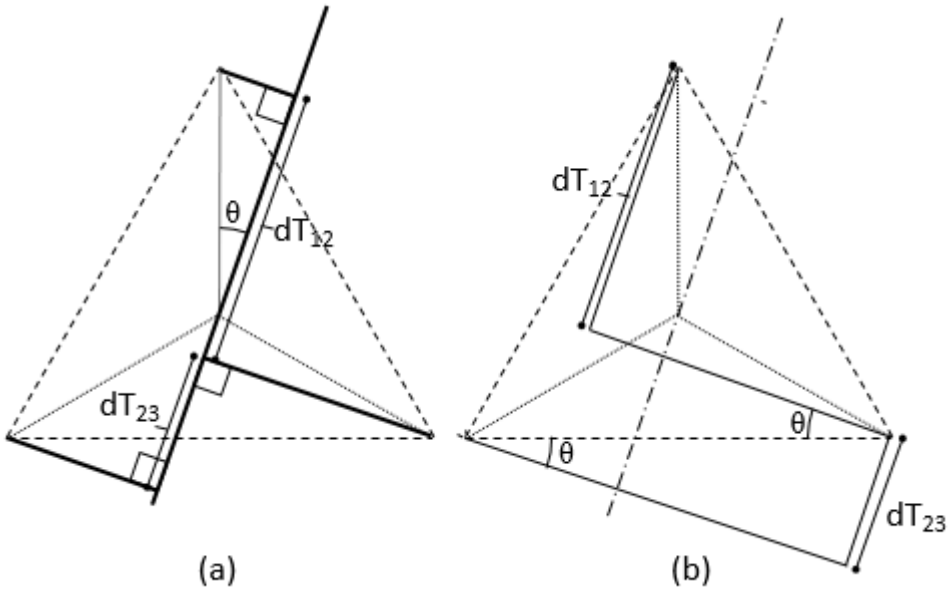

Figure 68 – dT_{12}/dT_{23} shown in terms of vectors

$$\frac{dT_{12}}{dT_{23}} = \frac{\sin(60-\theta)}{\sin\theta} \tag{15}$$

$$\frac{dT_{12}}{dT_{23}} = \frac{\sin 60\cos\theta - \cos 60\sin\theta}{\sin\theta} \tag{16}$$

$$\frac{d_{T12}}{dT_{23}} = \sin 60 \cot \theta - \cos 60 \quad (17)$$

$$\theta = \cot^{-1}\left\{\frac{1}{\sin 60}\left(\frac{dT_{12}}{dT_{23}} + \cos 60\right)\right\} \quad (18)$$

The predicted angle between 0^o-60^o combined with the knowledge gained from the first and second hit sensor allow the zone to be selected, as shown in Figure 69. Suitable logic within the code allows the angle to be found by taking the first hit sensors angle (i.e. 0^o, 120^o or 240^o) ± the predicted angle dependent on the second hit sensor.

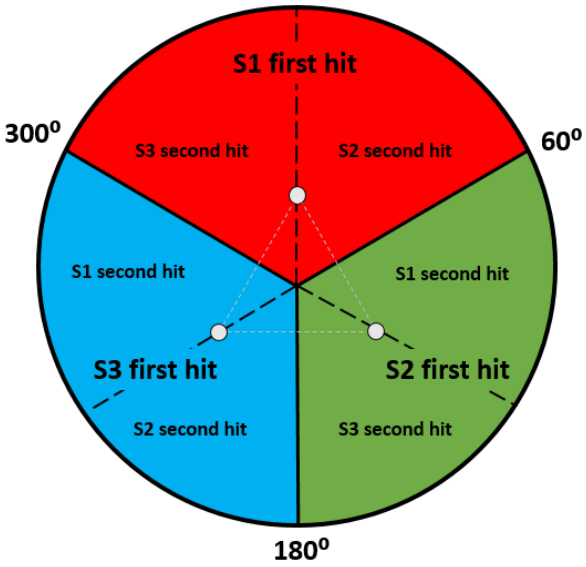

Figure 69 – Diagram showing how areas are defined based on the first and second hit sensors

4.1.4 Test procedure

In order to test the location accuracy of the different approaches, testing was conducted on a variety of structures. Information about the structures tested upon can be found in Section 3.2. To test the structures firstly the area of interest was selected, once this was done points were drawn on the structure to identify test locations. In early testing points were marked at varying angles and distances from the location where the sensors were to be bonded i.e. using polar coordinates. This was very efficient at testing the technique's effectiveness at locating varying angles however led to a high number of test points close to the sensors rather than evenly over the structure. This can clearly be seen in Figure 70 where a polar co-ordinate grid is compared

to a Cartesian one. In order to properly assess the ability of a node to accurately detect AE over different structures the testing presented within this thesis therefore was conducted with a regular Cartesian grid.

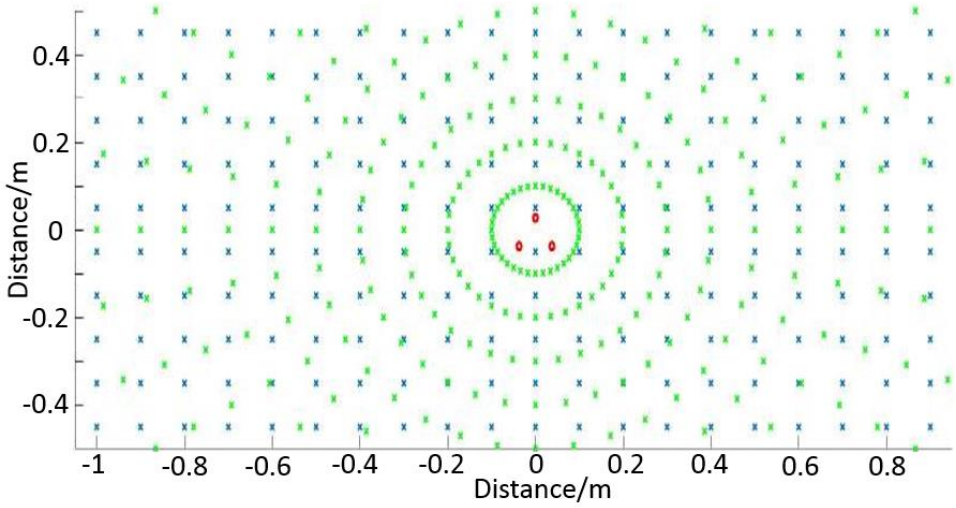

Figure 70 - Cartesian (blue) versus polar (green) co-ordinate grids with sensors shown as red circles

Once test points had been identified the sensors were bonded in a triangle, typically 75 mm apart, using Loctite 595 silicone gel which creates a semi-permanent bond to the structure. A distance of 75mm was used as preliminary testing indicated that this was an effective distance. Bonding the sensors closer than this increased the likelihood that an identical wave was seen by all sensors as attenuation which occurs between the sensors sometimes caused enough of a drop in amplitude for a channel to have a late arrival time. However, it also causes the time of arrival difference between the sensors to be significantly decreased, meaning any late arrivals would lead to a high inaccuracy in the angle prediction.

A 3D printed spacer, shown in Figure 71, was used to ensure sensor separation was accurate. A 1.5 kg weight was then placed on top of this for a 24-hour period to ensure the silicone had cured fully, this weight was removed prior to any testing. When possible the sensors were left in place as modifications were made to the specimens.

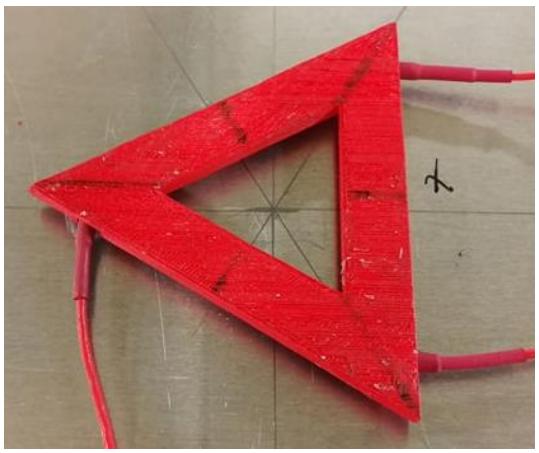

Figure 71 – 3D printed spacer used to ensure regular sensor bonding

Once the sensors were bonded, H-N sources were conducted at each location over the grid, Figure 72 shows a typical grid with notation. Data was collected using a Mistras Express 8 AE monitoring system and a line of data collected at a line in each file. Time markers were made using the system between each point on the line. Typically five H-N sources were made in each location, however in some cases what are often referred to as 'Bad breaks' were made, where a pencil lead didn't break properly, so not producing the required source. In these situations an extra event was conducted to ensure adequate data was collected. This test procedure was used throughout this thesis, any changes from this are noted in the relevant section.

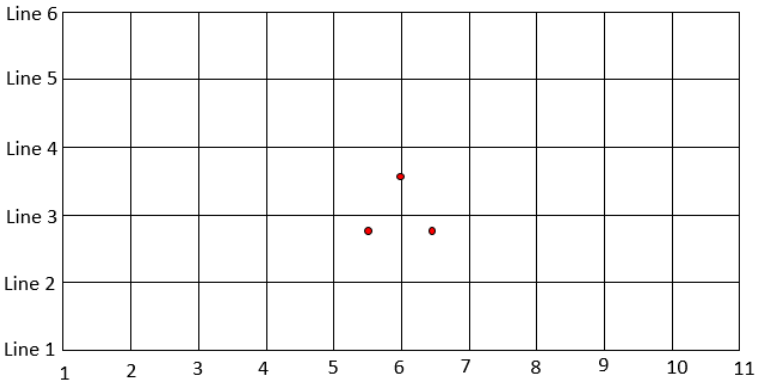

Figure 72 – Typical grid for Delta-T map

4.1.5 Testing

In order to test the accuracy of the $dT_{min/max}$ method compared to the ratios method, tests were performed on the simple aluminium plate (Section 3.2.3) and on composite panel A (Section 3.2.1).

The first structure tested on was the simple aluminium panel, for this test three Nano-30 sensors were bonded in an equilateral triangle 75mm apart in the centre of the panel. A grid was drawn over the 1250mm x 1250mm panel at 100mm intervals, the outside test locations were 25mm from the edge of the panel. Five H-N sources were then created at each of these locations. The data was collected and processed in Matlab.

The S_0 mode arrival was predicted using the threshold crossing method with a 45dB (0.01778V) threshold. In order to find the A_0 arrival a bandpass filter with limits 20 kHz above and below the peak A_0 frequency predicted using an FFT in Chapter 3. A 250^{th} order bandpass filter was applied to the waveform, which removed the majority of the S_0 mode. A 250^{th} order filter was used as it was found to be adequate the range of structures used. It could be seen that a fixed threshold of 45dB led to significant early triggering because of the remaining S_0 mode, to solve this a 55 dB (0.05623 V) threshold was used in order to detect the mode's arrival. The results from the $dT_{min/max}$ method can be seen in Figure 73 (a) and the ratio method in Figure 73 (b).

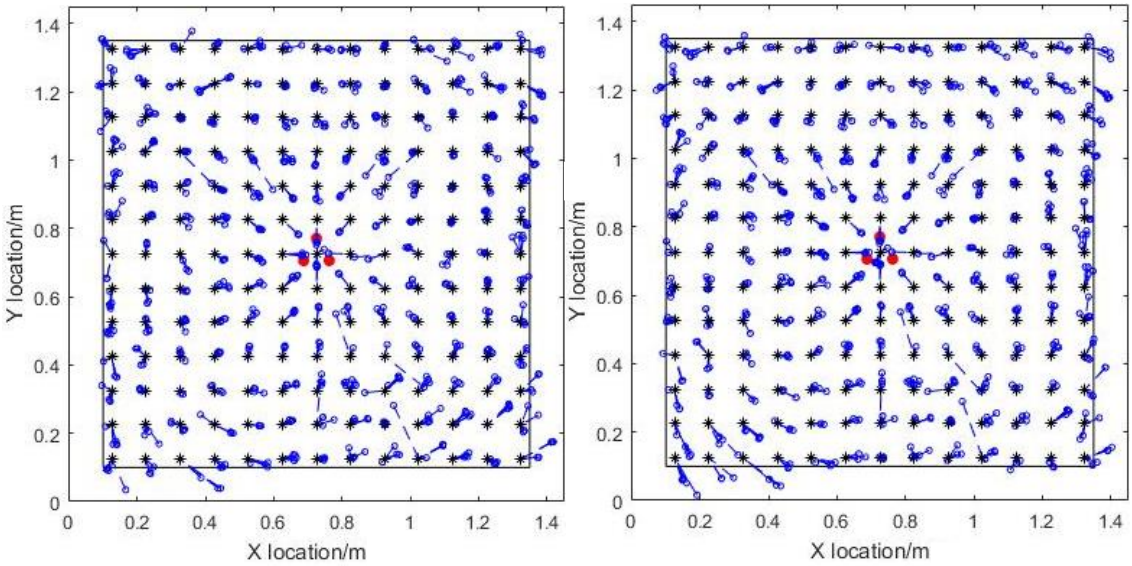

Figure 73 – Predicted locations on the simple aluminium panel using the $dT_{min/max}$ method to predict angle (a) and using the ratios method (b). Sensors shown in red, H-N source locations shown in black and calculated events in blue. The edge of the panel is shown by black lines. Data with errors above 200mm excluded.

The average error in angle prediction, overall location error and the percentage of data with less than 50mm, 100mm and 200mm error for the two methods are shown in Table 2.

Table 2 – Errors when locating H-N sources in the simple Aluminium panel using the $dT_{min/max}$ and ratios methods

	$dT_{min/max}$	Ratios
Average Angle error (°)	3	3
Average Overall error (mm)	40	41
Data less than 50mm error (%)	83	81
Data less than 100mm error (%)	97	97
Data less than 200mm error (%)	99	99

The data was also processed using the ratios method with variable thresholds dependent on the maximum amplitude of the filtered signal, with the threshold set at a range of percentages from 1% up to 100% of the maximum A_0 amplitude. The most accurate percentage was 6%, giving 83% of the data within a 50mm accuracy, 98% within 100mm and 99% within 200mm. At this

percentage the average angle error was 3.2° with an average location error of 39mm. The results varied significantly depending on the threshold percentage used, the change in the amount of data within a given accuracy against the change in threshold is shown in Figure 74.

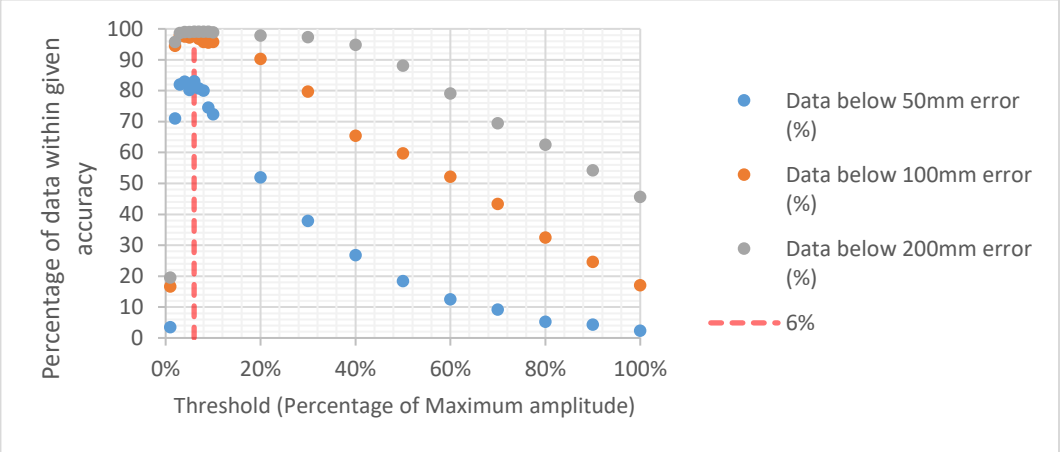

Figure 74 - Percentage of data within different levels of accuracy with varying threshold levels in the simple aluminium pane. Optimum threshold of 6% indicated by dashed line.

Testing was then conducted on composite panel A. The sensors were not bonded in the centre of the panel but instead at x = 0.29m and y = 0.29. This was because the results from the preliminary tests showed that the technique was able to detect events further away than would be possible if the sensors were bonded in the centre. Preliminary testing also showed that a 45dB threshold was adequate to detect the A_0 arrival on the filtered signal, this was therefore used instead of the higher one that was used for the aluminium panel. The rest of the processing procedure was identical to the simple aluminium panel test. The actual test points and the predicted locations from the $dT_{min/max}$ method can be seen in Figure 75 (a) and the ratio method in Figure 75 (b).

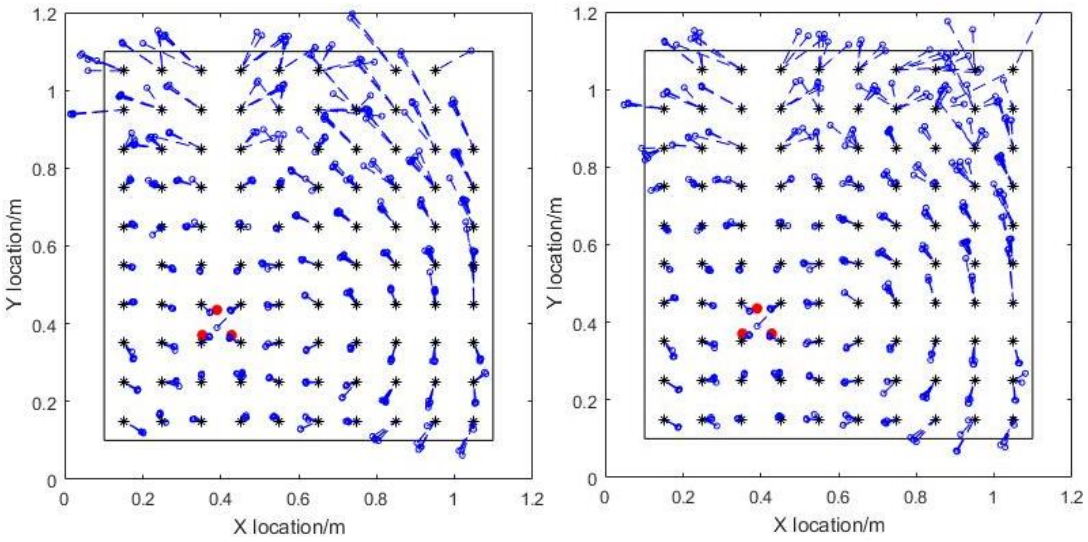

Figure 75 – Predicted locations on Composite Panel A using the $dT_{min/max}$ method to predict angle (a) and using the ratio's method (b). Sensors shown in red, H-N source locations shown in black and calculated events in blue. The edge of the panel in shown by black lines. Data with error above 200mm excluded.

The average error in angle prediction, overall location error and the percentage of data with less than 50mm, 100mm and 200mm error for the two methods are shown in Table 3.

Table 3 – Errors when locating H-N sources in composite panel A using the $dT_{min/max}$ and ratios methods

	$dT_{min/max}$	Ratios
Average Angle error (^{o})	6	5.7
Average Overall error (mm)	69	68
Data less than 50mm error (%)	60	57
Data less than 100mm error (%)	85	89
Data less than 200mm error (%)	96	96

As with the previous specimen the data was also processed using the ratios method with variable thresholds dependent on the maximum amplitude of the filtered signal. The most accurate threshold percentage was 10%, giving 74% of the data within 50mm accuracy, 93% within 100mm and 97% within 200mm. In this case the average angle error was 2.9^o and the average

location error was 49mm. The results varied significantly depending on the percentage used, the change in the amount of data within a given accuracy against the change in threshold is shown in Figure 76.

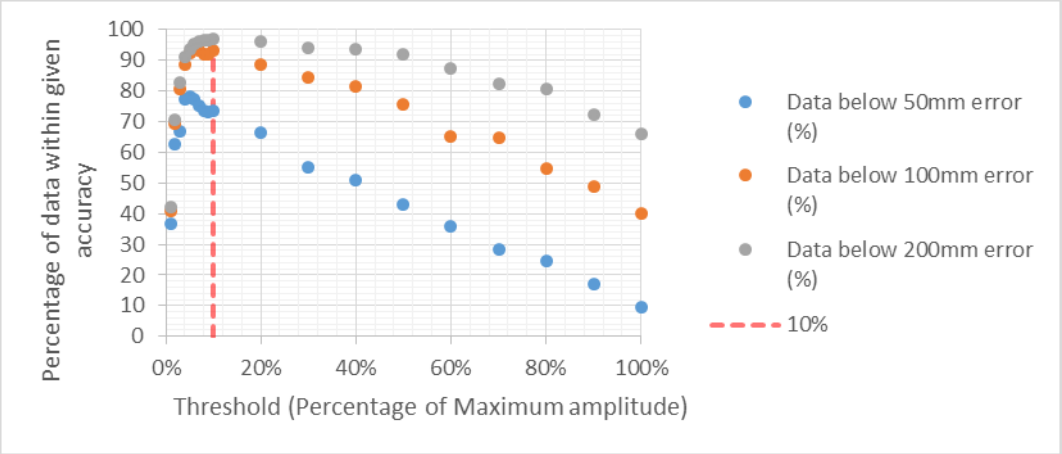

Figure 76 – Percentage of data within levels of accuracy with varying threshold levels in Composite Panel A. Optimum threshold of 10% indicated by dashed line.

4.1.6 Analysis of Errors

For a number of locations in both tests an error of between 50mm and 200mm is present, most of this inaccuracy is as a result of the angle prediction. This error is due to late A_0 detection at one or more of the sensors causing the difference in arrival at the sensors to be incorrect, altering the predicted angle. This is demonstrated in Figure 77 where the A_0 arrivals at the three sensors from a H-N source in the top right of the composite panel, as far away as was tested, are shown. In this example sensors one and three trigger after approximately one wavelength from the start of the wave whereas sensor two triggers after two wavelengths. This one wavelength difference equates to approximately 10µs delay in the triggering of the second sensor. In this example the angle was predicated as 34° by the ratios method and 30° by the $dT_{min/max}$ method when it was actually 45°. Overall, using the ratio method only 69% of data was within 5° accuracy in the composite panel and only 89% was within the same limit for the aluminium panel. Late prediction of the S_0 and A_0 modes also affects the accuracy of the distance approximation, however not to the same degree as the angle prediction.

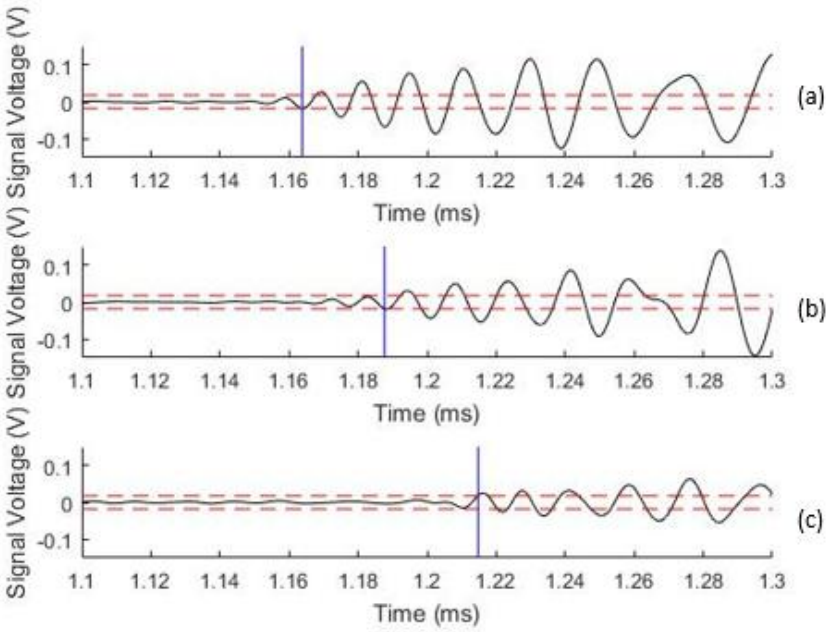

Figure 77 –H-N event A_0 waveform (black) with arrival time (blue) and threshold level (red) for sensor 1 (a), sensor 2 (b) and sensor 3 (c) at location x = 0.95, y = 0.95 on Composite Plate A.

In a number of locations an error greater than 200mm was present, some of which were caused as a result of the distance approximation being significantly wrong. The reason for a number of these was that the S_0 mode was not detected by the threshold crossing technique due to attenuation of the signal, as shown in Figure 78, this meant that the distance calculation was ineffective.

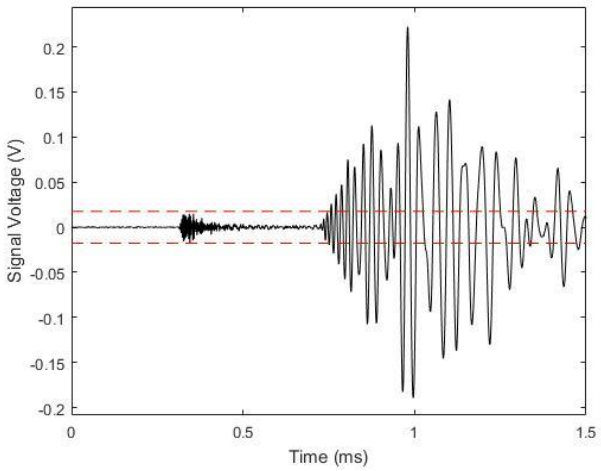

Figure 78 – H-N event at x=0.95 and y=0.95 where S_0 attenuation has caused it to be lower than the threshold (red dashed lines)

4.1.7 Discussion

Within this section a method of locating AE sources using a closely spaced array of three PZT sensors was tested. This was initially presented by Aljets (Aljets et al., 2011, Aljets et al., 2012, Aljets, 2011) who used wavelet transforms to predict the distance the waveforms travelled. In order to make the methods as transferable to a wireless system as possible digital filtering has been used in this thesis to remove the S_0 mode and find the A_0 arrival time, and from this SSMA was possible. To predict the angle of arrival two methods have been presented and tested within this section. The first method has been tested extensively by Aljets to locate artificial and real damage in simple plate like structures, which has been replicated for artificial sources to a similar level of accuracy within this section. An alternative method has also been presented and tested that was able to achieve a similar level of accuracy to the technique used by Aljets. This method's ability to calculate the angle of arrival without a known velocity makes it a more reliable method as it is effective for sources with varying velocities.

Some error was present within the methods, both due to the ability of SSMA to predict the distance the wave had travelled and the angle prediction accuracy. This was primarily due to late detection of the A_0 mode, improving the accuracy of the detection of this mode would significantly improve the accuracy of the system. It is worth mentioning that a 10^o error in accuracy isn't necessarily a problem for applications where a high level of accuracy isn't required, in some cases a general idea of the location of damage is satisfactory.

The use of a variable threshold to detect the arrival of the A_0 mode was also investigated. Unlike a fixed threshold this, in theory, allows the start of heavily attenuated signals to be detected without having to set a very low threshold which would trigger early on a signal closer to the sensor. For detecting H-N sources on Composite Panel A this approach significantly improved the accuracy of location prediction, decreasing the average error from 68mm to 49mm when the correct threshold was selected. No significant improvement was seen in the test on the simple aluminium panel, the most effective percentage threshold only decreased the average

error by 1mm compared with the fixed threshold result. Although this approach indicates that it may be more effective than a fixed threshold, incorrect selection of the percentage used could lead to early triggering which would cause significant error in the predicted location. Using a fixed threshold is not without problems, a higher threshold was needed within the aluminium panel than the composite panel, as the frequency filtering was not fully removing some low frequency components of the S_0 signal. If optimised this approach could lead to improved location prediction, however as is the case with a variable threshold, this is not ideal as if chosen incorrectly in a real test application, the location of events would be very inaccurate. A perfect solution would be one where no threshold is required to detect the A_0 mode, allowing any low frequency part of the S_0 mode to go undetected. This in reality is not possible, however being able to set a higher threshold so as to guarantee that the S_0 mode is not detected would be effective if further processing to detect the exact arrival of the wave was available.

4.2 Complexity Problem

The methods presented in the previous section have been shown (Aljets et al., 2011, Aljets, 2011, Aljets et al., 2012) to locate artificial and real AE sources in simple aluminium and composite plate-like structures. Real structures however are rarely so simple. Aircrafts for example contain lots of complexity including holes, stiffeners and thickness changes. These significantly affect the propagation of Lamb waves discussed in (Section 2.1.3) causing reflections, mode conversion and attenuation of the signal. The mode conversion is a particular issue, as S_0 converting to A_0 when passing stiffeners causes an early trigger when using a threshold method. This problem means that the three sensor methods presented in the previous section are ineffective in complex structures as an accurate A_0 arrival time is difficult to predict automatically. This is shown in Figure 79 (a) where a H-N source 300 mm away from a Nano-30 sensor on composite panel B with no stiffeners is shown alongside a filtered signal. Here the filtering successfully removes the S_0 mode, which allows a threshold method to be used successfully. Figure 79 (b) shows the same location on the panel after the stiffeners have been

bonded on, in this case the S_0 mode arrival contains a lower frequency component, making a threshold based A_0 mode arrival prediction difficult. Though it is possible to use a higher threshold, doing so becomes less accurate as the start of the wave is less likely to be detected. In addition to this the signal is significantly attenuated, with the peak amplitude in the complex panel being around 20% of that in the simple panel. This lower amplitude means that a threshold based detection of the S_0 and A_0 mode may miss the wave completely which will make localisation impossible.

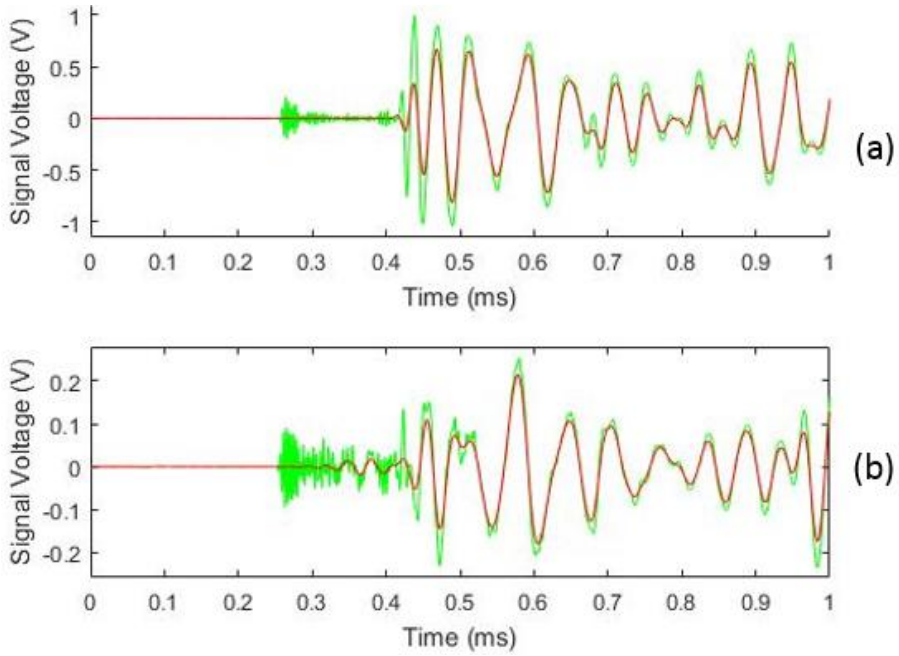

Figure 79 – H-N source in composite panel B unfiltered (green) and filters (red) on a panel with no stiffeners (a) and with four stiffeners (b). Note that the 'Y' axis is different in each plot.

4.3 Modified Three Sensor Location

This section outlines a number of modifications that have been made in order to improve the ability of the technique to predict the location of AE events in complex structures. Some of these changes are suitable for a low power wireless system, others less so.

4.3.1 Akaike Information Criterion for S_0 detection

In the testing presented within Section 4.1 it was impossible to locate certain events due to the S_0 mode being too attenuated to be detected using a threshold method. This is not only a problem that is present within 0/90 layup composites, but also in complex structures where signals are heavily attenuated when interacting with complexity. Detailed in Section 2.2.4 the Akaike Information Criterion (AIC) is able to accurately and repeatedly predict the arrival of Lamb waves even when heavily attenuated. Although not feasible in a low power wireless system as it is a processing intensive technique which would take a lot of power, this method has been investigated as it has been shown to significantly improve the accuracy and reliability of traditional localisation algorithms (Pearson et al., 2017, Holford et al., 2017). By applying the AIC technique to the three closely spaced sensors method a more reliable arrival time was found, potentially improving the accuracy of the distance prediction but more importantly ensuring the detection of the S_0 mode when heavily attenuated. The AIC technique is not able to detect the arrival of the A_0 mode as the filters used create regularity in the noise and filtered S_0 mode which triggers the AIC algorithm. The application of the AIC technique to the data changes the locations slightly however it has very little effect on this data set. As the AIC technique is most effective on heavily attenuated signals when applied to complex structures it can be assumed that accuracy will be significantly better using AIC than a threshold based method.

4.3.2 Using S_0 Mode for Angle Prediction

In the results presented in Section 4.1 a small error in angle prediction was often present, in total for the aluminium panel 75% of the data was predicted within 5^o accuracy and 95% within 10^o. This is due to the late triggering of the A_0 mode affecting the ability of the techniques to accurately predict the results, and although not a serious problem the addition of complexity to the structure will further reduce the accuracy of the technique. A solution to this problem is to use the S_0 mode arrival to calculate the angle, which when predicted by the AIC technique has a significantly more accurately predicted arrival time. The AIC technique will also accurately

predict S_0 arrival in complex structures, as mode conversion is not a problem for S_0 arrival prediction. A drawback of using the S_0 mode to predict the angle of arrival is that the technique is not feasible in composite structures with 0/90 layups due to the elliptical propagation of the S_0 mode (Paget et al., 2003). This is shown by reprocessing the composite panel A data using this approach, shown in Figure 80, where all angles are predicted as either 45°, 135°, 225° or 315° depending on the quarter of the panel the event occurred within.

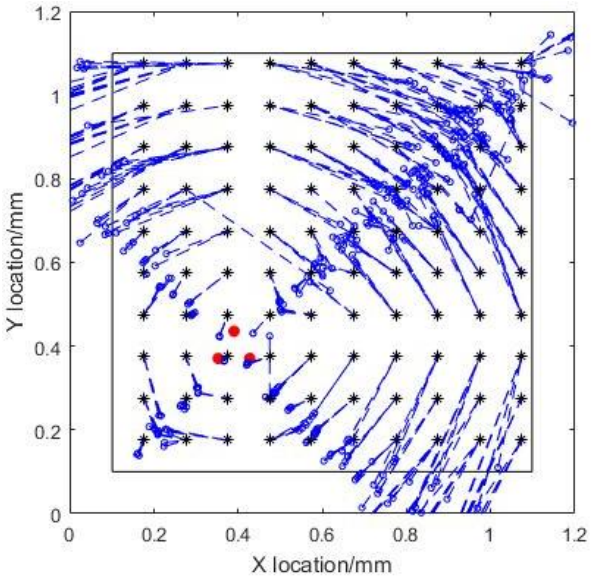

Figure 80 - Predicted locations on Composite Panel A using the ratios method to calculate angle using the S_0 mode arrival.

The data from the aluminium panel was reprocessed using the S_0 mode to predict the angle of arrival instead of the A_0 mode. Using both the AIC and threshold methods were trailed. The results from this, compared to using the A_0 mode, are shown in Table 4.

Table 4 – Location results on the simple aluminium panel using the S_0 and A_0 modes to calculate the angle of arrival, with the S_0 mode predicted with a threshold technique and the AIC technique

S0 prediction method	Threshold (Fixed)	AIC	Threshold (Fixed)	AIC
A0 prediction method	Threshold (Fixed)	Threshold (Fixed)	Threshold (Fixed)	Threshold (Fixed)
Mode used for angle prediction	A0	A0	S0	S0
Average Angle error (^{o})	3.0	3.0	7.5	3.3
Average Overall error (mm)	41	44	73	44
Data less than 50mm error (%)	81	73	54	76
Data less than 100mm error (%)	97	97	79	97
Data less than 200mm error (%)	99	99	97	99

4.3.3 A_0 mode Arrival Detection Using the Second Differential Method

Although the aforementioned modifications improve the ability of the system to accurately locate AE events whilst removing the need for highly precise A_0 arrival detection, its arrival is still needed. Within simple structures this can be done as before with a threshold crossing method. However due to mode conversion doing so within complex structures makes the likelihood of early triggers high. Although tailoring of the threshold is possible with either a high fixed threshold or a high variable threshold, what works well for one location or type of signal is unlikely to be effective with significant attenuation and so would lead to major errors. It also requires extensive calibration testing for not only every type of structure, but every location. A technique to detect the A_0 mode using no threshold, or at least a single high threshold, would be ideal.

In this section a new method is proposed which was developed to detect the arrival of the initial A_0 mode, even with the presence of stiffeners and thickness changes causing mode conversion. The technique still requires a threshold in order to detect the A_0 mode, however this is set relatively high (40% of the maximum amplitude). The technique analyses the second differential

of the wave before this crossing point for a more precise A_0 arrival prediction. Combined with the S_0 arrival this allows for SSMA within complex structures.

The technique was developed by applying an intelligent empirical approach. H-N source data from a range of complex structures was viewed, the A_0 arrival in each of these waves was then approximated by human eye. A clear pattern was noticed: an obvious change in gradient with the arrival of the A_0 mode when compared to the A_0 to S_0 mode conversion before it. The second differential technique was developed to identify this point within a waveform both with and without the presence of S_0 to A_0 mode conversion. The thresholds and filters used within the technique was selected based of the results obtained from a number of data sets and once chosen where kept constant throughout analysis of data.

A brief step by step summary of the method is given below which combined with Figure 81 concisely describes each stage of the technique. Each step is described in greater detail after the concise description.

1. Find the S_0 arrival time (T_{s0} in Figure 81 (a))
2. Perform a bandpass filter on the waveform (Figure 81 (b))
3. Convert to absolute values (Figure 81 (c))
4. Find the maximum of each peak (Green markers Figure 81 (c))
5. Profile the waveform using the 'Fit – smoothingspline' function on the peaks (Red dashed line, Figure 81 (c))
6. Identify the peaks within the calculated wave profile (Green markers Figure 81 (d))
7. Find the peak with the maximum value
8. Find T_p the first of these peaks greater than 40% of the max peak
9. Perform a second order differential on the profile (plotted in blue in Figure 81 (d))
10. The location of the maximum differential between T_{S0} and T_p is the location of the A_0 arrival (S_{A0})

11. If the amplitude of the wave profile is greater than 40% of the value of T_p find the next highest peak (repeat until below 40%)

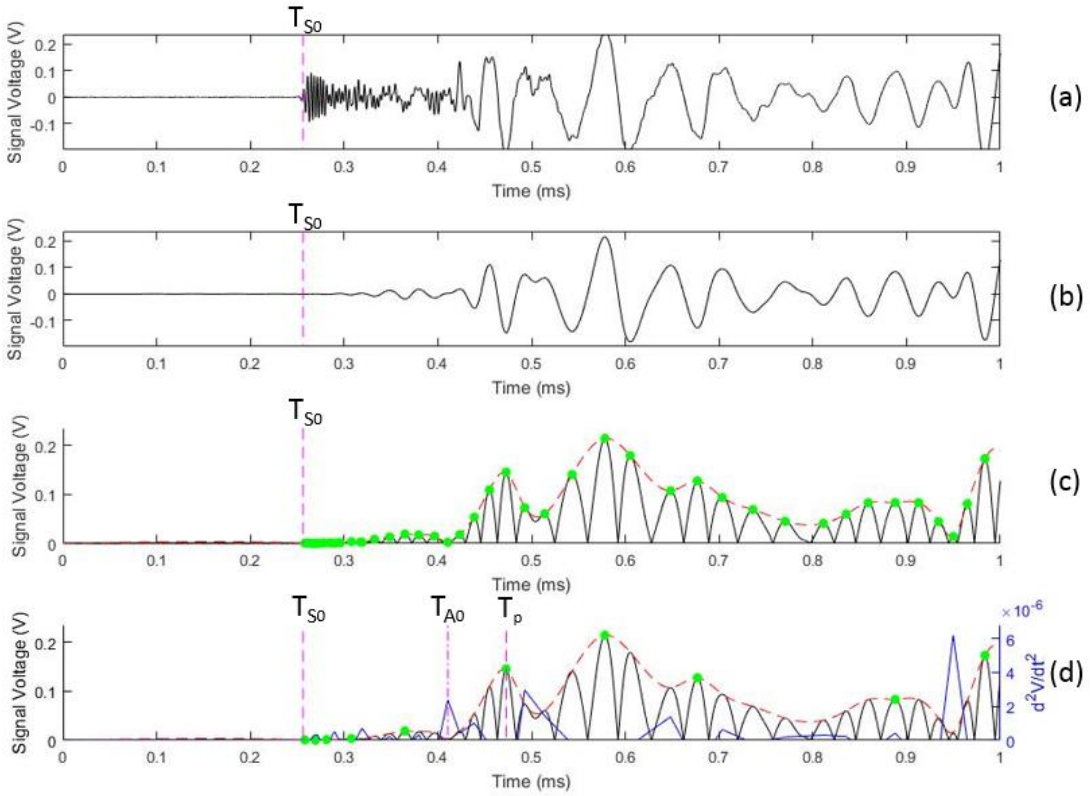

Figure 81 – Waveform of complex composite panel (a), filtered waveform (b), absolute values of filtered waveform with profile (c) and the addition of the positive elements of the second differential (d)

The first stage of the process is to identify the arrival of the S_0 mode (T_{s0}), this is because any noise occurring prior to this has the potential to give a high second differential value and by ignoring this it reduces the likelihood of an early trigger. The bandpass filter used in step two is the same as used in previous filtering in this chapter, a digital filter within Matlab using the 'designfilt' function to produce a bandpass filter 20 kHz either side of the dominant frequency of the A_0 mode. Step three utilises the 'abs()' function within Matlab, which is equivalent to $\sqrt{y^2}$. Step four finds any peaks, i.e. any point where the values before and after it are both lower than itself. Step five utilises the 'fit' function which produces a curve from the peak data points. A smoothing spline is applied to interpolate between the points and produce a smooth curve. The

sixth step identifies the peaks from the array of peaks, i.e. ones that are greater than those before and after them. The seventh step is simply finding the maximum peak. Step eight finds the first of the array of peaks calculated in step six that is greater than a 40% of the max peak, this is the variable threshold approach presented previously, set very high so as not to trigger any S_0-A_0 mode conversion, this is identified in Figure 81 (d) as T_p. The ninth step requires a second order differential to be performed on the curve produced in step five, this identifies the location of high changes in the rate of change. The final step is identifying which of these peaks correlates with the arrival of the original A_0 mode ignoring any part of the wave caused by mode conversion, noise or later parts of the A_0 mode. The preliminary value is then chosen; this is the greatest peak occurring between T_{s0} and T_p, identified as T_{A0}. The final step is to ensure that the chosen value is not near the peak T_p as sometimes the approach to the peak gives a high second differential, this is avoided by checking if the curvefit value at this location is greater than 40% of the amplitude at T_p.

The technique was tested on the filtered waveform of a H-N source at a point 300mm away from a sensor on composite panel B collected both before and after the addition of stiffeners to the panel. It would be expected that the difference in S_0 and A_0 arrival would be similar in each case, with a small difference due to the change in wave velocity when crossing complexity such as a stiffener (Lammering et al., 2018). Figure 82 (b) shows the filtered waveform from the complex panel, the second differential technique predicted arrival time is marked in green. The same arrival time is also marked in Figure 82 (a) which shows the waveform of the simple panel synchronised with Figure 82 b's S_0 arrival time predicted by AIC. The predicted arrival time using a threshold of 45dB is shown as a black dashed line, which only differs by 1µs.

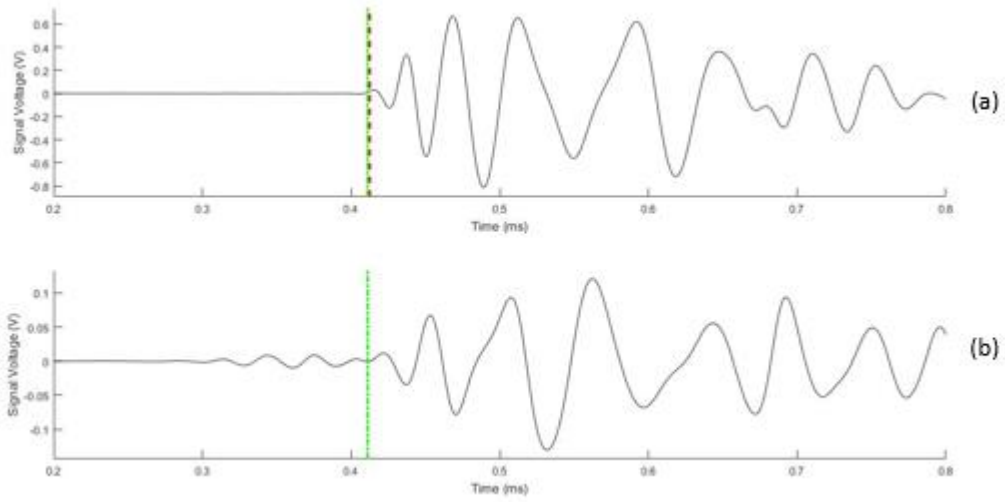

Figure 82 – A_0 mode from a H-N source on composite panel B without complexity (a) with markers indicating the arrival time through a threshold crossing technique (black dashed line) and the arrival calculated by the second differential technique (green line). Also shown is the A_0 waveform from a H-N source in the identical location on the panel with complexity, shown with the second differential technique predicted arrival time (green line).

To ensure the repeatability of the technique in a simple structure the data from the simple aluminium panel test was reprocessed using the second differential method alongside AIC. Although not the original reason this method was developed, as a threshold technique has shown to be very effective at predicting A_0 arrival times in simple structures, it was hoped that the second differential method would have a near similar level of accuracy. The results obtained by processing the data using the second differential methods for A_0 arrival time prediction as well as changing the mode used for the angle prediction are shown in Table 5.

Table 5 – Errors from processing the aluminium panel data using different arrival time prediction methods and the mode utilised for angle prediction

S0 prediction method	AIC	AIC	AIC	AIC
A0 prediction method	Threshold (Fixed)	Second Differential	Threshold (Fixed)	Second Differential
Mode used for angle prediction	A0	A0	S0	S0
Average Angle error (^{o})	3.0	6.9	3.3	3.3
Average Overall error (mm)	44	69	44	42
Data less than 50mm error (%)	73	66	76	74
Data less than 100mm error (%)	97	86	97	92
Data less than 200mm error (%)	99	93	99	98

4.3.4 Discussion

Three major changes to the technique of locating AE events using three sensors in a triangular array have been proposed in this section. The intention of these is not only to improve the ability of the system to locate AE sources in simple plates, but to allow the technique to be effective in complex structures. The use of the AIC technique is shown to be effective at removing the possibility of not detecting the S_0 mode, so increasing reliability if the A_0 mode is used to predict the angle of arrival. Applying the technique to the aluminium panel did not significantly change the accuracy of the results, however it can be expected that in complex structures with greater S_0 attenuation or when detecting lower amplitude sources, it will be significantly more effective than a threshold method.

The switch to using the S_0 mode arrival time to calculate the angle of arrival was completely ineffective at locating sources within the 0/90 layup composite panel A. This was because the wave front can no longer be assumed to be straight, as is required by the angle of arrival prediction methods (Section 4.1.2). It also showed a substantial drop in angle prediction accuracy in the aluminium plate if a threshold crossing method was used to predict the S_0 mode arrival. Combining the angle prediction using the S_0 mode with the AIC technique to predict its

arrival shows a significant improvement in accuracy compared to the threshold method and gives it an accuracy slightly worse than using the A_0 mode to predict the angle of arrival. This change is likely to be more effective on complex panels, where mode conversions will make a precise enough A_0 mode arrival prediction impossible. Although this method is ineffective in composites with a 0/90 layup, by using the S_0 mode to predict the angle of arrival, the detection of the A_0 mode is less vital as any error will only influence the distance prediction, rather than both. It is however still required in order to predict the distance the wave has travelled, and so the location of the event. It was shown in Section 4.1 that in a simple structure the most accurate way to do this is with a variable threshold crossing method performed on a filtered waveform. This approach however, requires significant calibration to ensure the threshold isn't too low.

An alternative approach which is able to detect the onset of the A_0 mode without the requirement for a low threshold has been proposed (the second differential technique) which has shown good repeatability in a simple structure. The accuracy of the second differential technique to predict the A_0 mode arrival is not high enough for effective angle prediction; within the aluminium plate the average error was over 50% higher than when using the S_0 mode, so if using this approach the S_0 mode must be used to predict the angle of arrival.

The modifications made haven't been shown to improve the performance of the technique, however the modifications which should show improvement in complex structures have been shown not to significantly decrease the accuracy of location. In the following section testing is presented that has been performed on complex structures in order to further assess the performance of the modifications in these cases.

Some of the modifications presented in this section have the potential to be applied to a wireless system. Using the S_0 mode to predict the angle of arrival is easy to apply and the second differential method is feasible with careful programming. The AIC method however is very processor intensive making it unlikely to be suited to wireless application due to power restrictions.

4.4 Testing on complex structures

Until this stage all testing has been performed on simple structures. Real components found in aircraft structures are more complex. This section aims to evaluate the performance of both the normal and the modified techniques presented in Sections 4.1 and 4.3 for more complex structures. Within this section a number of structures have been evaluated, initially those manufactured for the testing within this thesis and then moving on to a real aircraft structure. Information on these structures can be found in Section 3.2 of this thesis.

4.4.1 Aluminium Panel

The first complex structure tested was the aluminium panel, both before and after the stiffeners were bonded/riveted to its surface, as described in Sections 3.2.3 and 3.2.4. Performing testing before and after the complexity was added allows for a direct comparison to be made on how the complexity affects the results. The sensors were not detached from the plate during the modification process and a H-N source near the sensor ensured they were still well bonded once the manufacturing was complete.

The errors obtained when processing the results from the simple panel are shown in Table 6 and the results from processing the data from the complex panel are shown in Table 7. For the simple panel a 4% variable threshold was found to be the most effective in accurately predicting the location of the H-N sources whereas the complex structure needed a higher threshold of 10%.

Table 6 – Errors on simple aluminium panel when processed with a number of techniques

S0 prediction method	Threshold (Fixed)	AIC	AIC	AIC	Threshold (Fixed)	AIC	AIC	AIC
A0 prediction method	Threshold (Fixed)	Threshold (Fixed)	Threshold (4%)	Second Differential	Threshold (Fixed)	Threshold (Fixed)	Threshold (4%)	Second Differential
Mode used for angle prediction	A0	A0	A0	A0	S0	S0	S0	S0
Average Angle error (^{o})	3.0	3.0	3.5	6.9	7.5	3.3	3.3	3.3
Average Overall error (mm)	41	44	39	69	73	44	37	42
Data less than 50mm error (%)	81	73	80	66	54	76	88	74
Data less than 100mm error (%)	97	97	98	86	79	97	97	92
Data less than 200mm error (%)	99	99	99	93	97	99	99	98

Table 7 – Errors on complex aluminium panel when processed with a number of techniques

S0 prediction method	Threshold (Fixed)	AIC	AIC	AIC	Threshold (Fixed)	AIC	AIC	AIC
A0 prediction method	Threshold (Fixed)	Threshold (Fixed)	Threshold (10%)	Second Differential	Threshold (Fixed)	Threshold (Fixed)	Threshold (10%)	Second Differential
Mode used for angle prediction	A0	A0	A0	A0	S0	S0	S0	S0
Average Angle error (^{o})	6.3	6.3	6.3	13.0	29.2	3.1	3.1	3.1
Average Overall error (mm)	80	87	86	160	270	60	60	75
Data less than 50mm error (%)	60	53	48	31	37	57	54	46
Data less than 100mm error (%)	78	75	76	60	61	85	84	80
Data less than 200mm error (%)	91	92	92	79	72	97	99	94

In summary the results show a drop in accuracy between the two setups, most of which can be attributed to the distance prediction error. Using the S_0 mode was more accurate in predicting the angle than using the A_0 mode after the increase in complexity. For the simple panel a threshold crossing technique to detect the S_0 mode showed equally accurate results to the AIC method however for the complex case the AIC method was more accurate for angle prediction. Overall very little difference could be seen between using the threshold and differential methods to detect the A_0 mode, however in both simple and complex panels the threshold method showed slightly higher accuracy.

4.4.2 Composite Panel B

As with the Aluminium Panel, composite panel B was tested before and after four stiffeners were bonded. A 50mm grid was marked up to 50mm from the edge of the panel and a full test performed in its initial state and after each stiffener was attached allowing the change in accuracy with the addition of each stiffener to be determined. As each stiffener was bonded a line of data was lost as the stiffener covered the test location. The bonding procedure is presented in Section 3.2.2 and the stiffeners were bonded in the order shown in Figure 83.

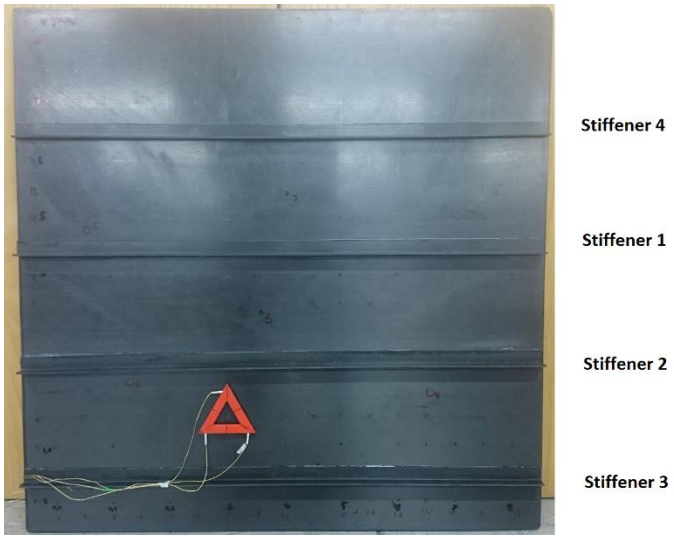

Figure 83 – Composite panel 'B' with four stiffeners bonded

Tables 8-12 show the errors incurred using a variety of methods of angle prediction and mode detection after the bonding of each stiffener. For the variable threshold technique, results for a 20% threshold are shown, this was found to be the most accurate threshold for this dataset.

Table 8- Errors for Composite panel B prior to the addition of any complexity when processed with a number of techniques

S0 prediction method	Threshold (Fixed)	AIC	AIC	AIC	Threshold (Fixed)	AIC	AIC	AIC
A0 prediction method	Threshold (Fixed)	Threshold (Fixed)	Threshold (20%)	Second Differential	Threshold (Fixed)	Threshold (Fixed)	Thr0eshold (20%)	Second Differential
Mode used for angle prediction	A0	A0	A0	A0	S0	S0	S0	S0
Average Angle error (^{o})	4.0	5.1	6.5	4.0	3.7	4.1	4.1	4.1
Average Overall error (mm)	36	49	69	37	36	40	57	39
Data less than 50mm error (%)	85	67	52	80	83	76	58	80
Data less than 100mm error (%)	98	91	80	98	95	94	87	95
Data less than 200mm error (%)	99	98	97	99	99	99	98	99

Table 9 - Errors for Composite panel B after the addition of one stiffener when processed with a number of techniques

S0 prediction method	Threshold (Fixed)	AIC	AIC	AIC	Threshold (Fixed)	AIC	AIC	AIC
A0 prediction method	Threshold (Fixed)	Threshold (Fixed)	Threshold (20%)	Second Differential	Threshold (Fixed)	Threshold (Fixed)	Threshold (20%)	Second Differential
Mode used for angle prediction	A0	A0	A0	A0	S0	S0	S0	S0
Average Angle error (^{o})	6.4	6.4	10.7	11.7	5.3	5.4	5.4	5.4
Average Overall error (mm)	60	62	90	110	53	52	70	54
Data less than 50mm error (%)	73	68	48	62	73	71	51	70
Data less than 100mm error (%)	90	90	65	76	89	91	76	87
Data less than 200mm error (%)	96	96	90	86	97	97	96	96

Table 10 - Errors for Composite panel B after the addition of two stiffeners when processed with a number of techniques

S0 prediction method	Threshold (Fixed)	AIC	AIC	AIC	Threshold (Fixed)	AIC	AIC	AIC
A0 prediction method	Threshold (Fixed)	Threshold (Fixed)	Threshold (20%)	Second Differential	Threshold (Fixed)	Threshold (Fixed)	Threshold (20%)	Second Differential
Mode used for angle prediction	A0	A0	A0	A0	S0	S0	S0	S0
Average Angle error (^{o})	24.5	24.5	13.3	21.9	6.5	5.1	5.1	5.1
Average Overall error (mm)	209	207	116	207	93	74	72	65
Data less than 50mm error (%)	27	28	38	45	40	46	44	58
Data less than 100mm error (%)	42	43	57	58	65	74	72	80
Data less than 200mm error (%)	66	67	83	70	94	97	97	93

Table 11 - Errors for Composite panel B after the addition of three stiffeners when processed with a number of techniques

S0 prediction method	Threshold (Fixed)	AIC	AIC	AIC	Threshold (Fixed)	AIC	AIC	AIC
A0 prediction method	Threshold (Fixed)	Threshold (Fixed)	Threshold (20%)	Second Differential	Threshold (Fixed)	Threshold (Fixed)	Threshold (20%)	Second Differential
Mode used for angle prediction	A0	A0	A0	A0	S0	S0	S0	S0
Average Angle error (^{o})	47.0	47.0	23.3	31.6	9.5	4.8	4.8	4.8
Average Overall error (mm)	345	349	189	273	132	96	77	63
Data less than 50mm error (%)	19	20	34	36	27	34	44	57
Data less than 100mm error (%)	29	30	47	48	50	59	69	81
Data less than 200mm error (%)	50	51	71	58	82	91	96	95

Table 12 – Errors for Composite panel B after the addition of four stiffeners when processed with a number of techniques

S0 prediction method	Threshold (Fixed)	AIC	AIC	AIC	Threshold (Fixed)	AIC	AIC	AIC
A0 prediction method	Threshold (Fixed)	Threshold (Fixed)	Threshold (30%)	Second Differential	Threshold (Fixed)	Threshold (Fixed)	Threshold (30%)	Second Differential
Mode used for angle prediction	A0	A0	A0	A0	S0	S0	S0	S0
Average Angle error (^{o})	55.5	55.5	25.6	40.0	8.7	5.2	5.3	5.3
Average Overall error (mm)	382	383	238	330	149	120	92	67
Data less than 50mm error (%)	16	17	34	37	23	27	45	57
Data less than 100mm error (%)	25	26	49	47	41	47	67	76
Data less than 200mm error (%)	44	46	65	55	75	83	86	94

Angular error when calculated using the S_0 mode does not change significantly with the addition of complexity, always varying between 4^o and 5^o if using AIC to detect the arrival of the S_0 mode. Using a threshold crossing method affects the results more with the average error going from a minimum of 3.1^o to a maximum of 9^o. Using the A_0 mode to calculate angle depreciates accuracy significantly with the addition of stiffeners meaning the average overall location error is very high for these. The average location errors with the addition of each stiffener calculated using the different methods and the S_0 mode to predict the angle are shown in Figure 84. Here it is clear that without complexity all methods have a relatively similar accuracy. Once stiffeners are added however using the second differential method to predict the A_0 arrival time is significantly more accurate than using a fixed threshold and slightly more accurate than the optimised variable threshold.

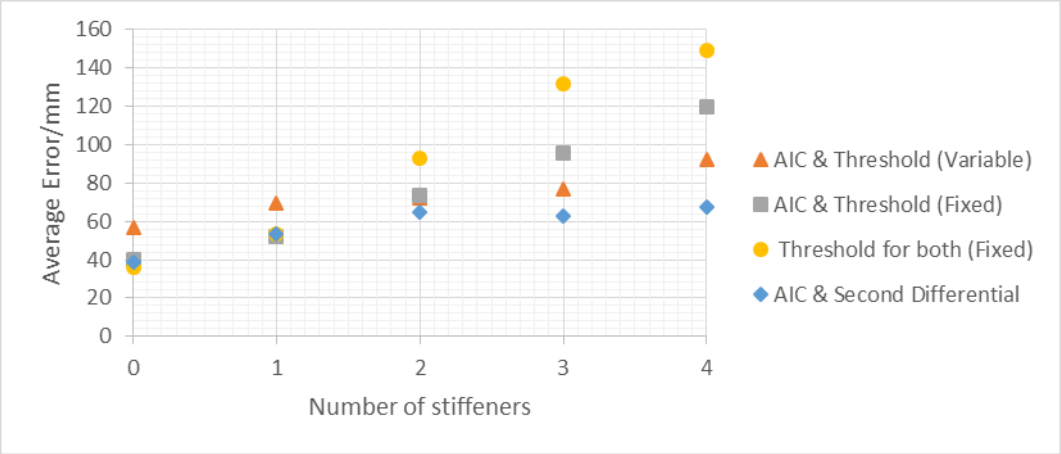

Figure 84 – Average location error for the different methods which use the S_0 mode to calculate the angle of arrival for Composite Panel B with the addition of each stiffener

The actual and predicted locations determined using AIC and the second differential method to predict the mode arrival times both before and after the addition of stiffeners are shown in Figure 85 and Figure 86. The angle has been predicted using the S_0 modes in these plots.

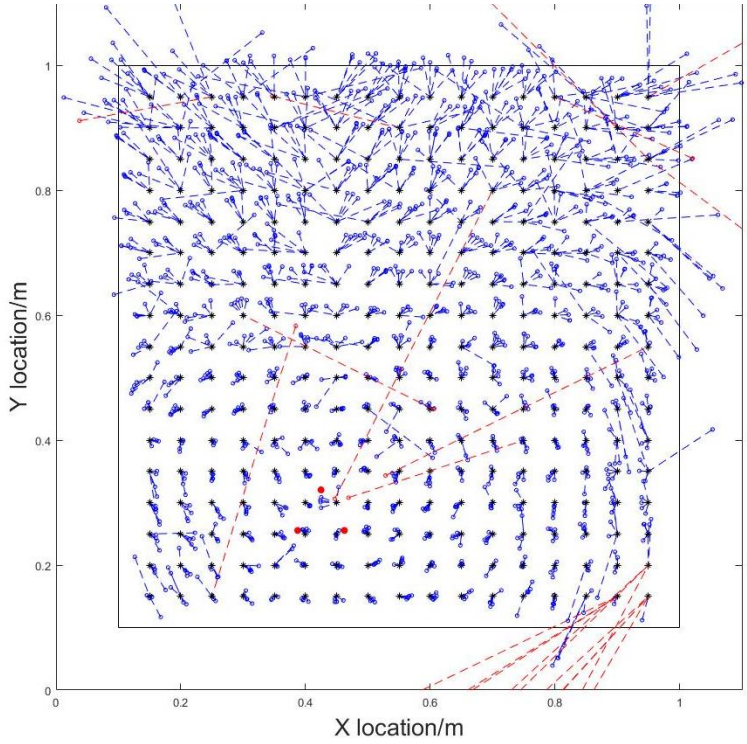

Figure 85 - Predicted locations using the modified three sensor technique for Composite Panel B without complexity. Sensors shown in red, H-N source locations shown in black and predicted events in blue. Data with error above 200mm shown in red. The edge of the panel in shown by black lines.

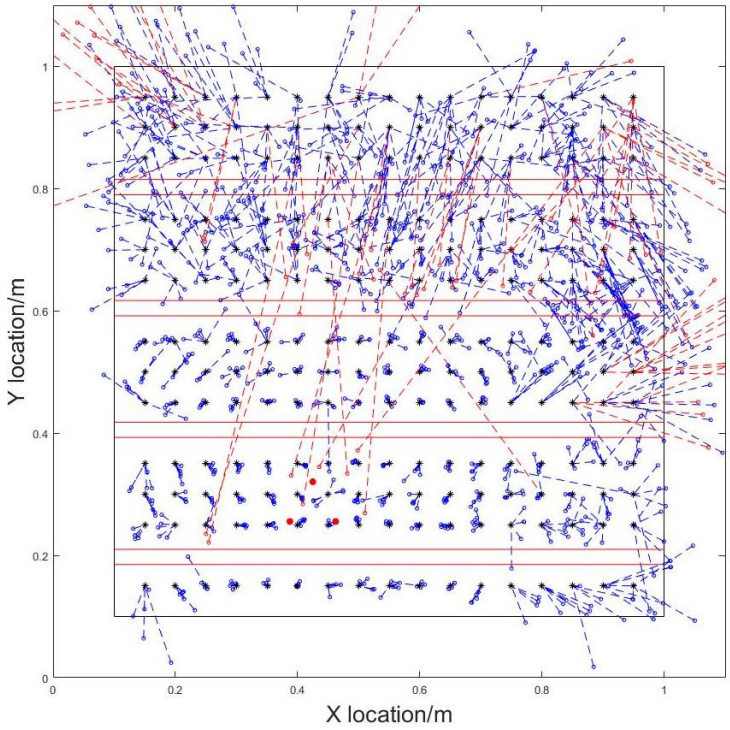

Figure 86 - Predicted locations using the modified three sensor technique for Composite Panel B with complexity. Sensors shown in red, H-N source locations shown in black and predicted events in blue. Data with error above 200mm shown in red. The edge of the panel in shown by black lines and edges of stiffeners in red.

As it is clear that error is particularly present in certain locations, colour plots of the location error in the specimens were created in order to see areas with low accuracy. These are shown in Figure 87 and Figure 88. Within these plots the scale is limited at 0.2 m in order to make contrast visible for lower errors, errors at 0.2 m and above are shown as bright yellow.

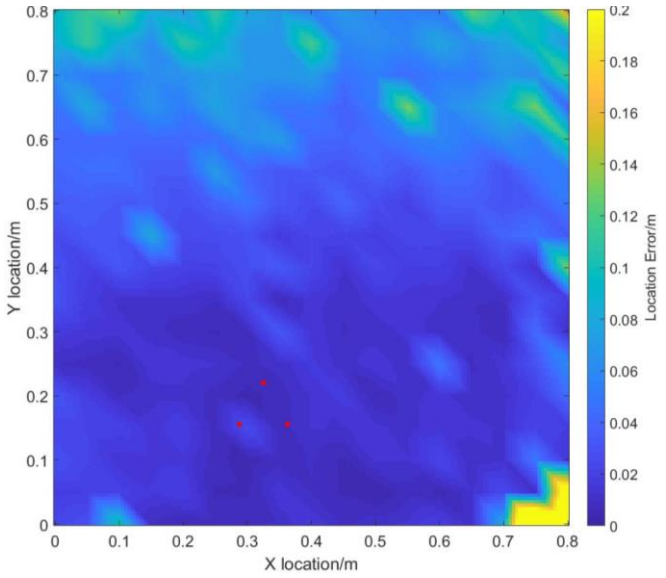

Figure 87 – Colour plot of average absolute location error using the modified three sensor technique in composite Panel B prior to the addition of stiffeners. Sensors marked in red

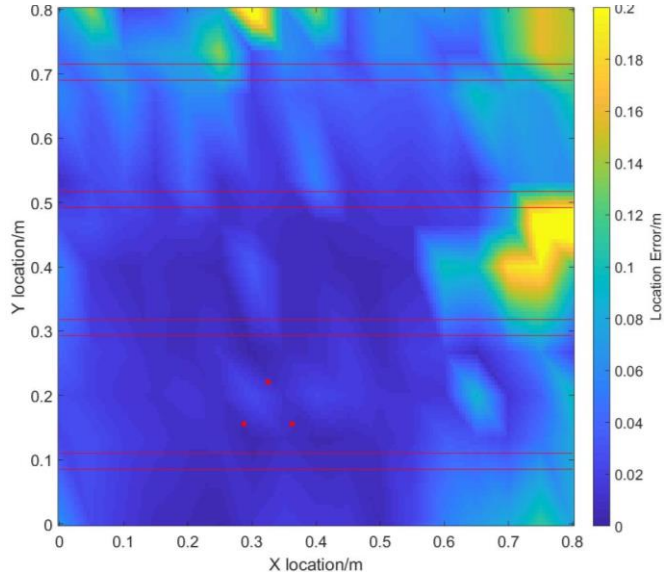

Figure 88 – Colour plot of average absolute location error using the modified three sensor technique in composite Panel B after the addition of stiffeners. Sensors and stiffeners marked in red.

4.4.3 A320 Wing

In order to test the proposed techniques on a real aircraft structure a grid test was performed on the A320 aircraft wing described in Section 4.1.4.

No dispersion analysis has been presented for the A320 wing up to this point, as a threshold technique was found to be ineffective at detecting the arrival of the A_0 mode in complex structures. Using the second differential technique a relatively accurate A_0 arrival can be found, so allowing the rate of dispersion to be determined. To do this five H-N sources were conducted at 50mm intervals at 0°, 45° and 90° from a Nano-30 sensor. The S_0 arrival was found using the AIC technique and the A_0 using the second differential technique on a waveform filtered with a 70 kHz-110 kHz filter. From the difference in arrival times the rate of dispersion of the two modes was predicted for each direction.

The differences in arrival times are shown in Figure 89, which shows clearly that direction is having some considerable effect. This is partially due to the effect of stiffeners on wave velocity but also more significantly, as a result of late triggering of the second differential method. Using the data presented in Figure 89 the average dispersion at 0° was 9570m/s, at 45° 6070m/s and at 90° 5050m/s. For the following test the average of the three rates of dispersion values was used in order to give the best results for all directions, which was 7000m/s. If further improvement in accuracy was desired the value of dispersion used to predict the distance could be changed dependent on direction, this would improve accuracy over the structure and was shown to be effective by Aljets in anisotropic composites (Aljets, 2011).

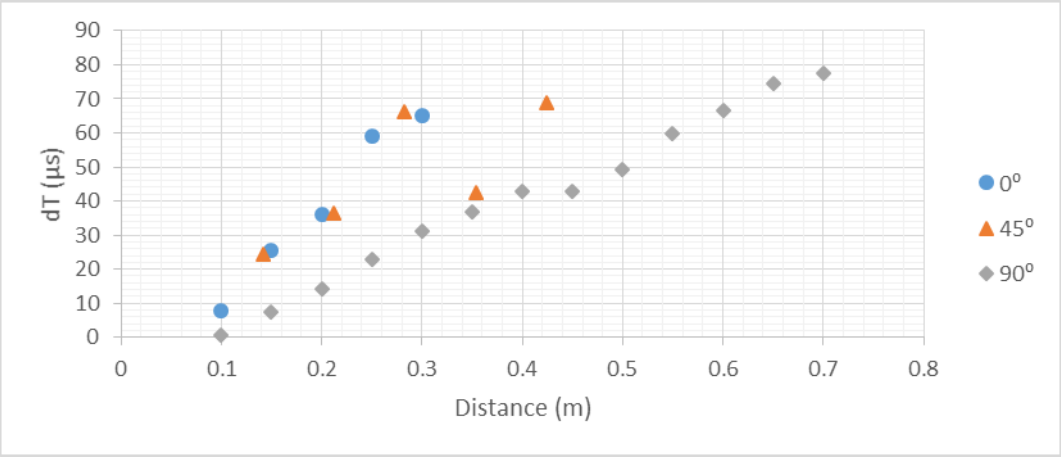

Figure 89 – Difference in arrival times of S_0 and A_0 modes at various angles on A320 Wing

For the full grid test a 1m x 0.5m grid with a spacing of 50mm was drawn on the outside of the top skin of the wing between ribs 10 and 12 avoiding the skin butting on the wing. Three sensors were bonded 75mm apart with the centre of the array at location x = 320mm, y = 285mm. Figure 90 shows the complexity within the test area, the H-N testing points and the sensor locations.

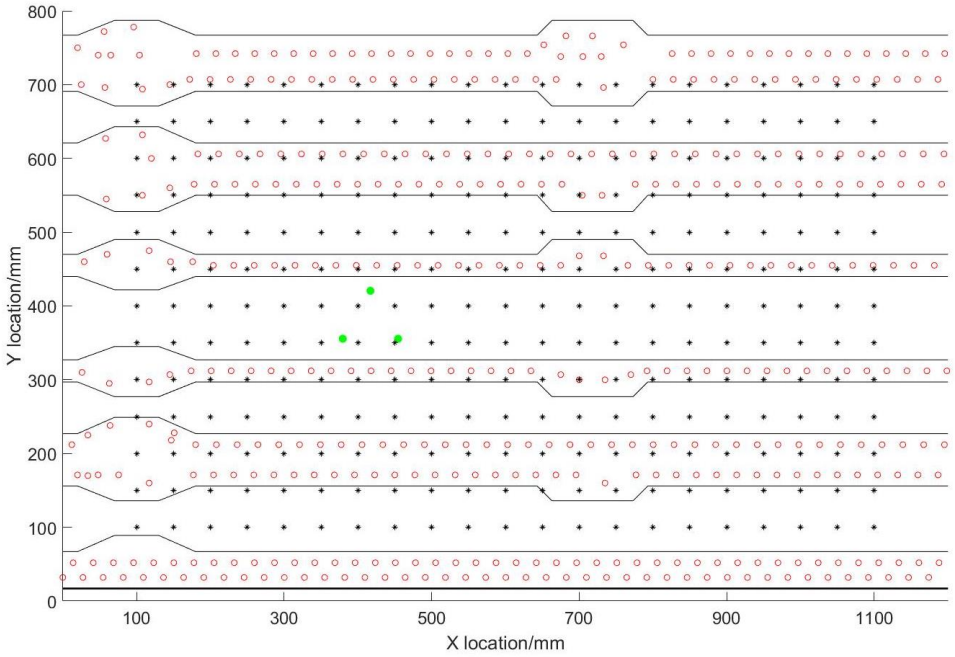

Figure 90 – Diagram of complexity (black lines show the edge of stiffeners and red the location of rivet holes), sensor (green) and H-N testing points (black) on the A320 wing. The thick black line indicates where the skin is butted.

The data was processed using the variety of different methods tested on the previous specimens, the average errors for these can be seen in Table 13.

Table 13 – Errors in A320 wing when a grid of H-N sources were predicted with different methods of localisation

S0 prediction method	Threshold (Fixed)	AIC	AIC	AIC	Threshold (Fixed)	AIC	AIC	AIC
A0 prediction method	Threshold (Fixed)	Threshold (Fixed)	Threshold (20%)	Second Differential	Threshold (Fixed)	Threshold (Fixed)	Threshold (20%)	Second Differential
Mode used for angle prediction	A0	A0	A0	A0	S0	S0	S0	S0
Average Angle error (°)	25.0	25.0	29.0	26.7	46.2	4.9	4.9	4.9
Average Overall error (mm)	217	218	220	224	288	99	68	80
Data less than 50mm error (%)	6	27	33	23	4	39	60	38
Data less than 100mm error (%)	41	61	55	58	27	77	80	80
Data less than 200mm error (%)	74	74	69	71	53	92	95	95

The most accurate of these is to use the S_0 mode to predict the angle, with the modes detected using AIC and a variable threshold set at 20%. How the error differs with changing threshold using the variable threshold method is shown in Figure 91 where it can be seen that the error changes significantly if a different percentage is used.

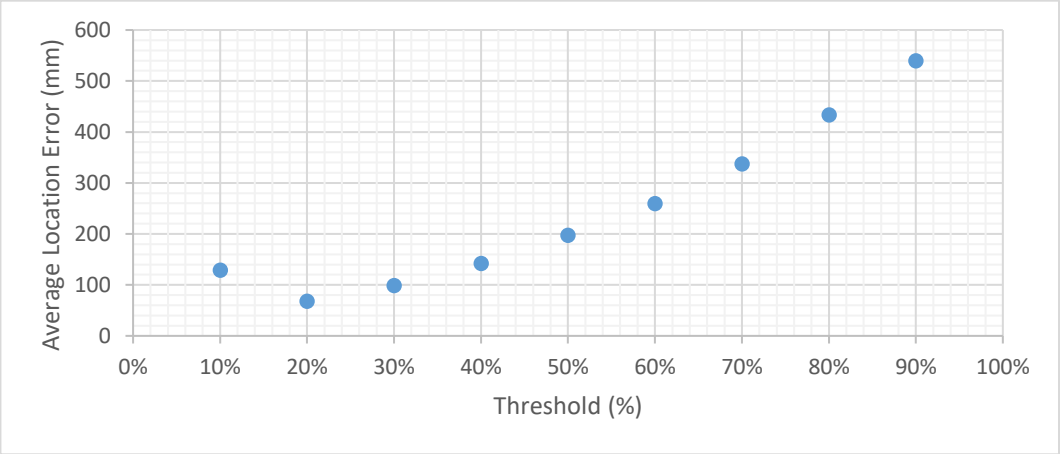

Figure 91 – Average location error for varying percentage threshold on the A320 test data

The second differential method gave similar results to the variable threshold method; both techniques located the same quantity of data within 100mm, however the variable threshold

method located significantly more data within 50mm. The predicted locations obtained from using the second differential method are shown in Figure 92.

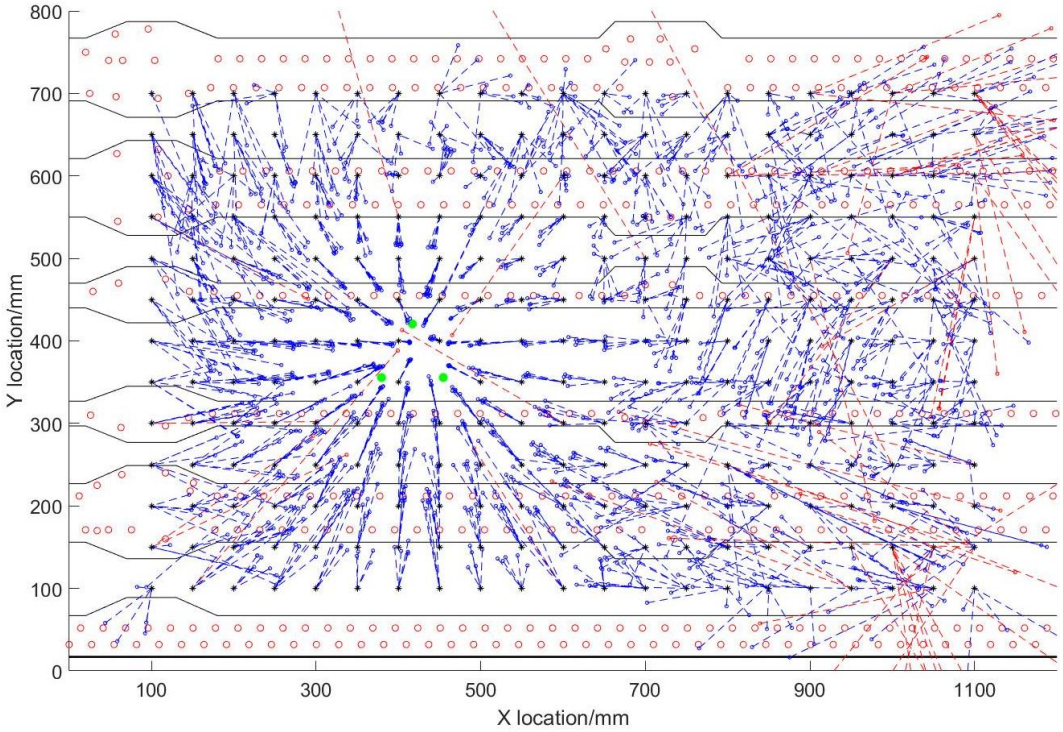

Figure 92 - Predicted locations on the A320 wing using AIC and the second differential method, with H-N source locations shown in black and predicted events in blue, any data with error above 200mm is shown in red.

In order to see the average error across the test area a colour plot was created, showing the average location error at each location and the structural complexity of the wing. This plot is shown in Figure 93. Within these plots the scale is limited at 0.2 m in order to make contrast visible for lower errors, errors at 0.2 m and above are shown as bright yellow.

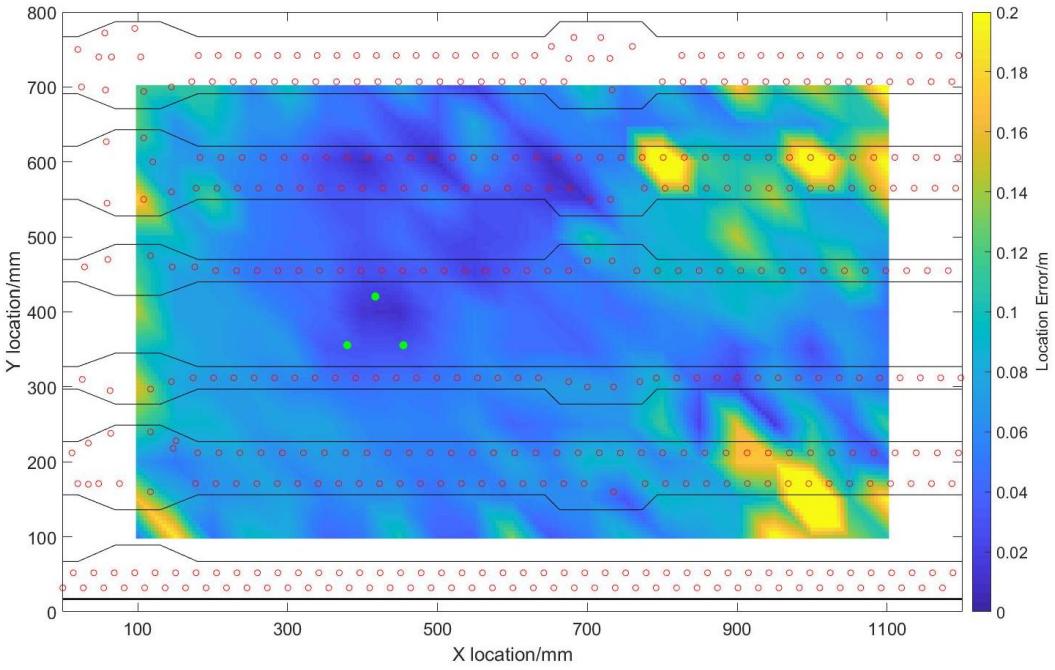

Figure 93 – Colour plot of average location error of the predicted locations on the A320 wing using AIC and the second differential method.

4.4.4 Discussion

Within this section a number of complex structures have been tested on with the three sensor localisation technique. Significant changes have been made to the technique that was developed by Aljets (Aljets et al., 2011, Aljets, 2011, Aljets et al., 2012) which was presented and tested in Section 4.1. These changes involved switching the mode used to calculate the angle of arrival to S_0, as well as modifications to the arrival prediction methods of the two modes. These modifications have been compared through a variety of techniques incorporating some, or none of the modifications.

One of the major changes to the method used by Ajlets is the mode used for angle prediction, instead of the slower A_0 mode, the S_0 was used. Whereas using the A_0 mode allows the technique to be effective in Anisotropic structures, such as the 0/90 layup composite panel A, the modification limits the technique from working in such structures. This is because the wave front of an incoming AE wave can no longer be assumed to be straight, as S_0 modes in anisotropic composites travel elliptically (Paget et al., 2003), as both the $dT_{min/max}$ and ratios method of

predicting the angle of arrival require. If only simple isotropic structures are considered, such as the simple aluminium panel or composite Panel B prior to the addition of stiffeners, both modes predict the angle to a similar level of accuracy if the AIC method is used to predict the S_0 mode arrival, with the A_0 mode being slightly more accurate. This is because the lower velocity of the A_0 mode means that a greater difference in arrival times between sensors is present, reducing the influence of any error in arrival detection on the angle prediction. When complex structures are considered the S_0 mode is significantly more accurate than the A_0. Although good accuracy can be seen closer to the sensor array using the A_0 mode to predict the angle, in complex structures at distance it was very ineffective. This error was a result of either S_0 to A_0 mode conversion causing early triggering, or attenuation of the signal causing a late detection, depending on the location of the H-N source. As the S_0 mode is significantly more accurate than the A_0 mode, discussion from this point onwards will purely focus on the results processed by techniques that utilise the S_0 mode for angle prediction.

Using the AIC technique rather than a fixed threshold to detect the S_0 mode for angle prediction showed a significant increase in accuracy for the simple aluminium panel but very little difference for composite panel B prior to the addition of stiffeners. With the simple aluminium structure the AIC technique predicted the angle with a 3.3° average error whereas the simple threshold method had a much larger average error of 7.5°. This was worse for the complex panel where the AIC technique predicted the angle with a similar accuracy prior to the stiffeners being added whereas the threshold technique had an average error of 29.2°. It can be seen that the threshold technique was ineffective anywhere but close to sensors. This is due to the S_0 mode having a relatively high attenuation rate, as shown in Chapter 3, compared to the other simple panels, which when attenuated additionally by the stiffeners will make accurate detection difficult.

Composite panel B produced significantly different results when comparing the accuracy of the threshold method with the AIC method to predict the arrival of the S_0 mode. Prior to the addition

of the stiffeners the threshold method showed an average angular error of 3.7° and the AIC technique an average error of 4.1°. Here it is clear that the threshold method is not just as good as, but is better than the AIC method, this is due to two reasons. Firstly unlike in the aluminium panel the S_0 mode has a high amplitude in composite panel B. The attenuation testing in Section 3.2 predicted a H-N source produced an S_0 mode with an amplitude of 82dB, meaning the threshold method gives a very accurate prediction in this specimen. The lower accuracy of the AIC technique is a result of the ability of the method to detect close to the start of the waveform, but not the exact same point on each wave, this sometimes causes delays in the order of tenths of microseconds which results in a few degrees error. The threshold method however typically detects a similar point on each waveform allowing the angle of arrival approximation to be slightly more accurate when the waveform is not significantly attenuated or has low amplitude which may cause late arrivals at one or more sensors. The addition of complexity reduces the accuracy of the threshold method, as would be expected because of the additional attenuation, however not to the same amount as for of the complex aluminium panel. The attenuation of the S_0 mode caused the threshold technique to have an angle error of 8.7° where the AIC technique didn't calculate an average error greater than 5.4°, showing again that it is a more accurate technique in complex structures.

The A320 results again showed that the threshold technique struggles to accurately predict the angle of arrival in a complex structure where an average angle error of 25.5° was seen, with the AIC technique being very accurate at 4.8°. The high errors when using a threshold method occur when the H-N sources are further away from the sensors, if only the events close to the sensors are considered, the accuracy is significantly better. This is because when the source isn't too heavily attenuated, the threshold method is able to make a more repeatable prediction of the arrival than the AIC technique, as was seen in the simple composite plate.

Three different methods have been tested in order to detect the arrival of the A_0 mode in order to predict the distance the wave has travelled. These were a simple threshold crossing approach,

a variable threshold crossing method and the second differential technique, which was developed for this thesis. Using a fixed threshold proved to be an effective way of predicting the arrival of the A_0 mode in both simple aluminium and composite structures, achieving an accuracy similar to that of the other methods. For this technique to be effective the threshold needed to be set correctly, otherwise early triggering would occur due to S_0 to A_0 mode conversion or a low frequency component of the S_0 mode. For both composite panels a threshold of 45dB was effective at detecting the mode arrival. When testing on the aluminium structures, both the simple and the complex panels, as well as the A320 wing, this value was too low and a higher 55dB threshold was required. This tailoring of thresholds, although not overly precise, is not desirable for any full scale testing as extensive calibration is required within any setup and doing so wrongly could result in missed data. Lower amplitude sources and those that have experienced significant attenuation are also at risk of being missed, if after filtering, their A_0 mode lies below the set threshold. Although accurate in simple structures the fixed threshold method for predicting the A_0 arrival time was ineffective in complex structures due to the attenuation that occurred on sources far away from the sensors causing late arrival time predictions.

A solution to attenuation causing late triggering was using a variable threshold which accounted for waveforms with lower amplitudes, allowing the A_0 mode to be accurately detected. This technique proved to be effective in all the structures tested, both before and after the addition of complexity. In the case of the Aluminium panel and the A320 wing the variable threshold technique achieved the lowest average error. This method was not as accurate as other techniques within the composite panel, however it stayed relatively consistent with the addition of complexity. The significant drawback to the variable threshold method is that to achieve a high level of accuracy the threshold must be tailored for each test setup. This ranged from as low as 4% in the simple aluminium panel up to as high as 30% in Composite Panel B. This is a problem when detecting real damage as some damage mechanisms are known to produce more in-plane (S_0) energy and others will produce more out-of-plane (A_0) (McCrory et al., 2015). This

means that if a threshold is set too low and more S_0 to A_0 mode conversion occurs than expected, an early A_0 prediction is made.

The final technique that was developed as part of this testing was the second differential technique which, by having a high threshold of 40%, is highly unlikely to be triggered by any low frequency S_0 mode. In terms of accuracy the technique was typically similar to the other methods, and its average error was never much higher than the two threshold based technique. Overall the level of accuracy seen using this technique was good, and in the real aircraft structure (A320 wing) 80% of H-N events were predicted within 100mm of their actual location, and 95% within 200mm. As would be expected most of the error was seen for events further from the sensor array, expanding this range would be very beneficial in order to space sensor arrays as far apart as possible. Further improvement in accuracy would be expected if the value of dispersion used to locate the event was dependent on direction, this would require additional calibration if applied on a large scale but could improve accuracy slightly in some cases.

4.5 Conclusions

Within this chapter a modified version of the three sensor technique used by Aljets has been presented and tested for three simple aluminium and composite structures, where the level of accuracy seen was similar to that achieved by Aljets. A revised angle of arrival prediction method which did not rely on wave velocity was also presented, and the accuracy of the two techniques were very similar. These techniques were then tested on complex structures which proved ineffective due to S_0 to A_0 mode conversion and attenuation of the signals causing significant arrival prediction error. Modifications have been proposed and tested which allow the three sensor technique to locate H-N sources over a large area in complex structures, including an A320 aircraft wing, without significant errors being present. The main alteration is the use of the newly proposed second differential method for A_0 mode arrival prediction, which is able to predict the arrival of the A_0 mode to a fairly good level of accuracy using a highly set threshold and analysis of the second differential of the waveform. The other (the first being accuracy) main

advantage of this method is that it does not require tailoring for each application. Another major change is using the S_0 mode, predicted using the AIC technique, instead of the A_0 mode to predict the angle of arrival. This modification prevents the technique from being applied on anisotropic composites, however it allows it to be used on complex structures. Overall a good level of accuracy and reliability has been seen when locating artificial H-N sources with the modified technique.

5 Development of a wireless system

The author of this thesis was funded as part of the SENTIENT (SENsors To Inform and ENable wireless neTworks) project which was funded by Innovate UK, with the aim of developing a state of the art wireless monitoring system to detect flaws in aircraft structures. A total of eight industrial and academic partners were involved in the project, Cardiff University, the University of Exeter, HW Communications, Airbus, BAE Systems, TWI, NEDEAS and Ultra Electronics, each working on a certain element of the project (Szczygiel, 2014).

As part of the SENTIENT project a wireless system was developed to detect fatigue damage growth in aircraft structures. The aim of this system was to detect and locate AE events in complex structures whilst requiring minimal power to operate, so allowing the potential for it to be powered by energy harvesting methods. This device shall be referred to as a 'node' throughout this thesis and is the combination of a sensing, processing and wireless communication module. Within this chapter the development of these nodes is presented, including an overview of each node and the motivation behind design choices. Additionally the results from power and AE location accuracy testing using the nodes are presented.

As discussed in Section 2.3.2 two types of wireless node would be possible for AE monitoring of a structure, either multiple nodes each attached to a single sensor all time-synchronised together or multiple sensors attached to a single node. The decision was made early in the development process, that to accurately synchronise the clocks between nodes would be too power intensive (discussed in greater detail in Section 2.4.4). This meant that an alternative approach would need to be taken. It was decided that the hardware would be designed to apply the three closely located sensors technique which was presented in Chapter 4, allowing all sensors to connect into one node with minimal wiring and no need to time synchronise nodes. The aim of this process was to develop a wireless system which would apply the technique using the ratios method, with threshold filters for the A_0 and S_0 modes using built in analogue filters. The development process consisted of three prototypes, each of which were tested on a variety

of structures to assess their accuracy of locating H-N sources. These prototypes will be referred to as Mk 1, Mk 2 and Mk 3. The author of this thesis took the lead in specifying the requirements of and testing of all three nodes presented in this work. Key areas include the specification of filter requirements, development of location techniques, identification of issues and proposal of corrections to these problems as well as identification of the requirement for substantial testing on a range of structures.

Wireless data communication is possible in all three versions of the system, and initially this was via a Bluetooth module that communicated with a tablet or phone. Although this approach was power intensive, it allowed a wireless system to be developed prior to a custom RF module being developed. The module requirements were specified by the author in collaboration with BAE Systems whilst the protocols were developed by HW communications. A brief overview of the communication system is given in this chapter. Once developed this module was integrated into the existing Mk 1 hardware and used for all the testing presented within this thesis.

A graphical user interface (GUI) was also developed as part of the SENTIENT project. This work was primarily conducted by Ultra Electronics with guidance from the author. A brief overview of the capability of this GUI will also be covered within this chapter.

5.1 Wireless communication

The communication method used for the wireless sensor had a number of key requirements. Overall it needed to be as low-power as possible while still performing adequately. The main feature required was the ability to pass small packets of information from the wireless sensor node to a computer where data could be processed and stored. Another essential criteria was the ability to pass information to the nodes allowing settings to be modified and the nodes to be put into sleep mode whilst the aircraft is on the ground. It was also a requirement that whatever topology was chosen had the ability to be scaled up allowing lots of sensors to operate in parallel. Communication must also achieve a suitable level of reliability as some messages

must be sent whilst others are less important, this is discussed in further detail later in this section.

For background information on some of the subjects covered within this section please refer to Section 2.4.

5.1.1 Hardware

The hardware used for RF communication was a 'NORDIC NRF51-SERIES SOC DEVICE' which utilises a 2.4 GHz IEEE 802.15.4 chip. This creates a low-power, small sized module with customisable protocols. The final module can be seen in Figure 94 (a), where it is plugged into the Mk 2 prototype. The module allows the prototype to communicate with either a USB RF module (Figure 94 (b)) or a wireless hub (Figure 94 (c)), both of which use the same module with different additional hardware and firmware.

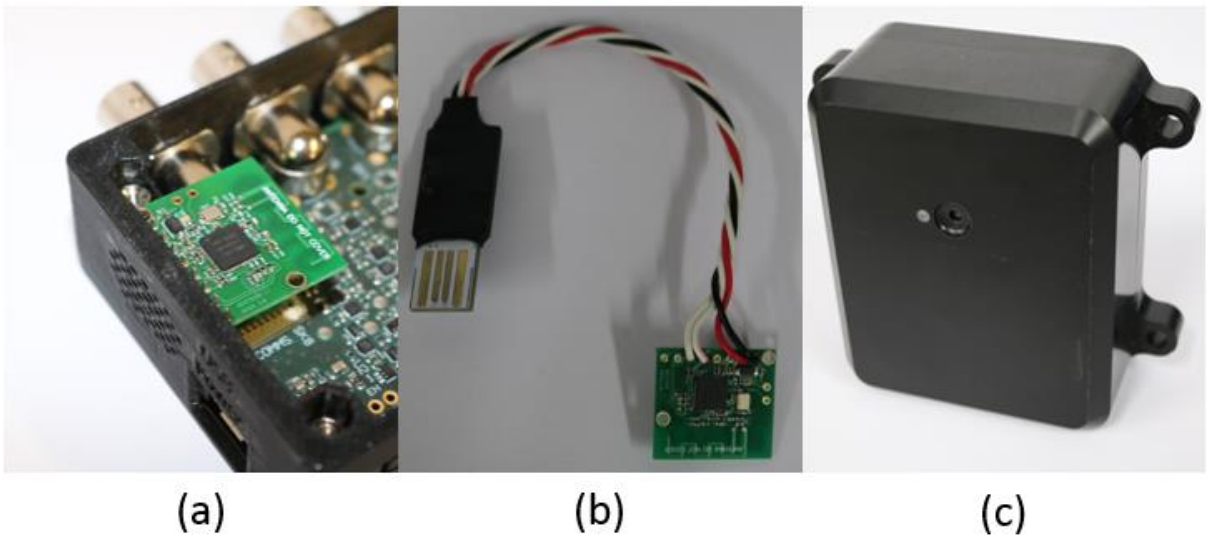

Figure 94 - Image of wireless communication module in Mk 2 node (a), USB communication module (b) and wireless hub (c)

In order to minimise the power requirements for RF communication in the node the module is duty cycled. This allows it to stay in a low powered sleep mode, only turning on at regular intervals to listen for incoming messages and when it needs to send a message of its own. The time interval between and duration of these windows is customisable based on the

requirements of the user, throughout testing this was every two seconds to allow for quick modifications to settings however it was envisaged that if used on-board an aircraft it would be every few minutes to minimise power requirements.

The simplest way in which the RF module communicates wirelessly is to the USB device connected directly to a computer. In this configuration any messages sent from the node are displayed on the computer and messages can easily be sent to the node, making the configuration perfect for device setup, small scale testing and troubleshooting.

The hub is able to receive messages from multiple nodes and upload the data wirelessly via GPS to a cloud-based network. If GPS is unavailable the hub is able to store data which can then be uploaded once this is possible. Figure 95 shows the flow of data from the node to the hub and then onto the cloud. This data can then be accessed using the GUI. Messages can also be sent in the opposite direction to a certain node, so effectively changes can be made to a node anywhere in the world as long as it's in range of the hub.

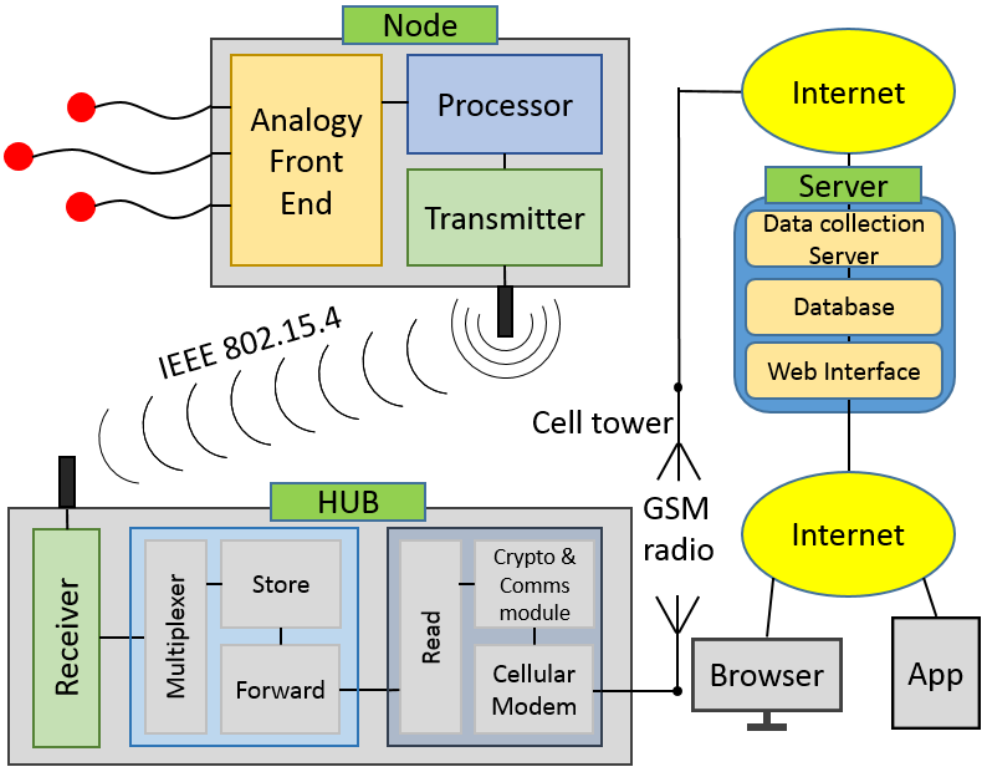

Figure 95 – Example of communication from node to hub then to the server (based on diagrams provided by HW Communications (Parkins, 2017))

5.1.2 Network Topology

The hub and its connectivity to the cloud gives the system the ability to be applied on a large scale and be controlled from a central point. A simple example of how this could look if applied to multiple aircraft structures is shown in Figure 96. In this example nodes are spread over multiple aircraft, each of which must be within direct range of a hub creating a star network topology (see Section 2.4.3 for more details). Most large aircraft will require multiple hubs all connected to a power source; this is because the RF range is unlikely to be large enough for a single hub to be used. An in-depth study has not been conducted into the range of RF propagation in an aircraft structure however preliminary testing in an open environment showed a range of around 30 m was possible. Each node has an individual ID which is stored with a timestamp alongside the event data within the hub. Once GPS is available the hub uploads the data to the cloud allowing the user to access the data associated with a required node, or all the nodes on an aircraft. The GUI, where a user can access this data is discussed further later in this thesis.

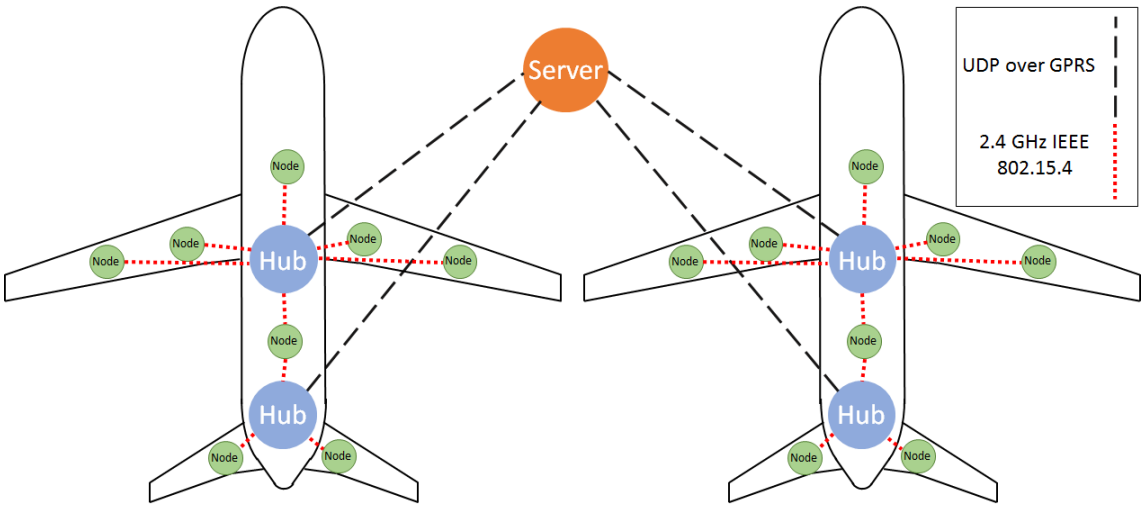

Figure 96 – Overview of an example wireless network

This chosen setup is effectively a star network, where the hub communicates with each node then passes then information forward. Further information on this as well as the advantages and disadvantages of this topology and others are covered in Section 2.4.3 of this thesis.

5.1.3 Reliability of Data Transfer

Reliability of the data being transferred was a key factor that was considered and taken into account throughout the process. It was clear that all messages sent to the node, to change settings or turn the hardware on and off, must be received or an alert shown if not received. Data sent from node to hub on the other hand was viewed as less vital as any fatigue damage continually produces AE, meaning one missed event isn't a problem. This meant in order to reduce power there is the potential for some data to be lost. Data is lost if either multiple nodes send data simultaneously or the hub is sending data at the same time as a node does. To reduce the likelihood of this occurring what is known as 'jitter' has been applied to each node. Jitter involves applying a random delay after an event and before data transmission to minimise the possibility of messages colliding when multiple nodes detect the same event. This protocol setup is only applied in its current form when each hit is sent individually from the node to the hub, which is useful for small scale testing where it was viewed that the loss of a single event was not a major problem. If this system where to be implemented for flight testing it was envisaged that data would not be sent individually, but clustered and only important data sent. This would reduce the traffic on the wireless network and so the power requirements of the nodes but would require modifications to the protocols to ensure data transmission was assured.

As the nodes are subject to duty cycling at a rate that the hub is unaware of, the hub cannot simply send a message and be certain that it has arrived. Instead, to ensure messages are received by a node, once the hub has been instructed to send a data packet it will do so repeatedly. Once the node receives this message it will respond with a confirmation, upon receiving this the hub will stop transmitting. This process ensures reliable data transfer with only a minor increase in power consumption in each node.

5.2 Graphical User Interface

The GUI was developed by Ultra Electronics and allows the user to access data from the server and display it on 3D models. Input on the specifications of the GUI was provided by the author

along with the other partners of the SENTIENT project. The general specification was that as well as retrieving and showing the data the GUI should allow the user to associate multiple nodes to a structure and assign their position. This information could then be saved as a project, allowing data over a given time period to be viewed quickly by an engineer wishing to understand the health of the structure, which could be done anywhere in the world.

In order to view data a project must be created and a structure can then be chosen from 3D CAD models created by the user and either saved to each device or retrieved from the server. In theory an entire aircraft could be presented in one view however, as at this stage of development data is only presented in 2D, this is unlikely to be feasible. Once the structure is selected the RoD can then be set by the user which allows the outputting difference in mode arrival times to be converted to a distance. Nodes can then be selected and associated with each specimen. Although many nodes can be added, in the majority of testing and demonstrations only a single node was used for each test. These nodes must then be positioned in the X, Y and Z plane, their orientation specified and the size of the array inputted. The user can then enter a time period they wish to see data from and the GUI will present the data in the form of a line from the sensor to the location, as shown in Figure 97 where the data from two nodes is presented on Composite Panel B. The time period can then be altered by the user using the sliding scale at the bottom to move between and zoom in on data.

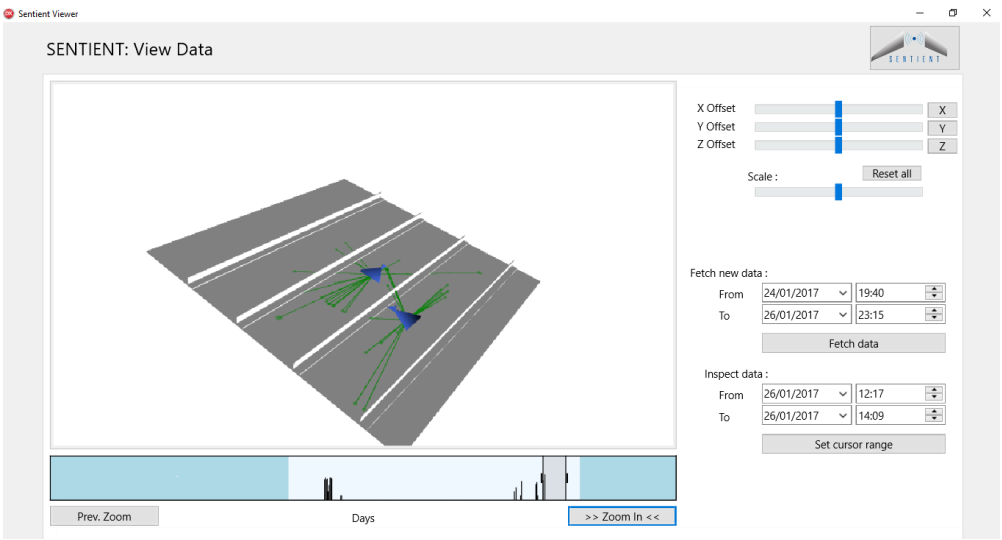

Figure 97 - Data presented from two wireless nodes on a 3-D model of composite panel B

The GUI also has the ability to push data to a node, as long as it is in range of a hub. This process allows the settings to be changed on a node or the node to be set to sleep mode to save power without an engineer needing to be in range of the test specimen. The sending of the message has similar protocols to sending data normally over RF to ensure that once a message is sent by a user it will reach the desired node, assuming the node is in range of a hub, as it will keep being sent until a confirmation is received.

5.3 Parameter Extraction

As discussed in Section 2.1.5 parameter extraction is the process of taking basic parameters from the AE wave. This is vital in order to understand the severity of an AE event, if only based on the amplitude of the signal. Studies have shown that it is also possible to distinguish between different types of damage using extracted parameters (Crivelli et al., 2014). The importance of this meant each version of hardware contained an analogue to digital converter (ADC) in order to allow parameter extraction to be performed on at least one channel. The author of this thesis wrote parameter extraction code in 'C' which was embedded into the hardware. The parameters extracted within this code were the rise time, maximum amplitude, count and mean square, these are described in more detail in Section 2.1.5. The mean squared is proportional to the root mean squared (RMS), other than it not having been square rooted, this was to reduce the power requirements of the sensor node. RMS is in turn proportional to the energy within the waveform, however energy is also dependant on a number of hardware variables. To collect these variables would increase power requirements, so the output was left as mean squared however this could be changed if required.

5.4 Test Procedure

The testing performed using the nodes was very similar to the testing performed using the wired system in Chapter 4 (procedure presented in Section 4.1.4) however extra steps were required. Before a full test was conducted calibration tests were performed, which involved probing the node with an oscilloscope in order to properly set gain and threshold levels. Where possible

these settings were left unchanged as specimens were modified, however in some cases improvements could be seen by altering gain levels; in these situations, tests were conducted with both new and old values. The USB RF communication module was used to display the recorded data on a laptop, this was then saved and further processing performed. In some cases, what are often referred to as 'Bad breaks' were made, which is where a pencil lead doesn't break properly, so not producing the required source. This would often trigger the system and give a false event. Also at times the RF transmission failed meaning no event was received by the laptop. In both these cases an extra event would be conducted to ensure five good events were recorded.

5.5 Distance Correction

The systems presented in the following sections all perform distance and angle of arrival calculations based on the S_0 and A_0 arrivals at 3 sensors in a triangular array using what is referred to in this thesis as the 'Ratios' method and is presented in Section 4.1.3. As shown in Section 4.1.3 the angle of arrival calculation used is dependent on all 3 sensors, meaning the angle is calculated from the centre of the array. In a wired system data is recorded on all channels allowing a distance calculation to be made on each of these, which when averaged predicts the distance from the centre of the array. In the wireless systems presented in the following sections, distance is only predicted from sensor 1, the sensor at the top (0^o) meaning some error will present in all measurements. Distance is only predicted at sensor one to remove the need to digitalise the waveforms on all channels, so reducing power. This is demonstrated in Figure 98 where the predicted distance D_p is significantly less than the actual distance D_a. The incorrect distance will give a potentially significant error. In the case of 0^o and 180^o this error is equal to the distance between the sensor and the centre of the array, D_s.

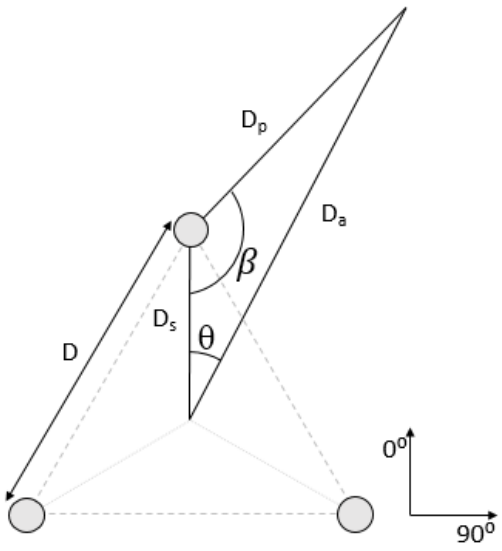

Figure 98 – Demonstration of the distance prediction problem

This problem can simply be accounted for using trigonometry to find the actual distance D_a, as is shown in Equations 19, 20 and 21 below:

$$D_s = {D \times (\tan 60 - \tan 30)}/{2} \quad (19)$$

$$\beta = 180 - \theta - \sin^{-1}\left(\frac{D_s \times \sin\theta}{D_p}\right) \quad (20)$$

$$D_a = \sqrt{{D_s}^2 + {D_p}^2 \times 2 D_s D_p \cos\beta} \quad (21)$$

Where D is the sensor spacing and D_p is the distance predicted by the system. All data presented within this chapter has been corrected with this approach and the GUI presented in Section 5.2 automatically corrects any data.

5.6 Mk 1

The Mk 1 prototype was the first full AE system manufactured by BAE Systems and tested by the author. The system, shown in Figure 99, was able to apply the three sensor location technique in a small and low-power device. The system was not optimal, however this first iteration enabled problems to be identified, which allowed modifications to be made on later versions of

the hardware. When the prototype was first delivered, HW Communications had not yet developed the RF communication module so the power intensive Bluetooth communication was used, however a modification was made when the communication module became available.

Figure 99 – Mk 1 node in 3D printed casing

The triangular shape allowed the case to contain three holes, one in each corner, to enable the sensors to be directly mounted within the case. This would require the sensors to be hardwired into the PCB board but allow the BNC connectors to be removed and the whole unit to be stuck to the test structure. This feature would be very beneficial in a final commercial system as it eases integration to a structure, however throughout testing and development it is not required.

Due to confidentiality only an overview of this prototype is given within this thesis as the technical specifications of the hardware cannot be shared.

5.6.1 System Overview

Previous implementation of the three sensor location technique has always been conducted using commercial wired systems which were able to acquire waveforms. These waveforms were post processed elsewhere using digital frequency filters or CWT in order to perform SSMA upon the waveforms, as discussed in Section 2.2.6. From this the arrival times of the A_0 and S_0 mode could be predicted allowing the source location to be found using the techniques covered in

Chapter 4. In the case of a wireless system, converting waveforms into digital form using an ADC is possible, although it is power intensive, but frequency analysis on-board is infeasible due to power and time requirements. The remaining option is to send entire waveforms wirelessly to be processed elsewhere, but this again would consume too much power.

Within the SENTIENT hardware an alternative approach was taken. Rather than converting the waveforms into digital form to analyse, filtering was applied to the original waveforms using analogue filters, similar to those found within the preamplifiers of a commercial AE system. To distinguish between the S_0 and A_0 modes two different types of filters were used, with their frequencies based on FFT results from composite panel A, the simple aluminium panel and the A320 wing presented in Chapter 3 of this thesis. The aim was to develop a one case fits all solution where the same hardware could be used on a variety of structures, so a frequency range in the middle of the peak frequencies of the tested specimens was chosen. The A_0 mode was detected using a bandpass filter (BPF) around 100 kHz (approximately 70 kHz to 130 kHz), the response for which can be seen in Figure 100.

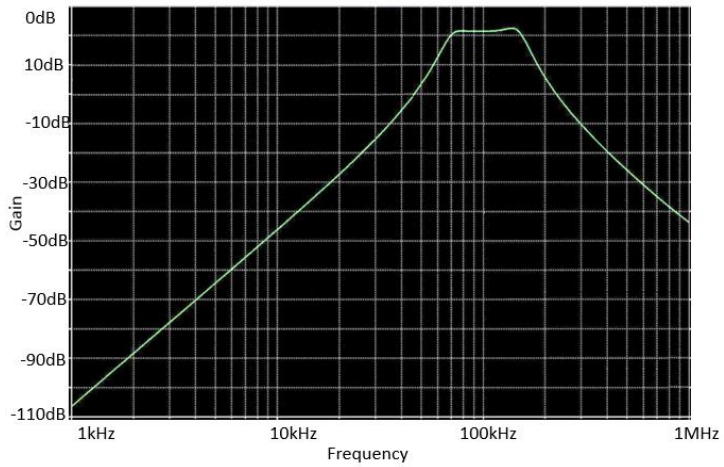

Figure 100 – Frequency response from A_0 filter (modified from (Jenman, 2016a))

The S_0 mode from an AE event is the first that arrives at the sensors, so a narrow filter is not needed to detect its arrival. However a high pass filter (HPF) at 300 kHz (approximate cut-off at

200 kHz) was used to reduce the likelihood of false triggers from noise and A_0 modes, the frequency response for this filter can be seen in Figure 101.

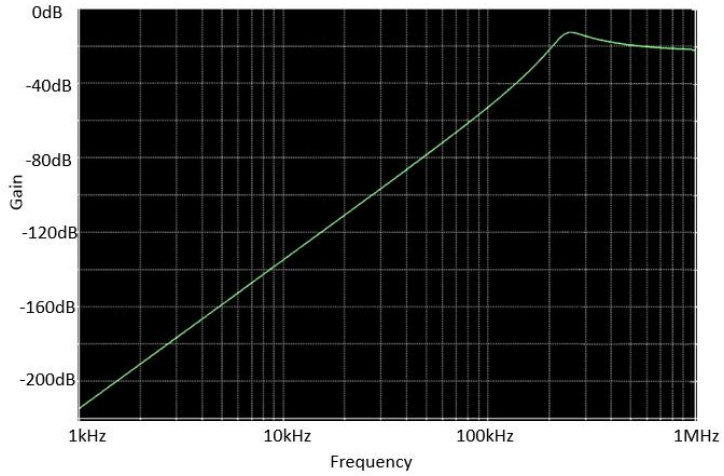

Figure 101 – Frequency response from S_0 filter (modified from (Jenman, 2016a))

The aforementioned filters are only a small part of the analogue front end architecture. Due to confidentiality a full schematic cannot be shown however a simplified flowchart can be seen in Figure 102. Figure 102 shows sensor inputs on the left-hand side, once armed the analogue signals from these pass through charge amps to increase their voltage. In the case of channel 1 the signal is then split, one for each frequency filter. Each then undergoes their applicable variable gain stage to amplify the signal further, before arriving at a comparator which determines if the voltage is greater than a predetermined threshold. If an A_0 waves crosses its threshold nothing will happen as the latch requires the S_0 channel to trigger first. Once the S_0 has been triggered a 22MHz clock is started. An A_0 trigger prompts the clock's value to be recorded meaning each channel has an A_0 arrival time (in bits) relative to the arrival time of channel 1's S_0 mode. For ease of explanation these shall be referred to as $A_0$1, $A_0$2 and $A_0$3.

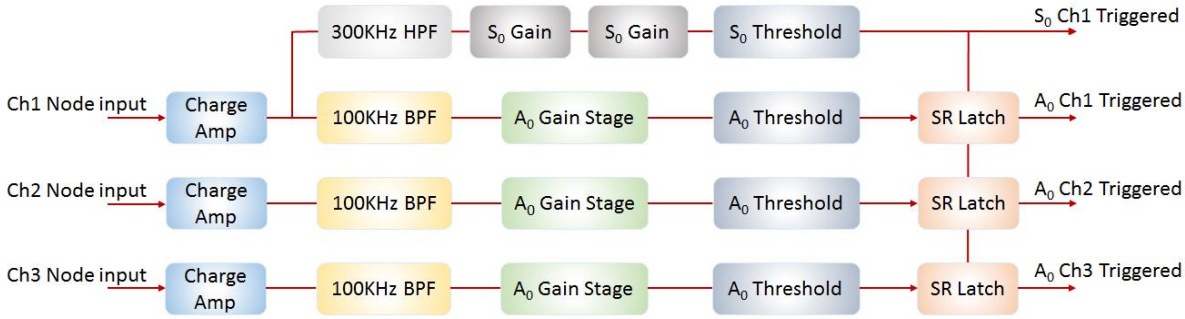

Figure 102 – Analog front end architecture for Mk 1 node

Subtracting these values from each other and dividing by the bit rate of the clock gives the actual time differences, however the ratios between them are adequate for calculating the angle of arrival. This is calculated on-board the wireless node, however it was envisaged that in any real application the angle would be calculated within the GUI to reduce power consumption on the node.

The distance of the source from sensor 1 is proportional to the difference in arrival of S_0 and A_0 at channel 1 and can be found using Equation 22.

$$D = \frac{A_0 1}{B} \times \left(\frac{V_{S_0} V_{A_0}}{V_{S_0} - V_{A_0}} \right) = A_0 1 \times ROD \qquad (22)$$

Where *B,* the clocks bit rate, can be combined with the known velocities of each mode to give the material's rate of dispersion in bits. This allows the distance to be easily calculated within post processing, as is done in the GUI.

In order to extract parameters from the waveform, a single ADC is able to convert a waveform at 1 MSPS, for 1 ms. The waveform to be processed is selected by the user and can be the output of any charge amp or filter. The extracted parameters, arrival times and calculated angle are then sent wirelessly.

The system has a number of data filters to enable events that are missing information or have trigger times that are not feasible to be ignored. In the nodes developed for this project the

arrival times are still sent to allow the user to understand what is wrong, however it was envisaged that in a final system these events will be discarded entirely. The first data filter in place ensures that an A_0 arrival time has been recorded on all three channels. Another filter ensures that the differences between A_0 mode arrivals are not too large, as this indicates that a channel has either detected the event too early or too late. For this testing the required difference for this to be triggered has been set quite high meaning that only very late or early triggers are filtered (such as the A_0 being triggered off the S_0 mode). The final filter checks that the S_0 trigger isn't too close to the A_0 triggers meaning the actual S_0 mode may have been missed and instead is triggering off the high frequency component of the A_0 mode. This trigger does mean that events very close to sensor 1 are ignored, however without this, lots of false positive events would occur close to this sensor.

As a result of the data filters as well as the A_0 channels only being active once an S_0 mode has been detected by the sensor there are certain areas close to the sensors where AE events will not be detected. The size of these is very dependent on the velocity of the S_0 and A_0 modes and whether the material is isotropic or not, but will typically look similar to the areas marked in Figure 103. These dead zones are not ideal, however the additional power consumption and increase in false positives that monitoring these areas would cause makes removing them infeasible.

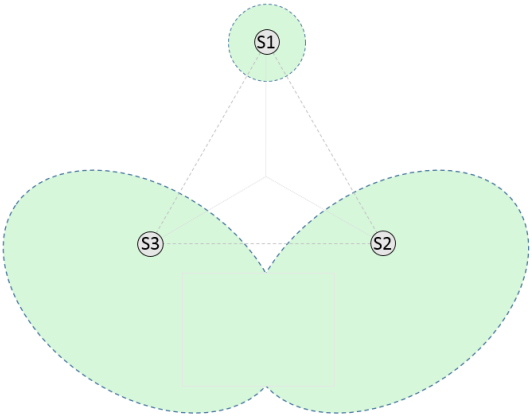

Figure 103 – Diagram outlining in green the dead region that occurs close to the second and third sensors, the size is dependent on wave velocity.

5.6.2 Power Consumption

In order to analyse the power usage of the Mk 1 node a Silicon Labs 'EFM32 Wonder Gecko' development board was used. This board has a 3.3V output which is able to power the wireless node and a low power mode which only requires 6 µW to run the board, a negligible amount. The Simplicity Studio energy profiler (software by Silicon Labs) was then used to analyse the board's power requirements, which will be the node's power consumption plus the negligible power the board requires. This allows the nodes power to be recorded and evaluated at a rate of 5000 SPS. This setup is shown in Figure 104.

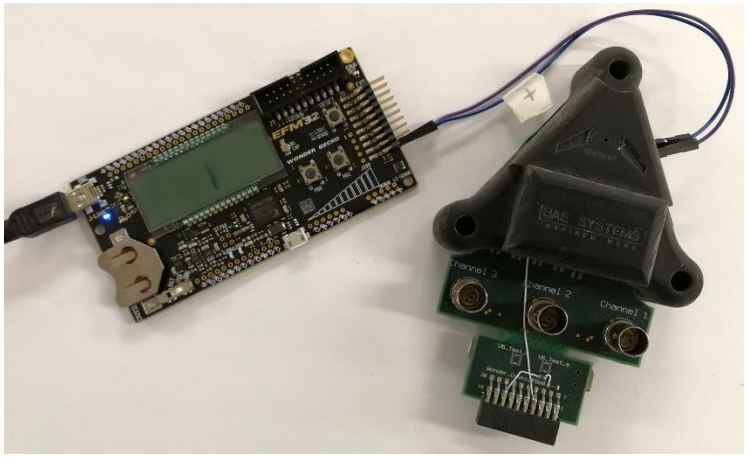

Figure 104 - EFM32 Wonder Gecko development board powering the Mk 1 node

The power requirements were analysed in both sleep mode and when the system was waiting for an event. The power required for the RF communications module to duty cycle was also analysed as well as the power required to receive, process and transmit an event. The results from this are shown in Table 14.

Table 14 – Power consumption of Mk 1 node in a variety of modes/performing certain tasks

	Sleep	Wait for event	RF Window	Event and send
Time(ms)	-	-	103	181
Average power (mW)	0.33	17.44	43.4	38.4
Max power (mW)	-	-	82.3	83.3
Total energy (mJ)	-	-	4.5	7.0

5.6.3 Structural Testing

In order to assess the location accuracies of the Mk 1 node it was tested using the procedure outlined in Section 4.1.4. For the Mk 1 node only simple structures were tested upon as preliminary testing on more complex structures identified that accuracy was poor. Further information about the test specimens is presented in Section 3.2 of this thesis. For each test, gain settings and threshold levels were calibrated using an oscilloscope to assess numerous H-N sources over the structure. These tests, and those presented later in this chapter using the later nodes, were performed in parallel to the wired testing presented in Chapter 4. The same sensors were used for both tests without moving the sensor.

Unless otherwise stated all data in this section has been capped at a 200mm error, meaning that if the inaccuracy in a location was over 200mm it was considered as an error of only 200mm, this is also the case for locations where no location was predicted. This was done since an event with an error of over this on a structure of this size can be regarded as not having been located with any accuracy, so the cap ensures that these do not affect the overall average disproportionally.

The first structure on which a full test was performed on was the aluminium panel prior to the addition of stiffeners. Figure 105 shows a colour map of the average location error at each location. Table 15 shows the overall average location error as well as the average error in distance and angle calculations. Additionally Table 15 shows the percentage of data within 50mm, 100mm and 200mm accuracy. The results from this test show that the accuracy at the edges of the panel was significantly lower than closer to the sensors, analysis of the results show that this was a result of inaccuracies in the angle prediction rather than the distance prediction.

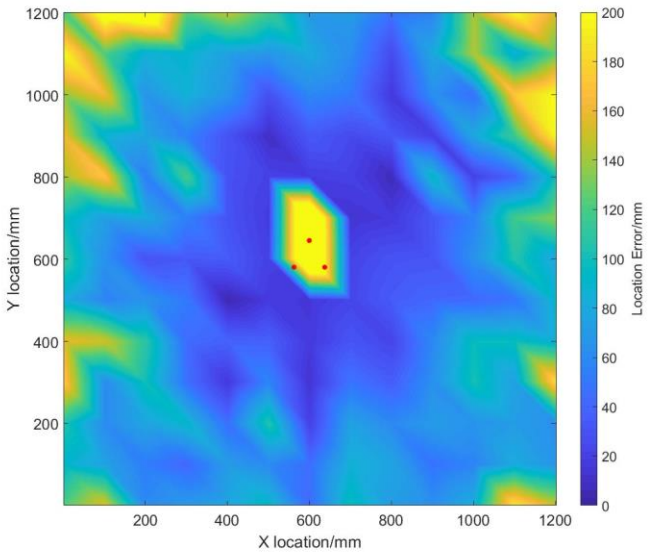

Figure 105 – Test results using the Mk 3 node on simple aluminium panel

Table 15 – Error and accuracy data from the test on the simple aluminium panel using the Mk 1 node

Average Angle Error (°)	5.3
Average Distance Prediction Error (mm)	36.0
Average Overall Location Error (mm)	79.0
Percentage of data with less than 50mm error (%)	37.0
Percentage of data with less than 100mm error (%)	77.4
Percentage of data with less than 200mm error (%)	93.5

Testing was also conducted on the anisotropic composite panel A. Figure 106 shows a colour map of the average location error at each location. Table 16 shows the average errors and accuracy of the technique. Unlike the aluminium test, where all locations were detected, on the composite panel A test a large number of locations (~30%) could not be predicted. This was due to the lack of an S_0 trigger prior to the arrival of the A_0 mode meaning no distance was predicted and the event was ignored by filtering.

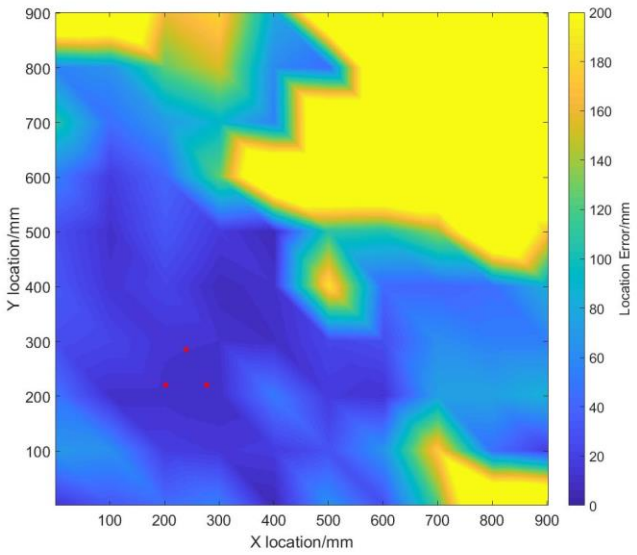

Figure 106 – Test results using the Mk 1 node on composite panel A

Table 16 - Error and accuracy data from the test on composite panel A using the Mk 1 node

Average Angle Error	9.9
Average Distance Prediction Error (mm)	93.0
Average Overall Location Error (mm)	116.9
Percentage of data with less than 50mm error (%)	45.4
Percentage of data with less than 100mm error (%)	63.4
Percentage of data with less than 200mm error (%)	72.8

Finally testing was conducted on the quasi-isotropic layup composite panel B. Figure 107 shows a colour map of the average location error at each location. Table 17 shows the average errors and accuracy of the technique. As with the testing performed on composite panel B a significant number of locations (~40%) could not be located. This again was as a result of the S_0 mode not being detected by the node prior to the arrival of the A_0 mode. The A_0 was also observed as being heavily attenuated at its arrival at the sensors, affecting the accuracy of the angle prediction.

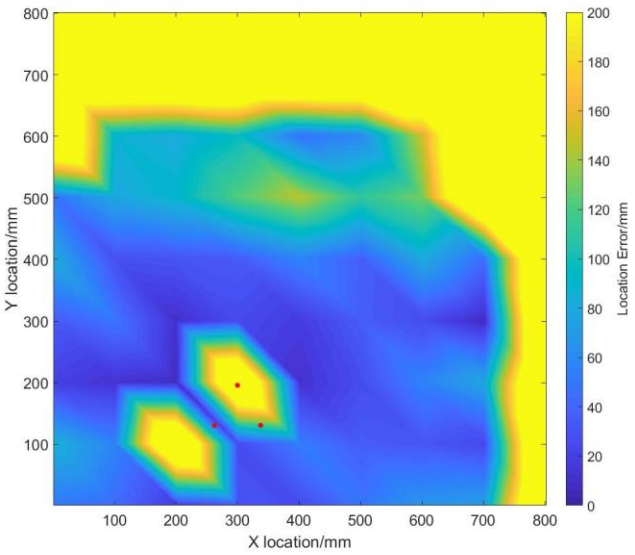

Figure 107 – Test results using the Mk 1 node on composite panel B with no stiffeners

Table 17 - Error and accuracy data from the test on composite panel B using the Mk 1 node

Average Angle Error	15.0
Average Distance Prediction Error (mm)	121.8
Average Overall Location Error (mm)	144.8
Percentage of data with less than 50mm error (%)	38.3
Percentage of data with less than 100mm error (%)	56.5
Percentage of data with less than 200mm error (%)	62.7

5.6.4 Additional Testing

It was apparent early in the testing process that the Mk 1 node had a number of areas that required improvement. One significant problem was crosstalk, the phenomenon where signals from one channel are undesirably seen on another. This occurred between channel 1's S_0 filter output and A_0 filter output, shown in Figure 108. This problem cannot be seen on $A_0$2 (channel two's A_0 filter output) or $A_0$3. The issue was found to be caused in the gain stage of the circuit board and can be eliminated with improved design. The problem was eliminated by setting the threshold higher to ensure early triggering didn't occur on $A_0$1.

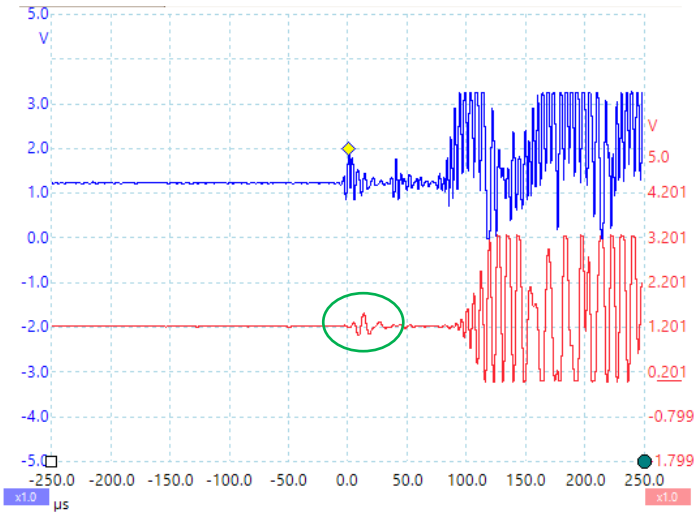

Figure 108 – Crosstalk from S_0 filter output of sensor one (blue) to A_0 filter output on sensor one (red). Crosstalk circled in green.

Another problem noticed was that the error was often present in the angle calculation. Within the testing conducted in Chapter 4 this was also a problem when using a threshold crossing technique, as attenuation sometimes caused the threshold on one of the sensors to miss the crest which triggered the other two sensors. If this occurred, it would then typically trigger half a wavelength later as a plus/minus threshold was present. In the case of the wireless system the arrival time is calculated using a comparator, which compares the input voltage (the input waveform) with a reference voltage (the threshold) and gives a digital output for whichever is greater (Mancini, 2001). This means that if a crest of the waveforms triggers one channel, but is too low to trigger another, then a delay of an entire wavelength will be present instead of half a wavelength which is likely to be the case with a negative trigger.

5.6.5 Mk 1 Discussion

Throughout the testing using the Mk 1 node a number of issues were identified. The comparator issue as well as the crosstalk are two problems that affected the results in all tests and removing these problems would improve the accuracy of locations. They are not however responsible for the large number of locations that could not be predicted within the two composite panels which were tested on. The reasons for the failure to locate in the composite specimens are

different for each panel. In composite panel A the S_0 attenuation was too great when not at 0^o or 90^o from the sensors whereas in composite panel B the A_0 mode was too attenuated over 400mm from the sensor and the S_0 was fully detectable anywhere on the panel.

The testing in Chapter 3 showed that a lower amplitude S_0 mode was produced by a H-N source in composite panel A than in any other specimen - 62dB where all the other specimens are 80dB or above. This, combined with a high attenuation rate of 43dB/m at 45^o means that the signal is quickly lost into noise. The reason that the S_0 mode could not be detected in the composite panel with the Mk 1 node, but was detected using a wired AE system (as shown in Chapter 4), is that the gain on the S_0 channel is not as great as that produced by a pre-amplifier as used with a wired system. This means that the signal is quickly lost into the noise.

The A_0 mode on composite panel B was heavily attenuated for a different reason. The Mk 1 node filters were designed to be as universal as possible, allowing it to work adequately on a range of structures, with the BPF chosen having frequency limits of around 70 kHz - 130 kHz, which were based on the frequency response of the Aluminium panel, A320 wing and composite panel A. Composite panel B was manufactured after the Mk 1 node, and has an A_0 peak frequency of 50 kHz, falling outside of the nodes filters. Combined with the crosstalk on channel 1 meaning the threshold needed to be set high meant that the mode was below the threshold when the H-N source was over 400 mm from the sensor array.

Overall the Mk 1 node identified a number of problems which assisted with the development of the wireless damage detection system overall. These changes were then implemented in the Mk 2 node.

5.7 Mk 2

The Mk 2 node was the second full system manufactured by BAE Systems and although very different in appearance (Figure 109) from the Mk 1 node, in terms of overall operation it is very similar. The aim of this second system was to increase sensor performance and where possible reduce overall power requirements. The rectangular shape was chosen to simplify manufacture as the sensor holes in the Mk 1 node were redundant. The additional BNC connecter was added to allow modifications to be made to the node which converted it into a four sensor impact detection system, this work will not be covered within this thesis.

Figure 109 – Mk 2 node within 3D printed case

5.7.1 System Overview

The Mk 2 node architecture is much the same as the Mk 1, meaning the architecture shown in Figure 102 is unchanged. Changes to individual hardware components were made based on the testing performed on the Mk 1 node, the overall aim being to increase the range and accuracy of the system. In order to achieve this, modifications were made to the charge amplifiers, filters and gain stages which led to an improvement in signal to noise ratio. This allowed heavily attenuated signals to be properly amplified and detected, meaning a larger area could be monitored with a single node.

To better detect the S_0 mode, which was particularly important in composite panel A, the frequency filters were modified. Instead of a HPF a BPF was used, which filtered the signal from approximately 150 kHz – 300 kHz as shown in Figure 110 (a). The change to a BPF means that the signal to noise ratio was increased, allowing a greater gain to be used, so increasing the range of the system. The A_0 filter was also broadened to 60 kHz – 140 kHz, and although not perfect, is much more able to detect the A_0 mode in composite panel B when combined with the other modifications.

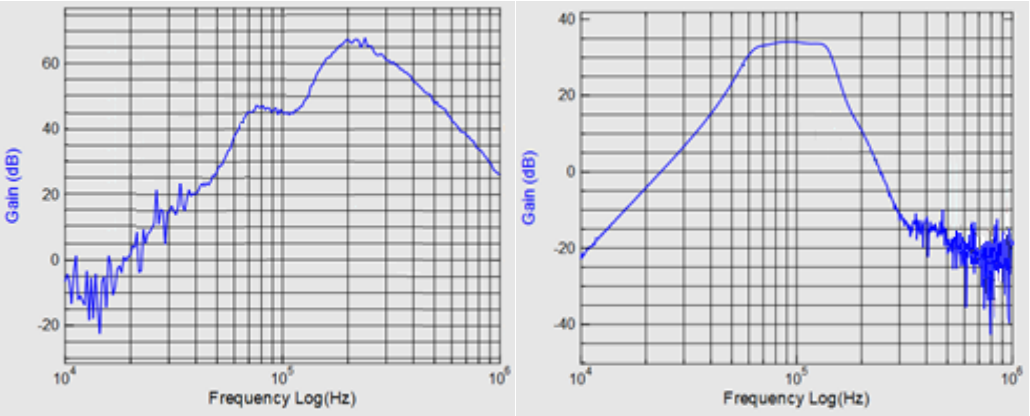

(a) (b)

Figure 110 – Mk 2 S_0 (a) and A_0 (b) frequency filter and gain stage responses (Jenman, 2016b)

In order to combat the inaccuracy caused by the comparator, the Mk 2 node uses a window comparator instead. As opposed to the comparator used in Mk 1, which checks whether the voltage is above a certain value, a window comparator checks if the voltage is between two values (Webster, 1999). This allows positive and negative user programmable thresholds to be set, as is the case for commercial systems.

Throughout the design process care was taken by BAE Systems to ensure that the likelihood of crosstalk on channel 1 was minimised. This proved effective and crosstalk was all but removed in the Mk 2 node.

Additional features were also added to the wireless node in addition to the extra channel mentioned above. These included temperature, humidity and pressure sensors which broaden

the potential application of the sensor. These additions will not be covered in detail within this thesis and were not active when power measurements were conducted.

5.7.2 Power Consumption

As for the Mk 1 node the Mk 2 node's power requirements were analysed using a Silicon Labs 'EFM32 Wonder Gecko' development board. The results, as well as those recorded with the Mk 1 node, are shown in Table 18.

Table 18 – Power consumption of Mk 2 node in a variety of modes/performing certain tasks

		Sleep	Wait for event	RF Window	Event and send
Mk 1	Time(ms)	-	-	103	181
	Average power (mW)	0.33	17.44	43.4	38.4
	Max power (mW)	-	-	82.3	83.3
	Total energy (mJ)	-	-	4.5	7.0
Mk 2	Time(ms)	-	-	103	192
	Average power (mW)	0.12	16.4	43.4	37.6
	Max power (mW)	-	-	82.3	95
	Total energy (mJ)	-	-	4.5	7.2

5.7.3 Structural Testing

Prior to the addition of stiffeners to the aluminium panel a test was performed with the Mk 2 node and a colour map of the errors from this is shown in Figure 111.

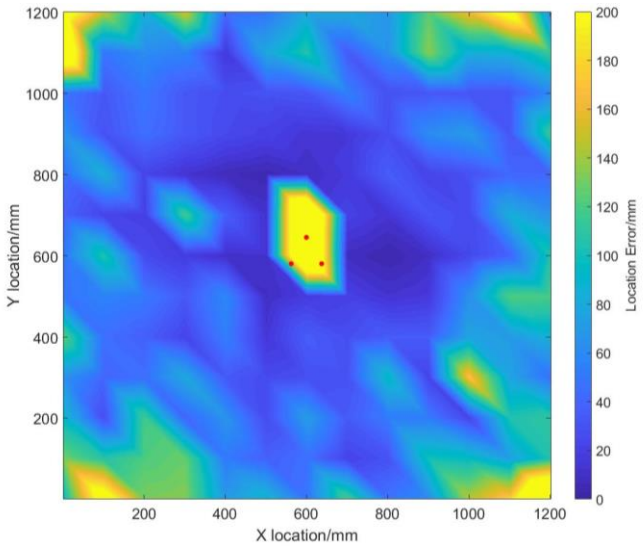

Figure 111 – Results for H-N test using the Mk 2 sensor on Aluminium panel with no stiffeners

Table 19 shows the errors and percentage accuracy of results from this data compared with the data from the Mk 1 node test. Most of the error that occurs in this test is a result of inaccuracy in the angle prediction at the edges of the plate. The number of highly inaccurate locations were similar with both nodes, with almost the same percentage of data being within 200mm accuracy, however the Mk 2 node has more data within 100mm and 50mm accuracy.

Table 19 – Error and accuracy data from simple Aluminium panel testing using the Mk 1 and Mk 2 nodes

	Mk 1	Mk 2
Average Angle Error	5.3	3.8
Average Distance Prediction Error (mm)	36.0	26.4
Average Overall Location Error (mm)	79.0	62.0
Percentage of data with less than 50mm error (%)	37.0	62.2
Percentage of data with less than 100mm error (%)	77.4	82.8
Percentage of data with less than 200mm error (%)	93.5	93.0

Once testing was conducted upon the simple aluminium panel stiffeners were bonded/riveted to it to make it complex, this process is described in Section 3.2.4 of this thesis. Throughout this process the sensors were left in place and checked afterwards with a wired AE system to ensure they were still well bonded.

A full test was then performed with the Mk 2 node, a colour map showing the location error at each location is shown in Figure 112.

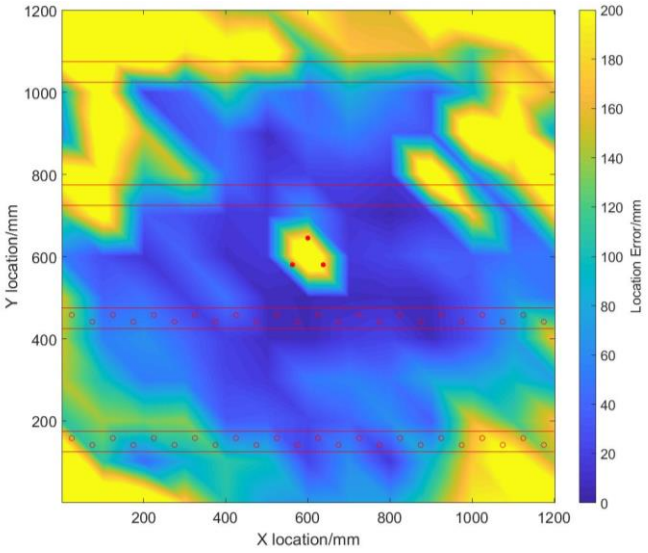

Figure 112 – Overall location error using the Mk 2 node on Aluminium panel with stiffeners to detect H-N sources. Stiffeners, sensors and rivet holes marked in red.

Table 20 shows the average errors and accuracies for the complex test compared to the simple panel results achieved with the Mk 2 node.

Table 20 – Error and accuracy data from simple and complex aluminium panel using the Mk 2 node

	Simple	Complex
Average Angle Error	3.8	7.1
Average Distance Prediction Error (mm)	26.4	44.1
Average Overall Location Error (mm)	62.0	107.3
Percentage of data with less than 50mm error (%)	62.2	39.6
Percentage of data with less than 100mm error (%)	82.8	59.6
Percentage of data with less than 200mm error (%)	93.0	80.2

The results in Table 20 show the addition of complexity has a significant effect on the overall accuracy of the test. This is partially due to a drop in accuracy of the distance calculation but more significantly due to a drop in the accuracy of the angle prediction. This is shown clearly in Figure 113 ((a) & (b)) where colour map plots of both average angle and distance errors are shown.

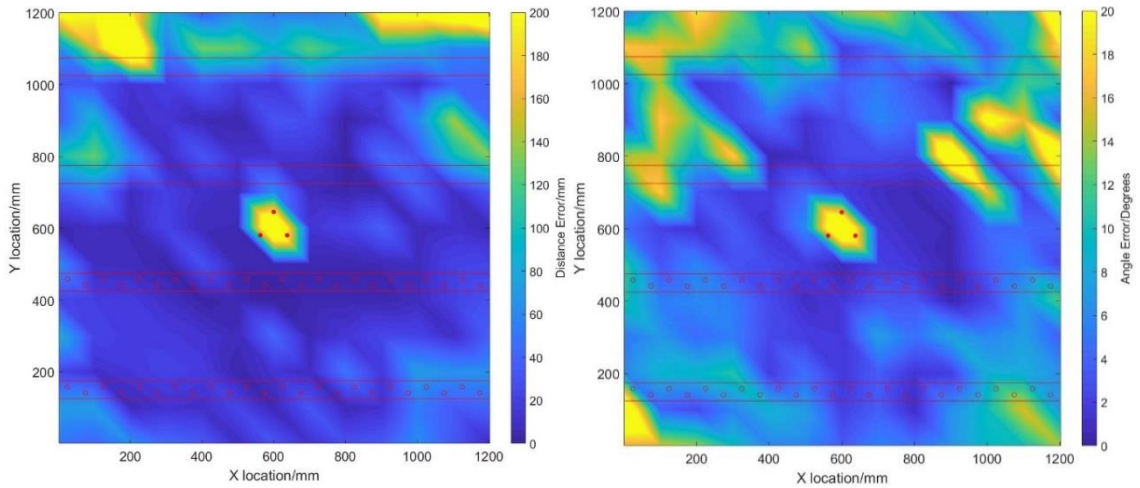

(a) (b)

Figure 113 – Distance prediction error (a) and angle prediction error (b) of the complex aluminium panel test using the Mk 2 node

A test was also conducted upon composite panel A with the Mk 2 node. The average error at each location are plotted on a colour map in Figure 114. A single location (x=300mm and y=900mm) gave a high error which was caused by an error in the angle prediction.

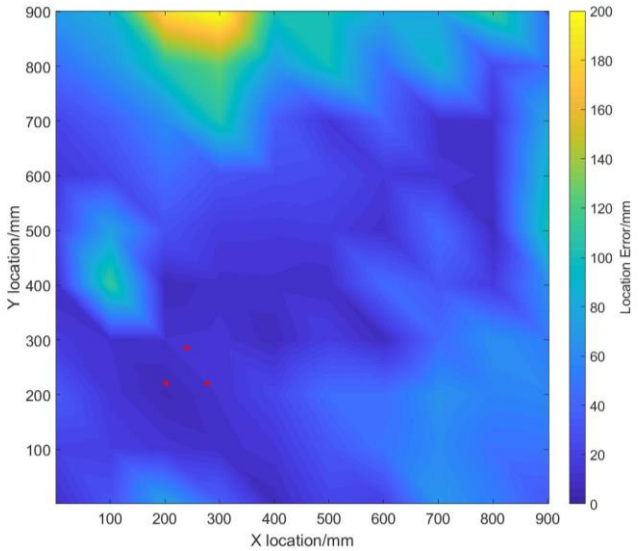

Figure 114 – Overall location error using the Mk 2 sensor on composite panel A to detect H-N sources

Table 21 shows the average errors and accuracies for the test using the Mk 2 node as well as those achieved with the Mk 1 node. A very large improvement can be seen between the results.

Table 21 – Error and accuracy data from composite panel A testing using the Mk 1 and Mk 2 nodes

	Mk 1	Mk 2
Average Angle Error	9.9	3.1
Average Distance Prediction Error (mm)	93.0	18.2
Average Overall Location Error (mm)	116.9	44.5
Percentage of data with less than 50mm error (%)	45.4	69.0
Percentage of data with less than 100mm error (%)	63.4	90.4
Percentage of data with less than 200mm error (%)	72.8	98.6

A test was also conducted on composite panel B with the Mk 2 node prior to the addition of any stiffeners, the average error at each location is shown in Figure 115.

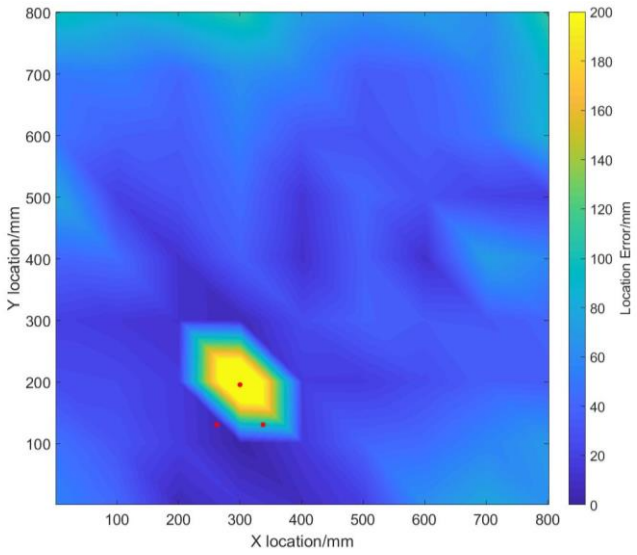

Figure 115 – Results for H-N test using the Mk 2 sensor on composite panel B with no stiffeners

Table 22 shows a summary of the accuracies and errors of the predicted locations using the Mk 2 node compared to the Mk 1 node, where a large improvement can be seen.

Table 22 – Error and accuracy data from composite panel B testing using the Mk 1 and Mk 2 nodes

	Mk 1	Mk 2
Average Angle Error	15.0	3.5
Average Distance Prediction Error (mm)	121.8	21.9
Average Overall Location Error (mm)	144.8	45.5
Percentage of data with less than 50mm error (%)	38.3	69.9
Percentage of data with less than 100mm error (%)	56.5	93.1
Percentage of data with less than 200mm error (%)	62.7	98.8

Once testing had been conducted on the simple composite panel B, stiffeners were bonded to add complexity, this process is described in more detail in Section 3.2.2. These were bonded one at a time and between each stiffener being added another test was conducted.

It was apparent after the addition of the first stiffener that by increasing the A_0 gain better accuracy could be achieved. Figure 116 (a) shows a colour map of the errors with the original settings and Figure 116 (b) shows those with increased A_0 gain. This increased gain was kept from the remainder of testing on the panel. In both cases some locations far from the sensors were still not possible to predict, this is because the A_0 wave was too low to trigger the threshold, meaning no angle prediction could be made.

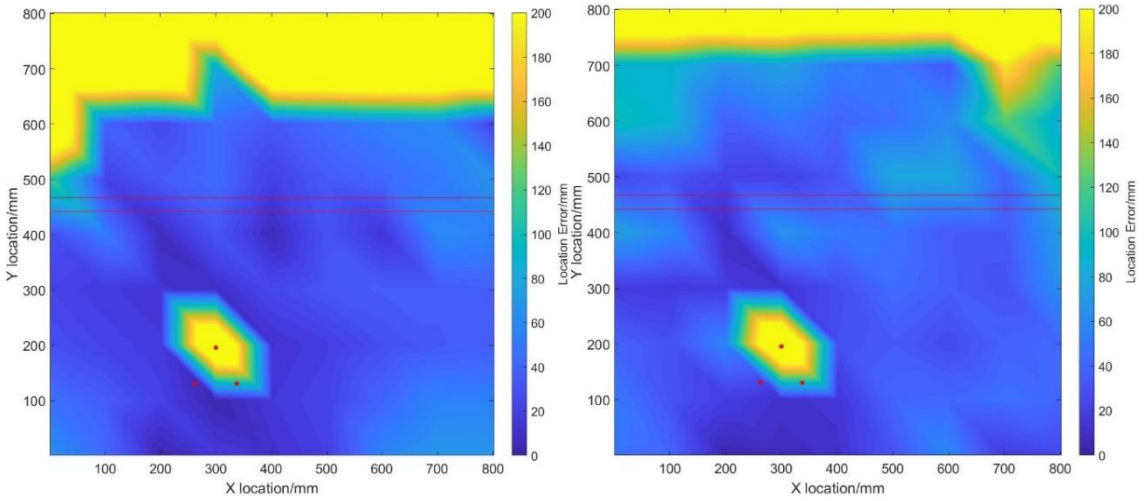

(a) (b)

Figure 116 – Results for H-N test using the Mk 2 sensor on composite panel B with one stiffener with original A_0 gain settings (a) and increased A_0 gain settings (b)

Figure 117 and Figure 118 shown colour maps of the errors on composite panel B with two and three stiffeners.

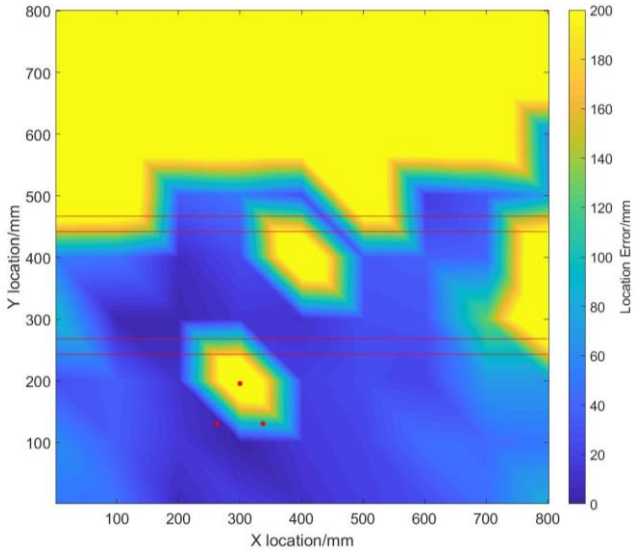

Figure 117 – Results for H-N test using the Mk 2 sensor on composite panel B with two stiffeners

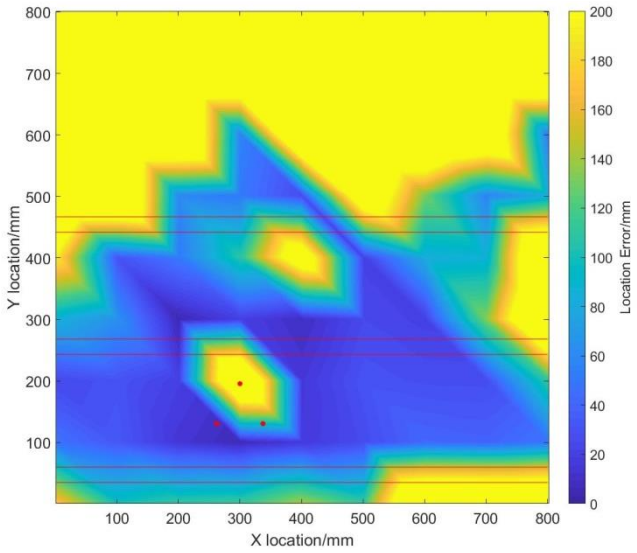

Figure 118 – Results for H-N test using the Mk 2 sensor on composite panel B with three stiffeners

Table 23 shows the summary of errors in each of the testing stages. With the addition of each stiffener the number of points where a location couldn't be predicted increased. This was due

to the attenuation of the A_0 causing no trigger. The addition of the 4th, and final, stiffener had no effect on the results.

Table 23 – Error and accuracy data from composite panel B with and without stiffeners testing using the Mk 2 node

Number of Stiffeners	0	1	2	3
Average Angle Error	3.5	7.3	14.0	16.8
Average Distance Prediction Error (mm)	21.9	52.2	122.2	131.1
Average Overall Location Error (mm)	45.5	78.6	142.6	161.8
Percentage of data with less than 50mm error (%)	70	58	48	36
Percentage of data with less than 100mm error (%)	93	81	58	45
Percentage of data with less than 200mm error (%)	99	86	60	55

Preliminary testing was conducted with the Mk 2 node on real composite and aluminium aircraft structures. The complexity of these structures caused significant S_0 to A_0 mode conversion, this makes accurately predicting the arrival of the A_0 mode at each sensor very difficult. Figure 119 shows the output of the S_0 and $A_0$1 filters when recording a H-N source which has travelled across two stiffeners on an A350 wing. In this example a lot of the S_0 mode has converted to a low frequency A_0 mode making an accurate arrival time based on a fixed trigger very difficult.

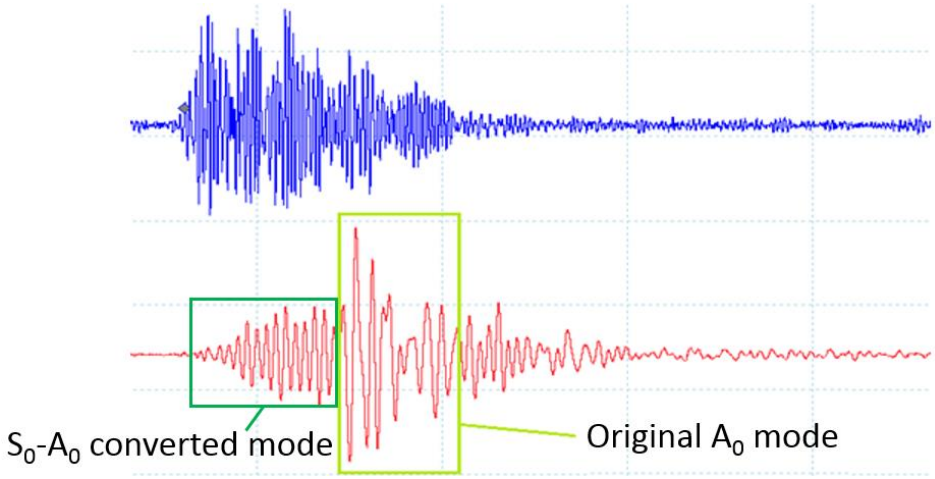

Figure 119 – Scoped waveforms from wireless system, $A_0$1 in red, S_0 in blue

5.7.4 Mk 2 Discussion

The Mk 2 node proved to be significantly better than the Mk 1 node when testing on simple structures. The Mk 1 node was unable to locate H-N sources at a large number of locations on the two composite panels and on the aluminium panel had high inaccuracies in the corners. The Mk 2 node on the other hand was able to locate sources over the entirety of the composite plates, other than in the dead zones close to the sensors, with very good accuracy in the majority of locations. On the aluminium panel the overall accuracy was increased significantly, however the errors still existed in the corners of the plate. This is partially due to the additional range at these points and also a result of reflections at the edge causing issues with the location prediction.

The accuracy of the Mk 2 node was tested on complex structures, where accuracy was seen to drop significantly because of wave attenuation caused by the complexity. On the complex aluminium panel accuracy was good up to a radius of 600 mm when interacting with riveted stiffeners and 400-500mm when interacting with bonded stiffeners. It can be seen that after interacting with a single stiffener, accuracy was still good, however after the second it significantly dropped. It was seen that the bonded stiffeners reduced the accuracy more than the riveted ones. The effect of complexity on the systems accuracy on composite panel B was similar, with one stiffener decreasing the range of the system and two making it impossible to reliably locate further than the location of the second stiffener. When scaling up to real structures, the accuracy was very poor and only a very small range was possible. The inaccurate source location beyond this was a result of attenuation and mode conversion making a precise prediction of the A_0 mode very difficult using a threshold prediction method.

One option to increase the range of the system would be to tailor the front end filters for the structure being tested by scoping the structure beforehand and designing the filters to match this. Doing so would allow more amplification and so a better detection of the S_0 and A_0 modes. To implement this would require a full scoping of a structure prior to the design of the system,

and different nodes for each location. This would dramatically raise the cost of applying such a system, and so is infeasible unless applied on a very large scale. It also doesn't eliminate the issues caused by mode conversion, however applying the A_0 detection techniques presented in Chapter 4 may improve this. Another option would be to make the change from using A_0 to S_0 to predict the angle of arrival.

5.8 Mk 3

In the final months of the SENTIENT project it became clear from testing presented in the previous section that the Mk 2 node was ineffective at locating AE on a real, complex aircraft structures except within a small range. This was due to both heavily attenuated signals and S_0 to A_0 mode conversion meaning that the threshold based triggering of the A_0 channels was inaccurately detecting the arrival of the A_0 mode. This led to both inaccurate angle and distance calculations. At this point in the project the A_0 detection methods presented in Chapter 4 had not yet been developed meaning that this was not an option, instead the decision was made to use the S_0 mode arrival to predict the angle of arrival in a Mk 3 node.

The Mk 3 node consists of the same initial hardware as the Mk 2 node, however it has undergone major retrofitting to significantly alter its architecture. The modified sensor is far from perfect due to noise and other problems that arose as a result of the required modifications however the changes gave the potential to significantly increase the overall location accuracy and range in complex structures. Power requirements are also greater than they would have been had the sensor been designed with this architecture, a dedicated redesign and manufacture would give better results.

5.8.1 System Overview

All previous versions of the wireless sensor nodes used the A_0 mode arrival times at the three sensors to calculate the angle of arrival. As accurately detecting the arrival of the A_0 mode became difficult in complex structures, the Mk 3 node uses the S_0 mode to do this. Earlier testing (Section 4.3.2) showed that this technique was ineffective at locating AE in an anisotropic

composite, however is perfectly adequate in quazisotropic composites and in complex aluminium structures. The Mk 2 nodes A_0 gain stages and filters were therefore exchanged for similar ones to those used for the original S_0 channel.

Calculating the distance was no longer possible using a threshold technique as testing on real aircraft structures had shown the attenuation of the signal was too great when at distance from the sensor. At the time the modification was made the second differential technique had not yet been developed so was not an option. Instead the author of this thesis proposed using the rise time (see Section 5.3) to give an approximation of the distance travelled by the wave, this was a quick solution to implement as the parameter extraction was already able to predict this. The approach adopted works on the assumption that the original A_0 mode is greater in amplitude than any S_0 to A_0 mode conversion, and therefore the maximum point within a filtered waveform is within the original A_0 group. This was tested on the A350 wing using the Mk 2 node prior to the Mk3 modifications and showed positive results. To achieve this the Mk 2 node's S_0 channel's gain stages and filters were modified to a 100 kHz filter BPF and suitable gain stage. This over-complication was required to keep the difference between the three S_0 channels on the Mk 3 node to a minimum.

The final analogue front-end architecture for the Mk 3 node is shown in Figure 120. Any of the three S_0 triggers will initiate the internal clock and the ADC on the A_0 channel, saving that channel's arrival time as zero. As each of the other channels is triggered, the value on the clock is saved giving a time relative to the first hit sensor. The events angle of arrival can then be calculated from these 3 values. The parameter extraction algorithm extracts the rise time from the digitalised 100 kHz BPF waveform from channel 1 which gives an approximation of distance.

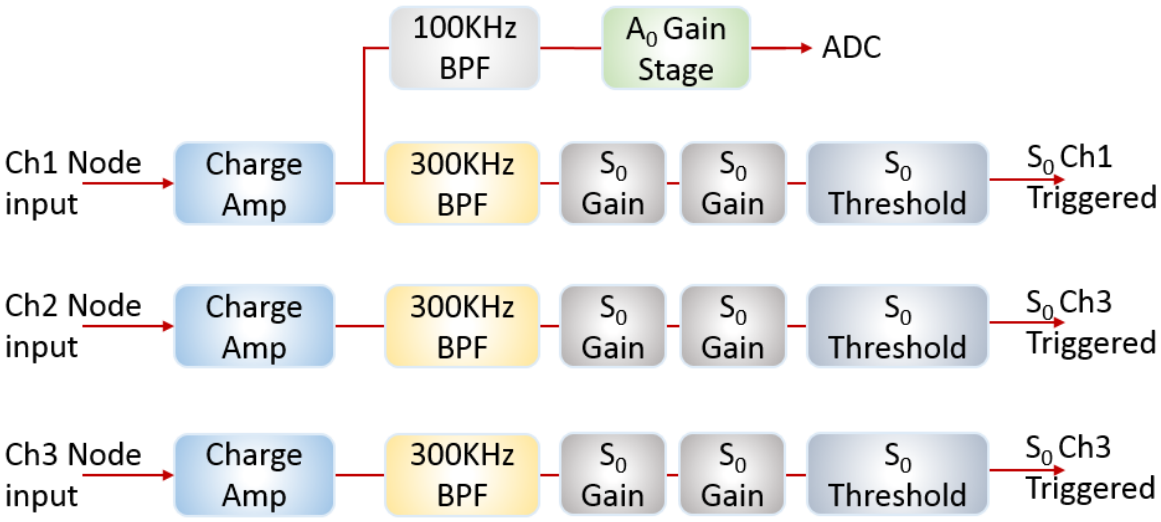

Figure 120 – Analogy front end Architecture for Mk 3 Sensor

5.8.2 Preliminary Testing

Initial testing with the Mk 3 node revealed a problem with the S_0 channels. In the Mk 2 node all channels had a regular centre voltage of 1250mV however in the Mk 3 node a small DC offset (shown in Figure 121) was present in each of the channels. This is believed to be produced during the gain stage, and is likely a result of the retrofit to the Mk 2 node causing unforeseen problems. The amount of offset was not regular between channels and worsened as gain was increased, meaning that in complex specimens where high amplification was required this offset was unavoidable. A small modification was made in order to reduce the effect of this which combatted the fact that all channels were seen to drop in voltage, albeit by varying amounts. In the Mk 2 node a single threshold was set for each channel, meaning that if a 1500mV threshold was set, a lower 1000mV was also applied. This meant that if the voltage went outside of this the system was triggered. The modification to the Mk 3 node allowed these thresholds to be set independently, so accounting for the general lowering of voltage. Unfortunately, it was not possible to have different thresholds on each channel, and this problem is likely to be the reason for some angle prediction inaccuracy within the testing presented. A full redesign of the hardware with the Mk 3 modification would remove this issue.

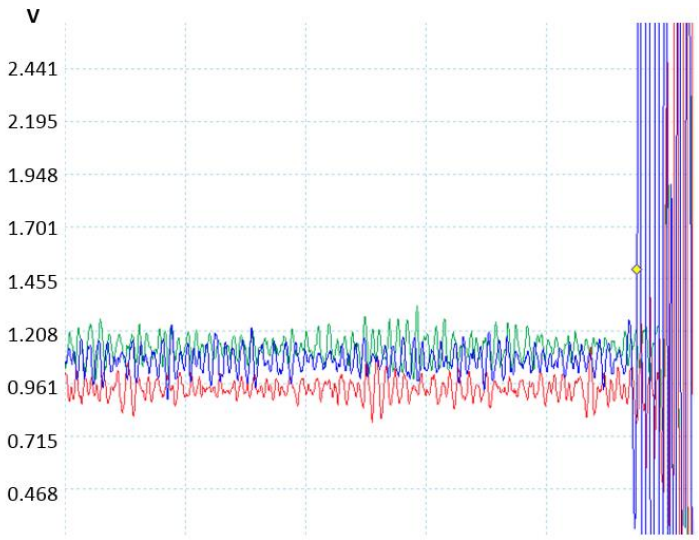

Figure 121 – DC offset between S_0 signals on channel 1 (blue), channel 2 (red) and channel 3 (green)

Once the node had been modified the new approach and distance prediction was tested, firstly on composite panel B. To do this the sensors bonded to the complex panel were plugged in to the Mk 3 node and five H-N sources created at 0°, 45° and 90° from the sensors at regular intervals, where 90° is parallel to the stiffeners. The outputted rise time for each was recorded and averaged for each location, the results of which can be seen in Figure 122.

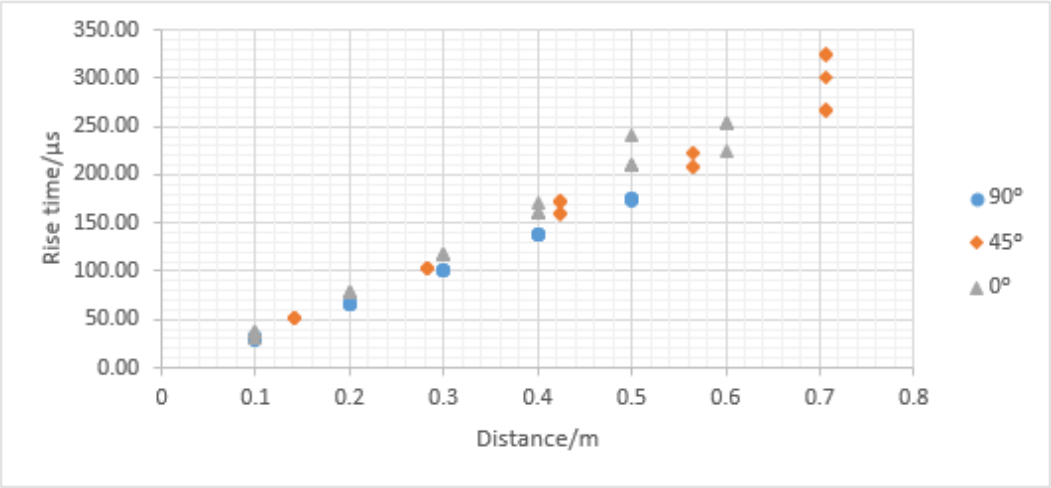

Figure 122 – Mk 3 distance prediction on composite panel B

The testing showed positive results with a clear linear relationship between rise time and distance for the Mk 3 system. The difference in results dependent on direction will cause some minor error in any tests using this method. If more accurate results are required this can be removed by altering the distance correction factor dependent on the angle of arrival based on calibration testing results, however the additional calibration time makes this infeasible for large scale application.

Once access was available to the A350 wing at Airbus Broughton a distance prediction test using the rise times was performed on it to ensure that this approach was suitable. The results from this test can be seen in Figure 123, where 90° is parallel to the stiffeners.

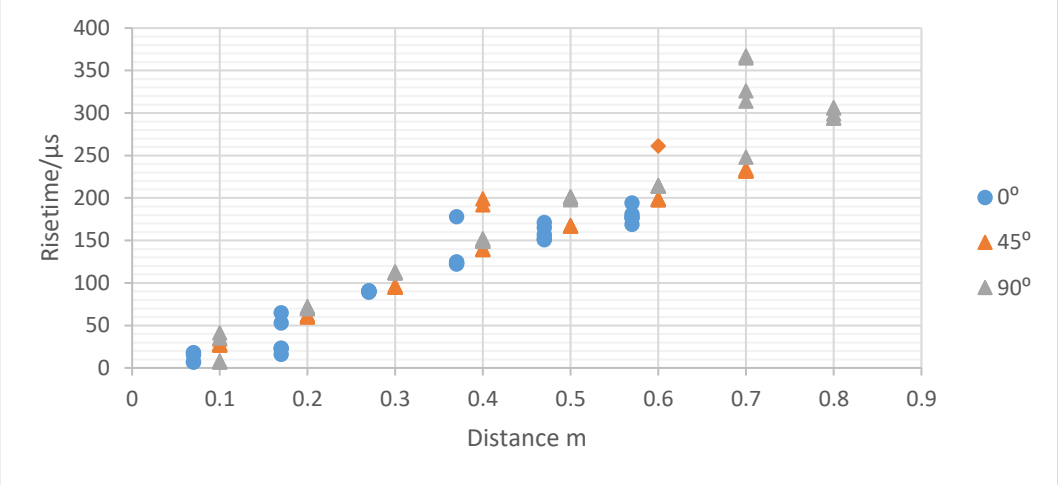

Figure 123 - Mk 3 distance prediction on A350 wing

When ignoring the angle and only considering the distance the R^2 value for all the A350 data was 0.925, for the composite panel this was 0.968. The results of this test are significantly less linear than for composite panel B, however a good relationship can still be seen. Some error in the distance prediction was expected in the full test on the structure but it still performed with greater accuracy than could be achieved in the Mk 2 node using a threshold crossing approach to predict the arrival of the A_0 mode.

5.8.3 Power Consumption

As for the Mk 1 and Mk 2 nodes the Mk 3 node's power requirements were analysed using a Silicon Labs 'EFM32 Wonder Gecko' development board. The results, as well as those recorded with the Mk 1 and Mk 2 nodes, are shown in Table 24. These were expected to be significantly higher than the Mk 2 node as the modifications were performed without consideration of the power requirements. If a full redesign of the hardware was performed, the power would be expected to be similar to the Mk 2 node as hardware would be selected based on the significantly better requirements, not retrofitted as they were for Mk 3 which increase power requirements.

Table 24 – Power consumption of Mk 1, Mk 2 and Mk 3 nodes in a variety of modes/performing certain tasks

		Sleep	Wait for event	RF Window	Event and send
Mk 1	Time (ms)	-	-	103	181
	Average power (mW)	0.33	17.44	43.4	38.4
	Max power (mW)	-	-	82.3	83.3
	Total energy (mJ)	-	-	4.5	7.0
Mk 2	Time (ms)	-	-	103	192
	Average power (mW)	0.12	16.4	43.4	37.6
	Max power (mW)	-	-	82.3	95
	Total energy (mJ)	-	-	4.5	7.2
Mk 3	Time (ms)	-	-	103	143
	Average power (mW)	0.39	22.7	43.4	47
	Max power (mW)	-	-	82.3	102.1
	Total energy (mJ)	-	-	4.5	6.7

5.8.4 Structural Testing

Once the preliminary testing and initial checks were completed with the Mk 3 node, full testing was performed on the panels tested previously, as well as on real aircraft structures. The first specimen tested was composite panel B, which had 4 stiffeners bonded to it. A colour map plot of the errors from this test is shown in Figure 124.

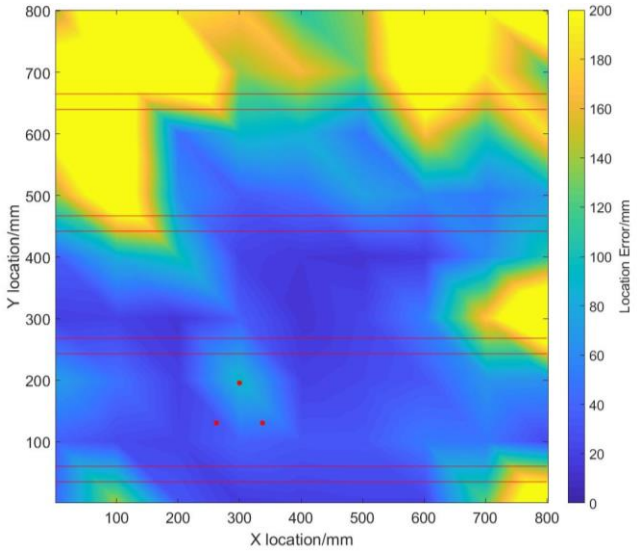

Figure 124 – Results for H-N test using the Mk 3 node on composite panel B with four stiffeners

The average errors and accuracies for this test compared to those predicted from the test with the Mk 2 node are shown in Table 25.

Table 25 – Errors and accuracy of Mk 2 and Mk 3 nodes testing on composite panel B

	Mk 2	Mk 3
Average Angle Error	16.8	4.7
Average Distance Prediction Error (mm)	131.1	68.7
Average Overall Location Error (mm)	161.8	101.4
Percentage of data with less than 50mm error (%)	36.3	45.9
Percentage of data with less than 100mm error (%)	45.4	65.2
Percentage of data with less than 200mm error (%)	55.3	79.3

The results from this test showed very little error in the angle calculation, indicating that the error present at certain locations is a result of errors in the distance prediction. This is reinforced by the individual average error and average distance error colour map plots in Figure 125, where very little angle prediction error can be seen anywhere on the plate, other than very close to the sensors.

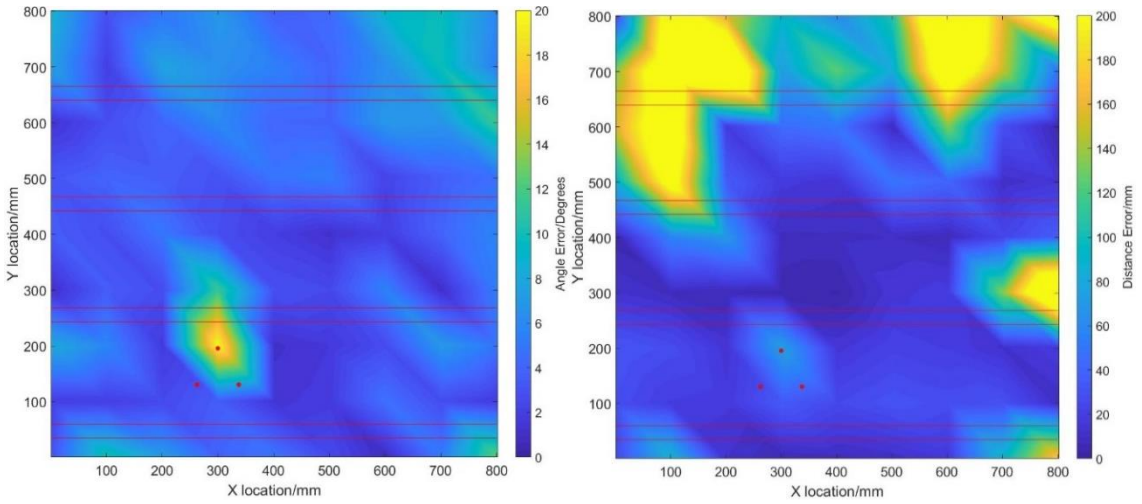

(a) (b)

Figure 125 – Angle (a) and distance (b) prediction error from H-N test using the Mk 3 node on composite panel B with four stiffeners

The Mk 3 node was used to predict the locations of H-N sources on the complex aluminium panel. Figure 126 shows a colour map of the location errors at each point across the panel.

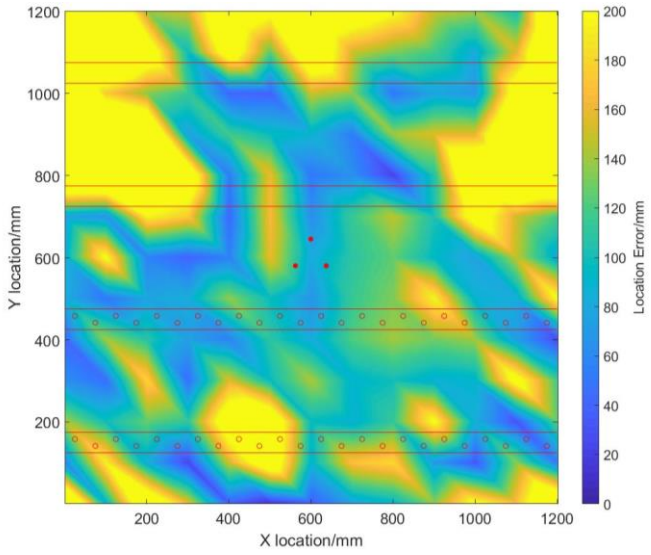

Figure 126 - Results for H-N test using the Mk 3 node on Complex aluminium panel, with stiffeners, holes and sensors marked in red.

Figure 126 clearly shows that the Mk 3 node has not accurately predicted the H-N source locations for the majority of locations. The error and accuracy data, shown in Table 26, shows that this error is due to the distance prediction which increased from 44.1mm with the Mk 2

node to 116.6mm with the Mk 3 node. This is a result of the A_0 gain stage being too high, even in its lowest setting resulting in the prediction maxing out for the majority of locations, making an accurate prediction impossible. Modifying the Mk 3 node to trigger the A_0 mode off a threshold would be a simple solution to this, and would be possible while processing the ADC output meaning no hardware modification would be required. Unfortunately, this was not possible due to the time scale of the SENTIENT project however post processing the Mk 3 predicted angles with the Mk 2 distances gave a good indication of how the system would perform if a threshold method was used in a wireless system with S_0 angle prediction. The error and accuracy results from this are shown in Table 26 and a colour map of the location errors is shown in Figure 127.

Table 26 – Error and accuracy data from Complex aluminium panel test with the Mk 2 node, Mk 3 node and the angle predictions from the Mk 3 node combined with the distance predictions of the Mk 2

	Mk 2	Mk 3	Mk 3 with Mk 2 distances
Average Angle Error	7.1	4.9	4.9
Average Distance Prediction Error (mm)	44.1	116.6	44.1
Average Overall Location Error (mm)	107.3	141.5	83.0
Percentage of data with less than 50mm error (%)	39.6	22.2	50.8
Percentage of data with less than 100mm error (%)	59.6	49.7	71.5
Percentage of data with less than 200mm error (%)	80.2	70.1	87.9

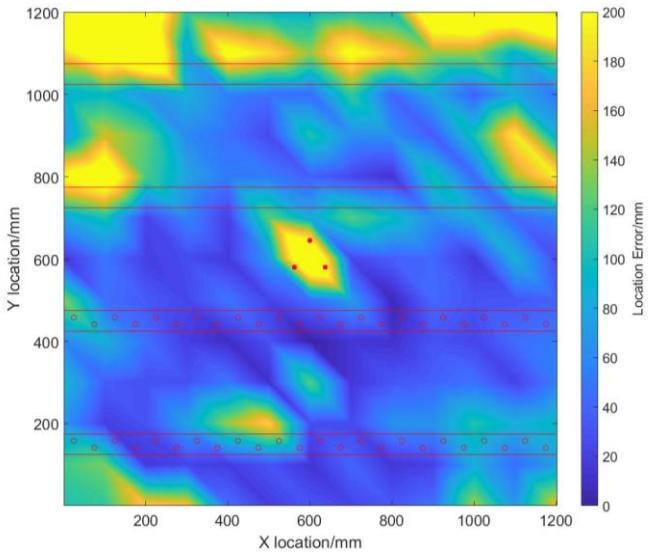

Figure 127 - Results for H-N test on Complex aluminium panel using the angles predicted with the Mk 3 node and distances from the Mk 2 node.

To confirm the modifications to the system, as it was no longer suitable for anisotropic layup composites, a test was performed with the Mk 3 node on composite panel A. As was expected with the change to using the S_0 mode to predict the angle, the testing of the Mk 3 node on composite panel A led to very poor angle prediction. The test showed that less than 50% of data was predicted to within 200mm accuracy. Figure 128 shows a colour map of the location errors across the plate.

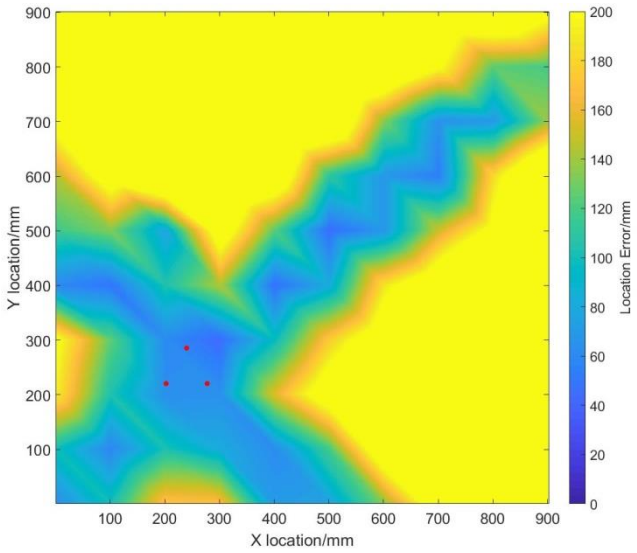

Figure 128 – Overall location error using the Mk 3 sensor on composite panel A to detect H-N sources

After the development of the Mk 3 node it became possible to get significantly better results on real aircraft structures. For the next test, a 700 x 1400 mm grid was drawn on the A320 aircraft wing covering an area with two ribs and 5 stringers. Every location was detected by the node, however errors were very high for a large number of locations. A colour map of the location errors from the test on the wing can be seen in Figure 129, within this plot the scale is set to a maximum of 300mm as a number of locations were able to be located with an accuracy of between 200mm - 300mm and although this is far from accurate, it is much better than the system not locating the events. Outside of a radius of approximately 300 mm location errors were significantly higher, angle and distance prediction error colour maps are shown in Figure 130 and Figure 131.

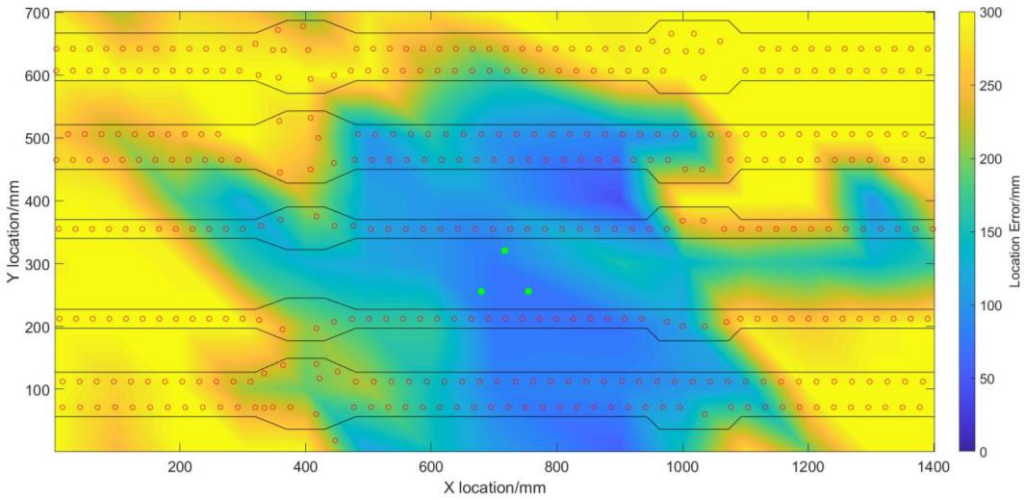

Figure 129 – Average location errors for H-N test using the Mk 3 node on A320 wing, with stiffeners marked in black and holes in red, sensors shown as green. Note scale is a max of 300mm.

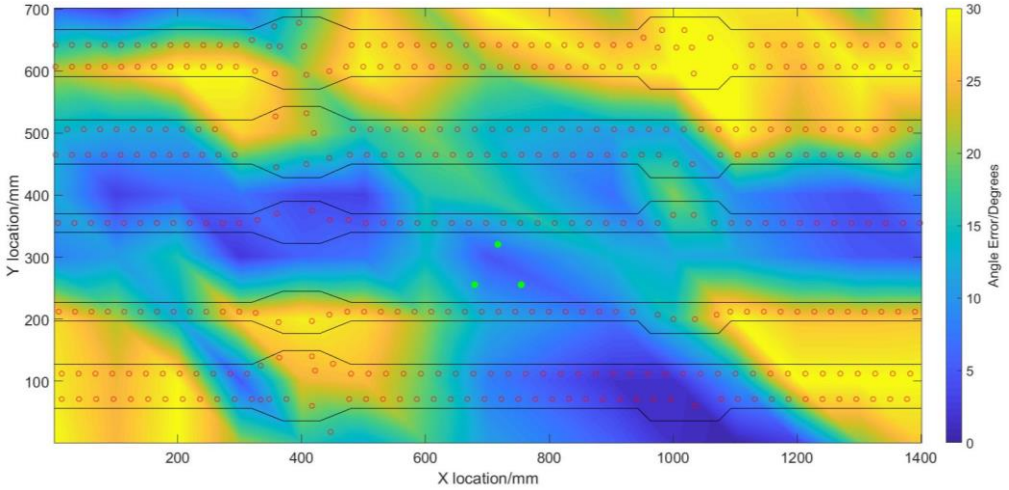

Figure 130 –Average angle error for H-N test using the Mk 3 node on A320 wing

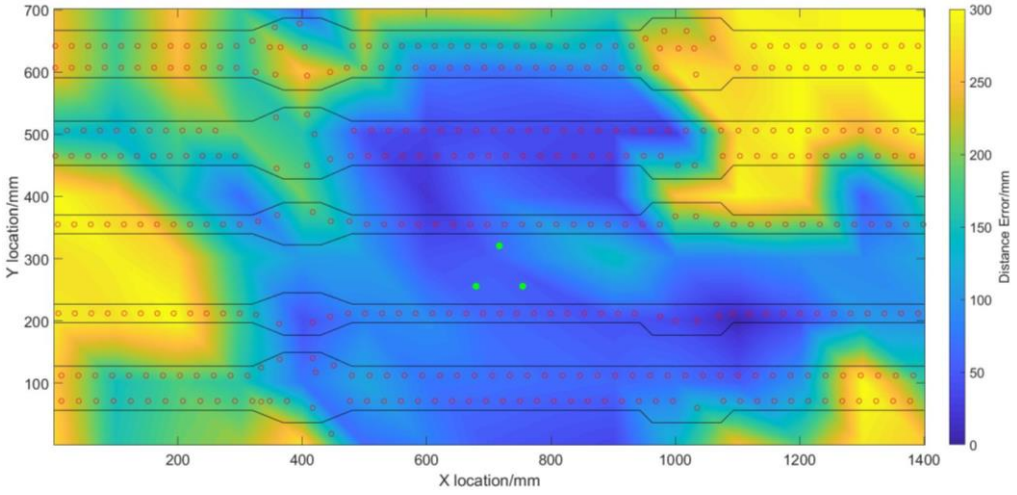

Figure 131 – Average distance error for H-N test using the Mk 3 node on A320 wing

The Mk 3 node was also tested on the composite A350 wing. For this test a 0.9 x 0.9m grid was drawn on the wing with test locations every 0.1m. In this test all but two locations ((0.8, 0.9) and (0.9, 0.9)) were detected by the node. A colour map of the average location errors from the test are shown in Figure 132. As in the A320 test the scale is set to a maximum of 300mm as a number of locations were located with an accuracy of between 200mm - 300mm.

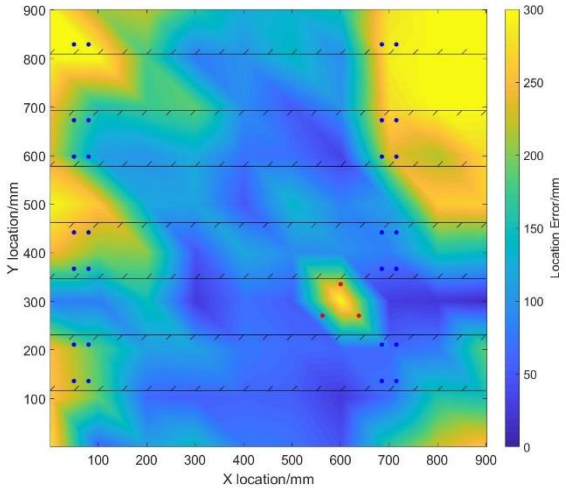

Figure 132 – Location error test using the Mk 3 node on A350 wing, with stiffeners marked in black and holes in blue

Colour plots which consider only the average distance and angle errors are shown in Figure 133 where very little error can be seen within the distance prediction at all but a few locations on the plate.

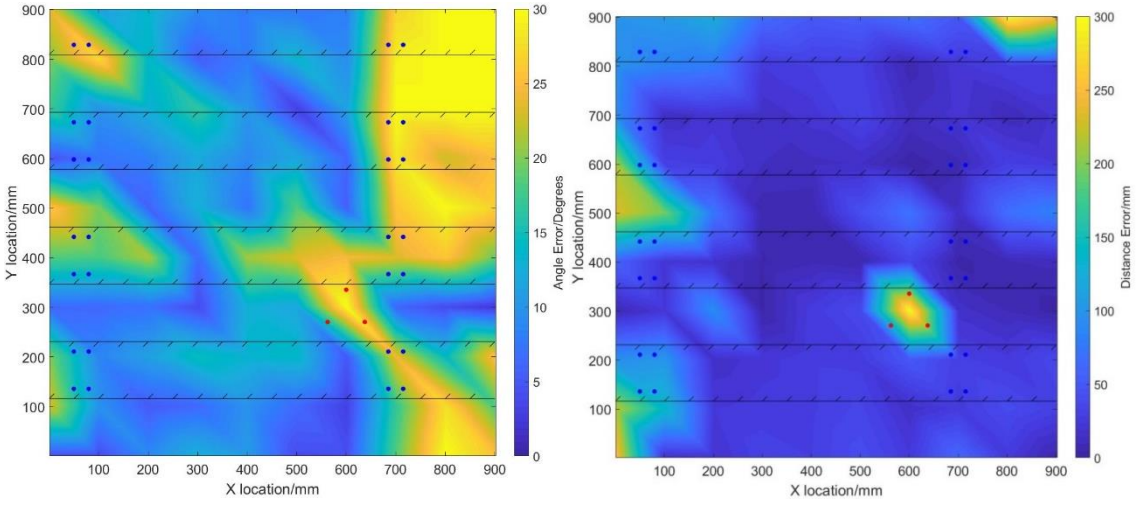

(a) (b)

Figure 133 – Angle (a) and distance (b) prediction error test using the Mk 3 node on A350 wing, with stiffeners marked in black and holes in blue

5.8.5 Mk 3 Discussion

Testing with the Mk 3 node showed great improvements in locating H-N sources in complex structures when compared to the results of the Mk 2 node, where the Mk 2 node was unable to predict a location at any distance in these structures due to significant attenuation of the A_0 mode combined with S_0 to A_0 mode conversion making accurate arrival predication impossible.

The change to using the S_0 mode removed the need for a highly accurate A_0 arrival time in order to locate the source. The S_0 mode was significantly easier to predict, as although attenuation of the signal did occur, mode conversion was not a problem so a precise arrival was found. This improved the angle prediction accuracy from 16.8^o to 4.7^o in the complex composite panel B and 7.1^o to 4.9^o in the complex aluminium panel. For the majority of locations in these tests the angle has been accurately predicted, however in some select locations the error is very high. This is as a result of the DC offset problem causing certain channels to trigger late. Testing on the composite panel confirmed that the Mk 3 node was unable to predict the angle of arrival in anisotropic composite structures.

Using the maximum A_0 to predict the distance gave mixed results. In both the composite panels the average distance location was very good, with every location's distance being accurately predicted. Composite panel A showed a drop in average distance prediction accuracy from 18.2mm to 33.8mm, however 33.8mm is still very good. Complex composite panel B however showed a decrease in error from 131.1mm to 68.7mm, primarily due to the number of failed locations when using the Mk 2 node. The results from the complex aluminium plate testing showed the distance prediction was completely ineffective with the Mk 3 node because the minimum possible A_0 gain was too high. Allowing the gain to be reduced further on any later versions of the hardware should allow the distance to be predicted to a suitable level of accuracy using the maximum A_0 time. Overall this approach to predicting the distance to a source was less accurate than a threshold approach when considering simple structures, however with the addition of complexity it became much more reliable. This improvement is primarily because of

the inability to correctly predict the arrival using a threshold method in complex structures. Integration of the second differential method presented in Chapter 4 to the wireless node would have been likely to increase the accuracy of the distance prediction, however it would also increase the processing requirements of the node. Depending on the required accuracy this may or may not be required.

When tested on real aircraft structures the technique proved significantly more effective than the Mk 2 node, which only worked effectively very close to the sensors. The results for the A350 test showed that the distance prediction technique was very effective for the majority of tested locations. Angle prediction was less accurate, and the presence of holes appeared to negatively affect the accuracy of the angle prediction. Without holes interrupting the wave path accurate results were obtained within a range of around 500mm. With better positioning of the sensors on the structure, for example in the centre of the bays between holes reliable coverage of this region could be achieved.

In the A320 wing, sources within a radius of approximately 300mm could be accurately located with the system, this is expected as the A320 wing is significantly more complex than the A350 wing as the stiffeners are riveted, meaning significantly more holes are present which were seen to disrupt the wave propagation. Both distance and angle were inaccurate above a 300mm radius, however not in all directions. This non-linearity in range is due both to the irregular complexity of the structure and the exact location of the H-N source. If the source is directly behind a hole location prediction is typically worse than if it is away from one. This inability to predict the angle of arrival of a wave that has interacted with a lot of complexity is primarily due to the DC offset problem causing each channel to be triggered at significantly different times as they effectively had different thresholds, and this was much more of a problem on heavily attenuated signals. If the DC offset problem was removed it can therefore be expected that the accurate range of the system would be increased. Utilising the second differential method for

A_0 mode detection also has the potential to increase the accuracy of the distance approximation, however the increased power requirements of this method would need to be considered.

5.9 Discussion and Conclusions

At each stage of testing the three versions of the SENTIENT hardware significant improvements have been made in the ability to locate artificial sources in plate-like structures. The Mk 1 and Mk 2 nodes were very similar in function, but improvements to the later design meant that the accuracy in locating sources in simple structures was significantly improved. The addition of complexity dramatically reduced the overall location accuracy of the Mk 2 system, as accurate prediction of the A_0 mode became difficult. This aligns with the findings within Chapter 4 of this thesis. The Mk 3 node is very different to the previous versions of hardware and by using the S_0 mode to predict the angle of arrival was much more effective in complex structures, which led to an overall improvement in location accuracy. Using this node gave a confident prediction range of between 300mm and 500mm in real composite and aluminium structures which could be increased further in a full re-design of the hardware to reduce noise and remove DC offset. Outside of this radius events were often detected, however with very high inaccuracy and often to the same position. In this situation damage can still be identified, however a larger NDT inspection would be required to find the exact location. Exact tailoring of filters would also potentially improve range and accuracy, however this would dramatically increase the cost to apply this system on a large scale.

The power consumption of the hardware is much lower than any other wireless systems on the market. The Mk 2 node had the lowest requirements as modifications required for the Mk 3 were not made with power consumption as a priority, in a future redesigned hardware this would be addressed. Whilst waiting for an event the Mk 2 node only required 16.4mW and whilst processing an event only 37.6mW. This is very low when considering a commercial wireless system consumes at least ten times this to operate (MISTRAS, 2013a). Although the power requirements for the system are very low, for the system to operate long term in an

aircraft environment it must be powered by energy harvesting methods. In an open environment 36mW is easily generated through solar harvesting (Yi et al., 2015) however on board an aircraft, where energy sources are limited for example to thermal and vibration this is not necessarily possible. A potential solution may be that the node operates when it has enough power, and sleeps when it does not allowing its energy storage to charge. Although this will mean lots of events are missed, this may not be an issue as fatigue damage grows over time, partial monitoring should reliably detect the location of the damage.

The hardware presented within this chapter has been tested on a wide range of structures however it has not yet been used to detect the growth of real damage. This must be the next stage of testing in any future work to ensure the assumptions made about the performance of the system are correct.

6 Delta-T Mapping for Three Closely Spaced Sensors

The Delta-T mapping method was introduced in Section 2.2.3 of this thesis, where the work of a number of authors who have applied the approach to the standard TOA method of locating AE events, was presented (Baxter et al., 2007, Hensman et al., 2010, Eaton et al., 2012b, Al-Jumaili et al., 2016, Marks, 2016, Pearson et al., 2017). This work showed the benefit of the technique in improving the location accuracy of AE events, with accuracy increasing from 18.9mm using standard TOA to 4.2mm when using Delta-T mapping when locating a crack in a complex structures.

In the work by Aljets, which focused on developing the three closely spaced sensor technique to locate AE in simple structures, a mapping approach was investigated (Aljets, 2011). The findings from this were that the normal method of locating sources with three closely spaced sensors, presented in Chapter 4, had better accuracy and was far simpler to implement as no mapping was required.

Within this chapter a mapping approach using the three closely spaced sensors is presented which integrates the modifications presented in Chapter 4; namely using AIC to detect the onset of the S_0 mode, using the S_0 mode to detect the angle of arrival and the novel second differential method to detect the A_0 mode. Testing is then presented where the technique has been used to locate artificial and real damage in simple and complex structures. This chapter aims to test whether the modifications, which showed improvements to the non-mapping based approach, enable a Delta-T mapping technique to achieve improved accuracy in complex structures.

6.1 Map creation

Traditional Delta-T maps are created based on the difference in arrival time between each pair of sensors, therefore using four sensors would create six maps (1-2, 1-3, 1-4, 2-3, 2-4 & 3-4). The three sensor method creates three maps based on the difference in S_0 arrival between sensors

(1-2, 1-3 and 2-3) with three more maps produced using the difference in arrival of the S_0 and A_0 mode at each sensor, often referred to as the dispersion.

Data for the maps was collected in the same way as data for the testing presented in Chapter 4 (described in Section 4.1.4). This was completed by drawing a regular grid on each structure with points typically 50mm or 100mm apart. Sensors were bonded in a triangle 75mm apart, and can be within the grid and or even sometimes outside of it. Five H-N sources were created at each point in the grid and the resulting waveforms recorded using a Mistras AE system. Each line of the grid was saved within the same file and a time mark was added in between each point to associate the relevant waveforms to each location.

Once collected the data was input into a Matlab code where it is processed into Delta-T maps. A flowchart outlining the important steps of this code is shown in Figure 134 with a full description given below.

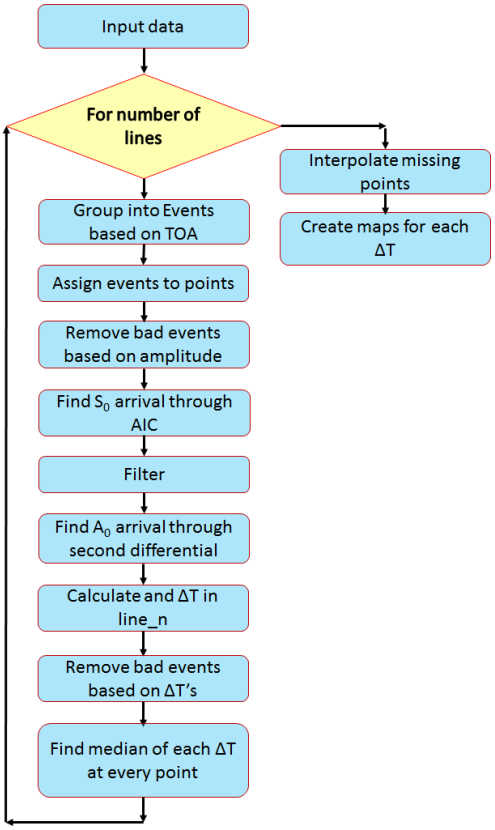

Figure 134 – Flowchart of Delta-T map creation code

Data was brought into the code for processing along with setup information and digital filter requirements which were dependent on the FFT results presented in Chapter 3. As with the testing in the previous chapter, a ±20kHz bandpass filter was used based around the peak A_0 frequency. Hit data is then grouped into events based on time of arrival at each sensor, an event being where all three sensors have triggered off the same waveform which is assumed if their arrival times are within 500µs of each other. This ensures that the waveforms which were produced by the same sources are being processed together. In most cases, as the sensors are close together, the difference in arrival times is much less than 500µs, however in some cases the S_0 mode was missed using the threshold method by one or two of the sensor, meaning their arrival time was much later. The AIC technique corrects for this. The time marks, which are made between events at each location, are then used to assign the events to each point on the grid. The amplitudes of the waveforms at each point are then compared, with any which are 10dB below the others removed as they indicate a 'bad break'. Next, each waveform has its S_0 arrival time re-calculated using the AIC function. The digital waveform filter is then applied to each waveform to remove its S_0 mode and the second differential method used to predict the A_0 arrival time. It is then possible to calculate the six time differences which are used to create the maps for each event, these are again filtered to remove bad events, for example where the A_0 has arrived before the S_0. All the data is then saved with its corresponding location number in an array containing all the data for the line. The filtered data (typically leaving five points) for each point is then analysed and the median value for each time difference exported and stored. This process is repeated for each line.

Once all the data has been exported it is possible to linearly interpolate any values that are missing either because it was not possible to collect data at this location due to an obstruction or possibly that data has been removed due to filtering. Maps are then created from the time difference data, by linearly interpolating between the calculated points, typically at a resolution of 5mm. A set of maps from the simple aluminium panel are shown in Figure 135. In Figure 135

and all other maps presented, sensor 1 is the top sensor, sensor 2 is the bottom right sensor and sensor 3 is the bottom left one.

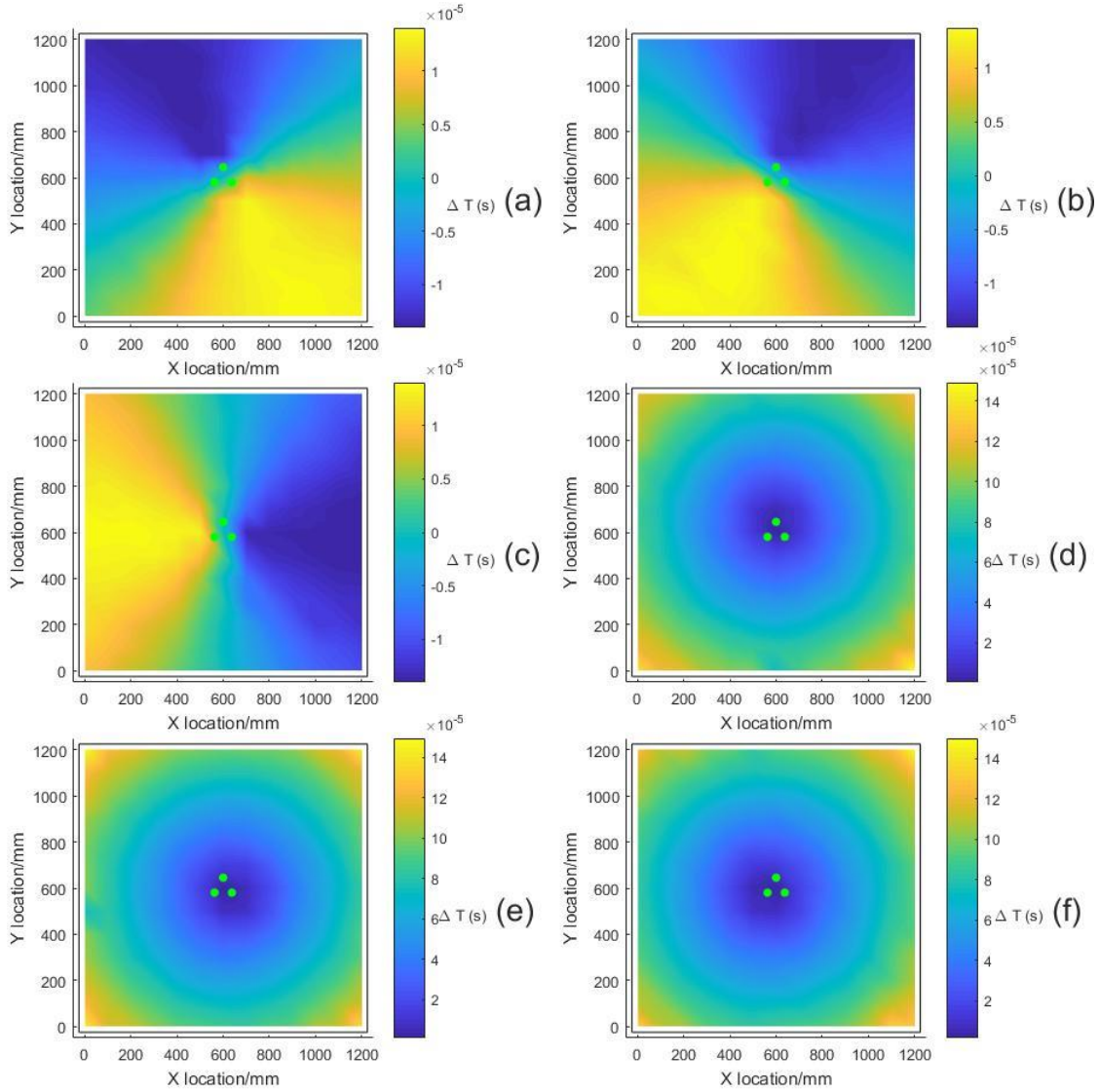

Figure 135 – Delta-T maps from the simple aluminium panel. (a), (b) and (c) show TOA difference between 1-2, 1-3 and 2-3 respectively. (d), (e) and (f) show dispersion at sensors 1, 2 and 3. Sensors shown in green.

6.2 Predicting Source Location with Delta-T Maps

After maps have been created they can be used to locate AE events. In order to test each map, points were selected at random within the mapped area and H-N sources conducted at them. The arrival times were then exported for this data using the same prediction methods and filters as were used to create the maps.

Another Matlab code compares the calculated time differences from the event to the grid in order to find the location of the event. Unlike when using a mapping technique with sensors spaced over the structure, where only TOA differences are used to locate the source, the mapping approach using three closely spaced sensors requires both TOA data and dispersion data to be compared. For this to be done they must be scaled so that they are comparable, as the TOA between sensors is typically tens of μs whereas the dispersion is often hundreds of μs. It does this using Equation 23 which outputs a scaled value for each location on the map allowing the six maps to be directly compared with each other without one map being more influential than another.

$$\text{Scaled error} = \frac{\text{Error at point n}}{\text{Mean error} - \text{Minimum error}} \tag{23}$$

Equation 23 is evaluated for every point on the grid. For each 'Error at point n', the 'mean error' and 'minimum error' are found from every point over the grid. Any points with a scaled error above 1 are given a scaled error of 1. This is so that if one grid is predicting a drastically different result due to an early/late trigger it will not overly affect the final results allowing the remaining five maps to correctly locate the event. The output of this process for each of the six maps when locating a H-N source on the simple aluminium plate is shown in Figure 136. The dark blue locations in each map are where the system has determined the event may have occurred. Plots (a), (b) and (c) give an indication of the direction from the sensors that the event occurred, combining any two of these should give an accurate angle of arrival. Plots (d), (e) and (f) show the predicted distance that the source has travelled, a single map is enough to predict the distance however using multiple maps adds redundancy against one of the distances having been incorrectly predicted.

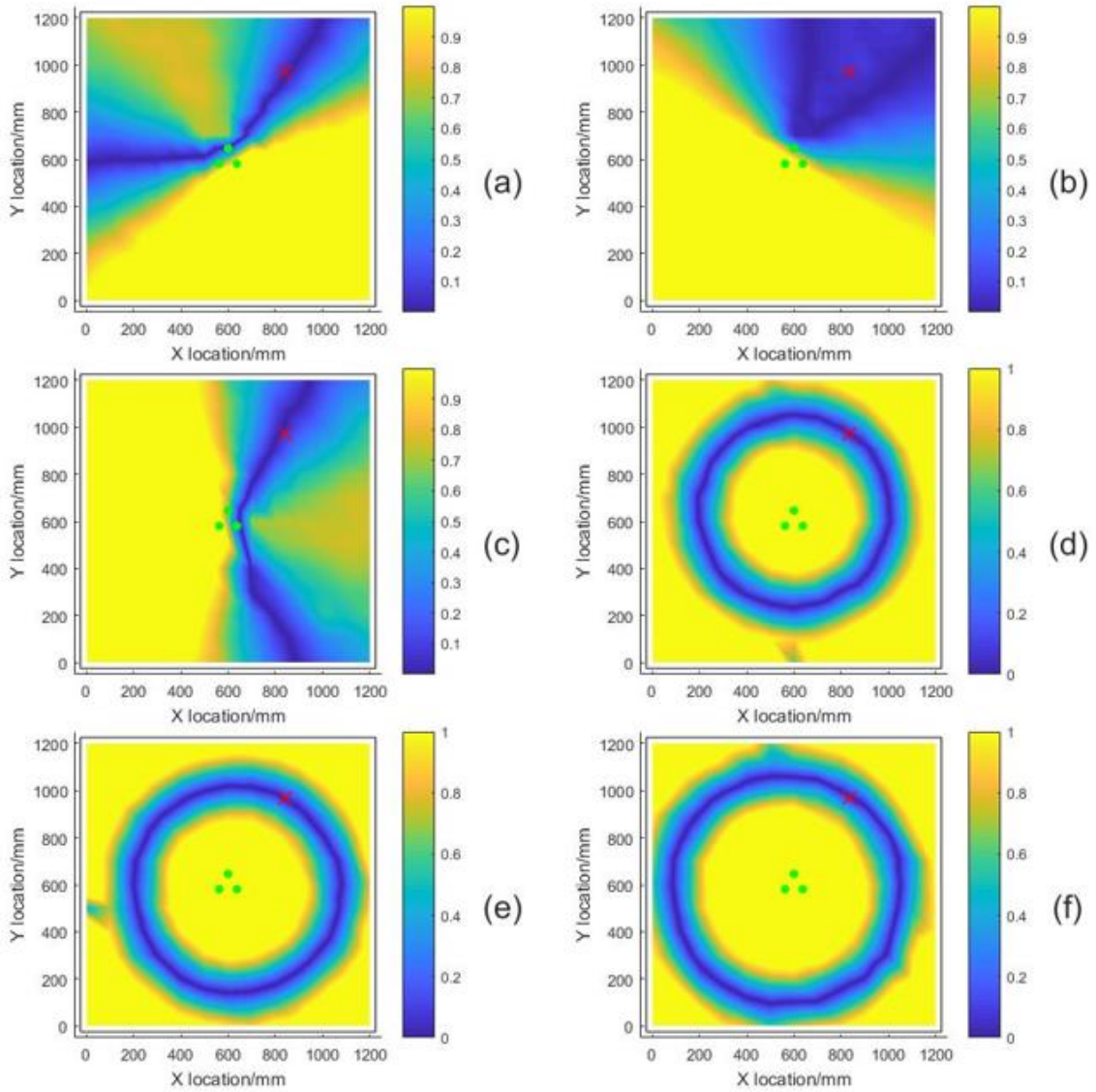

Figure 136 – Scaled error plots for each map. (a), (b) and (c) show errors in TOA difference between 1-2, 1-3 and 2-3. (d), (e) and (f) show errors in dispersion at sensors 1, 2 and 3. Sensors shown in green and predicted location shown as a red cross.

After the error plots for each map have been calculated they are combined in order to find the event location. This is done by simply adding the scaled error at each point from all the maps together, as has been done in Figure 137. The minimum scaled error reveals the predicted location of the event, shown by a red cross in Figure 137.

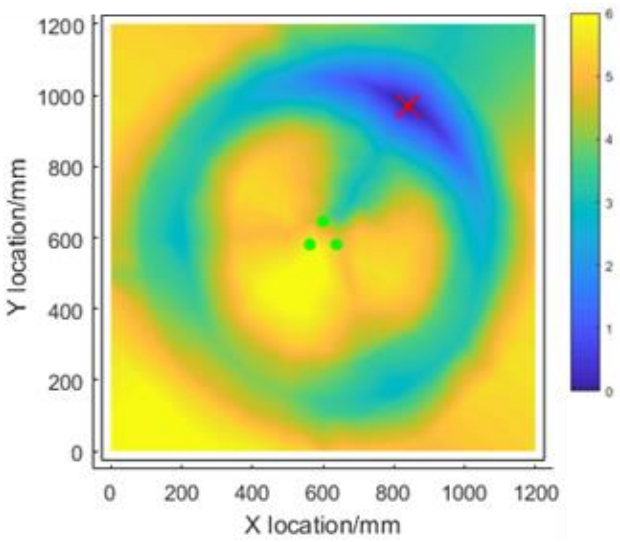

Figure 137 – Combined error plot with estimated location shown as a red cross

6.3 Artificial Source Testing

A number of structures were mapped using the method presented in Section 6.1. H-N tests were then conducted at ten or more random locations within these grids and these were located using the traditional location approach (presented in Chapter 4) and the mapping method. In both cases the S_0 arrival was predicted using the AIC method and the A_0 was predicted using the second differential method. In the majority of cases, the same data as was used to trial the traditional method, presented within Chapter 4, was able to be used to create the maps, as the Cartesian grid was identical. In the majority of cases the grid density was 50mm, testing was also conducted using a 100mm as well as a 50mm grid on the aluminium panel in order to compare their accuracies. More discussion on grid spacing is included later in this chapter.

Two simple structures were tested (composite panel B and the aluminium panel, described in Sections 3.2.2 and 3.2.3) both before and after their stiffeners were added. The maps were re-created and the same test locations checked with H-N sources. Maps were also produced from the A320 wing and A350 wings.

6.3.1 Aluminium Panel

Two grids were produced for the aluminium panel test. The first used the data presented in Chapter 4, which covered the entire panel with a grid density of 100mm. The map from this is shown in Figure 135 and covers the majority of the panel. The second grid produced had a density of 50mm and covered a 750mm^2 area in a corner of the panel, the area of the panel these grids covered are shown in Figure 138.

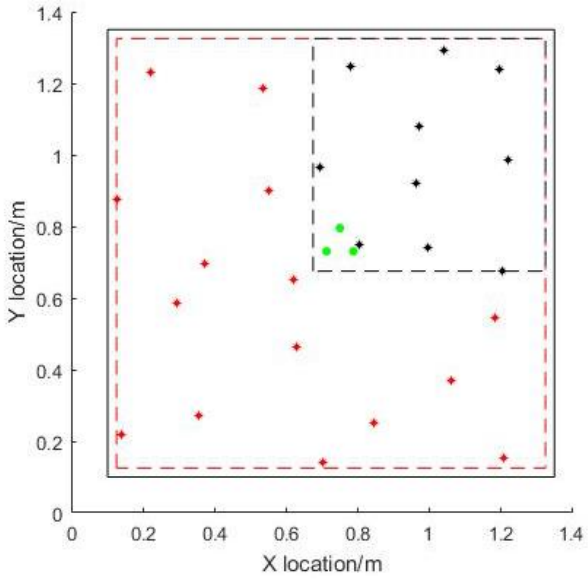

Figure 138 – Aluminium panel (solid lines), showing area mapped with a 100mm density (dashed red lines) and area mapped with 50mm density (dashed black lines). Test locations shown as (*) in their corresponding colour and sensors shown as green circles.

The intention of the two grids was to understand if a greater density grid significantly affected the accuracy of the technique. Pearson et al. (Pearson et al., 2017) identified that using a 50mm grid instead of a 100mm grid increased the accuracy of traditional Delta-T to locate H-N sources in an aluminium aerospace panel by reducing error from an average of 7mm to 4.5mm. Reducing the size of the grid further had minimal effect, with a 10mm grid having an average error of 4mm,which was put down to the size of the sensor (8mm diameter) giving an no exact sensor location, hence testing on a smaller grid was not deemed worthwhile. The Delta-T map on the

simple panel using the 100mm grid is shown in Section 6.1, Figure 135 and the 50mm grid map is shown in Figure 139. The maps for the complex panel are shown in Figure 140 and Figure 141.

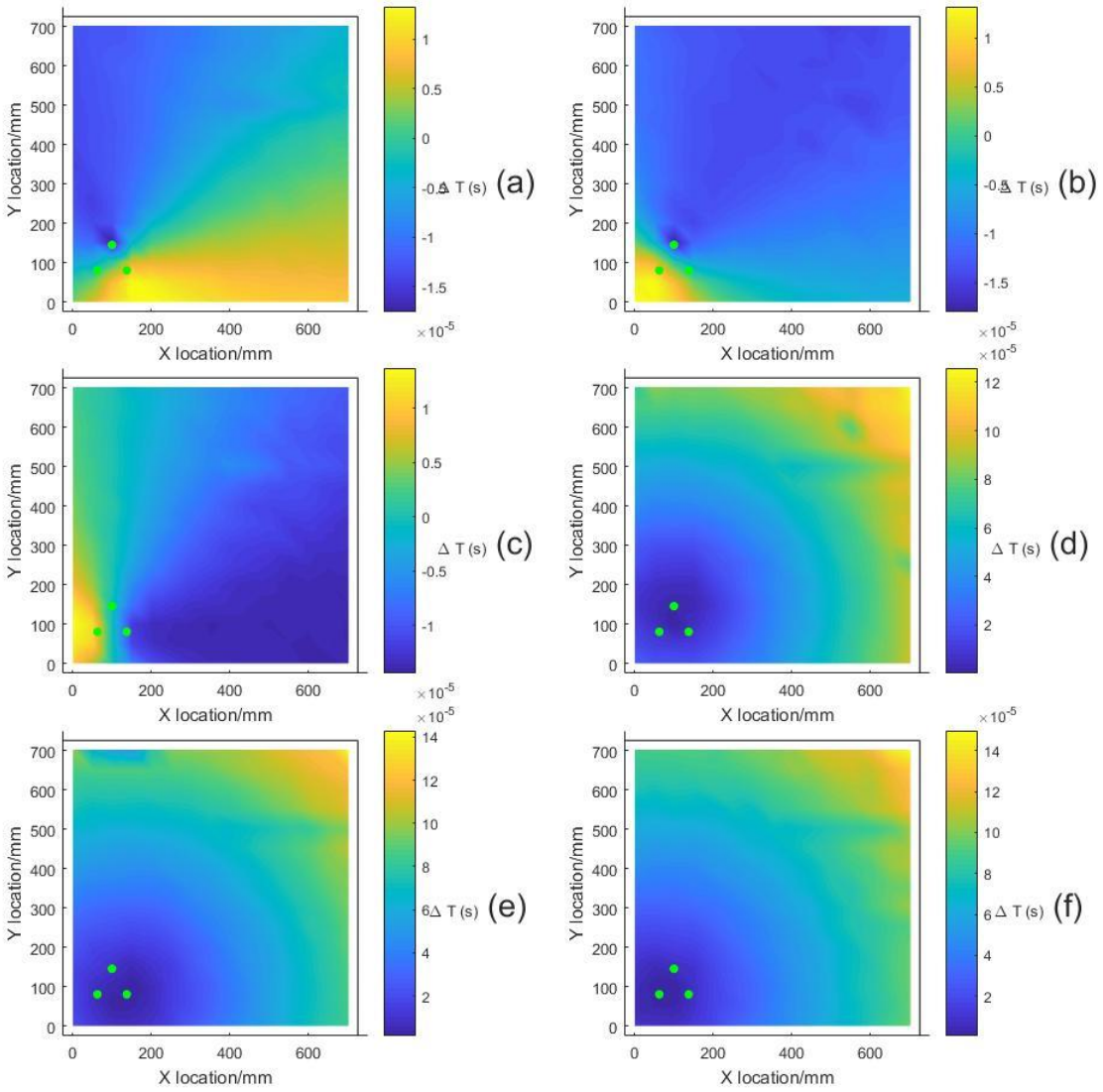

Figure 139 – Delta-T maps from the 50mm grid on the simple aluminium panel. (a), (b) and (c) show TOA difference between 1-2, 1-3 and 2-3 respectively. (d), (e) and (f) show dispersion at sensors 1, 2 and 3. Sensors shown in green.

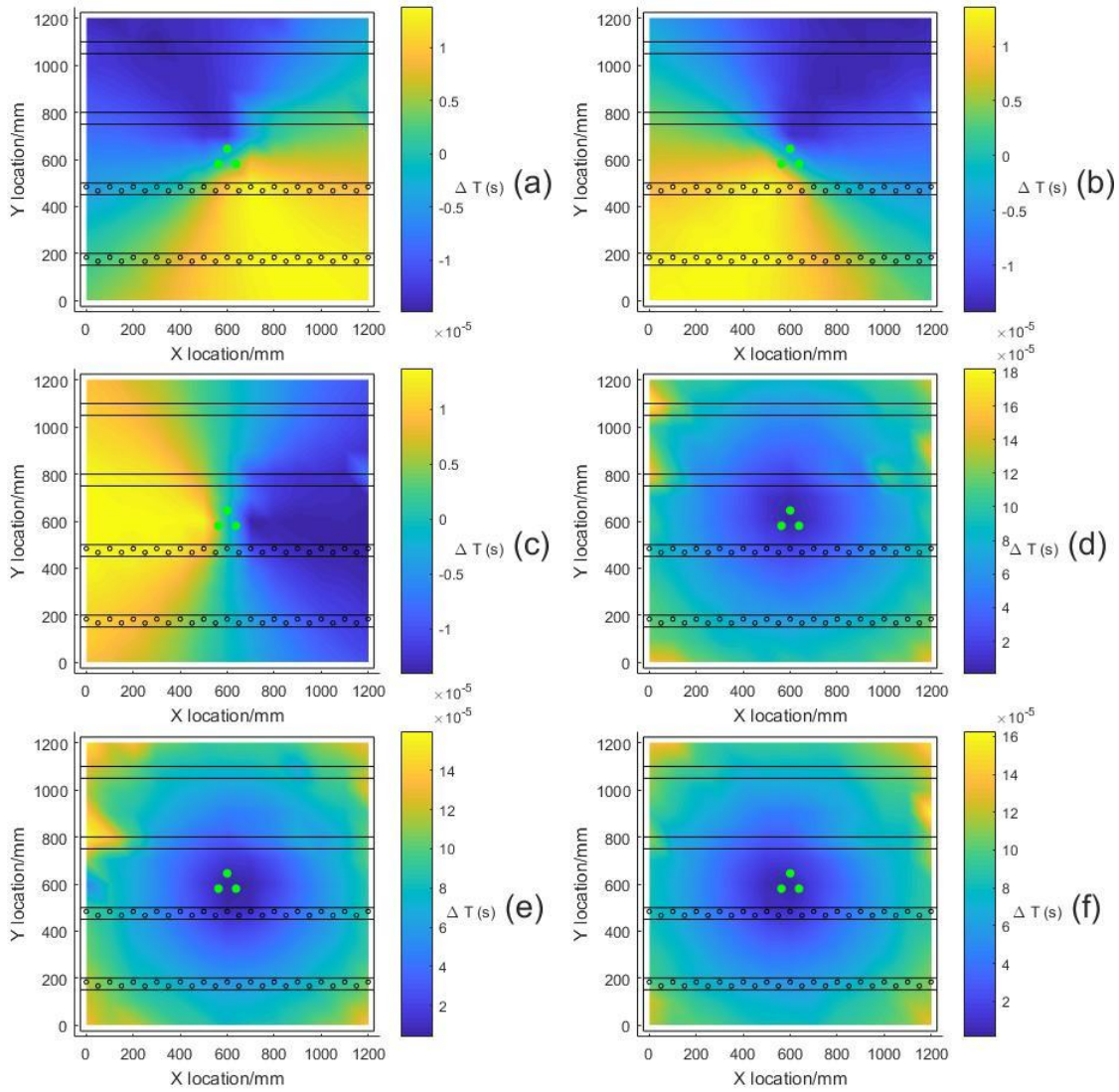

Figure 140 – Delta-T maps from the complex aluminium panel. (a), (b) and (c) show TOA difference between 1-2, 1-3 and 2-3. (d), (e) and (f) show dispersion at sensors 1, 2 and 3. Sensors shown in green and structural complexity in black.

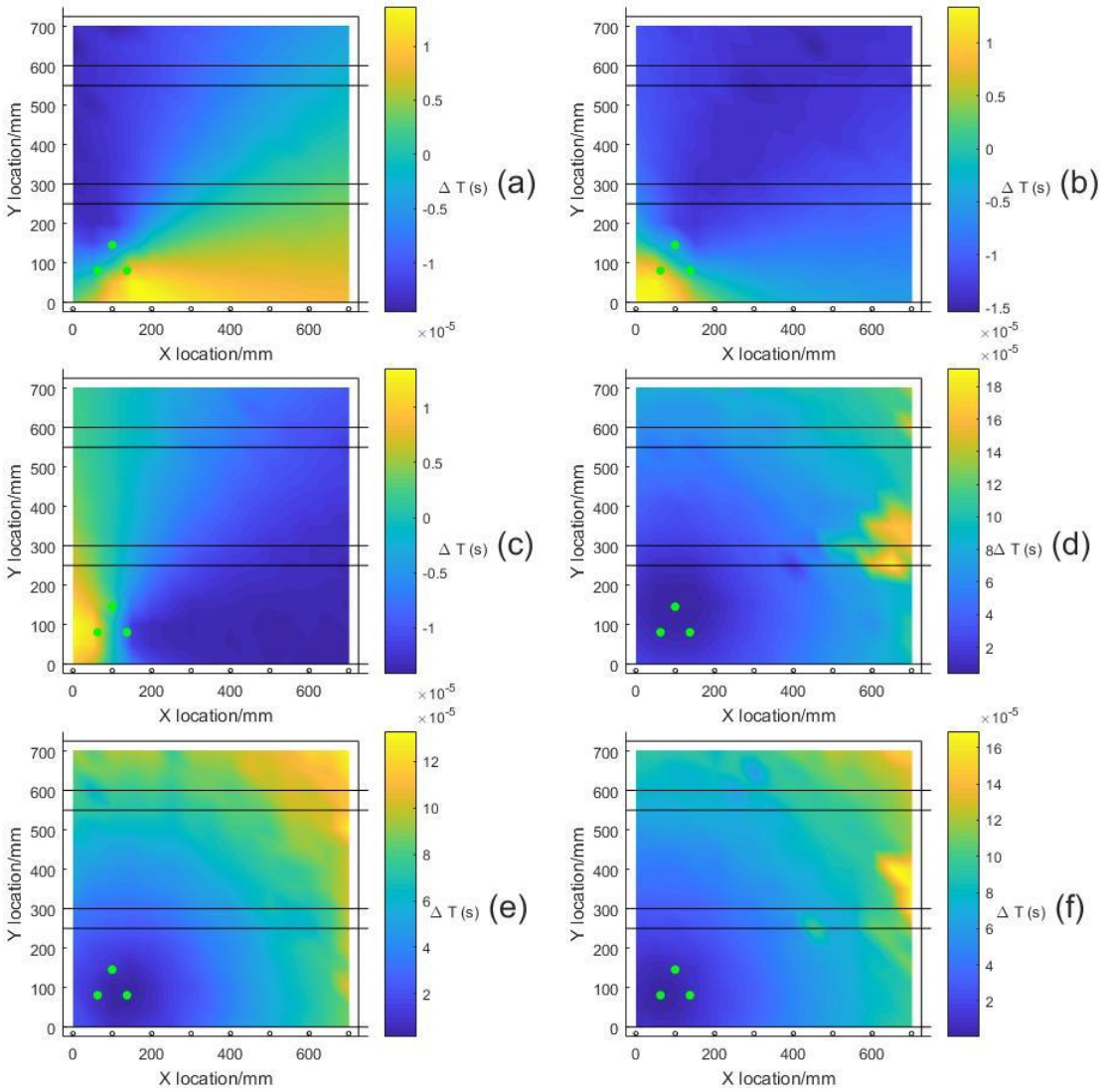

Figure 141 – Delta-T maps from the 50mm grid on the complex aluminium panel. (a), (b) and (c) show TOA difference between 1-2, 1-3 and 2-3. (d), (e) and (f) show dispersion at sensors 1, 2 and 3. Sensors shown in green and structural complexity in black.

A total of 25 test locations were randomly selected over the panel, ten within the area of the 50mm grid (identified as the black locations) and the others outside of the 50mm grid but still within the 100mm grid (known as the red locations). The location of these points are shown in Figure 138. The black locations were predicted with both sets of maps to compare the accuracy of each whereas the red locations were only predicted with the 100mm map. All the events were also located using the normal (non-mapped) three sensor method which was presented in Chapter 4.

Data was deemed to have been somewhat located if it was predicted to within 200mm of its actual location. 200mm was selected by the author as at this distance the event is somewhat located given the size of specimens being tested. If applied on a larger scale this accuracy may be more than acceptable or a higher level of accuracy may be required. The 100mm and 50mm thresholds allow how many events were located to within greater levels of accuracy, this precision may, or may not, be required by an end user.

Table 27 shows the percentage of data within 200mm accuracy using both techniques. In both cases all, or almost all, of the data is within the required accuracy and data outside of this was typically due to the distance approximation being wrong due to an early, or late, A_0 arrival prediction. The average location, angle and distance errors also presented in Table 27 only consider the events located within 200mm accuracy.

Table 27 – Errors when locating H-N sources at red and black locations on the simple and complex aluminium panels when processed using the Delta-T method and normal three sensor location technique

		Delta-T			Normal	
		100mm grid		50mm grid	-	
		Red points	Black Points	Black points	Red points	Black Points
Simple	Average location error (mm)	26	19	19	46	27
	Average Angle error (^{o})	1.8	1.9	1.5	2.2	2.0
	Average Distance error (mm)	16	11	12	36	21
	Data less than 50mm error (%)	88	98	97	73	89
	Data less than 100mm error (%)	95	99	100	86	99
	Data less than 200mm error (%)	98	100	100	99	100
Complex	Average location error (mm)	32	32	26	42	33
	Average Angle error (^{o})	2.3	3.1	1.9	2.7	1.9
	Average Distance error (mm)	17	21	17	28	26
	Data less than 50mm error (%)	71	77	86	77	86
	Data less than 100mm error (%)	99	96	100	89	95
	Data less than 200mm error (%)	100	100	100	99	98

6.3.2 Composite Panel B

Using the data presented in Chapter 4, maps were created of composite panel B. The grid used to collect this data had a density of 50mm and covered 800mm x 800mm of the 900mm x 900mm

total panel area. Grids were created on both the simple panel without any complexity, and the fully complex panel with four stiffeners bonded to the surface. It was expected that the addition of complexity would add error to the location prediction, this testing aimed to see the extent of this. The position of these stiffeners and the process of bonding is described in Section 3.2.2. Where H-N sources couldn't be created due to the stiffeners the data was interpolated from the nearby points. The two sets of maps are shown in Figure 142 and Figure 143.

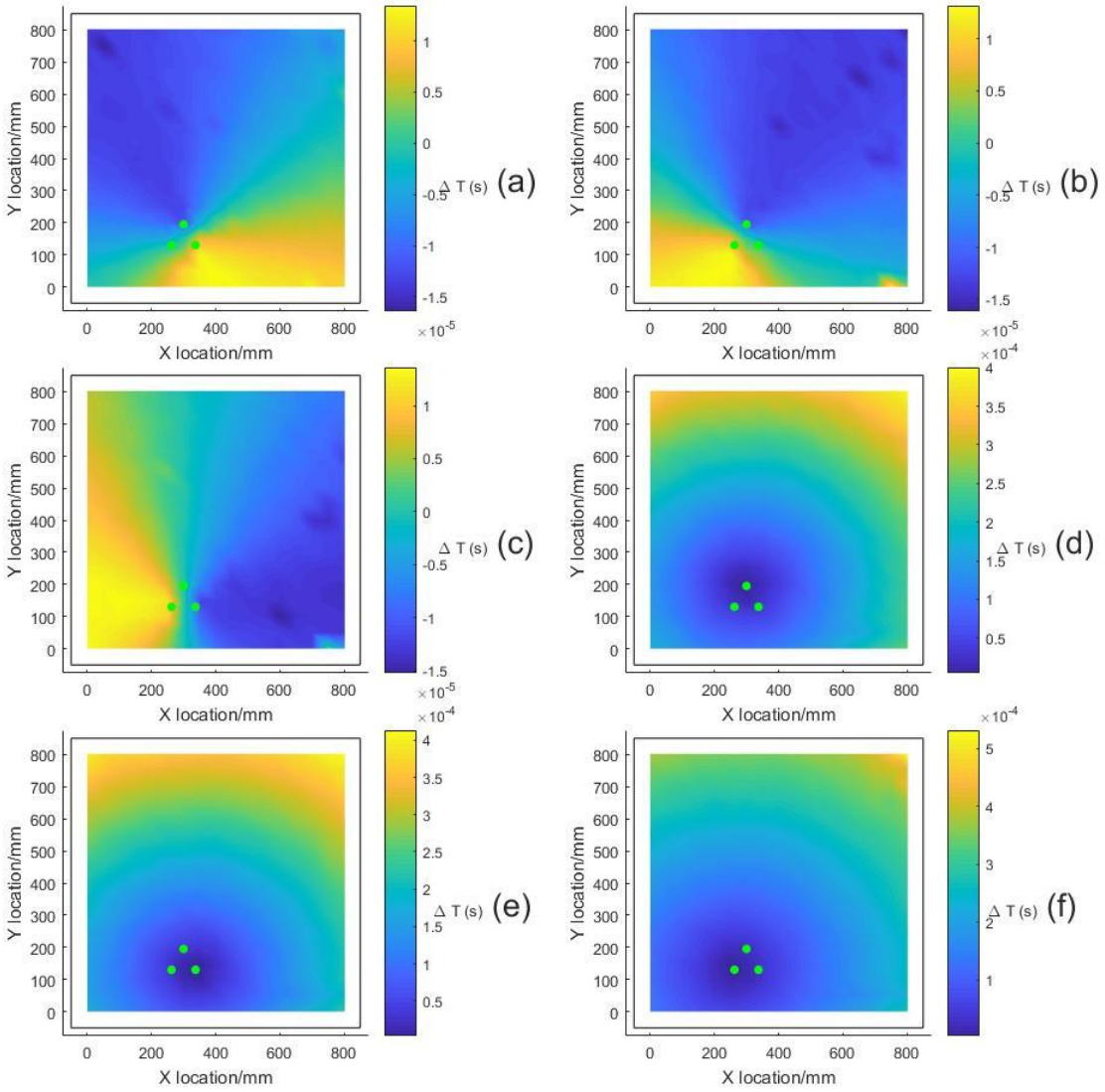

Figure 142 – Delta-T maps from composite panel B without stiffeners. (a), (b) and (c) show TOA difference between 1-2, 1-3 and 2-3. (d), (e) and (f) show dispersion at sensors 1, 2 and 3. Sensors shown in green.

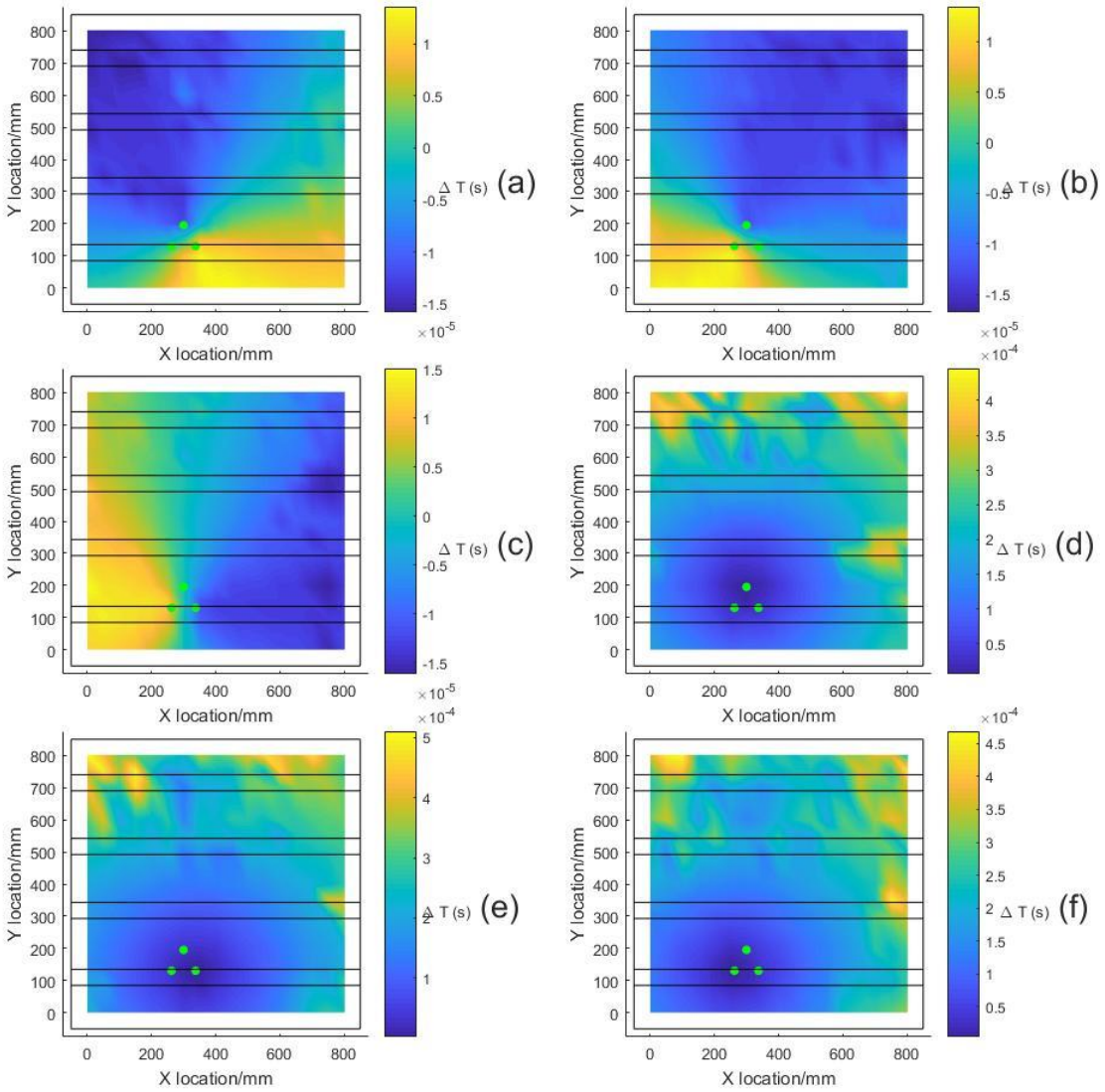

Figure 143 – Delta-T maps from composite panel B with four stiffeners. (a), (b) and (c) show TOA difference between 1-2, 1-3 and 2-3. (d), (e) and (f) show dispersion at sensors 1, 2 and 3. Sensors shown in green.

Ten points were selected at random and ten H-N sources were created both before, and after, the addition of stiffeners to the structure. The predicted locations for the simple panel are shown in Figure 144 and for the complex panel in Figure 145.

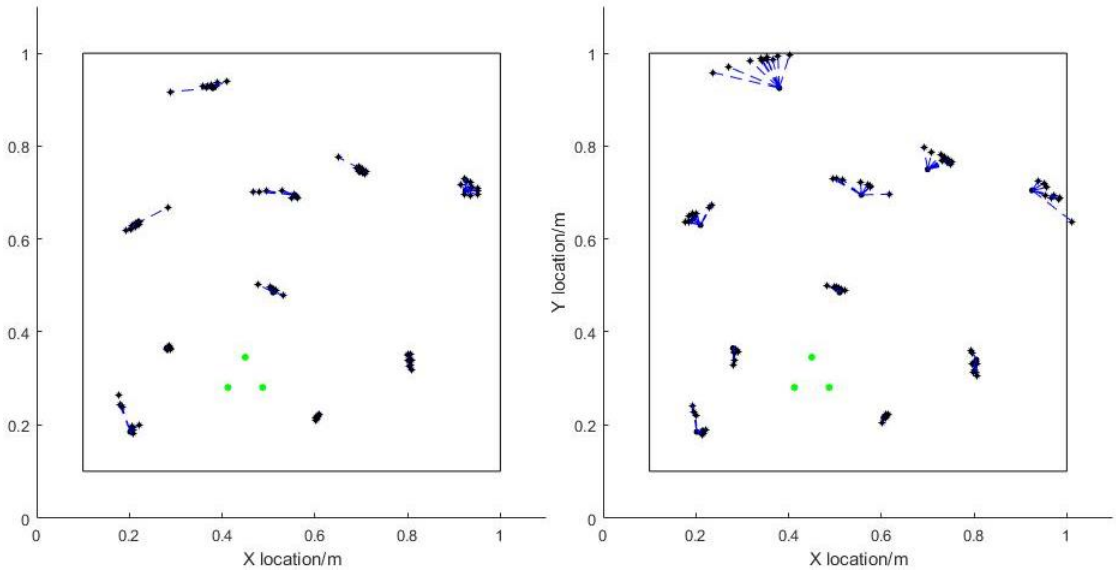

(a) (b)

Figure 144 - Predicted locations of sources on the simple composite panel B using the Delta-T mapping technique (a) and normal three sensor approach (b). Sensors shown in green, test locations black circles and predicted locations are black ''.*

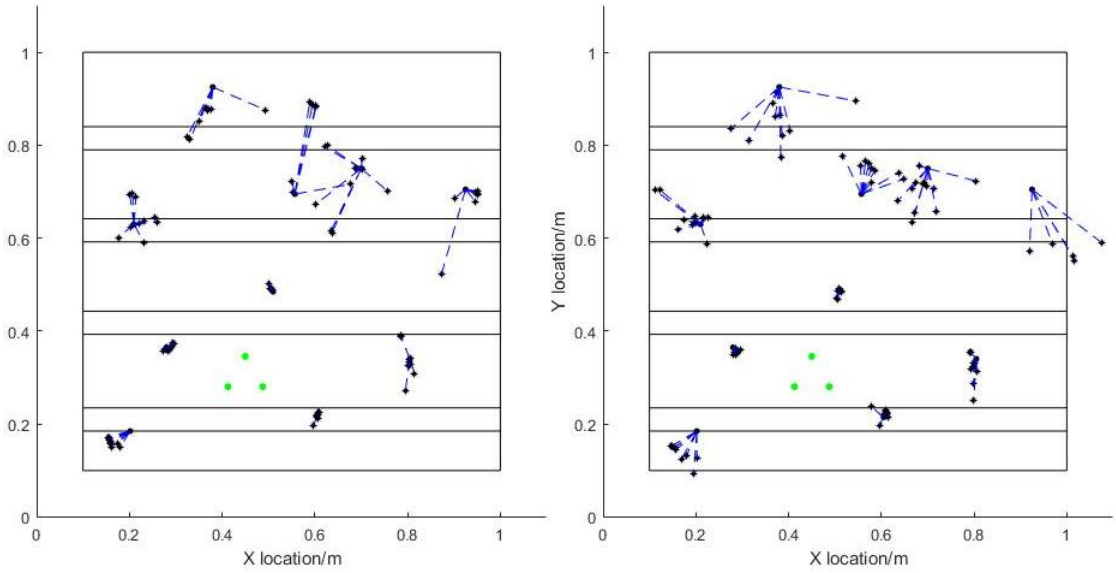

(a) (b)

Figure 145 - Predicted locations of source on the complex composite panel B using the Delta-T mapping technique (a) and normal three sensor approach (b). Sensors shown in green, test locations black circles and predicted locations are black ''.*

The average location, angle and distance errors as well as the percentages of data within 50mm, 100mm and 200mm error are shown in Table 28.

Table 28 - Errors when locating H-N sources at the test locations on the simple and complex composite panel A when processed using the Delta-T method and the normal three sensor location technique

		Delta-T results	Normal results
Simple panel	Average location error (mm)	16	33
	Average Angle error (^{o})	2.3	3.1
	Average Distance error (mm)	5	22
	Data less than 50mm error (%)	91	80
	Data less than 100mm error (%)	100	97
	Data less than 200mm error (%)	100	100
Complex panel	Average location error (mm)	42	50
	Average Angle error (^{o})	2.8	3.8
	Average Distance error (mm)	31	34
	Data less than 50mm error (%)	70	56
	Data less than 100mm error (%)	85	84
	Data less than 200mm error (%)	97	98

6.3.3 A320 Wing

The data used in Chapter 4 to test the normal three sensor technique was used to create a map on the A320 wing, described in Section 3.2.5. This grid covered an area of 1m x 0.7m with a density of 50mm. The Delta-T maps for this structure are shown in Figure 146.

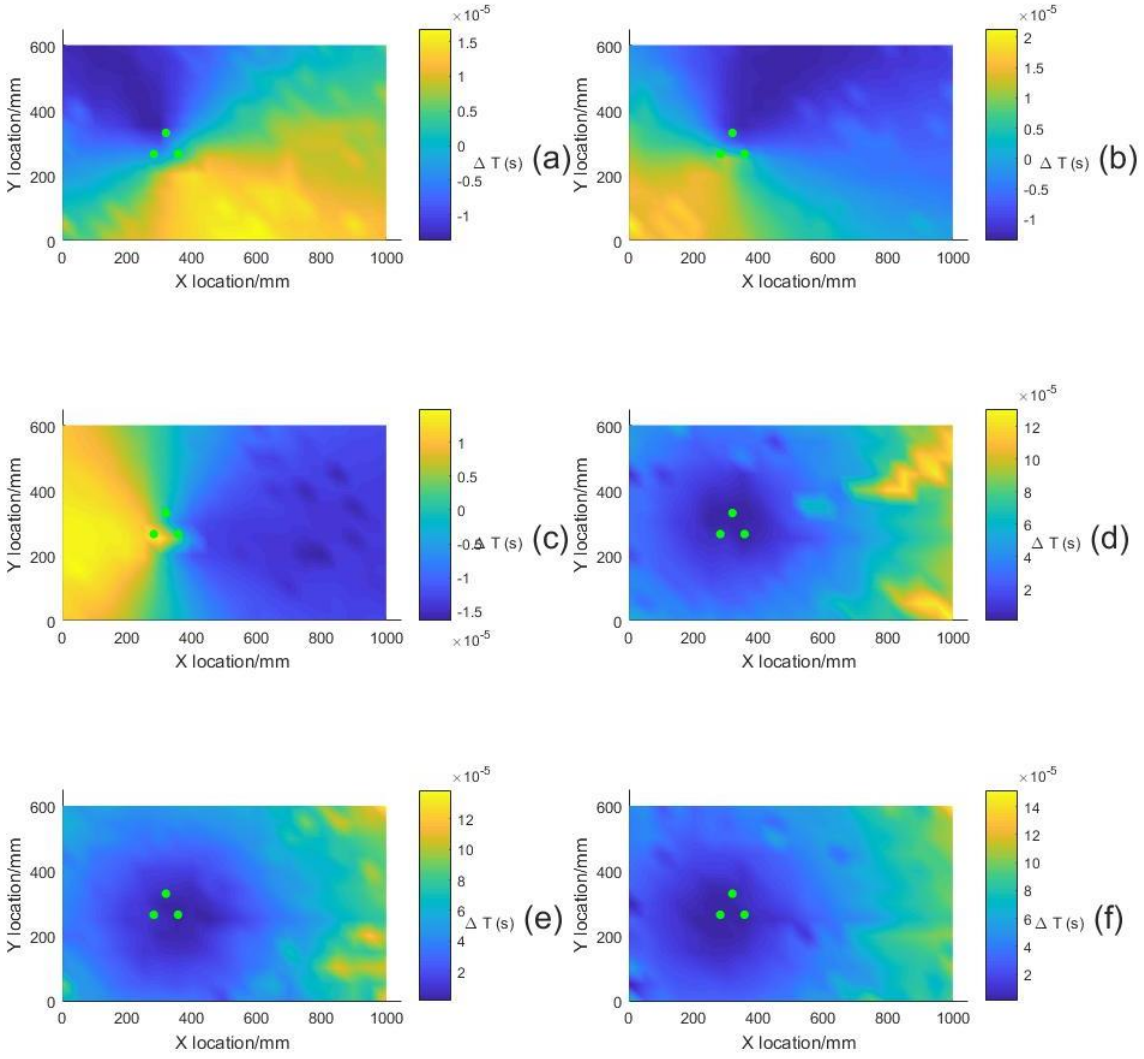

Figure 146 – Delta-T maps from the A320 wing. (a), (b) and (c) show TOA difference between 1-2, 1-3 and 2-3. (d), (e) and (f) show dispersion at sensors 1, 2 and 3. Sensors shown in green.

20 test points were then chosen at random and five H-N sources created at each. These events were located using the Delta-T mapping technique as well as the normal three sensor technique. The locations predicted using the Delta-T mapping technique are shown in Figure 147, and using the normal three sensor method in Figure 148.

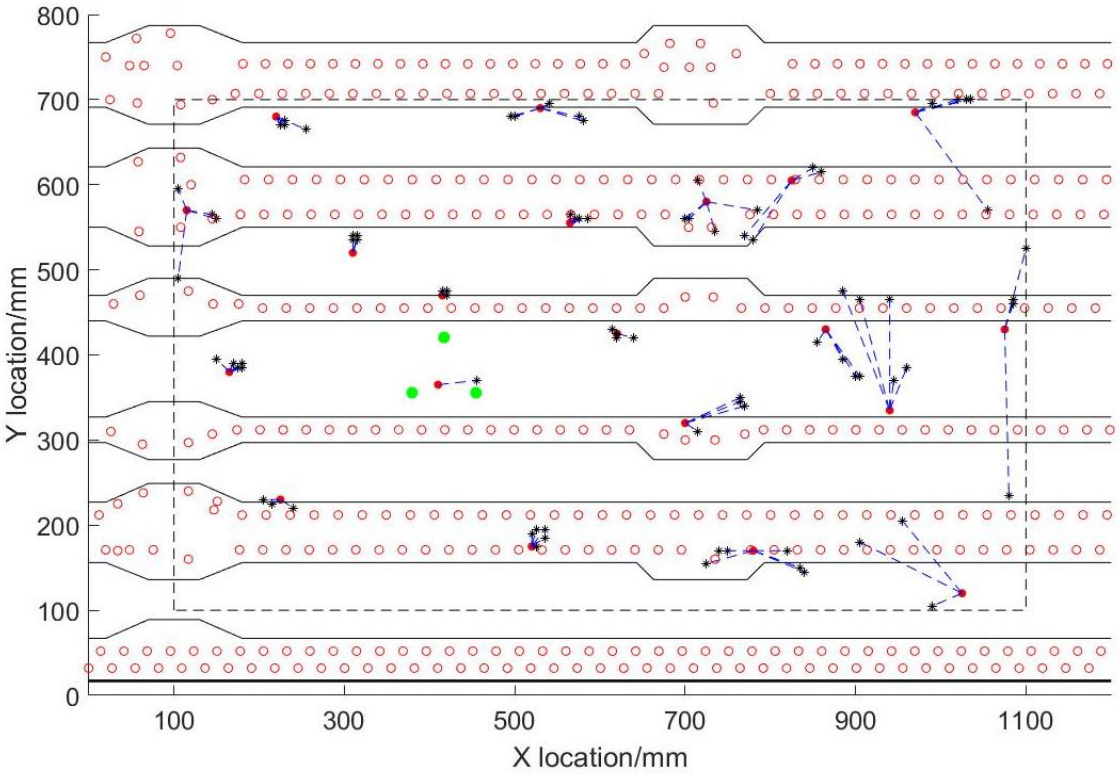

Figure 147 - Predicted locations of data predicted within 200mm accuracy on the A320 wing using the Delta-T mapping technique. Sensors shown in green, test locations red and predicted locations and black ''. The map outline is shown as dashed lines.*

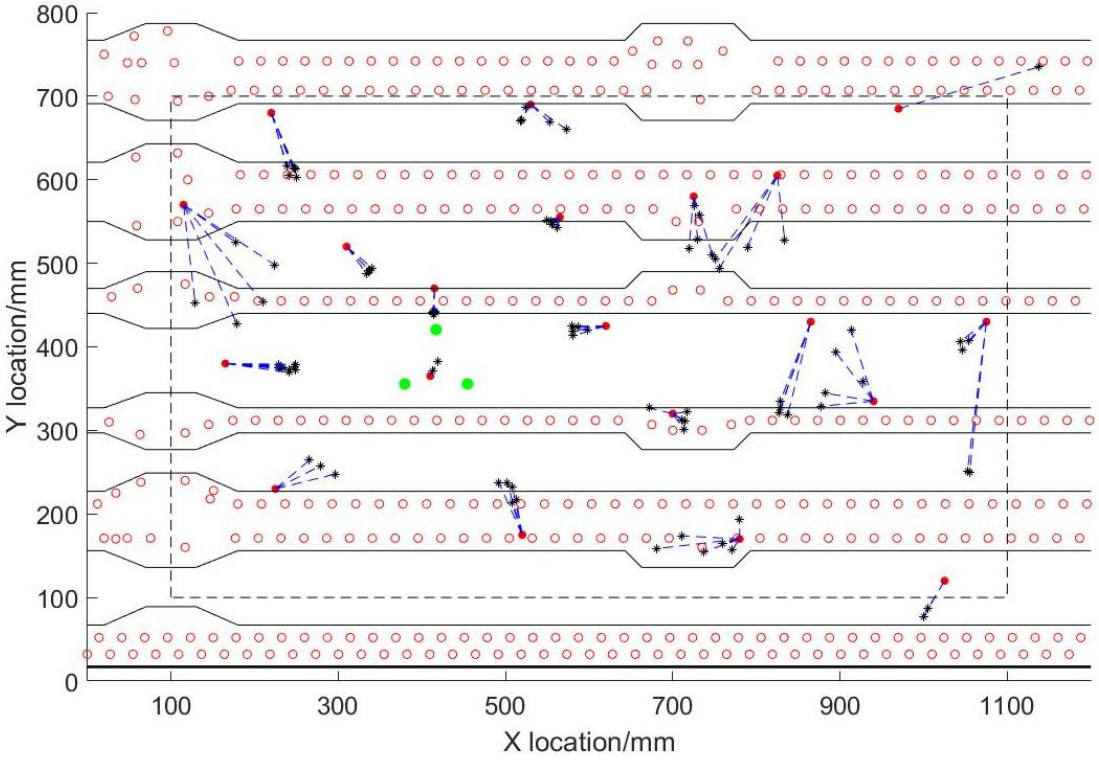

Figure 148 - Predicted locations of data predicted within 200mm accuracy on the A320 wing using the normal three sensor technique. Sensors shown in green, test locations red and predicted locations and black ''. The map outline is shown as dashed lines.*

The percentage of data predicted within 50mm, 100mm and 200mm of its actual location and the average location, angle and distance error of the data within 200mm accuracy is shown in Table 29. The high average angle error using the Delta-T method is a result of data at the centre of the sensor array, where two events with an angle error over 90^{o} increased the average error significantly. This did not result in a high location error, as the distance was very small.

Table 29 - Errors when locating H-N sources at the test locations on the A320 wing when processed using the Delta-T method and normal three sensor location technique.

	Delta-T	Normal
Average location error (mm)	40	59
Average Angle error (^{o})	5.7	4.5
Average Distance error (mm)	24	43
Data less than 50mm error (%)	69	44
Data less than 100mm error (%)	88	77
Data less than 200mm error (%)	95	91

6.3.4 A350 wing

Testing was also conducted on the A350 aircraft wing at Airbus Broughton, described in Section 3.2.7. A 800mm x 800mm area of the wing was selected and a grid with a density of 50mm drawn on to its outside surface. This was in the same area as was tested on in Chapter 5 with the wireless node. Five H-N sources were conducted in each location which were used to create the six Delta-T maps for the structure, shown in Figure 149. Additionally ten locations were chosen at random over the grid, and at each of these locations ten H-N sources were created which were recorded and used to test the grids.

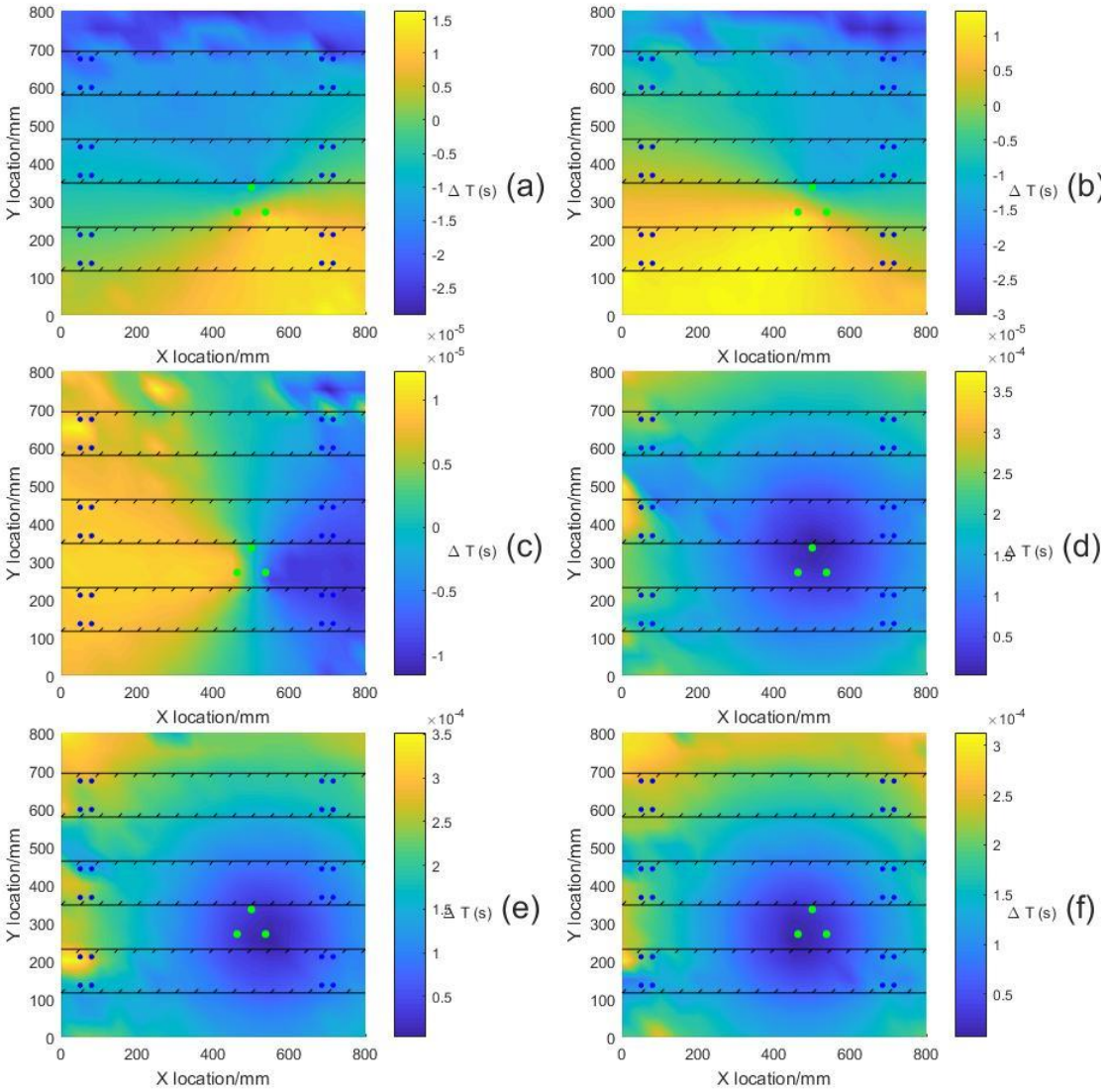

Figure 149 – Delta-T maps from the A350 wing. (a), (b) and (c) show TOA difference between 1-2, 1-3 and 2-3. (d), (e) and (f) show dispersion at sensors 1, 2 and 3. Sensors shown in green.

In order to predict the location using the normal three sensor method the Rate of dispersion (ROD) in the A350 wing was calculated by analysing the separation of the S_0 and A_0 modes at 0^o, 45^o and 90^o, where 0^o was across the stiffeners, between 100mm and 500mm from a nano-30 sensor. The data was processed using the AIC technique to detect the S_0 mode and the second differential technique to detect the A_0. The average ROD for 0^o was 2390 m/s, for 45^o 2470 m/s and 2070 m/s at 90^o. For processing the data using the normal technique the average of these values was used, this being 2290 m/s.

The actual and predicted locations when testing on the A350 wing are shown in Figure 150. The area within this figure was all mapped and the figure also includes the location of complexity on the wing as well as the location of sensors. Within this figure the mapped approach can be seen to have located the sources very well.

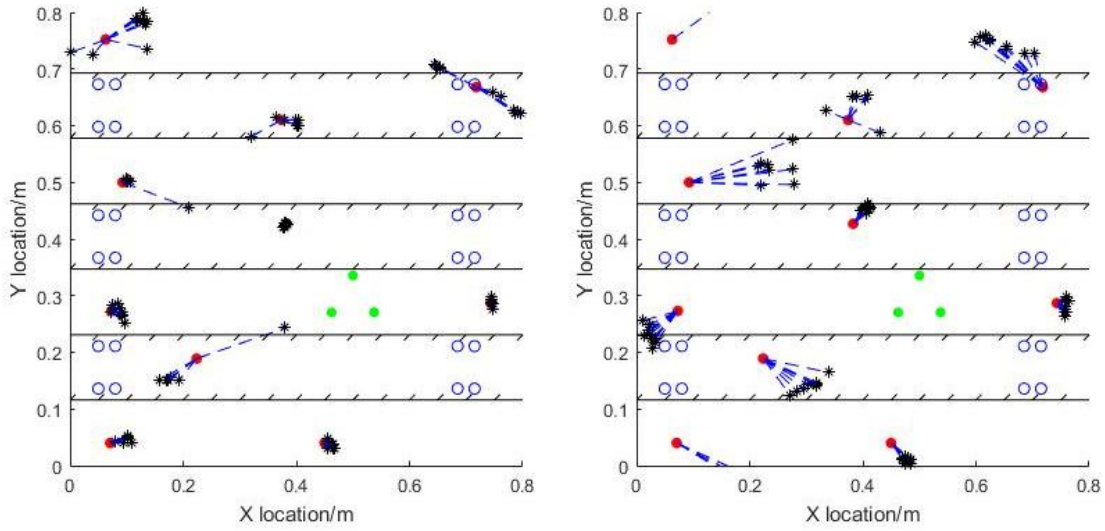

Figure 150 – Predicted locations (Black '') and actual locations (red circles) of H-N sources on the A350 wing using the Delta-T mapping method (a) and traditional three sensor approach (b). Sensors shown in green, holes in blue and stiffeners in black.*

The percentage of events within each level of accuracy and the average location, angle and distance error of these events using both techniques are shown in Table 30, where almost all of the mapped data has been located to within 100mm accuracy.

Table 30 – Errors when location H-N sources on the A350 wing using the Delta-T and traditional three sensor methods

	Delta-T	Normal
Average location error (mm)	34	80
Average Angle error (^{o})	3.1	10.2
Average Distance error (mm)	16	41
Data less than 50mm error (%)	69	37
Data less than 100mm error (%)	97	60
Data less than 200mm error (%)	99	87

6.3.5 Discussion

Within Section 6.3 the Delta-T method was tested on a number of complex plate-like structures using three sensors in a closely spaced triangular array. The data from these tests was also processed using the standard three sensor technique in order to assess the improvement in accuracy.

The first map presented was for the simple aluminium panel where H-N sources were located with an average error of around half that obtained when using the normal technique. Most of this improvement was as a result of improved distance prediction, however a slight reduction in average angle prediction error also improved the results. This improvement was primarily seen at the edges of the panel where the effect of mode conversion due to reflection at the edges was accounted for. The addition of complexity did not significantly affect the accuracy of the technique only resulting in a small increase in error when using the Delta-T method. Strangely the error produced when using the normal technique was reduced, the exact reason for this is unclear however it is likely that the addition of stiffeners negated the effect of reflections at a single event, so influencing the results positively.

In total two grids were created on the aluminium panel, one at 100mm spacing and a second at 50mm. A study by Pearson et al. (Pearson et al., 2017) identified that this reduction in grid density improved results significantly when applying a normal Delta-T map using a spaced array on a complex aluminium part. The results from this testing showed no difference when a simple panel was tested, but that the addition of complexity did lead to a small improvement in accuracy when using a 50mm grid rather than a 100mm one. This result is to be expected as a simple panel is unlikely to have any significant divergence from linearity over the space of 100mm, a complex one however will do in some locations.

The Delta-T mapping technique greatly improved the accuracy on composite panel B prior to the addition of stiffeners, giving an average error of only 16mm compared to 33mm when using the normal technique. The distance prediction in particular was very accurate, with an average error

of 5mm compared to 22mm using the normal technique. This large improvement is primarily because the Delta-T technique is able to account for the slight changes in ROD that are present with change in direction over the panel. Although the panel was manufactured to be Quasi-Isotropic (meaning that its extensional stiffness is the same as for an isotropic material (Paradies, 1996)) and therefore wave velocity should not be dependent on direction, the dispersion testing presented in Section 3.2.2, Figure 38, shows that this is not quite the case. These results showed that the ROD varied by around 250m/s (≈10%) between 0^o and 90^o, which although not too significant does add error to the normal technique which is removed with the mapping approach. The work by Aljets (Aljets, 2011) changed the ROD depending on predicted direction, which is effectively the same as what is done with the mapping approach. Varying ROD with direction is quicker to implement than mapping the entire structure, so is most probably the better approach for simple structures.

The addition of complexity to the panel reduced the accuracy of the techniques significantly as heavily attenuated A_0 modes meant their detection was very difficult, even when using the second differential approach. This makes the distance prediction very inaccurate using either technique and meant that the mapped and unmapped approaches gave similar levels of error, with the mapping method having slightly increased accuracy overall.

The first real structure mapped with the three sensor Delta-T mapping method was the A320 wing. This very complex wing gave quite high errors when testing with the normal approach, the average error for the twenty points being 59mm and almost 10% of sources (primarily due to two locations far from the sensor array) locating with an error greater than 200mm. The mapping approach was able to reduce this average error to 40mm and predict 95% of events within 200mm accuracy i.e. provide more accurate predictions over a greater range.

The testing on the A350 wing was where the mapping approach showed the most improvement over the normal method. All but one event, where the distance was inaccurately predicted due to an early A_0 trigger, was located within 200mm accuracy compared to 87% using the normal

approach. Accuracy was therefore significantly better, with the average error being only 34mm compared to 80mm when using the previous method.

Overall the mapping approach increased the accuracy of location H-N sources in all the structures tested. It should be noted however that, other than on the A350 wing, the normal method still achieved good levels of accuracy compared to the Delta-T method, with no more than 5% more data predicted outside of 200mm and an average error within 20mm of the Delta-T method. This means that in most cases the three sensor method could be applied without mapping, the Delta-T method just improves the achievable accuracy. Most improvement was seen in the distance prediction however in the case of the A320 wing in some cases, the angle prediction was also significantly improved. One final aspect that is improved by using the Delta-T mapping approach, is that if the sensors are not correctly orientated, e.g. they are 1^{o} off axis, then all the results will be 1^{o} inaccurate using the normal approach but not using the Delta-T approach. Although great care was taken to ensure this was not the case within this testing, it is still entirely possible and if applied on a larger scale care would be required to ensure orientation was correct.

6.4 A320 Vertical Stabiliser Impact Testing

6.4.1 Test overview

This section presents an investigation into whether the three sensor technique could be used to detect impact events in a real composite structure rather than artificial sources. For a system to be useful on a real structure it must not only detect the presence of an impact, but locate it to a suitable level of accuracy. This does not have to be incredibly precise, as NDT techniques can quickly scan a small area for damage. For the purpose of this testing a 200mm accuracy was considered acceptable, however if the entire side of the vertical stabiliser could be monitored by just three sensors a lower accuracy may be deemed adequate.

The aim of the test was to use AE to monitor for impact damage in the A320 vertical stabiliser described in Section 3.2.6. For this a 500mm x 500mm area which contained a total of four

stiffeners was selected and a grid with a density of 50mm drawn onto the outside surface of the structure. The three sensors were bonded outside of this grid, to reduce the possibility of them being struck during impact. To create the normal Delta-T grid, four McWade sensors with a resonance of approximately 200 kHz – 400 kHz were bonded in the corners of the test area. The sensor locations relative to structural complexity and the mapped area is shown in Figure 151. These grids were then used to locate the damage using both the TOA and Delta-T techniques.

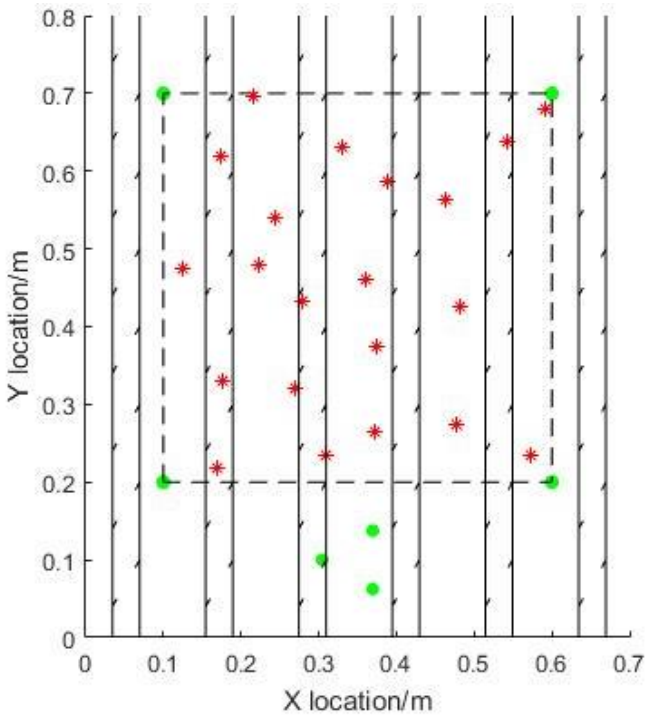

Figure 151 – Sensors (green) and test points (red '') shown against the location of stiffeners (solid lines) on the A320 vertical stabiliser. Mapped area also shown (dashed lines)*

Delta-T maps were created for both sets of arrays from the same data collected over the grid. The maps created using the traditional technique were based on the arrival times at each sensor calculated using the AIC technique and can be seen in Figure 152, the three sensor Delta-T maps can be seen in, Figure 153. In order to assess the accuracy of the maps 21 points were selected at random in the test area, these are shown in Figure 151. These were located with the three closely spaced sensors using the normal and Delta-T methods as well as with the four sensors using the TOA and Delta-T methods.

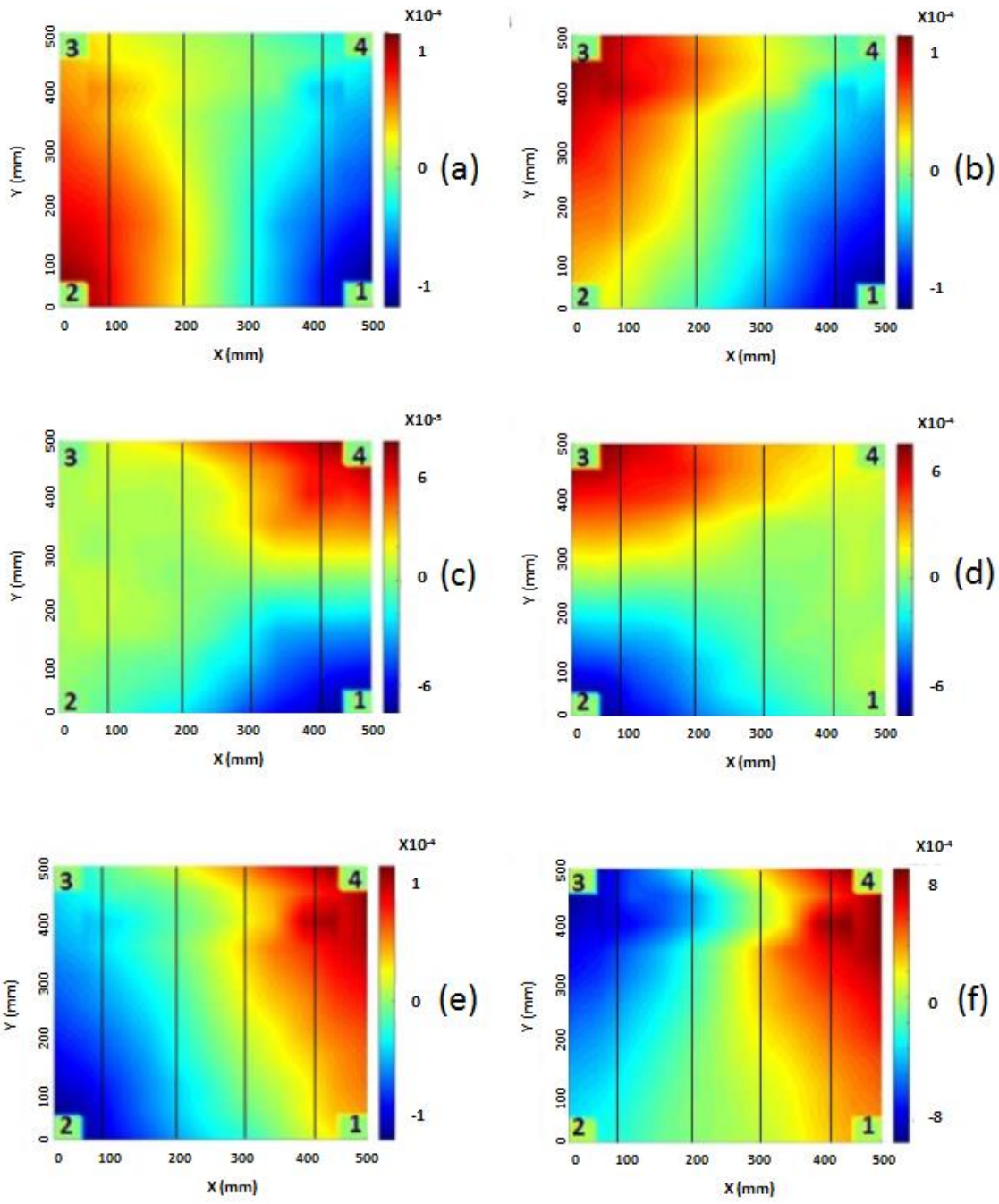

Figure 152 – Traditional Delta-T maps using the four sensors in the corners of the test area. Between sensors 1-2 (a), 1-3 (b), 1-4 (c), 2-3 (d), 2-4 (e) and 3-4 (f). Black lines indicate the location of the stiffeners. (Murray, 2016)

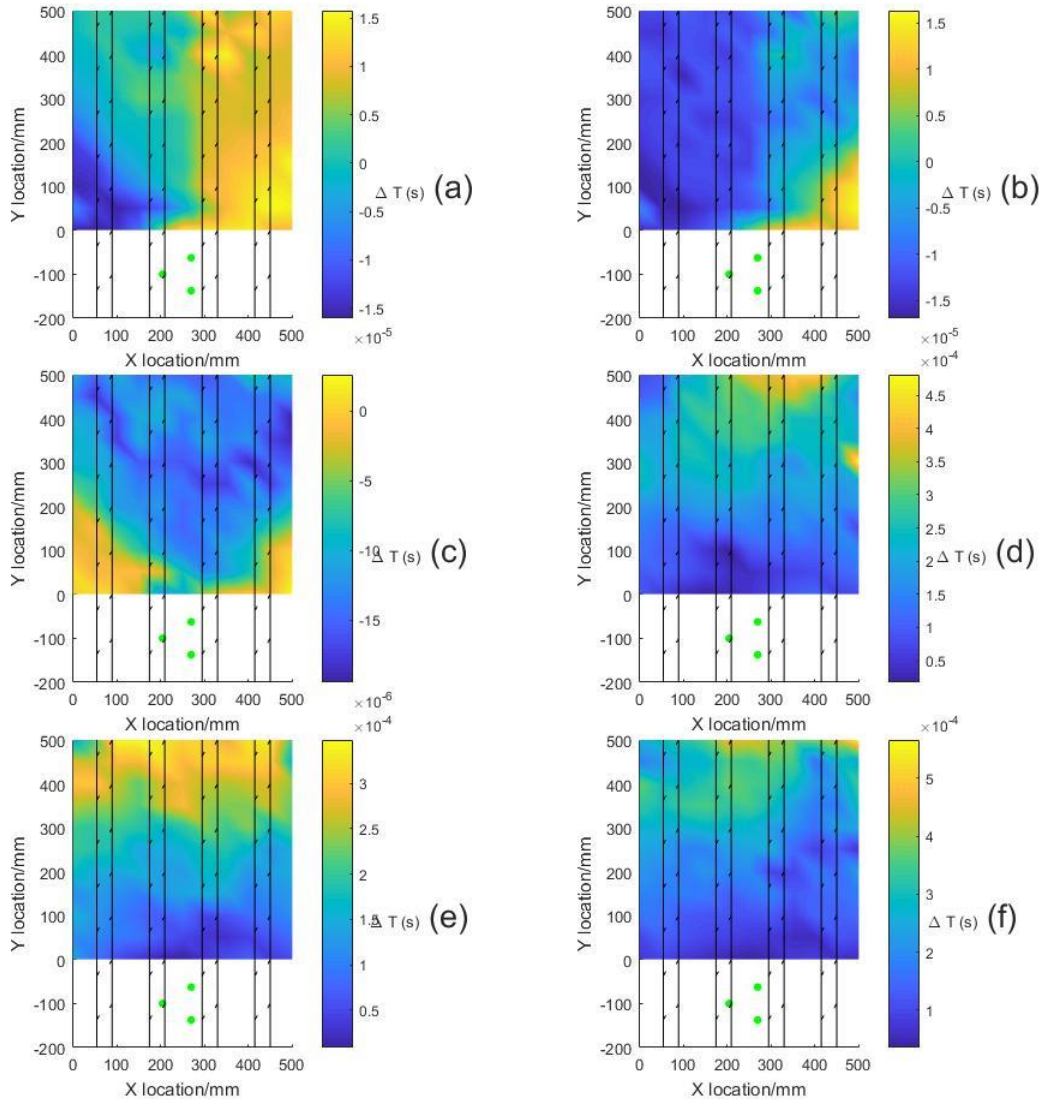

Figure 153 – Delta-T maps from the A320 Vertical Stabiliser. (a), (b) and (c) show TOA difference between 1-2, 1-3 and 2-3. (d), (e) and (f) show dispersion at sensors 1, 2 and 3. Sensors shown in green.

Once the maps had been constructed and tested the specimen was impacted in five locations within the test grid. Due to its size it was not feasible to use an impact test-rig to perform these impacts so instead they were made by hand using a hammer with an 18mm diameter rounded steel tip. These impacts varied in intensity, and so the damage that was caused to the structure. In the final location two impacts were conducted in order in increase the size of the damage at this location.

6.4.2 Artificial Testing Results

The locations of the 21 H-N sources predicted using the four sensors in the corners of the grid are shown in Figure 154, where the results using both the Delta-T and TOA methods can be seen. Table 31 shows the percentage of data within 50mm, 100mm and 200mm accuracy as well as the average error for data within 200mm accuracy for both methods.

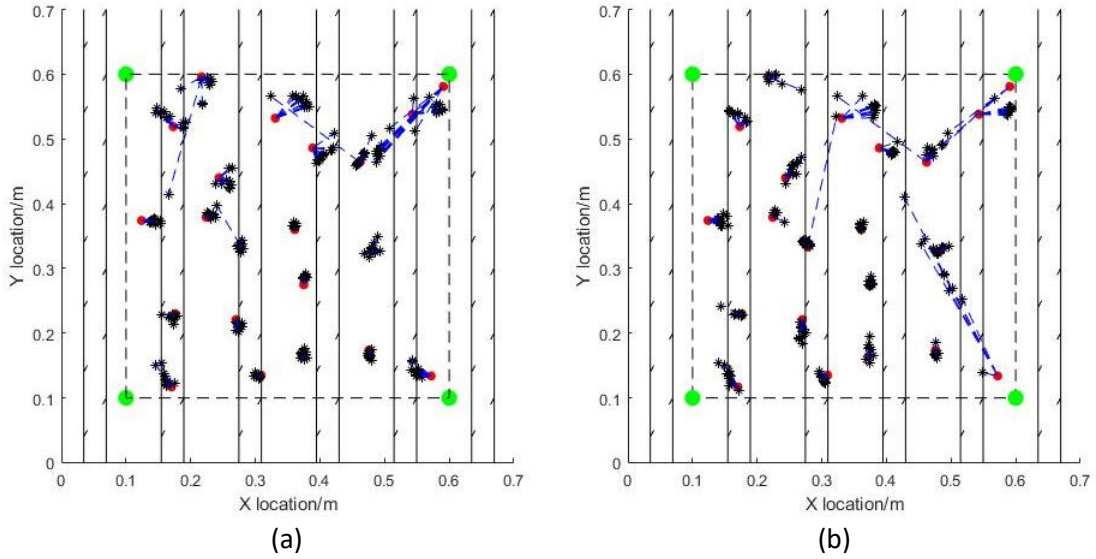

Figure 154 – Predicted locations (Black '') and actual locations (red circles) of H-N sources on the A320 vertical stabiliser using the tradition Delta-T mapping method (a) and TOA approach (b). Mapped area outlined with dashed lines, sensors shown in green and stiffeners in black.*

Table 31 – Average location error and percentage of data within given accuracies using the TOA and Delta-T methods with four sensors in the corners of the test area

	Delta-T	TOA
Average location error (mm)	24	24
Data less than 50mm error (%)	91	88
Data less than 100mm error (%)	95	93
Data less than 200mm error (%)	100	98

In order to find the event locations using the normal three sensor method the ROD in the specimen was found. This was calculated by analysing the separation of S_0 and A_0 mode at 0^o, 45^o and 90^o between 100mm and 400mm from a nano-30 sensor. The data was processed using

the AIC technique to detect the S_0 mode and the second differential technique to detect the A_0. The ROD was very similar for all directions and with an average of 2300 m/s.

The locations predicted using the three sensor method with and without Delta-T mapping are shown in Figure 155. Table 32 shows the percentage accuracies using the two techniques as well as the average distance, angle and location error for data with less than a 200mm error.

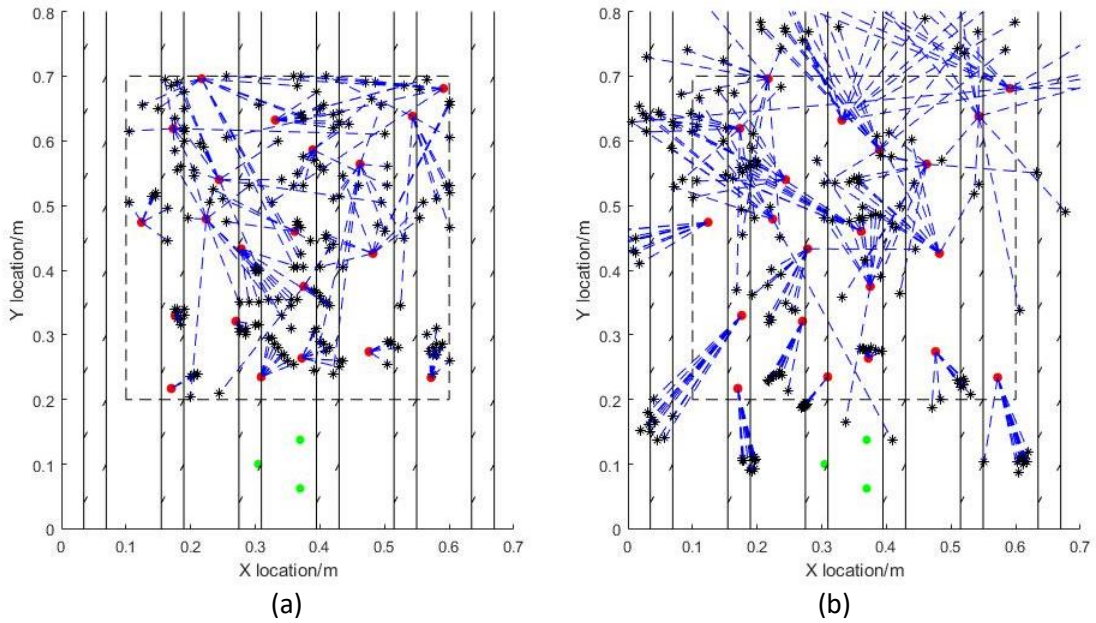

Figure 155 – Predicted locations (Black '') and actual locations (red circles) of H-N sources on the A320 vertical stabiliser using the Delta-T mapping method (a) and traditional three sensor approach (b). Mapped area outlined with dashed lines, sensors shown in green and stiffeners in black.*

Table 32 – Average errors and percentage accuracies when location H-N sources on the A320 vertical stabiliser using the Delta-T and traditional three sensor methods

	Delta-T	Normal
Average location error (mm)	64	110
Average Angle error (^{o})	7.1	15.4
Average Distance error (mm)	39	61
Data less than 50mm error (%)	44	5
Data less than 100mm error (%)	72	29
Data less than 200mm error (%)	92	72

6.4.3 Impact Testing Results

In total six impacts were made on the specimen, two of which were in the same place at the fifth location, the first being significantly lighter than the second. The final visible impact damage at each location are shown in Figure 156. Impacts 1 and 2 shown in Figure 156 (a) and (b) are both medium sized impacts, which caused some damage to the structure. Impact 3, shown in Figure 156 (c), is barely visible, however the applied force for this impact was similar to the previous two impacts. The reason for the lower level of visible damage is the location of the impact. Impact 3 was on a stiffener whereas impacts 1, 2, 4 and 5 all avoided stiffeners. Although the impact shows minor visual indications of damage a phased array scan showed that no damage was present in the material at this location, indicating the visual signs were merely to the paint. Impact 4, shown in Figure 156 (d), produced the most damage, punching fully through the specimen. The fifth impact location was struck twice. The first of which created similar damage to impact 1 and the second increased this to the level shown in Figure 156 (e).

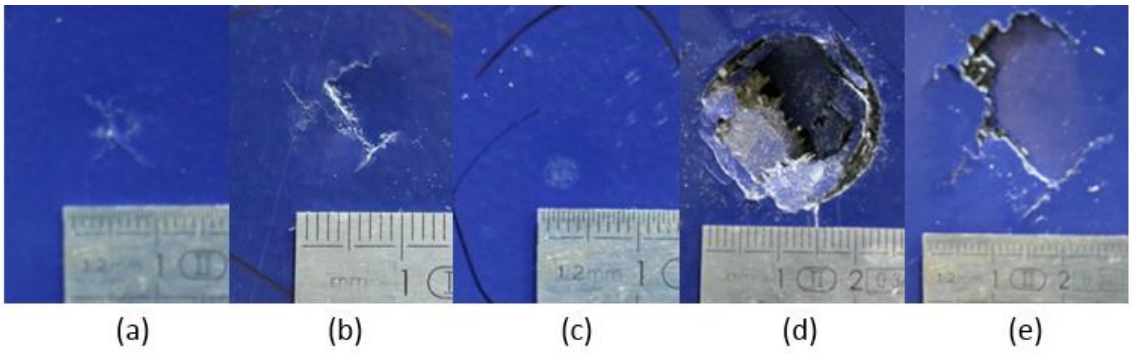

Figure 156 – Damage as a results of impact on the A320 vertical stabiliser wing. Impacts location '1' to '5' labelled 'a' to 'e'.

All the impacts were then located using both arrays, with and without Delta-T mapping in both cases. The predicted locations using the four sensor array are shown in Figure 157 and the predicted locations from the three sensor array are shown in Figure 158. The location errors for each of the impacts using all of the techniques are compared in Figure 159.

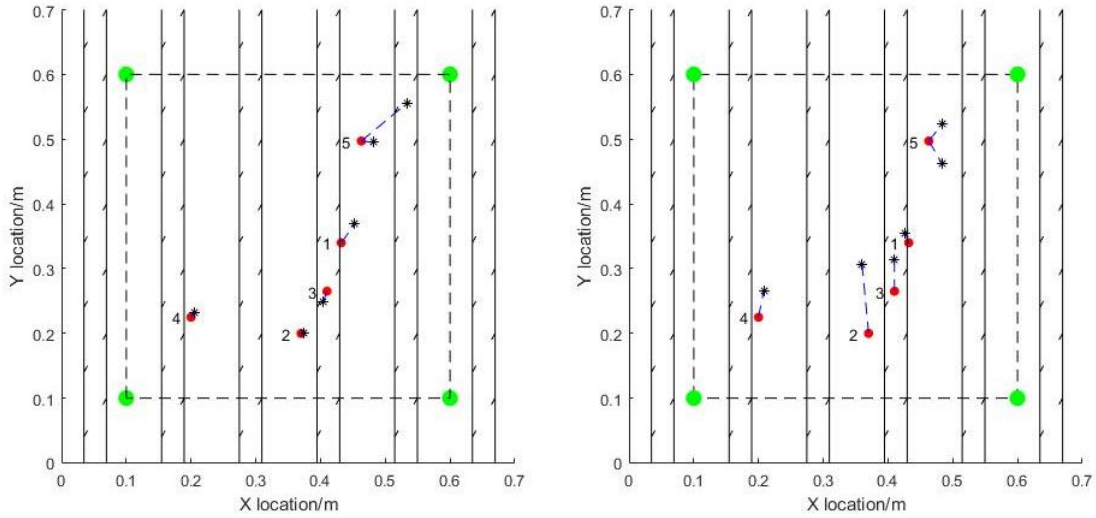

Figure 157 – Predicted locations (Black '') and actual locations (red circles) of impacts on the A320 vertical stabiliser using the tradition Delta-T mapping method (a) and TOA approach (b). Mapped area outlined with dashed lines, sensors shown in green and stiffeners in black.*

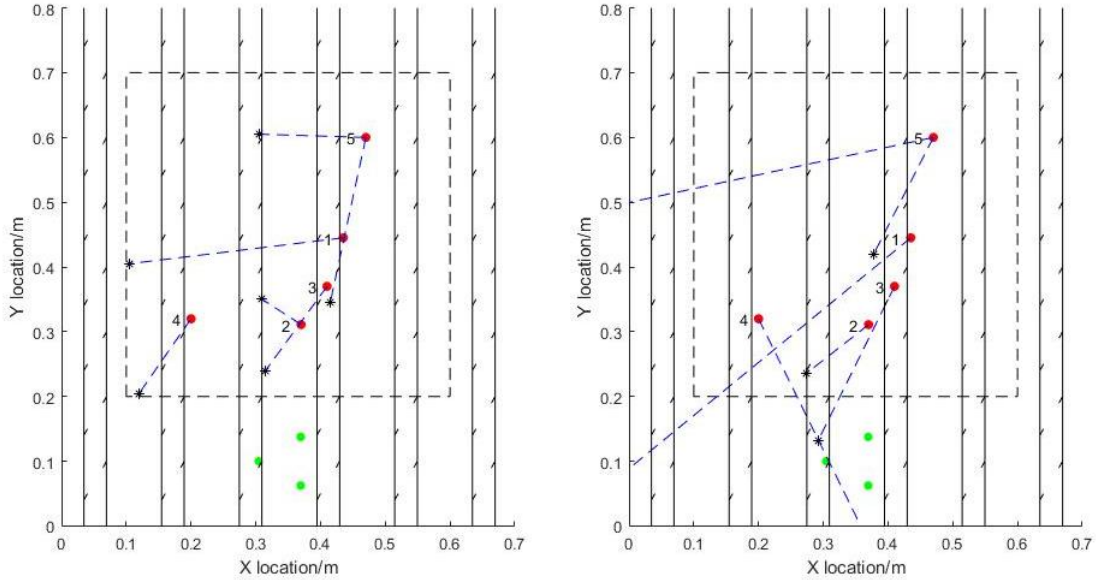

Figure 158 – Predicted locations (Black '') and actual locations (red circles) of impacts on the A320 vertical stabiliser using the Delta-T mapping method (a) and traditional three sensor approach (b). Mapped area outlined with dashed lines, sensors shown in green and stiffeners in black.*

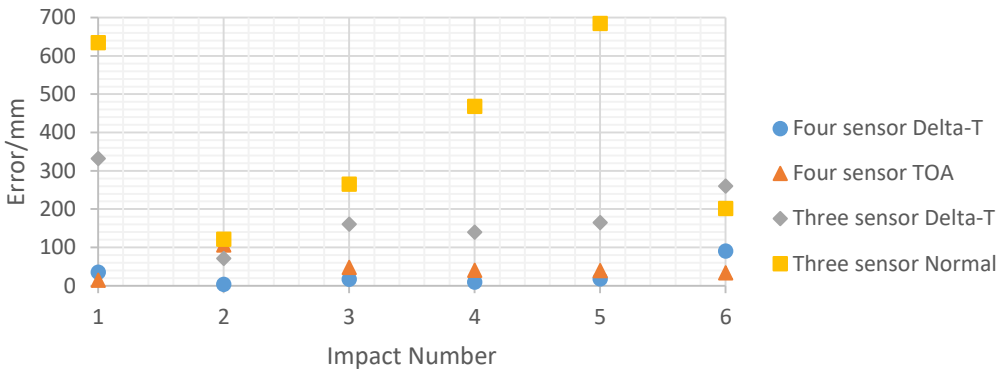

Figure 159 – Location error for each impact using the four different methods of location prediction

6.4.4 Discussion

The testing within Section 6.4 compares the location accuracy using not only the two different three closely spaced sensor methods, but an array of four sensors spaced over the structure as is used in traditional AE testing. It is clear from the H-N source testing that the traditional array of spaced sensors is significantly more accurate, the mapped approach having an error of 24mm compared to 64mm using the mapped three closely spaced sensor method. The three sensor approach however was at a significant disadvantage as it was located outside the array, with some of the events being 600mm away from the sensors. If the sensors were in the centre of the grid the maximum distance would only be 0.35m, and taking into consideration only those events with a distance less than this gives an average error of 44mm. Given the advantages of the three sensor method, primarily the reduced number of sensors and its applicability to be applied to a wireless system, this is very positive.

When locating impacts, as for the H-N sources, the four sensor method was significantly more accurate. The maximum error when locating an impact was 91mm for Delta-T and 106mm for TOA, both of which are within the 200mm target. The sensors in this setup are too close together to be feasible for large scale application, however it would be expected that when scaling up the error would scale at a similar level as long as the arrival of the waves can be accurately predicted. The three sensor technique however was much less effective, without mapping only a single

impact was within the 200mm accuracy that was being aimed for. Mapping improved the technique significantly, meaning four of the six impacts were located to within 200mm. Although the mapping technique was significantly better this may be a slightly false result for impacts 1 and 4 which were located right at the edge of the mapped area, as the system locates it to the best location, not necessarily the right one. If the entire specimen was mapped it is likely that the system would predict the locations outside of what is currently mapped, meaning the error would be much greater. It could also be seen that for all but one of the impacts the distance error was significantly less than 200mm meaning that the reason for the large errors were primarily due to the angle prediction accuracy, which was caused by inconsistencies in the AIC prediction method. As discussed in Chapter 4, the AIC technique is able to accurately detect the start of the waveform, however it doesn't consistently pick the same point on each wave. This is made worse with impacts as the S_0 frequencies are much lower than for a H-N source, meaning that the time error caused by the AIC being 10% of a wavelength off will be much larger for impacts than for higher frequency sources. One potential solution to this would be to increase the size of the sensor array, which would increase the TOA difference between the sensors, reducing the influence of the AIC error on the angle prediction.

Overall the four sensor technique was significantly more accurate in detecting H-N sources and impacts than the three sensors in a close array, however the three sensors were monitoring a significantly larger area than was being monitored by the four sensors. The three sensors also have the advantage of being easier to integrate on a structure, as wiring is required in less locations. Further investigation is required for both approaches before application on a larger scale, particularly in terms of aiming to increase the area which is being monitored.

6.5 Conclusions

Overall applying the Delta-T mapping approach increased the reliability of the three sensor method in all structures, with more data predicted within 200mm accuracy than when using the normal approach. The technique also increased the precision; in every test the average error was lower and more events were identified with an error of less than 50mm. The greatest improvements were seen in composite structures, where small changes in dispersion with changing direction could be accounted for. When the mapped three sensor approach was compared with the traditional Delta-T mapping method in a complex composite structure, it was seen that the spaced sensor approach gave a higher level of precision and was able to reliably detect more of the trial events. Being outside the mapped area the three sensor method was at a significant disadvantage, but when considering only events which were within a similar distance to the four sensor approach, the reliability was similar. Although a lower level of precision was seen, considering that less sensors are able to cover a similar area, the mapped three sensor approach could be considered to be as effective at detecting H-N sources in complex structures as using a traditional spaced array, depending on requirements.

Using the three sensor approach to detect impact damage in a complex composite structure showed potential, however the accuracy seen in the testing presented within this chapter was low. Nevertheless modifications to the setup could make the technique viable for monitoring a large area with very few sensors, if a high level of accuracy is not a requirement.

7 Fatigue Testing on a Real Aircraft Structure

The majority of testing within this thesis, of both with wired and wireless systems, has been tailored to detect fatigue damage in aircraft structures, however only H-N sources have been detected. The H-N source is a standard used within industry and academia for AE testing, and is generally accepted to produce a similar wave to fatigue damage growth. It has been used extensively by a number of authors (Baxter et al., 2007, Eaton et al., 2012a, Al-Jumaili et al., 2016, Holford et al., 2017) to produce and test Delta-T maps, using arrays of spaced sensors, which have been used to accurately locate fatigue growth in complex composite and aluminium structures. The testing performed by these authors reinforces the applicability of the H-N source, however it can never fully replace locating real fatigue damage, meaning fatigue testing is required using the three sensor technique prior to any real case implementation of the system.

Aljets (Aljets, 2011) showed that the three closely spaced sensors could be used to detect cracking and stiffener debonding on simple composite structures. These two tests showed that the technique was able to locate real damage, however a number of factors made this testing very simple and so unrepresentative of a real aircraft structure. Firstly both tests were loaded statically, this means that the background noise present within the testing was low compared to a fatigue test. Additionally, as the specimens were failed statically, the damage occurring was not due to fatigue as is typically the case in real structures. Finally the tests were setup with the sensors between 100mm and 200mm from the damage location, this only proves the ability of the technique to detect damage over a small region. Although this testing showed that the technique works with real damage in simple structures, as it intended to, the approach is a long way off being suitable as a SHM technique in a real structure.

This chapter presents the results from fatigue testing of the aluminium A320 wing panel, where the techniques presented within Chapters 4 and 6 are used to locate real damage in the real aircraft structure. Additionally, traditional Delta-T mapping using a spaced array is tested and compared to the three sensor techniques. The aim of this test was to compare the accuracy of

the three techniques to detect real damage in a test which is as representative as possible to an inflight aircraft.

7.1 Test Overview

The aluminium A320 wing panel (introduced in Section 3.2.8) was used to test the normal three sensor technique presented within Chapter 4, and the mapping technique presented within Chapter 6, to detect real damage on a real aircraft structure. Throughout this chapter these will be referred to as the 'normal three sensor technique' and the 'three sensor Delta-T technique'. To test these methods three Nano-30 sensors were bonded 60mm apart (this spacing was used due to space restrictions between stiffeners) on the inside skin of the panel. The sensors were located in the position shown in Figure 160, where the complexity in the structure is also shown.

Additionally, this testing aimed to test the normal Delta-T technique where sensors are bonded far apart, the code for which was written by Pearson (Pearson et al., 2017) and within this chapter will be referred to as the 'four sensor Delta-T technique'. To do this four Nano-30 sensors were bonded in a spaced array covering an area of 0.5m x 0.3m, the location of the sensors on the panel are shown in Figure 160. The spacing was based on the attenuation testing presented in Section 3.2.8, where at 45^{o} A_0 attenuated at 74 dB/m and S_0 at 49 dB/m. The separation used ensured that a source anywhere within the array was no more than 0.5m from three of the sensors (three being the minimum needed for location). This ensured the detection of a source with a high amplitude, however if the event was very low it may still not be detected.

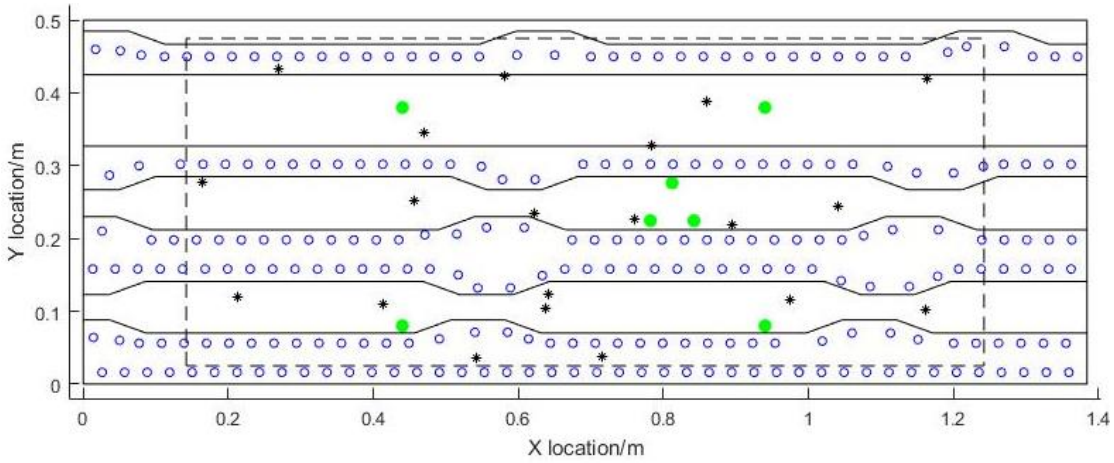

Figure 160 – Location of sensors (green filled markers) on A320 panel with stiffeners (black lines), rivets (blue circles), H-N test locations (*) and mapped area (dashed lines)

A 1.1m x 0.45m grid was drawn at a density of 50mm on the outside skin of the A320 panel, the area mapped is indicated by dashed lines in Figure 160. The maps for the three sensor array are shown in Figure 161 and the maps for the four spaced sensors are shown in Figure 162. A total of 20 locations were then selected, these locations are shown in Figure 160. 18 of these locations were selected at random, two (the ones near x=0.6m and y=0.1m) were not. Later in the testing a hole and notches were created between these points to induce a crack, the test points were therefore chosen to ensure that the technique was able to detect an AE source produced at these locations. Ten H-N sources were created at each location in order to test the maps which were produced.

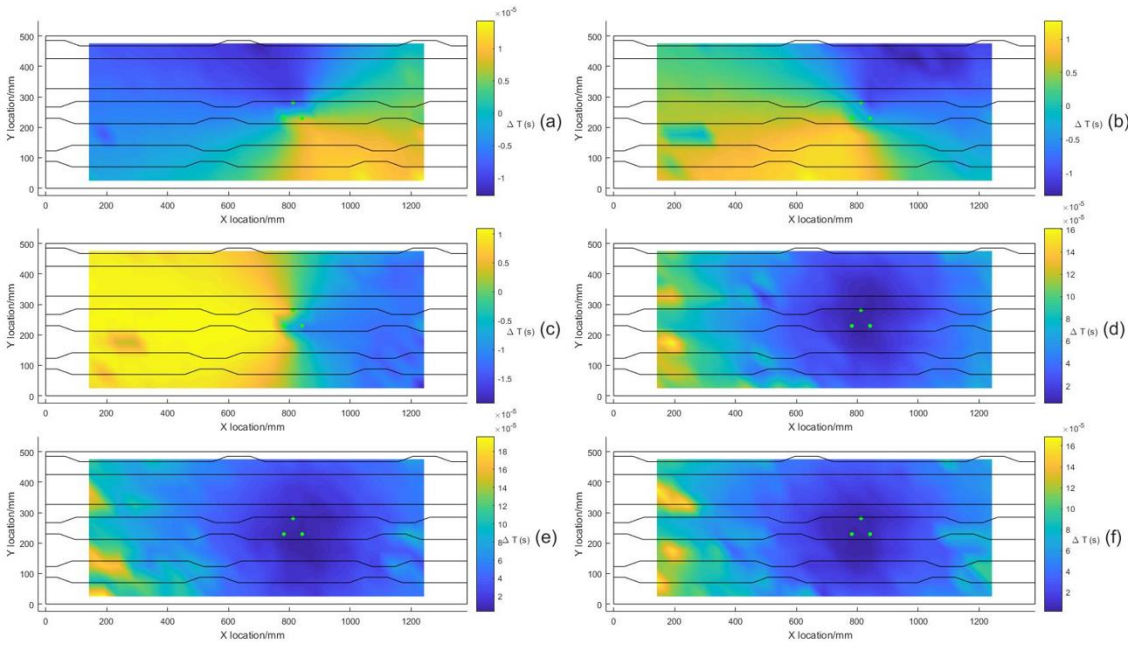

Figure 161 – Delta-T maps from the three closely spaced sensors on the A320 wing panel. (a), (b) and (c) show TOA difference between 1-2, 1-3 and 2-3. (d), (e) and (f) show dispersion at sensors 1, 2 and 3. Sensors shown in green.

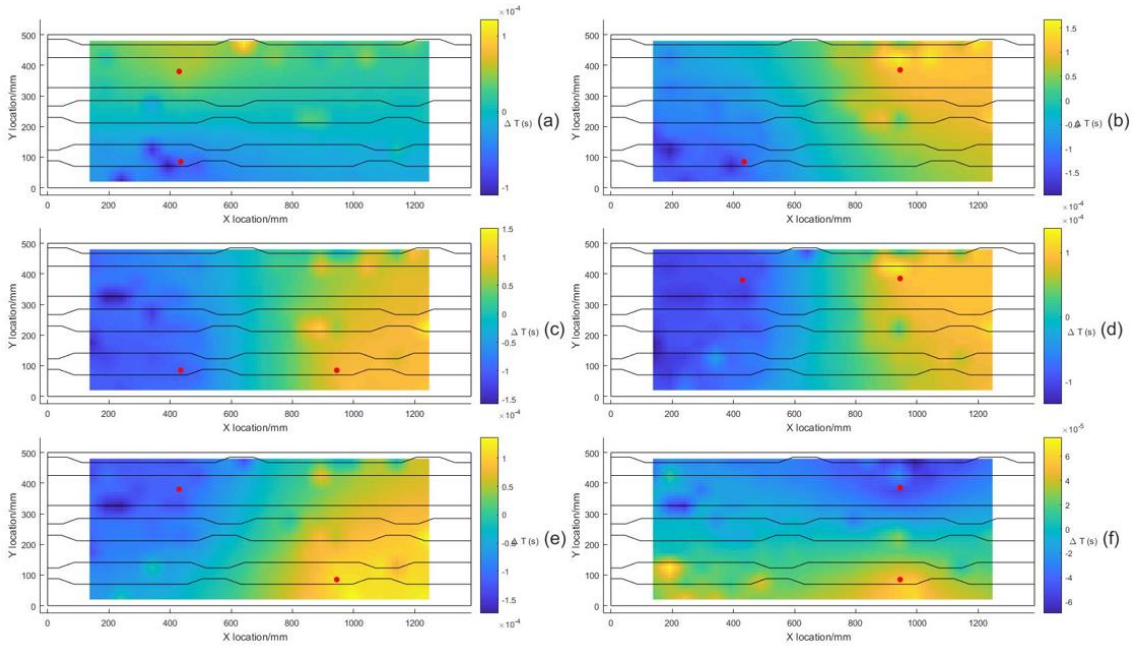

Figure 162 – Delta-T maps from the four spaced sensors on the A320 wing panel with sensors pair 1-2 shown in (a), 1-3 (b), 2-3 (c) 1-4 (d), 2-3 (e) and 3-4 (f). Sensors used to create each map are shown in red

7.2 Artificial Testing Results

In order to test the accuracy of the maps produced using the two arrays of sensors the data recorded from the H-N sources produced at 20 locations on the panel was processed using the different localisation techniques. The locations predicted using the three closely spaced sensors with both the Delta-T and the normal methods are shown in Figure 163.

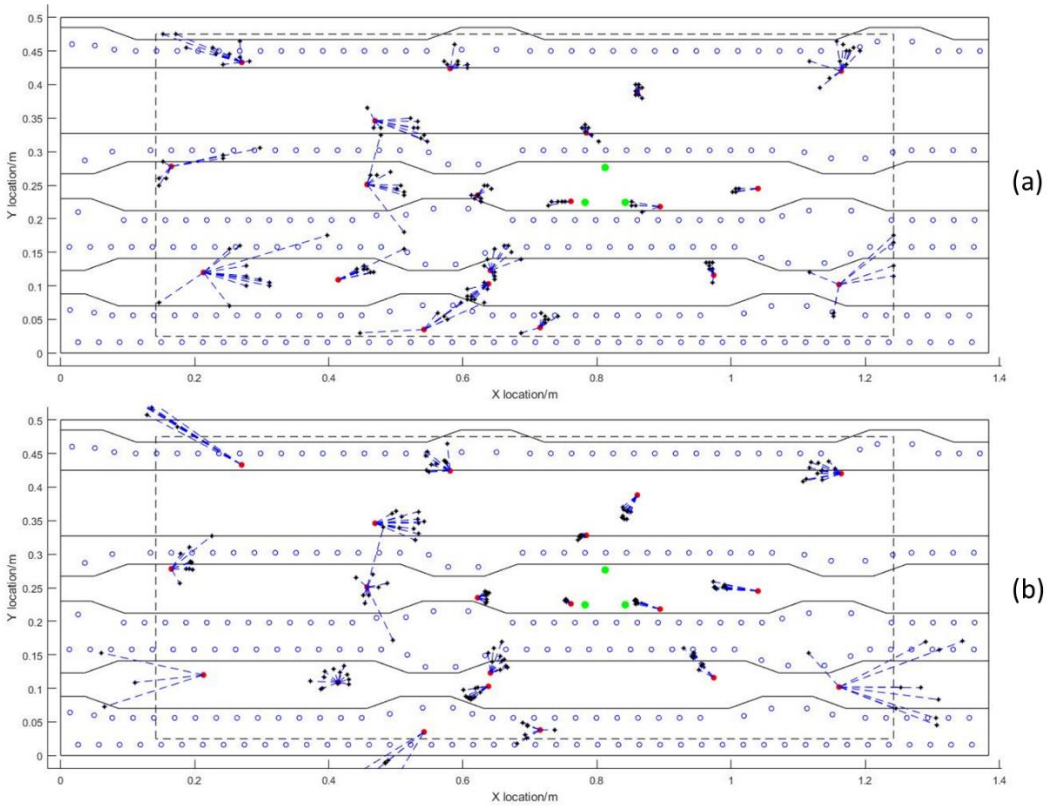

Figure 163 – Predicted locations (Black '') and actual locations (black circles) of H-N sources on the A320 wing panel using the Delta-T mapping method (a) and traditional three sensor approach (b). Mapped area outlined with dashed lines, sensors shown in green, holes as blue circles and stiffeners in black.*

The predicted locations using the Delta-T map with the four spaced sensors is shown in Figure 164.

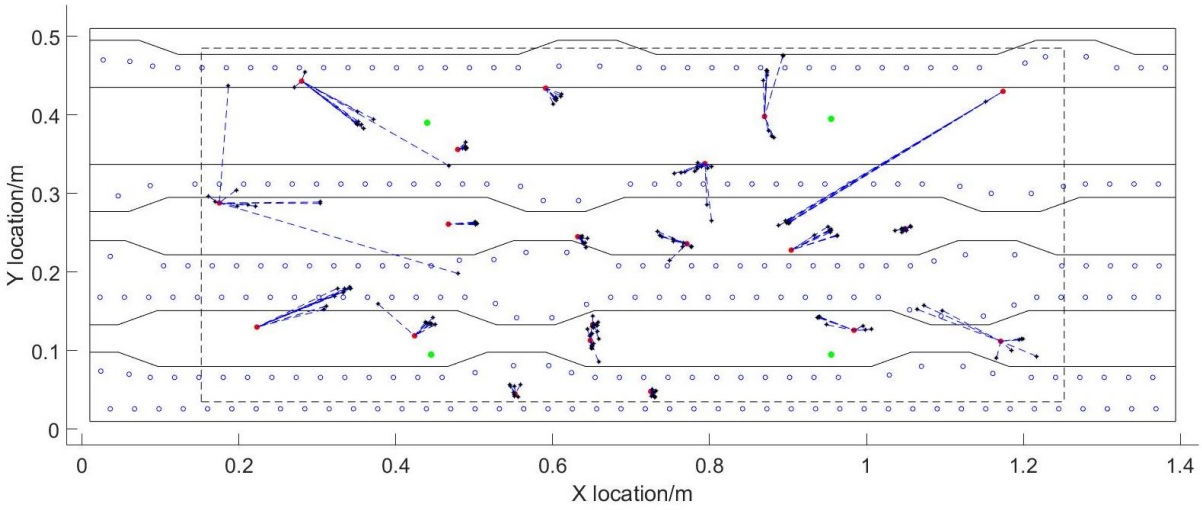

Figure 164 – Predicted locations (Black '') and actual locations (black circles) of H-N sources on the A320 wing panel using the Delta-T mapping method from four spaced sensors. Mapped area outlined with dashed lines, sensors shown in green, holes as blue circles and stiffeners in black.*

The average location, angle and distance accuracies as well as the percentage of data within 50mm, 100mm and 200mm error for the two techniques which utilise the three closely spaced sensors are shown in Table 33. Additionally within Table 33 the average location error and the percentage of data within each level of accuracy when locating the H-N events using the four sensor Delta-T technique is shown.

Table 33 – Average errors and percentage accuracies when locating H-N sources on the A320 wing panel using the three sensor Delta-T, traditional three sensor methods and Delta-T of four sensors in a spaced array

	Delta-T 3 sensors	Normal 3 sensors	Delta-T 4 sensors
Average location error (mm)	37	46	34
Average Angle error (°)	2.9	3.2	-
Average Distance error (mm)	32	41	-
Data less than 50mm error (%)	78	71	72
Data less than 100mm error (%)	95	84	87
Data less than 200mm error (%)	100	94	94

7.3 First Stage Fatigue Testing

The panel was initially loaded as a six point bend test, as shown in Figure 165, where the specimen was supported on the outside skin at each end with roller supports and a system of beams and roller supports spread the load between four points across the stiffeners.

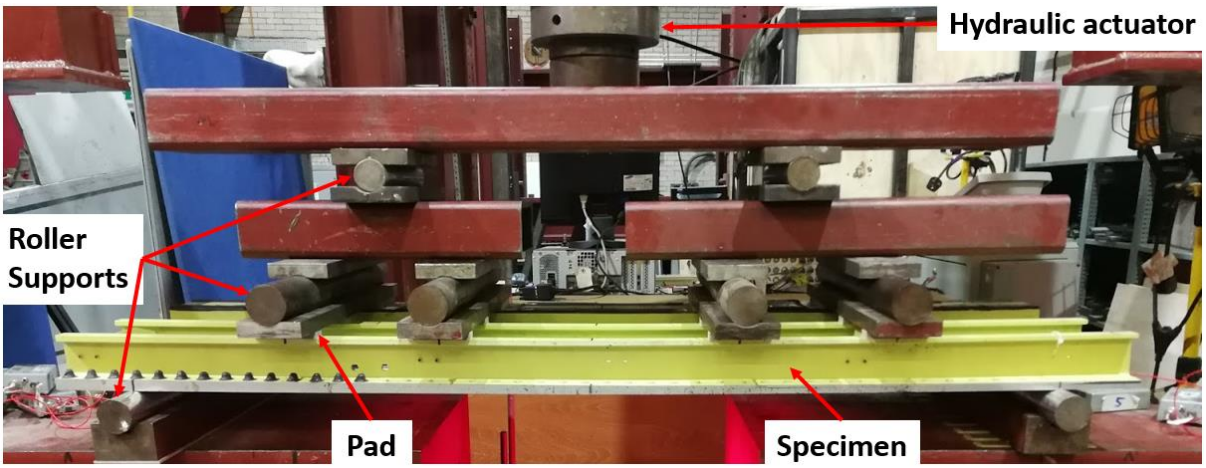

Figure 165 – Panel in six point bend test

Prior to the addition of any damage to the structure eight loading schedules of 10,000 cycles were performed on the specimen, the greatest load in these tests was 25kN. A full list of the loading performed on the specimen can be seen in Appendix A.

After the initial loading a 7mm hole was drilled in the skin of the panel between two stiffeners. A small saw was then used to create a notch on either side of this hole. A razor blade and hammer were then used to create a sharp end to the notch to promote crack growth. An image of the hole and notches is shown in Figure 166 (a) as well as the location of the hole in Figure 166 (b).

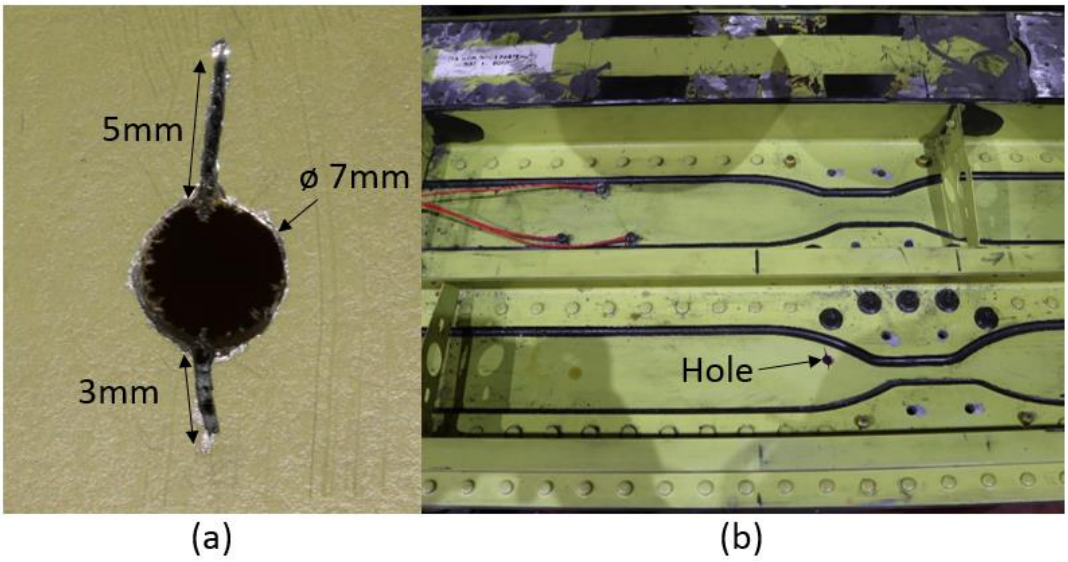

Figure 166 – Image of hole and notch (a) and location of hole and notch (b)

Once the hole and notches had been made additional loading was performed on the specimen with the aim of inducing a crack from one of the notches which could be detected (and located) using the AE sensors. 37 more fatigue tests were then performed on the specimen using this setup, with the maximum load steadily increased up to 85kN, information about all the loads can be seen in Appendix A. Within this time minor changes were made to the setup in an attempt to reduce noise within the testing, which increased as the load was raised. All of these tests were performed at a loading rate of 1Hz and a minimum load of 5kN.

7.3.1 Results

Each test generated very large amounts of data, this meant that between each test it was not possible to process all the data being generated. Instead, a small sample of data was processed to identify if events were being located to a particular area which would indicate the presence of damage.

Early testing did not reveal any damage and although a large number of events were being detected by the system, these were either randomly spread over the structure or being located at the ends of the panel or near to where the panel was loaded. It is believed that the events at

the ends of the panel were a result of the specimen moving over the roller supports and causing noise or where the pads were moving and generating noise. This was the case throughout the preliminary testing and the tests after the addition of the hole to the structure.

As the load was increased more data was recorded by the system, however no areas of interest could be identified. In the final test conducted as a six point bend test, at a load of 85kN, the data rate was too high for the Mistras system to record fully, meaning that it automatically lowered the sample rate to 1MHz. This data rate was too low for waveforms to be properly analysed.

After the final 85kN test stage a crack (approximately 4.5mm long) could be seen by eye at the end of one of the 3mm notches, which can be seen in Figure 167.

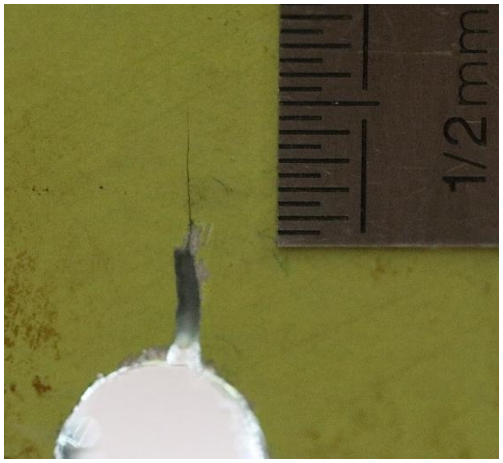

Figure 167 – Crack as viewed from outside skin of the plate when the specimen was loaded to 85kN.

7.4 Second Stage Fatigue testing

After preliminary analysis of the data it was clear that the noise produced by the rig was causing too much data to be recorded by the AE system. The number of moving parts within the test setup, movement and degradation of the pads being used to connect the rig to the specimen and movement of the specimen within the rig all played a part. In some cases, for example Test '37' where the load was taken to 85kN, the data rate was so high that the AE system

automatically dropped the sample rate to 1MHZ, which was too low for the technique to be effectively applied.

In an attempt to reduce background noise, testing from this stage onward was conducted in a four point bend test, as shown in Figure 168, to reduce the number of moving parts. Additionally, supports were added to stop the specimen moving whilst being loaded and shaped nylon pads used to stop the degradation and movement of the pads. The rate of loading was also reduced from 1Hz to 0.5Hz and in the final tests to as low as 0.1Hz. The load was taken to a maximum of 80kN in this set of testing. A total of 20 load cycles were applied to the specimen in this configuration, information on these cycles can be found in Appendix B. Throughout this testing the induced crack (shown in Figure 167) was monitored using a camera in-between each test.

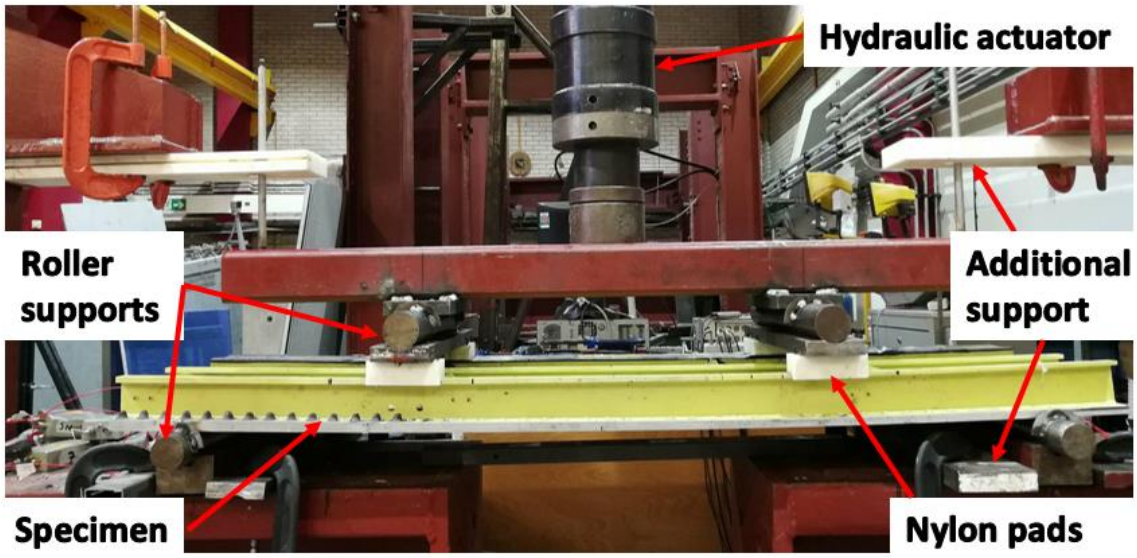

Figure 168 – A320 panel in four point bend test

7.4.1 Results

During tests 1 – 15 once each test had been conducted the data was processed using the three sensor Delta-T technique, due to time limitations this was the only method used to analyse the results before the next test was conducted. A set of example results, recorded during test 15 and predicted using the three sensor Delta-T method, are shown in Figure 169. This set of data

is typical of all data using the Delta-T method, and although it shows a lot of data coming from certain locations, as these locations are typically close to the edge of the panel it was deemed that they were a result of noise from the roller supports (shown as dashed lines in Figure 169) and from the loading on the stiffeners locating badly as they are not in the mapped area. A visual inspection of the plate gave no indication of cracks in any of these areas. It was also noted that no areas of substantial AE activity could be seen near the crack, this was despite the gradual growth of the crack, as shown in Figure 170.

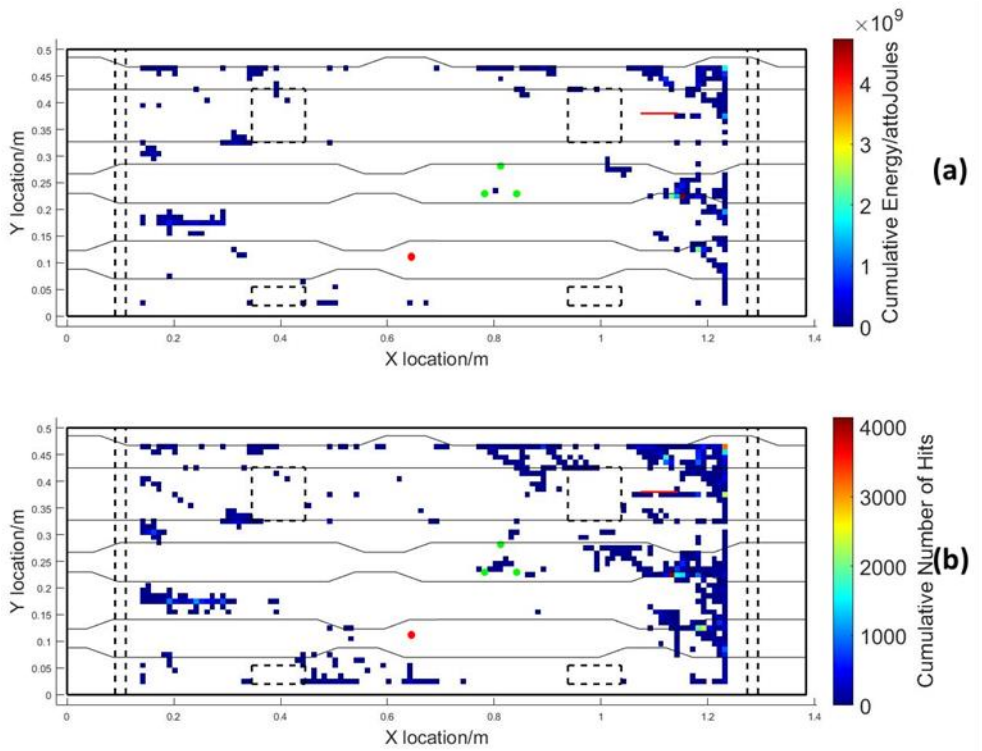

Figure 169 – AE data from four point bend test 15 located using the three sensor Delta-t method showing cumulative energy (a) and cumulative number of hits (b) with a bin size of 10mm. Loading locations shown by dashed lines and edge of panel and stiffener locations indicated by solid lines. Hole with notches shown as red circle.

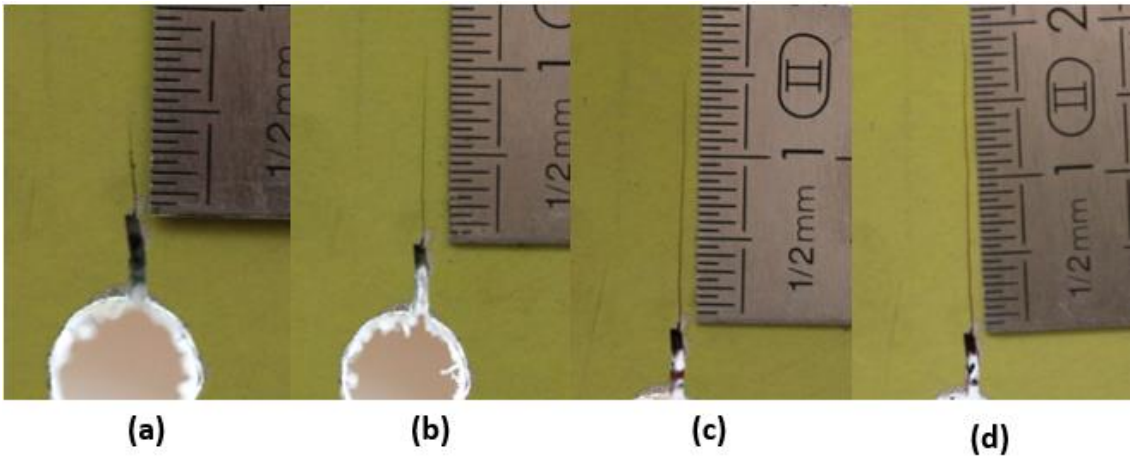

Figure 170 – Imaged of the crack in the notch before test 1 (a), test 15 (b), test 17, (c) and after test 20 (d)

After test 15 the data was processed using the normal three sensor technique to give a different representation of the data. The results from processing test 15 using the normal method are shown in Figure 171. These results show the AE data is a lot clearer, with in particular a large number of events occurring where the panel was supported on its far right hand side, but also a location to the right of where it was being loaded by the nylon pad (shown by dashed lines in Figure 171). These results prompted a thorough visual inspection to be performed on this area. The skin of the panel showed no signs of damage however an inspection of the stiffeners revealed a 60mm crack. The stiffeners in this area are connected by a 2mm thick aluminium plate, shown in Figure 172 (a), which is riveted and bonded to the top of the stiffeners. On this plate was a 60mm long crack, shown in Figure 172 (b) and (c). Dye penetrant was used to confirm the size of the crack, and that it passed through the depth of the plate. The location of the crack is indicated by a red line on the plots in Figure 171 at x=1.1m and y=0.37m.

Analysis of earlier data revealed that this location was present throughout the entirety of the second stage of testing, and first occurred part way though test 34 in the six point bending test setup. Test 34 was the first test where the panel was taken to 85kN, its maximum load.

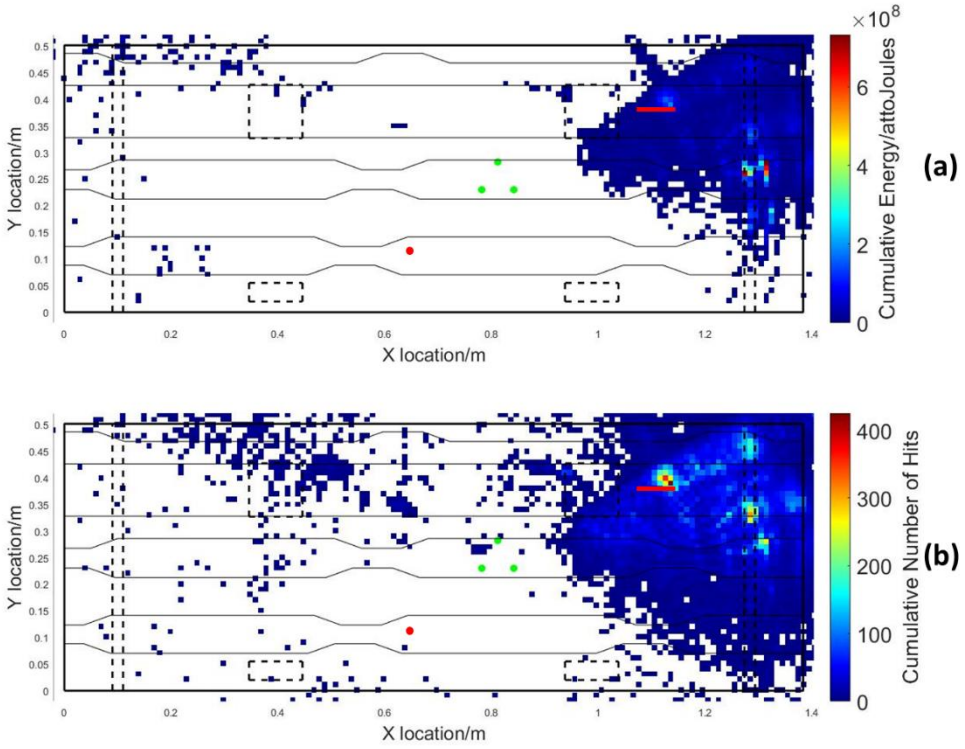

Figure 171 – AE data from four point bend test 15 located using the three closely located sensors normal technique showing cumulative energy (a) and cumulative number of hits (b) with a bin size of 10mm. Loading locations shown by dashed lines and edge of panel and stiffener locations indicated by solid lines. Crack on stiffener shown as red line.

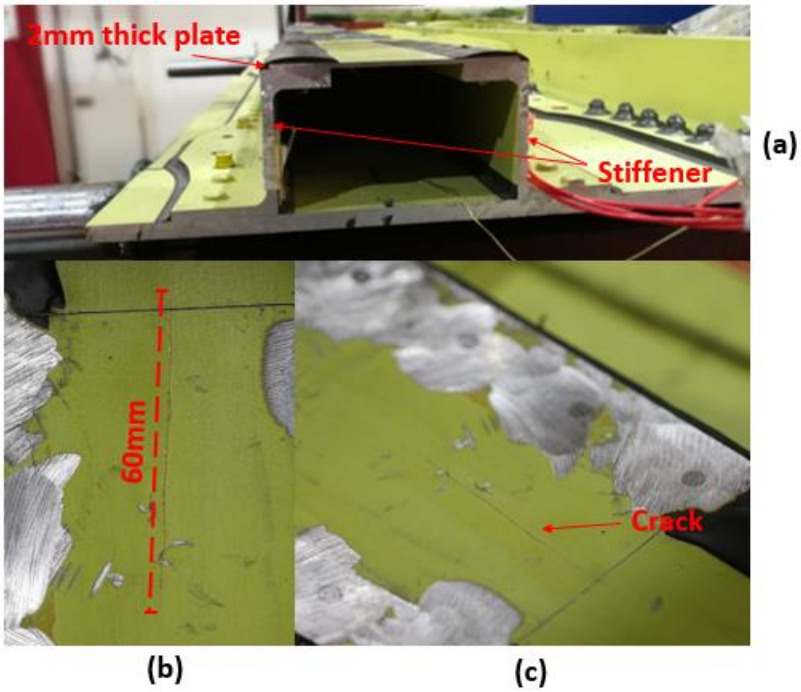

Figure 172 –Image of plate connecting two stringers (a) and images of crack on plate (b) and (c).

Although the crack was almost exactly where the data was showing a lot of AE activity because the damage was very close to where the panel was being loaded it cannot be said for certain that the AE events are due to the damage. To better understand how the techniques would locate an event coming from the location of a crack H-N events were conducted every 10mm along the length of the crack and the waves produced recorded using the three sensors. This data was then processed using the Delta-T and normal methods and shown in Figure 173.

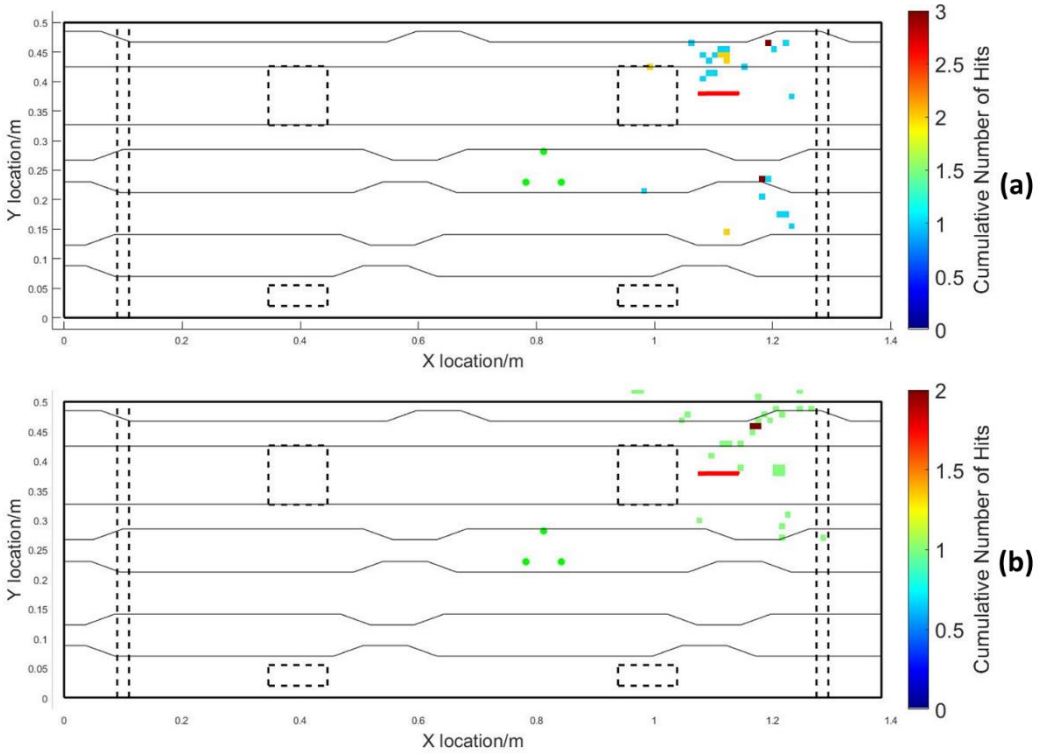

Figure 173 – H-N events along the crack on top of stiffnerer (shown as a red line) located using the three sensor Delta-T method (a) and normal method (b).

The data from 500 cycles of test 15 recorded by the four spaced sensors and processed using the Delta-T method is shown in Figure 174. In Figure 174 although some data is located near the crack the area of highest AE activity (x=0.9, y=0.25) is over 200mm away from the crack.

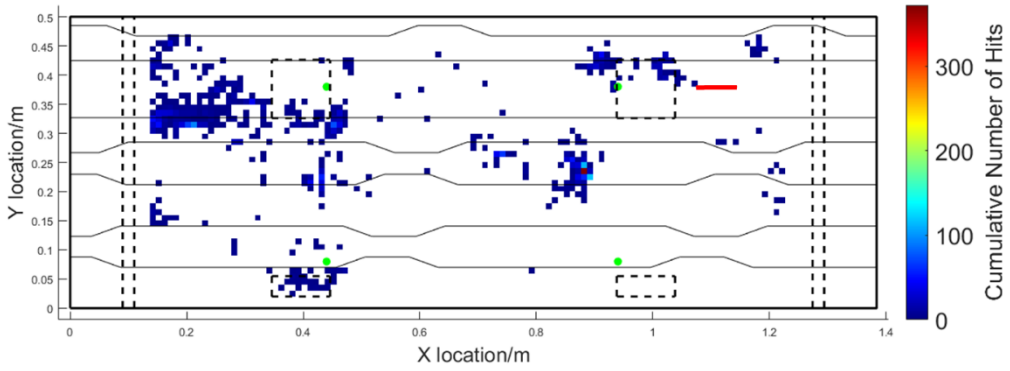

Figure 174 – AE data from 500 cycles of four point bend test 15 located using the four spaced sensors Delta-T method, with a bin size of 10mm. Loading locations shown by dashed lines and edge of panel and stiffener locations indicated by solid lines. Crack on stiffener shown as red line.

Processing the H-N data, which was presented in Figure 173, using the four sensor Delta-T technique gave the locations shown in Figure 175.

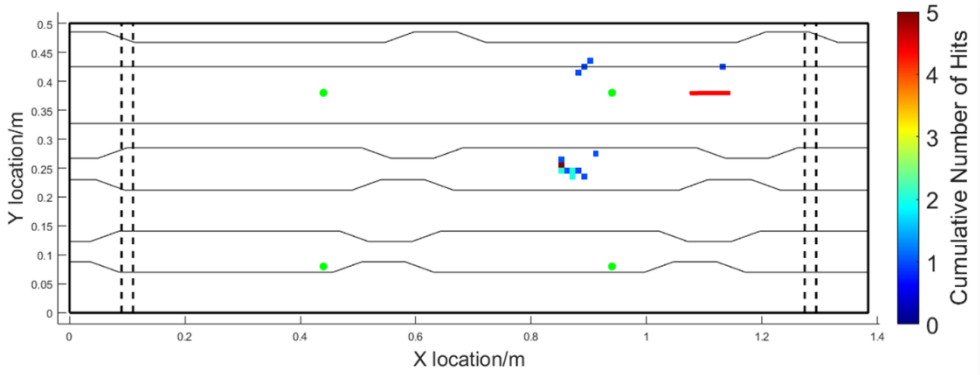

Figure 175 – H-N events along the crack on top of stiffnerer (shown as a red line) located using the four sensor Delta-T method

7.4.2 Discussion of Results

The three sensor Delta-T results in Figure 173 (a) give a good indication that the technique was detecting the crack on the stiffener, as the areas of high AE activity shown in Figure 169 (approximately 150mm below the crack and 50mm above it) are the areas where most of the H-N sources have been located to.

Using the four spaced sensor Delta-T method to locate the data recorded in test 15 showed the peak of AE data over 200mm away from the crack location. This location however matched perfectly with the predicted locations of H-N sources along the crack, giving another good indication that the large amounts of data being recorded are a result of the crack on the stiffener.

The normal three sensor techniques results are less conclusive, in Figure 171 the area of peak activity is located almost exactly on the crack; the H-N data in Figure 173 (b) is less precise.

Although entirely possible, based on this set of testing alone it cannot be confirmed that the approach has detected the crack on the stiffener. In order to understand if the crack was being detected the test setup was changed significantly, as is presented in the following section.

7.5 Third Stage Fatigue testing

Within the testing presented in Sections 7.3 and 7.4 it wasn't possible to conclusively show that the crack on the stiffener was detected using the three sensor method as in both cases the panel was being loaded close to its location. To remove this problem in the final stage of testing the panel was loaded in a three point bend test, as shown in Figure 176. For this testing only a single loading cycle was performed, this consisted of 1,000 cycles at 0.1Hz ranging from 1kN – 60kN.

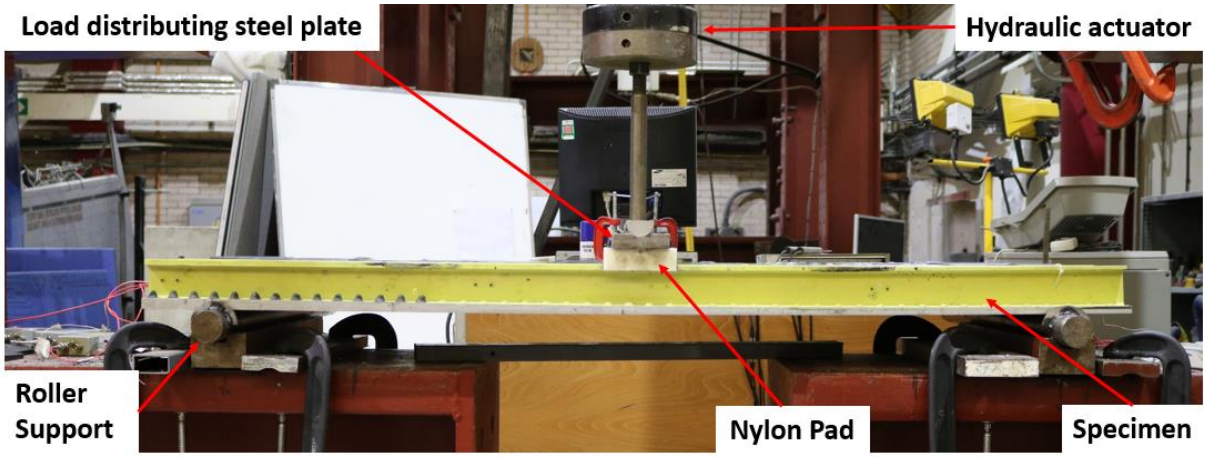

Figure 176 –Annotated image of A320 panel in three point bend test

7.5.1 Results

The AE data from the three point bend test of the panel processed using the normal technique are shown in Figure 177. Here, as in the results from the previous setup shown in Figure 171, the location of peak AE activity is exactly on the crack.

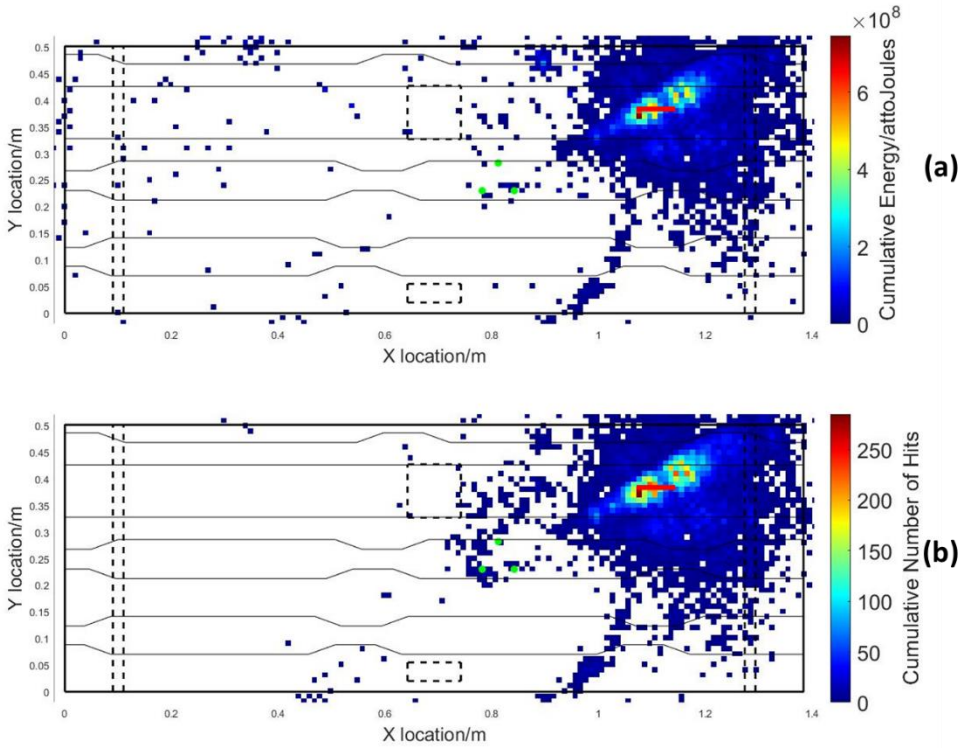

Figure 177 – AE data from three point bend test located using the three closely located sensors normal technique showing cumulative energy (a) and cumulative number of hits (b) with a bin size of 10mm. Loading locations shown by dashed lines and edge of panel/stiffener locations indicated by solid lines. Crack on stiffener shown as red line.

The AE data recorded using the four spaced sensors and processed using the Delta-T technique for the three point bend test is shown in Figure 178.

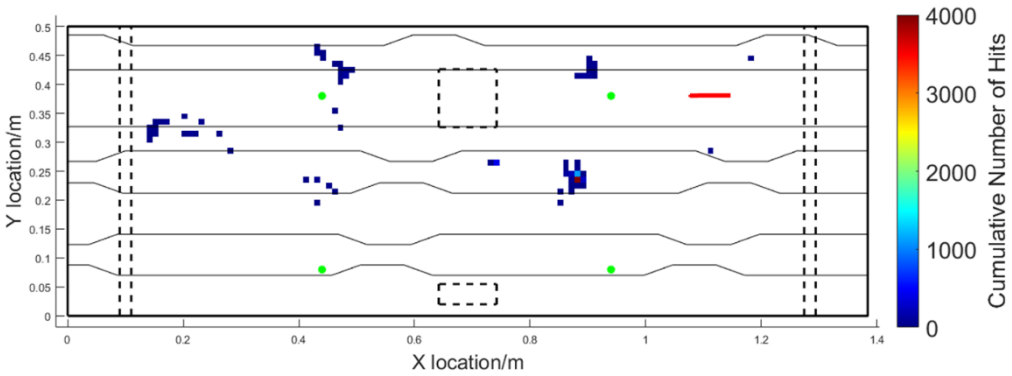

Figure 178 – AE data from the three point bend test located using the four spaced sensors Delta-T method, with a bin size of 10mm. Loading locations shown by dashed lines and edge of panel and stiffener locations indicated by solid lines. Crack on stiffener shown as red line.

7.6 Discussion

The trial data was located well across the panel with all three techniques locating the majority of the data to within 200mm. The three sensor Delta-T technique was seen to be slightly better than the other two methods, locating 100% of data within 200mm, compared to 94% with the other two techniques. Considering only the eight events performed within the four sensors used for the four sensor Delta-T method, the average error was much less at 21mm compared to 38mm using the three sensor Delta-T and 35mm using the normal three sensor method. This is to be expected as the approach of spacing sensors over the structures tends to mean accurate location is only possible within the array, as outside of the array a constant difference in arrival exists for some of the sensor pairs.

During the fatigue testing a crack formed on the skin of the panel from the hole and notches artificially added to the panel. This was not successfully located by any of the techniques used, even though it was seen to be growing throughout the four point bend test. It is believed that the reason that the growth of this crack was not detected is that its growth only gave off a very low amplitude source, which had attenuated before being detected by the sensors. The reason for this is that when a crack grows in aluminium it is due to a ductile fracture which occurs at a slower rate than a brittle one, as would occur in steel (Scruby, 1987). Although it must be

considered that cracks do not typically form on the middle of a plate like in this test and loading on an aircraft is typically not just in a single direction, meaning that the damage induced within this test is not typical of what would be found on an inflight aircraft. A crack also formed on the 2mm thick aluminium plate connecting two of the stiffeners. This crack is believed to have formed as result of the 85kN loading during the six point bend testing, as this was when data was first located to this area, however it was not seen to grow after its detection during test 15. This means that the AE given off from this crack was due to rubbing of its faces, not from the growth of the crack. It is believed that the reason the crack on the 2mm plate produced a lot of AE is that it runs parallel to the stress in the plate, meaning its faces are always in contact, and rubbing. The crack on the skin of the plate at the end of the notch however runs perpendicular to the load, so only releasing energy when the crack closes at low loads.

The crack on the stiffener was located best using the normal three sensor method, where in all tests the area of highest AE activity was at the location of the crack. This was confirmed to be a result of the crack and not due to loading of the structure by the results from the three point bend test presented in Section 7.5.1, where the loading point was not near to the crack and yet data was still seen in the area of the crack. This was despite the crack not being on the same plane as the sensors, meaning that the wave had to travel a longer distance to reach the sensor. This issue caused inaccuracies in the distance prediction of the H-N tests presented in Figure 173.

None of the mapping techniques on the other hand were very accurate at locating the crack on the stiffener. This is likely to be because the mapping only occurred on the skin of the panel meaning that if events occurred outside of this, the technique struggled to locate the event and so output a best fitting scenario. The four sensor Delta-T technique calculated the location between the two right hand sensors, which is to be expected as the quickest wave path from the crack on the top of the stiffener to the sensors on the skin is very close to this location. The three sensor Delta-T technique was able to accurately predict the distance to the source but was

unable to find the angle of arrival. It is not fully clear why this is, however it is likely to be due to the multiple wave paths of the S_0 mode triggering the three sensors differently to the way in which the mapping approach did, making an accurate prediction difficult. The normal three sensor technique on the other hand is based on the ratios between arrival times, so is less affected.

7.7 Conclusions

The test presented in this chapter aimed to show the techniques presented in Chapters 4 and 6 were able to be used to locate a real fatigue crack in an aircraft structure. Unfortunately the crack induced in the skin of the structure within the mapped area did not produce a 'loud' enough source to be detected by the sensors used within the test. A secondary crack however was detected by the techniques, but was only accurately located using the normal technique which was presented in Chapter 4. The success of this shows that the second differential method is able to predict the distance in which a source from a real damage AE event travelled, despite the complexity of the structure. It also shows that it is possible to predict the angle of arrival of a real source using the ratios method. The failure of this test to detect the main crack must question the ability of the AE monitoring, both using a closely spaced array and a spaced array, for the detection of fatigue cracks in thick ductile structures, such as aluminium wings, if it is only possible when sensors are very close to the source. However additional testing, aimed at detecting more representative damage is required.

8 Conclusions and Future Work

Within this work, further development of the three closely spaced sensor technique to locate AE events has been presented, in which it was taken from a technique which was only suitable for simple plate like structures, to accurately locating a crack in a complex aluminium aircraft panel. The main changes made to the technique, when compared to that used by previous authors, was the utilisation of frequency filters, the use of the AIC technique and the application of the newly developed second differential method. With each change to the technique testing was performed on a simple structure to ensure an improvement was observed.

The use of frequency filters instead of wavelet analysis allowed non-threshold based time of arrival prediction techniques to be used to detect the arrival times of the S_0 and A_0 modes. The AIC technique was shown to be very reliable at detecting the start of the S_0 mode, however more precise detection of the same point in each wave was seen with a threshold trigger. This was only the case in simple structures. When complexity was added the AIC technique was significantly more accurate. The novel second differential method was shown to be effective in predicting the A_0 which was used for SSMA, both in simple and complex structures. The high threshold of the technique allows reasonably accurate detection of the A_0 mode even when S_0 to A_0 mode conversion is present. These changes, as well as using the S_0 mode to predict the angle of arrival, enabled the technique to accurately locate AE sources in complex metal and quasi-isotropic composite structures. The ability of the SSMA technique to be able to predict the distance a wave has travelled within a complex structure has potential application outside of the three sensor technique and aerospace application. There are a number of fields of engineering where this could be beneficial, and so more research should be conducted. One area being long, linear structures such as wind turbine blades where, by using well selected localisation techniques, very few sensors may be able to monitor a large portion of the structure.

The development and application of a Delta-T mapping technique, which was tested on a range of structures, has also been presented. Testing showed an increase in the accurate range of the

approach, in particular within composite materials, when compared to the unmapped method. Overall both mapped and unmapped techniques were shown to be able to locate AE sources over similar areas as when using a spaced array of sensors, however to a lower level of accuracy. The advantages regarding ease of integration, the ability to monitor areas where sensors cannot be bonded and the reduced number of sensors make using an array of closely spaced sensors to monitor a structure an option that should be considered instead of a spaced array.

The techniques developed within this work were used to detect a crack within an aluminium A320 wing panel under fatigue loading. This was done successfully with one crack using the non-mapped method, however due to the damage being outside of the mapped area, the Delta-T mapping was unable to accurately locate the crack. This was also the case using the Delta-T approach with a spaced array of sensors. Another crack was not detected by any of the methods used as the AE being released from the crack, and any rubbing of its faces, was too low energy to be detected by the sensors. The techniques were also applied to detect impact damage in a complex composite structure. Although some impacts were accurately located overall the approach was unsuccessful. This was not the case using a spaced array, which was able to locate all the impacts to a good level of accuracy.

The testing within this thesis showed that the three sensor technique, both with and without Delta-T, was able to locate artificial H-N events in a range of simple and complex structures. The testing with real loading however was limited, only a single test being performed which achieved mixed results. This means that significantly more testing is required before the method can be considered as a viable option for SHM in a structure. This testing should focus on composite materials, as this is the direction the aircraft industry is heading in and also the failure to detect the crack in the skin of the A320 panel indicates that AE monitoring of aluminium structures is a challenge without sensors being very close to the damage. The failure to accurately locate the crack on the stiffener using either of the Delta-T methods shows that more research is required

to properly apply this approach to complex structures, ideally detecting more representative damage.

The development of a low power wireless damage detection system has also been presented within this thesis, with three different versions of the hardware being discussed. Two way wireless communication was possible in all versions of the system, including the ability to communicate with a GPS hub which uploaded the data to a cloud based server and accessed it via a bespoke GUI. All versions applied a simplified version of the three sensors technique developed in this work, using analogue front end frequency filters to split the S_0 and A_0 modes. The arrival times of these modes were then detected using a threshold technique or, in the case of the Mk 3 node, a parameter extraction algorithm to detect the maximum amplitude of the A_0 mode. The systems were very low power in comparison to any commercially available wireless AE systems, the only available options operating upwards of 300mW. The SENTIENT system in comparison requires between 16.4mW and 37.6mW depending on the operations being performed. This is moving much closer to the power levels which can be generated through energy harvesting on an aircraft structure significantly increasing the possibility of an autonomous system. Each of the wireless systems created was tested on a range of aluminium and composite structures, with the final system being trialled on real aircraft structures. The accuracy and range of the systems in complex structures significantly improved with each stage of development, however they did not reach the levels achieved using a wired system.

Although the system developed is currently too high power for it to be feasibly power constantly by energy harvesting on board an aircraft, this isn't necessarily a problem as periodically putting the node into sleep mode to recharge should still enable the system to detect fatigue damage. The energy available through energy harvesting is also constantly increasing, so more function will become possible as further development occurs. An alternative option is to consider applications where more power is available. If the node was operating in an environment where solar energy was an option then it would have no problem operating for an extended period, if

correctly combined with a supercapacitor or battery to store energy when solar is not available. In the civil and renewables sectors this is often the case, meaning the system could be applied effectively in certain applications in these fields and any future development should consider these and other industries, not just aviation.

The testing within this thesis shows that the wireless system developed has the potential to be applied within aircraft structures to detect AE caused by real damage. Before this could happen further research and development is required in a number of areas. Immediate improvements would be seen with the implementation of the second differential method to detect the A_0 arrival, and so the distance to the source. Although this would improve the accuracy it would also increase processing requirements so consideration would need to be given as to whether this power increase would be worthwhile; as discussed earlier, the best option isn't necessarily the most accurate, but the one that provides the best compromise in terms of fulfilling the full range of requirements. Another option that is worth considering is modifying the hardware filters for each application. Currently the relatively broad A_0 filter works for a number of structures, but tailoring for each application, or at least having a selection of different options, could significantly improve performance. Once the options for potential modifications are considered a full redesign of the Mk 3 hardware is required, doing so would fix the DC offset issue as well as reducing power and crosstalk. This then needs to be tested with real damage to see how it performs, since aspects such as high data rates could prove a problem as the processing is being performed live.

Implementation of AE monitoring in aircraft has the potential to make them more profitable, increase their safety and reduce weight. The techniques developed within this work will allow AE monitoring to be more easily applied to aircraft structures either through a fully wireless system or, if using a wired system, because of the additional ease of integration and reduced number of sensors compared to traditional methods.

9 Appendices

9.1 Appendix A - Loading performed on the A320 panel as six point bend test

Test number	Rate of loading (Hz)	Load Range (kN)	Number of Cycles
1	1	5 - 20	10000
2	1	5 - 25	10000
3	1	5 - 10	6000
4	1	5 - 20	10000
5	1	5 - 25	10000
6	1	5 - 25	10000
7	1	5 - 25	10000
8	1	5 - 25	10000
Hole and Notches introduced			
9	1	5 - 25	10000
10	1	5 -30	10000
11	1	5 -30	10000
12	1	5 -30	300
13	1	5 -30	5000
14	1	5 -30	5000
15	1	5 -30	10000
16	1	5 -30	5000
17	1	5 -30	25000
18	1	5 -30	10000
19	1	5 - 35	10000
20	1	5 - 40	20000
21	1	5 - 45	20000
22	1	5 - 45	5000
23	1	5 - 45	10000
24	1	5 - 45	10000
25	1	5 - 45	10000
26	1	5 - 45	20000
27	1	5 - 45	25000
28	1	5 - 45	10000
29	1	5 - 50	10000
30	1	5 - 70	10000
31	1	5 - 75	10000
33	1	5 - 80	10000
34	1	5 - 85	5870
35	1	5 - 85	10000
36	1	5 - 85	10000
37	1	5 - 85	10000

9.2 Appendix B - Loading performed on the A320 panel as four point bend test

Test number	Rate of loading (Hz)	Load Range (kN)	Number of Cycles
1	0.5	5 - 40	5000
2	0.5	5 - 40	10000
3	0.5	5 - 65	10000
4	0.5	5 - 70	7500
5	0.5	5 - 75	2500
6	0.5	5 - 60	2500
7	0.5	5 - 60	2500
8	0.5	5 - 70	2500
9	0.5	5 - 70	2500
10	0.5	5 - 70	1500
11	0.5	5 - 70	10000
12	0.5	5 - 80	2000
13	0.5	5 - 80	2500
14	0.5	5 - 80	5000
15	0.5	5 - 80	10000
16	0.5	5 - 80	10000
17	0.5	5 - 80	15000
18	0.1	5 - 80	1000
19	0.1	5 - 80	1000
20	0.1	1 - 80	1000

10 References

ABBAS, S., LI, F. & QIU, J. 2018. A Review on SHM Techniques and Current Challenges for Characteristic Investigation of Damage in Composite Material Components of Aviation Industry.

AIRBUS. 2017. *A350 XWB* [Online]. http://www.aircraft.airbus.com/aircraftfamilies/passengeraircraft/a350xwbfamily/. [Accessed 10/10/2017 2017].

AKHLAQ, M. & SHELTAMI, T. R. 2013. RTSP: An Accurate and Energy-Efficient Protocol for Clock Synchronization in WSNs. *IEEE Transactions on Instrumentation and Measurement,* 62**,** 578-589.

AL-JUMAILI, S. K., PEARSON, M. R., HOLFORD, K. M., EATON, M. J. & PULLIN, R. 2016. Acoustic emission source location in complex structures using full automatic delta T mapping technique. *Mechanical Systems and Signal Processing,* 72**,** 513-524.

ALEXANDROV, N., HOLMES, B. J. & HAHN, A. S. 2016. A Benefit Analysis of Infusing Wireless into Aircraft and Fleet Operations - Report to Seedling Project Efficient Reconfigurable Cockpit Design and Fleet Operations Using Software Intensive, Network Enabled, Wireless Architecture (ECON).

ALGHISI, D., FERRARI, V., FERRARI, M., CRESCINI, D., TOUATI, F. & MNAOUER, A. B. 2017. Single- and multi-source battery-less power management circuits for piezoelectric energy harvesting systems. *Sensors and Actuators A: Physical,* 264**,** 234-246.

ALJETS, D. 2011. *Acoustic Emission Source Location in Composite Aircraft Structures using Modal Analysis.* University of Glamorgan.

ALJETS, D., CHONG, A. & WILCOX, S. 2011. Acoustic Emission Source Location during the Monitoring of Composite Fracture using a Closely Arranged Sensor Array *ASME 2011 International Design Engineering Technical Conferences & Computers and Information in Engineering Conference* Washington.

ALJETS, D., CHONG, A., WILCOX, S. & HOLFORD, K. 2012. Acoustic emission source location on large plate-like structures using a local triangular sensor array. *Mechanical Systems and Signal Processing,* 30**,** 91-102.

ANASTASI, G., CONTI, M., DI FRANCESCO, M. & PASSARELLA, A. 2009. Energy conservation in wireless sensor networks: A survey. *Ad Hoc Networks,* 7**,** 537-568.

ASTM 1999. Determining the Reproducibility of Acoustic Emission Sensor Response.

ASTM COMMITTEE E07 ON NONDESTRUCTIVE TESTING 2017. Standard Guide for Mounting Piezoelectric Acoustic Emission Sensors. ASTM.

BAARAN, J. 2009. Visual Inspection of Composite Structures. European Aviation Safety Agency: Institute of Composite Structures and Adaptive Systems.

BAKER, A. 1999. Bonded composite repair of fatigue-cracked primary aircraft structure. *Composite Structures,* 47**,** 431-443.

BANNISTER, K., GIORGETTI, G. & GUPTA, S. K. Wireless sensor networking for hot applications: Effects of temperature on signal strength, data collection and localization. Proceedings of the 5th Workshop on Embedded Networked Sensors (HotEmNets' 08), 2008.

BAXTER, M. G., PULLIN, R., HOLFORD, K. M. & EVANS, S. L. 2007. Delta T source location for acoustic emission. *Mechanical Systems and Signal Processing,* 21**,** 1512-1520.

BBCNEWS. 2013. Dreamliner: Boeing 787 planes grounded on safety fears.

BOEING. 2017. *787 Dreamliner by Design* [Online]. http://www.boeing.com/commercial/787/by-design/#/advanced-composite-use. [Accessed 10/10/2017 2017].

BOUZID, O. M., TIAN, G. Y., CUMANAN, K. & MOORE, D. 2015. Structural health monitoring of wind turbine blades: Acoustic source localization using wireless sensor networks. *Journal of Sensors,* 2015.

CALLAWAY, E., GORDAY, P. & HESTER, L. 2002. Home Networking with IEEE 802.15.4: A Developing Standard for Low-Rate Wireless Personal Area Networks. *IEEE Communications Magazine.* IEEE.

CARBAUGH, D. 2001. Airplane Vibration. *AERO Magazine.* Boeing.

CARPINTERI, A., LACIDOGNA, G., MANUELLO, A. & NICCOLINI, G. 2013. Acoustic Emission Wireless Transmission System for Structural and Infrastructural Networks. *8th Internation Conference on Fracture Mechanics of Concrete and Concrete Strucures.* Toledo-Spain.

CHANG, Z. & MAL, A. 1999. Scattering of Lamb waves from a rivet hole with edge cracks. *Mechanics of materials,* 31**,** 197-204.

CHO, Y. 2000. Estimation of ultrasonic guided wave mode conversion in a plate with thickness variation. *IEEE transactions on ultrasonics, ferroelectrics, and frequency control,* 47**,** 591-603.

CHO, Y. & ROSE, J. L. 1996. A boundary element solution for a mode conversion study on the edge reflection of Lamb waves. *The Journal of the Acoustical Society of America,* 99**,** 2097-2109.

CHOI, M., SHRESTHA, M. M., LEE, J.-R. & PARK, C.-Y. 2018. Development of a laser-powered wireless ultrasonic device for aircraft structural health monitoring. *Structural Health Monitoring,* 17**,** 145-155.

CHUANG, S. 1987. Real-Time Aircraft Structural Monitoring Using Acoustic Emission. *Review of Progress in Quantitative Nondestructive Evaluation.* Springer.

CIVIL AVIATION AUTHORITY, C. 2015. *Lithium batteries* [Online]. www.caa.co.uk. Available: https://www.caa.co.uk/Commercial-industry/Airports/Safety/Dangerous-goods/Lithium-batteries/ [Accessed 15/10/2017 2017].

CRACKNELL, A. P. 1980. *Ultrasonics*, Wykeham Publications LTD.

CRAWFORD, F. S. 1968. *Waves*.

CRIVELLI, D., GUAGLIANO, M. & MONICI, A. 2014. Development of an artificial neural network processing technique for the analysis of damage evolution in pultruded composites with acoustic emission. *Composites Part B: Engineering,* 56**,** 948-959.

DAQAQ, M. F., MASANA, R., ERTURK, A. & QUINN, D. D. 2014. On the role of nonlinearities in vibratory energy harvesting: a critical review and discussion. *Applied Mechanics Reviews,* 66**,** 040801.

DENG, X. 1995. Mechanics of debonding and delamination in composites: Asymptotic studies. *Composites Engineering,* 5**,** 1299-1315.

DRINKWATER, B. W., CASTAINGS, M. & HOSTEN, B. 2003. The measurement of A 0 and S 0 Lamb wave attenuation to determine the normal and shear stiffnesses of a compressively loaded interface. *The Journal of the Acoustical Society of America,* 113**,** 3161-3170.

DUTOIT, N. E., WARDLE, B. L. & KIM, S.-G. 2005. Design Considerations for MEMS-Scale Piezoelectric Mechanical Vibration Energy Harvesters *Integrated Ferroelectrics,* 71**,** 121-160.

EATON, M., MAY, M., FEATHERSTON, C., HOLFORD, K., HALLET, S. & PULLIN, R. Characterisation of damage in composite structures using acoustic emission. Journal of Physics: conference series, 2011. IOP Publishing, 012086.

EATON, M., PULLIN, R. & HOLFORD, K. 2012a. Towards improved damage location using acoustic emission. *Proceedings of the Institution of Mechanical Engineers, Part C: Journal of Mechanical Engineering Science,* 226**,** 2141-2153.

EATON, M. J., PULLIN, R. & HOLFORD, K. M. 2012b. Acoustic emission source location in composite materials using Delta T Mapping. *Composites Part A: Applied Science and Manufacturing,* 43**,** 856-863.

ELSHEIKH, M. H., SHNAWAH, D. A., SABRI, M. F. M., SAID, S. B. M., HASSAN, M. H., BASHIR, M. B. A. & MOHAMAD, M. 2014. A review on thermoelectric renewable energy: Principle parameters that affect their performance. *Renewable and Sustainable Energy Reviews,* 30**,** 337-355.

ERTURK, A., RENNO, J. M. & INMAN, D. J. 2009. Modeling of Piezoelectric Energy Harvesting from an L-shaped Beam-mass Structure with an Application to UAVs. *Journal of Intelligent Material Systems and Structures,* 20**,** 529-544.

FEDERAL AVIATION ADMINISTRATION 2011. RTCA Document DO-160 versions D, E, F, and G, "Environmental Conditions and Test Procedures for Airborne Equipment". *In:* ADMINISTRATION, F. A. (ed.).

FENG, B., RIBEIRO, A. L. & RAMOS, H. G. 2017. Interaction of Lamb waves with the edges of a delamination in CFRP composites and a reference-free localization method for delamination. *Measurement*.

FOTEDAR, N. & SAINI, P. An Energy Efficient Algorithm for Time Synchronization in Sensor Networks. Proceedings of the International Conference on High Performance Compilation, Computing and Communications, 2017. ACM, 91-96.

GODIN, N., HUGUET, S. & GAERTNER, R. 2005. Integration of the Kohonen's self-organising map and k-means algorithm for the segmentation of the AE data collected during tensile tests on cross-ply composites. *NDT & E International,* 38**,** 299-309.

GODÍNEZ-AZCUAGA, V. & OBDULIA, L. Structural Health Monitoring of Aerospace Structures Using a Low-Power, Wireless, Multichannel Acoustic Emission Node. 5th International Symposium on NDT in Aerospace, 2013. 13-15.

GRIGG, S., PEARSON, M., MARKS, R., FEATHERSTON, C. & PULLIN, R. 2015. Assessment of Damage Detection in Composite Structures Using 3D Vibrometry. *Journal of Physics: Conference Series,* 628**,** 012101.

GROSSE, C. U., GLASER, S. D. & KRUGER, M. 2010. Initial development of wireless acoustic emission sensor Motes for civil infrastructure state monitoring. *Smart Struct. Syst,* 6**,** 197-209.

GÜEMES, A., FERNÁNDEZ-LÓPEZ, A., DÍAZ-MAROTO, P., LOZANO, A. & SIERRA-PEREZ, J. 2018. Structural Health Monitoring in Composite Structures by Fiber-Optic Sensors. *Sensors,* 18**,** 1094.

GUO, H. & CROSSLEY, P. 2017. Design of a Time Synchronization System Based on GPS and IEEE 1588 for Transmission Substations. *IEEE Transactions on Power Delivery,* 32**,** 2091-2100.

HALL, M. P. M., BARCLAY, L. W. & HEWITT, M. T. 1996. *Propagation of Radiowaves*, The Institurion of Electrical Engineers.

HAMSTAD, M., O'GALLAGHER, A. & GARY, J. 2002. A wavelet transform applied to acoustic emission. *J. Acoust. Emiss,* 20**,** 39-61.

HENSMAN, J., MILLS, R., PIERCE, S. G., WORDEN, K. & EATON, M. 2010. Locating acoustic emission sources in complex structures using Gaussian processes. *Mechanical Systems and Signal Processing,* 24**,** 211-223.

HERRASTI, Z., VAL, I., GABILONDO, I., BERGANZO, J., ARRIOLA, A. & MARTÍNEZ, F. 2016. Wireless sensor nodes for generic signal conditioning: Application to Structural Health Monitoring of wind turbines. *Sensors and Actuators A: Physical,* 247**,** 604-613.

HEW, Y., DESHMUKH, S. & HUANG, H. 2011. A wireless strain sensor consumes less than 10 mW. *Smart Materials and Structures,* 20**,** 105032.

HOLFORD, K. M., EATON, M. J., HENSMAN, J. J., PULLIN, R., EVANS, S. L., DERVILIS, N. & WORDEN, K. 2017. A new methodology for automating acoustic emission detection of metallic fatigue fractures in highly demanding aerospace environments: An overview. *Progress in Aerospace Sciences,* 90**,** 1-11.

HONG, W., XIAO, P., LUO, H. & LI, Z. 2015. Microwave axial dielectric properties of carbon fiber. 5**,** 14927.

HORN, M. 1996. *Acoustic Emission Source Location by Reverse Ray Tracing*. United States patent application.

IEEE 1998. IEEE Standard Definitions of Terms for Radio Wave Propagation. *IEEE Std 211-1997***,** i.

JENMAN, D. 2016a. *RE: MK3 Design Handbook.* Type to GRIGG, S.

JENMAN, D. 2016b. *RE: Sentient Filter characteristics.* Type to GRIGG, S.

JIANHUA, L., DEMIRKIRAN, I., YANG, T. & HELFRICK, A. Communication schemes for aerospace wireless sensors. 2008 IEEE/AIAA 27th Digital Avionics Systems Conference, 26-30 Oct. 2008 2008. 5.D.4-1-5.D.4-9.

JOSHI, P., IMADABATHUNI, M., HE, D., AL-KATEB, M. & BECHHOEFER, E. 2012. Application of the condition based maintenance checking system for aircrafts. *Journal of Intelligent Manufacturing,* 23**,** 277-288.

KADRI, U., CRIVELLI, D., PARSONS, W., COLBOURNE, B. & RYAN, A. 2017. Rewinding the waves: tracking underwater signals to their source. *Scientific Reports,* 7**,** 13949.

KAMINSKI-MORROW, D. 2012a. Airbus admits no quick-fix for A380 wing-rib crack issue. *Flightglobal.com*.

KAMINSKI-MORROW, D. 2012b. Airbus traces A380 wing cracks to manufacturing process. *Flightglobal.com*.

KIM, M. & DEMO, J. Aircraft contaminant and leak detection sensor system for condition based maintenance. IEEE Aerospace Conference Proceedings, 2017.

KIM, S., PAKZAD, S., CULLER, D., DEMMEL, J., FENVES, G., GLASER, S. & TURON, M. 2007. Health monitoring of civil infrastructures using wireless sensor networks. *Proceedings of the 6th international conference on Information processing in sensor networks.* Cambridge, Massachusetts, USA: ACM.

KURZ, J. H., GROSSE, C. U. & REINHARDT, H.-W. 2005. Strategies for reliable automatic onset time picking of acoustic emissions and of ultrasound signals in concrete. *Ultrasonics,* 43**,** 538-546.

LAMB, H. 1917. On Waves in an Elastic Plate. *Proceedings of the Royal Society of London. Series A,* 93**,** 114-128.

LAMMERING, R., GABBERT, U., SINAPIUS, M., SCHUSTER, T. & WIERACH, P. 2018. *Lamb-Wave Based Structural Health Monitoring in Polymer Composites*, Springer International Publishing.

LEDECZI, Á., HAY, T., VOLGYESI, P., HAY, D. R., NADAS, A. & JAYARAMAN, S. 2009. Wireless Acoustic Emission Sensor Network for Structural Monitoring. *IEEE Sensors Journal,* 9**,** 1370-1377.

LEWIS, F. L. 2004. Wireless sensor networks. *Smart environments: technologies, protocols, and applications***,** 11-46.

LEWIS, M. F. 1995. Rayleigh waves-a progress report. *European Journal of Physics,* 16**,** 1.

LIU, C. & JING, X. 2016. Vibration energy harvesting with a nonlinear structure. *Nonlinear Dynamics,* 84**,** 2079-2098.

LIU, P., LIM, H. J., YANG, S., SOHN, H., LEE, C. H., YI, Y., KIM, D., JUNG, J. & BAE, I.-H. 2017. Development of a "stick-and-detect" wireless sensor node for fatigue crack detection. *Structural Health Monitoring,* 16**,** 153-163.

LOGAN, S. & SANKARESWARAN, U. M. 2015. Performance analysis of wireless sensors for aircraft control. *Journal of Vibration and Control,* 21**,** 211-216.

LOWE, M. J. 1995. Matrix techniques for modeling ultrasonic waves in multilayered media. *IEEE transactions on ultrasonics, ferroelectrics, and frequency control,* 42**,** 525-542.

LU, C., DING, P. & CHEN, Z. 2011. Time-frequency Analysis of Acoustic Emission Signals Generated by Tension Damage in CFRP. *Procedia Engineering,* 23**,** 210-215.

MAEDA, N. 1985. A Method for Reading and Checking Phase Time in Auto-Processing System of Seismic Wave Data. *Zisin (Journal of the Seismological Society of Japan. 2nd ser.),* 38**,** 365-379.

MAHMOOD, A. & JÄNTTI, R. Time synchronization accuracy in real-time wireless sensor networks. 2009 IEEE 9th Malaysia International Conference on Communications (MICC), 15-17 Dec. 2009 2009. 652-657.

MANCINI, R. 2001. Designing with comparators.

MARKS, R., CLARKE, A., FEATHERSTON, C., PAGET, C. & PULLIN, R. 2016. Lamb Wave interaction with adhesively bonded stiffeners and disbonds using 3D vibrometry. *Applied Sciences,* 6**,** 12.

MARKS, R., CLARKE, A., FEATHERSTON, C. A. & PULLIN, R. 2017. Optimization of acousto-ultrasonic sensor networks using genetic algorithms based on experimental and numerical data sets. *International Journal of Distributed Sensor Networks,* 13**,** 1550147717743702.

MARKS, R. A. 2016. *Methodology platform for prediction of damage events for selfsensing aerospace panels subjected to real loading conditions.* Doctor of Philosophy, Cardiff University.

MATT, H. M. & DI SCALEA, F. L. 2007. Macro-fiber composite piezoelectric rosettes for acoustic source location in complex structures. *Smart Materials and Structures,* 16**,** 1489.

MCCRORY, J. P., AL-JUMAILI, S. K., CRIVELLI, D., PEARSON, M. R., EATON, M. J., FEATHERSTON, C. A., GUAGLIANO, M., HOLFORD, K. M. & PULLIN, R. 2015. Damage classification in carbon fibre composites using acoustic emission: A comparison of three techniques. *Composites Part B: Engineering,* 68**,** 424-430.

MCKEON, J. & HINDERS, M. 1999. Lamb wave scattering from a through hole. *Journal of Sound and Vibration,* 224**,** 843-862.

MILLER, R. K. 1987. *Nondestructive Testing Handbook, Second Edition:Volume 5, Acoustic Emission Testing,* USA, American Society of Nondestructive Testing.

MISTRAS. 2013a. *1284: The first Multi Channel Wireless Acoustic Emission System* [Online]. http://www.mistrasgroup.com/products/company/Publications/2$Acoustic_Emission/1284_AE_Wireless_Node.pdf. [Accessed 20/01/2018].

MISTRAS 2013b. EXPRESS-8: An Eight-Channel Acoustic Emission Board & System. *In:* MISTRAS (ed.). http://www.mistrasgroup.com/products/company/Publications/2$Acoustic_Emission/EXPRESS-8.pdf.

MISTRAS. 2017. *STRUCTURAL MONITORING* [Online]. http://mistrasgroup.co.uk/structural-monitoring/#AE-Monitoring. [Accessed 13/11/2017 2017].

MURRAY, K. 2016. Impact Detection in a Composite A320 Vertical Stabiliser using Ultrasonic Techniques. *Undergraduate Dissertation.* Cardiff University.

NAIR, A. & CAI, C. S. 2010. Acoustic emission monitoring of bridges: Review and case studies. *Engineering Structures,* 32**,** 1704-1714.

NEWS-DIRECT 2012. Airbus A380 wing repairs to take up to eight weeks. https://www.youtube.com/watch?v=jSspwCWZaOk

NOEL, A., ABDAOUI, A., BADAWY, A., ELFOULY, T., AHMED, M. & SHEHATA, M. 2017. Structural Health Monitoring using Wireless Sensor Networks: A Comprehensive Survey. *IEEE Communications Surveys & Tutorials,* PP**,** 1-1.

OSTASEVICIUS, V., JURENAS, V., AUGUTIS, V., GAIDYS, R., CESNAVICIUS, R., KIZAUSKIENE, L. & DUNDULIS, R. 2017. Monitoring the condition of the cutting tool using self-powering wireless sensor technologies. *The International Journal of Advanced Manufacturing Technology,* 88**,** 2803-2817.

PAGET, C. 2012. *RE: Vibration Data from A380 Wing.* Type to PEARSON, M.

PAGET, C. A., ATHERTON, K. & O'BRIEN, E. Triangulation algorithm for damage location in aeronautical composite structures. Proceedings of the 4th International Workshop on Structural Health Monitoring (F. Chang, ed.),(Stanford, CA, USA), 2003. 363-370.

PAGET, C. A. & REHMAN, M. A. Multimodal location algorithm for Lamb waves propagating through anisotropic materials. SPIE Smart Structures and Materials + Nondestructive Evaluation and Health Monitoring, 2017. SPIE, 9.

PANATIK, K. Z., KAMARDIN, K., SHARIFF, S. A., YUHANIZ, S. S., AHMAD, N. A., YUSOP, O. M. & ISMAIL, S. Energy harvesting in wireless sensor networks: A survey. 2016 IEEE 3rd International Symposium on Telecommunication Technologies, ISTT 2016, 2017. 53-58.

PARADIES, R. 1996. Designing quasi-isotropic laminates with respect to bending. *Composites Science and Technology,* 56**,** 461-472.

PARKINS, A. 28/07/2017 2017. *RE: Index of HW Communications Sentient Presentations.* Type to GRIGG, S.

PEARSON, M. 2013. *Development of lightweight structural health monitoring systems for aerospace applications.* PhD, Cardiff University.

PEARSON, M. R., EATON, M., FEATHERSTON, C., PULLIN, R. & HOLFORD, K. 2017. Improved acoustic emission source location during fatigue and impact events in metallic and composite structures. *Structural Health Monitoring,* 16**,** 382-399.

PEARSON, M. R., EATON, M. J., PULLIN, R., FEATHERSTON, C. A. & HOLFORD, K. M. Energy harvesting for aerospace structural health monitoring systems. Journal of Physics: Conference Series, 2012. IOP Publishing, 012025.

PHYSICAL ACOUSTICS CORPORATION 2004. AEwin Software Users Manual. MISTRAS Holdings Corp.

PHYSICAL ACOUSTICS CORPORATION 2011a. 2/4/6 Preamplifier. *In:* MISTRAS (ed.). http://www.physicalacoustics.com/content/literature/preamplifiers/2-4-6_Preampliflier_Product_Data_Sheet.pdf: Physical Acoustics Corporation,.

PHYSICAL ACOUSTICS CORPORATION 2011b. Nano30 Sensor - Product Data Sheet. http://www.physicalacoustics.com/content/literature/sensors/Model_Nano30.pdf: Physical Acoustics Corporation,.

PHYSICAL ACOUSTICS CORPORATION. 2017. *NANO30 - 150-750 KHZ MINIATURE AE SENSOR WITH INTEGRAL COAXIAL CABLE* [Online]. http://www.physicalacoustics.com/by-product/nano30-150-750-khz-miniature-ae-sensor-with-integral-coaxial-cable/. [Accessed 21/11/2017 2017].

PIECZONKA, Ł., AMBROZIŃSKI, Ł., STASZEWSKI, W. J., BARNONCEL, D. & PÉRÈS, P. 2017. Damage detection in composite panels based on mode-converted Lamb waves sensed using 3D laser scanning vibrometer. *Optics and Lasers in Engineering,* 99**,** 80-87.

POTTIE, G. J. & KAISER, W. J. 2000. Wireless integrated network sensors. *Commun. ACM,* 43**,** 51-58.

PRIETO, M. D., MILLAN, D. Z., WANG, W., ORTIZ, A. M., REDONDO, J. A. O. & MARTINEZ, L. R. 2016. Self-Powered Wireless Sensor Applied to Gear Diagnosis Based on Acoustic Emission. *IEEE Transactions on Instrumentation and Measurement,* 65**,** 15-24.

PROSSER, W. H. 2003. Development of Structural Health Management Technology for Aerospace Vehicles. NASA; Washington, DC, United States.

PULLIN, R., EATON, M. J., PEARSON, M. R., FEATHERSTON, C., LEES, J., NAYLON, J., KURAL, A., SIMPSON, D. J. & HOLFORD, K. 2012. On the Development of a Damage Detection System using Macro-fibre Composite Sensors. *Journal of Physics: Conference Series,* 382**,** 012049.

RADIO TECHNICAL COMMISSION FOR AERONAUTICS 2004. RTCA DO-160E. *Environmental Conditions and Test Procedures for Airborne Equipment*

REUSSER, R. S., HOLLAND, S. D., CHIMENTI, D. E. & ROBERTS, R. A. 2014. Reflection and transmission of guided ultrasonic plate waves by vertical stiffeners. *The Journal of the Acoustical Society of America,* 136**,** 170-182.

ROSE, J. L. 2014. *Ultrasonic Guided Waves in Solid Media*, Cambridge University Press.

SACHSE, W. H. & SANCAR, S. 1986. Acoustic emission source location on plate-like structures using a small array of transducers. Google Patents.

SAMSON, D., KLUGE, M., BECKER, T. & SCHMID, U. 2011. Wireless sensor node powered by aircraft specific thermoelectric energy harvesting. *Sensors and Actuators A: Physical,* 172**,** 240-244.

SCHIJVE, J. 2009. Fatigue damage in aircraft structures, not wanted, but tolerated? *International Journal of Fatigue,* 31**,** 998-1011.

SCHILLER, J. 2003. *Mobile Communications*, Pearson Education Limited.

SCHUBEL, P. J., CROSSLEY, R. J., BOATENG, E. K. G. & HUTCHINSON, J. R. 2013. Review of structural health and cure monitoring techniques for large wind turbine blades. *Renewable Energy,* 51**,** 113-123.

SCRUBY, C. B. 1987. An introduction to acoustic emission. *Journal of Physics E: Scientific Instruments,* 20**,** 946.

SHEN, G. 2017. Progress of Acoustic Emission Technology on Pressure Equipment in China. *Proceedings of the World Conference on Acoustic Emission-2015.* Spinger Proceedings in Physics.

SHI, Y., HALLETT, S. R. & ZHU, M. 2017. Energy harvesting behaviour for aircraft composites structures using macro-fibre composite: Part I – Integration and experiment. *Composite Structures,* 160**,** 1279-1286.

SILVA, E. D. 2001. *High Frequency and Microwave Engineering*, Butterworth-Heinemann.

SMART MATERIAL CORP 2017. Macro Fibre Composite - MFC. Smart Materials Corp.

SOUNDWEL. 2017. *SAEW2 distributed acoustic emission* [Online]. http://www.soundwel.cn/pro/235.html: Soundwel. Available: http://www.soundwel.cn/pro/235.html [Accessed 06/07/2017].

SPECKMANN, H. H. R. 2006. Structural Health Monitoring: A Contribution to the Intelligent Aircraft Structure. *ECNDT.* Berlin.

STANKOVIC, J. A. 2008. Wireless Sensor Networks. *Computer,* 41**,** 92-95.

STASZEWSKI, W., LEE, B. & TRAYNOR, R. 2007. Fatigue crack detection in metallic structures with Lamb waves and 3D laser vibrometry. *Measurement Science and Technology,* 18**,** 727.

SU, Z., YE, L. & LU, Y. 2006. Guided Lamb waves for identification of damage in composite structures: A review. *Journal of Sound and Vibration,* 295**,** 753-780.

SWIFT, T. 1987. *Damage tolerance in pressurized fuselages*, McDonnell Douglas.

SZCZYGIEL, M. 2014. *SENTIENT Project* [Online]. http://www.sentientproject.co.uk/. [Accessed 17/05/2018 2018].

TALRENJA, R. 1981. Fatigue of composite materials: damage mechanisms and fatigue-life diagrams. *Proceedings of the Royal Society of London. A. Mathematical and Physical Sciences,* 378**,** 461-475.

TENSI, H. M. The Kaiser-effect and its scientific background. EWGAE, 2004.

THANGARAJ, K., ELEFSINIOTS, A., BECKER, T., SCHMID, U., LEES, J., FEATHERSTON, C. A. & PULLIN, R. 2014. Energy storage options for wireless sensors powered by aircraft specific thermoelectric energy harvester. *Microsystem Technologies,* 20**,** 701-707.

VALLEN 2002. AE Testing Fundamentals, Equipment, Applications. *In:* VALLEN (ed.).

VIEIRA, D. R. L., PAULA LAVORATO 2016. Maintenance, Repair and Overhaul (MRO) Fundamentals and Strategies: An Aeronautical Industry Overview. *International Journal of Computer Applications,* 135.

WAANDERS, J. W. 1991. *Piezoelectric Ceramics - Properties and applications,* Eindhoven, Philips Components.

WAITE, A. D. 2005. *Sonar for Practicing Engineers*, John Wiley & Sons Ltd,.

WEBSTER, J. P.-A., R 1999. *Analog Signal Processing*, John Wiley & Sons.

WEI, C. & JING, X. 2017. A comprehensive review on vibration energy harvesting: Modelling and realization. *Renewable and Sustainable Energy Reviews,* 74**,** 1-18.

WEIR, W. B. 1974. Automatic measurement of complex dielectric constant and permeability at microwave frequencies. *Proceedings of the IEEE,* 62**,** 33-36.

WEVERS, M. 1999. One sensor linear location of acoustic emission events using plate wave theories. *Materials Science and Engineering: A,* 265**,** 254-261.

WILSON, W. C. & ATKINSON, G. M. 2014. Passive Wireless Sensor Applications for NASA's Extreme Aeronautical Environments. *IEEE Sensors Journal,* 14**,** 3745-3753.

WORDEN, K. 2001. Rayleigh and Lamb Waves - Basic Principles. *Strain,* 37**,** 167-172.

WU, X., LIN, J., KATO, S., ZHANG, K., REN, T. & LIU, L. 2008. A frequency adjustable vibration energy harvester. *Proceedings of PowerMEMS***,** 245-248.

YEDAVALLI, R. K. & BELAPURKAR, R. K. 2011. Application of wireless sensor networks to aircraft control and health management systems. *Journal of Control Theory and Applications,* 9**,** 28-33.

YI, J. M., KANG, M. J. & NOH, D. K. 2015. SolarCastalia: Solar Energy Harvesting Wireless Sensor Network Simulator. *International Journal of Distributed Sensor Networks,* 11**,** 415174.

ZHANG, S., YAN, B., LUO, Y., MIAO, W. & XU, M. 2015. An Enhanced Piezoelectric Vibration Energy Harvesting System with Macro Fiber Composite. *Shock and Vibration,* 2015**,** 7.

ZHANG, S. S., XU, K. & JOW, T. R. 2003. The low temperature performance of Li-ion batteries. *Journal of Power Sources,* 115**,** 137-140.

ZHAO, X., GAO, H., ZHANG, G., AYHAN, B., YAN, F., KWAN, C. & ROSE, J. L. 2007. Active health monitoring of an aircraft wing with embedded piezoelectric sensor/actuator network: I. Defect detection, localization and growth monitoring. *Smart materials and structures,* 16**,** 1208.

ZHU, L., FU, Y., CHOW, R., SPENCER, B. F., PARK, J. W. & MECHITOV, K. 2018. Development of a High-Sensitivity Wireless Accelerometer for Structural Health Monitoring. *Sensors,* 18**,** 262.

ZIGBEE. 2017. *ZigBee Certified Products* [Online]. http://www.zigbee.org. Available: http://www.zigbee.org/zigbee-products-2/ [Accessed].